Matched Field Processing With Broadband Random Sources

by

Reza Mokhtari Dizaji

B. Sc., Sharif University of Technology, Tehran, Iran, 1992
M. Sc., K. N. T. University of Technology, Tehran, Iran, 1994

A Dissertation Submitted in Partial Fulfillment of the Requirement for the Degree of

DOCTOR OF PHILOSOPHY

in the

Department of Electrical and Computer Engineering

UNIVERSITY OF VICTORIA

Supervisors: Dr. N. Ross Chapman, Dr. R. Lynn Kirlin

Abstract

The goal of this thesis is to introduce new matched field processors (MFPs) for estimating the source location and the environmental parameters of a shallow water waveguide in which the source transmits either broadband or narrowband random signals. The processors provide higher resolution in localizing sources in a noisy environment, and have lower side lobe levels compared to conventional MFPs. MFPs are developed for non-stationary (NS), and wide sense stationary (WSS) random sources. For time varying sources, formulations based on an evolutive spectrum concept are proposed to obtain the advantages of time-frequency analysis. For each of the above formulations, two estimation methods are proposed, a self-CR (cross relation) or a cross-CR according to which output signal channel is used to construct the estimator. In addition, the new high resolution MFPs are also formulated for use with deterministic sources. All the above formulations derive second order MFPs. We extend the second-order cross-relation concept to higher order MFPs.

The MFPs developed in this thesis are applied for source localization and estimation of waveguide model parameters. We propose an adaptive matched field processing system for estimating geoacoustic parameters of the ocean bottom. The method makes use of ambient noise from signals of opportunity such as broadband random signals radiated by passing ships to estimate the geoacoustic properties of a new environment. We also propose a novel phase-regulated back wave propagation (BWP) technique to increase the sensitivity of MFP for geoacoustic model parameters having low sensitivity. We show theoretically that we can increase the sensitivity by a factor using the phase regulation procedure. We also show that the spatial resolution of signal energy that is focused by the BWP algorithm is increased when the sensitivity factor increases. This leads us to define a criterion based on the spatial distribution of signal energy around the true source location. We also propose a multi-step search process to avoid using a complicated multi-dimensional search process. We present an evaluation of new matched field processors for source localization and geoacoustic parameter estimation with other MFPs. The evaluation is conducted using results obtained from both simulation and the Pacific Shelf experiment.

Table of Contents

List of Figures

List of Tables

List of Abbreviations

MFP	Matched Field Processor
CW	Continuous Wave
MV	Minimum Variance
TF-MFP	Time-Frequency Matched Field Processing
MEVA	Multi-Element Vertical Array
ODP	Ocean Drilling Program
VLA	Vertical Linear Array
GPS	Global Positioning System
PDF	Probability Density Function
CR	Cross-Relation
CR-MFP	Cross-Relation Matched Field Processing
TF	Time-Frequency
WSS	Wide Sense Stationary
SNR	Signal-to-Noise Ratio
Self-CR	Self-Cross-Relation
Cross-CR	Cross-Cross-Relation
FFT	Fast Fourier Transform
TFD	Time-Frequency Distribution
AF	Ambiguity Function
SVD	Singular Value Decomposition
MUSIC	Multi Signal Classification
STD	Standard Deviations
BWP	Back Wave Propagation
MFI	Matched Field Inversion
PE	Parabolic Equation
BSI	Blind System Identification
FIR	Finite Impulse Response

BMF	Bilinear Matched Field Processor
NS	Non-Stationary
STFT	Short-Time Fourier Transform
WT	Wavelet Transform
PSD	Power Spectral Density
CS	Channel Subspace
AOP	Approximate Orthogonal Processor
MDL	Minimum Description Length
MC	Multiple Constraint
MMP	Matched Mode Processor
OUFP	Optimum Uncertain Field Processor
MLMFP	Maximum Likelihood Matched Field Processor

Acknowledgment

I would like to thank my supervisors, Professor R. Lynn Kirlin of the Department of Electrical and Computer Engineering and Professor N. Ross Chapman of the School of Earth and Ocean Sciences, for their supports, close supervisions, continuous encouragement, patience and advice during my research work.

Financial assistance provided by MacDonald-Dettwiler Company, National Science and Engineering Research Council of Canada, and National Defense Department is also gratefully acknowledged.

I thank my family for their continuous support, patience, and encouragement throughout my life.

Dedication

To my mother Mrs. Akram Shakiba,

To my father Mr. Vali Mokhtari Dizaji,

Chapter One
Introduction, Thesis outline

Advanced signal processing techniques for detecting and localizing underwater targets in shallow water make use of environmental information about the ocean waveguide in order to achieve improved performance over conventional array processing techniques. Model-based methods such as matched field processing provide this capability. Matched field processing is a full-field signal processing method in which measured acoustic fields from a sound source are compared to modeled fields calculated for a specific source-receiver geometry and ocean waveguide environment. The matching is carried out for many candidate target locations within a specific search region (range and depth) to form ambiguity surface whose values indicate the likelihood that a source is present. Optimum performance (i.e. localization) is achieved for the condition that the modeled ocean environment and experimental geometry match the true conditions. Initially, matched field processing methods were formulated for narrow band, deterministic sources; however an extension to wideband sources has been proposed and applied for localization with multiple-frequency continuous wave (CW) data by averaging matched field processor (MFP) results for single frequencies over a band of CW tones.

The goal of this thesis is to introduce new matched field processors (MFPs) for estimating the source location and the environmental parameters of a shallow water waveguide in which the source transmits either broadband or narrowband random signals. The processors provide higher resolution in localizing sources in a noisy environment, and have lower side lobe levels compared to conventional MFPs. In addition, the new high resolution MFPs are also formulated for use with deterministic signals.

In parallel to the applications for target localization, matched field processing has been applied to estimate ocean bottom properties. In the thesis, we propose an adaptive matched field processing system for estimating geoacoustic parameters of the ocean bottom. The method makes use of ambient noise from signals of opportunity as sound sources to estimate the geoacoustic properties of a new environment. Such information is available by processing

broadband noise radiated by passing ships. Ships are strong sources of underwater sound, the signal generally consisting of a combination of machinery tonal signals along with propeller and hydrodynamic noise. The ships signal is random and broadband, with a complicated probability distribution function which characteristically produces both continuous spectrum components and a set of line components. We also propose a novel phase-regulated back wave propagation technique to increase the sensitivity of MFP for geoacoustic model parameters having low sensitivity.

Matched field processing can be considered as a sub-category of a more general approach known as blind system identification (BSI). Blind system identification is a fundamental signal processing technique for estimating both unknown source and unknown system parameters when only the system output data are known. The technique has widespread application in a number of different areas, such as speech recognition, cancellation of reverberation, image restoration, data communication, and seismic and underwater acoustic signal processing. In many instances, especially in sonar and seismic applications, the transfer function, or signal propagation model, is nearly known, and the desired result is not the transfer function itself, but the unknown parameters of the signal propagation model. In underwater acoustics numerical methods based on ray theory, wave-number integration, parabolic equation and normal modes are available for calculating the acoustic field in an arbitrary waveguide to very high accuracy. The task is instead to find the unknown parameters of the waveguide by modeling the acoustic field. In chapter two, we derive methods that can be used to determine the unknown parameters of the transfer function from the basic formalism of BSI. We show that the widely used Bartlett family of matched field processors can be obtained from this formalism. Section 2.1 considers the formulation for acoustic wave propagation in the ocean environment. After a brief explanation of practical methods for the solution of the wave equation we discuss in more detail the normal modes method in section 2.2. The normal mode code ORCA (see section 2.3) is our primary model because of its ease of use, versatility and computational speed. In section 2.4 the theoretical background of the currently-used matched field processors is considered.

Chapter three introduces a cross-relation (CR) based matched field processing technique for estimating the source location and environmental parameters in shallow water (section 3.1). The source is assumed to be broadband or narrow-band random noise. However the processor is

applicable for broadband and narrow-band deterministic sources. The estimation formulas are derived for deterministic (section 3.2) and random sources (section 3.3) including non-stationary (NS) (sections 3.3.1), and wide sense stationary (WSS) (section 3.3.2) random sources. For time varying sources, formulations based on an evolutive spectrum concept are proposed to obtain the advantages of time-frequency analysis (section 3.4). For each of the above formulations, two estimation methods are proposed, a self-CR or a cross-CR according to which output signal channel is used to construct the estimator.

All the above formulations derive second order MFPs. We extend the second-order cross-relation concept to higher order MFPs (section 3.5). The higher order characteristic of this kind of processor provides the ability of canceling the effect of Gaussian random sources (either white or non-white) since the third and some higher odd moments of Gaussian random signals are zero.

In chapter four we consider the concept of back wave propagation (BWP) as an inversion method to estimate ocean bottom geoacoustic parameters for which the source location is known. A phase-regulation technique is introduced to increase the sensitivity of the method for geoacoustic model parameters having low sensitivity. We address the case of data consisting of signal plus additive noise. We show theoretically that we can increase the sensitivity by a factor using the phase regulation procedure. We also show that the spatial resolution of signal energy that is concentrated is increased when the sensitivity factor increases. This leads us to define a criterion based on the spatial distribution of signal energy around the true source location. This criterion is formulated based on the spatial variance of the back-propagated pressure field in a window around the known source location. We also propose a multi-step search process to avoid using a complicated multi-dimensional search process.

Chapter five presents an evaluation of cross-relation matched field processors for source localization, and compares their performance with other MFPs. The evaluation is conducted using results obtained from both simulation and experiment. The waveguide model used for the simulations is based on the environment at the site of the Pacific Shelf experiment. The replica or modeled fields are calculated using the normal mode model, ORCA [15]. Environmental parameters are assumed known in the simulation, and for the real data we rely on values obtained from seismic ground truth data in the region of experiment. At first we consider a random source generator to simulate ship noise. After adding measurement noise to the simulated data, the

performance of two different kinds of cross-relation MFPs (self and cross) is compared with the representatives of major MFP classes, i.e. Bartlett, minimum variance, and Westwood matched field processors. The comparison is based on both resolution and side-lobe level. In another subsection, we apply the time-frequency MFP to synthetic chirp signal for an environment that contains other random sources (such as wind noise, ocean waves, ship noises, and etc.). We show the performance of time-frequency MFP in recovering the chirp source location from only one pulse, and compare with the performance of other MFPs. We then apply higher order MFP data to evaluate the information content of higher order statistics of the ship noise in localization. This processor is helpful for environments in which there are Gaussian interference signals, either coherent in the form of a source or non-coherent in the form of measurement noise. The regular MFPs are insensitive to the higher order statistical content of ship noise, so can not use the complete information embedded in the ship noise.

Inversion results for estimating geoacoustic parameters from both simulated and experimental data from Pacific Shelf are given in chapter six. The components of the matched field inversion method include a geoacoustic model, a propagation model for calculating the acoustic field at the receiver, a cost function based on a matched field processor for assessing specific models, and an efficient search algorithm for searching the model parameter space. The practical application of the inversion depends in part on having an efficient method for searching the space of ocean bottom models. In the back wave propagation technique, we present a successive search algorithm in which the most sensitive environmental parameters are first estimated and then less sensitive parameters are estimated. For the case where broadband sources are considered as the inversion source, we can significantly reduce the search space by classifying the geoacoustic parameters based on the depth of acoustic wave penetration in the ocean bottom with respect to frequency. In this procedure we first estimate environmental parameters of upper layers near the sea floor using high frequencies, and then estimate parameters of deeper layers using lower frequencies. In section 6.1 we consider simulation and experimental results for an inversion using the back wave propagation technique. We estimate values for three model parameters, including water depth, compressional speed at the base of sediment (second) layer and the density of the sediment layer. These parameters can be classed as examples of high, medium and weak sensitivity to the ocean field. A broadband inversion

using the cross relation matched field processor (see section 3.3.2) is then considered in section 6.2. The inversion uses the ship radiated noise as a sound source to estimate the water depth, upper compressional speed of the first layer, and first layer thickness.

Chapter Two

Matched Field Processing Techniques, An Overview

Acoustic sensing continues to be the most practical form of remote sensing in the ocean since electromagnetic waves are significantly attenuated after a short range. In shallow water the geoacoustic properties of the sea bottom are required in order to accurately model acoustic wave propagation. In section 2.1 the formulation for acoustic wave propagation in the ocean environment is considered. There are a number of different methods for the practical solution of the wave equation. After a brief explanation of each method we discuss the normal modes method in section 2.2. The normal mode code ORCA is our primary model because of its ease of use, versatility and computational speed. ORCA allows us to use model-based methods to accurately estimate source location or environmental parameters.

Over the last decade the underwater acoustic community has shown an increasing strong interest in a model-based technique called matched field processing. This interest stems from its successful application to the localization of passive sources and the estimation of environmental parameters needed for accurate prediction of acoustic propagation in shallow water.

Matched field processing may be interpreted as an inversion process to estimate both target geometry (source localization) and geoacoustic parameters. Both types of inversion are generally cast as optimization processes in which a global search process is carried out over candidate model parameters or possible source locations. For geoacoustic inversion the components of the method are: a cost function based on a MF processor; an acoustic propagation model for calculating replica fields a form for the geoacoustic bottom model; and an efficient global search method. The geoacoustic model generally consists of profiles of the sound speed, density and attenuation in the bottom. These processes, applied primarily to continuous wave (CW) data, are described in Tolstoy [1]. Some researchers have recognized the potential improvement in performance available from broadband sources. Booth et al [2] reported improved detection and target localization by averaging MFP results for single frequencies over a band of CW tones.

Westwood [3] designed an efficient algorithm based on ray theory for target localization using pseudo-random broadband noise data received by a vertical array of hydrophones. Westwood's approach was extended for acoustic fields modeled by normal modes by Knobles and Mitchell [4]. Both these methods provided improved performance over incoherent frequency averages. A coherent MFP over frequency was developed by Porter and Michalopolou [5] and applied to source tracking.

In parallel to the development of algorithms for target localization, MFP has been applied to estimate ocean bottom properties. Although target localization can be carried out for an arbitrary array geometry, geoacoustic inversions have generally been done using vertical line arrays that provide a measure of the depth profile of the field in the water. The first investigations were carried out using CW signals [6,7]. However, the use of broadband signals has been considered. Hermand and Gerstoft [8] analyzed multi-tone CW data and observed that the inversion results at single frequencies were inconsistent across the band. An incoherent average over the band was essential for producing stable geoacoustic estimates that were in agreement with ground truth data. The same erratic behavior of estimates from single frequency inversion was observed by Tolstoy [1] in her analysis of spectral components of explosive charge data, using a high resolution MFP. In light of these difficulties, Hannay and Chapman [9] applied a fully coherent (in frequency and space) MFP to the analysis of their experimental data from explosive charges. This procedure is similar to the waveform matching approach used in seismology. The result indicated improved performance for the coherent processor over single frequency estimates.

In a related study Deane and Buckingham [10] have investigated the use of broadband noise from the sea surface in geoacoustic estimation. In this method the coherence of sea surface ambient noise measured at vertically separated sensors is used to invert the properties of the sediment in shallow water. Although these studies are primarily at high frequencies (1-20 kHz), the use of background noise as sound sources is a significant result.

The theoretical background of the currently-used matched field processors is considered in section 2.4.

2.1. Acoustic modeling

In the classical way of deriving the pressure field equation we assume a linear and stationary environment; i.e., the speed of sound and the quiescent density are independent of time, and only the first term of the adiabatic equation of state is involved in the wave equation. In this case the adiabatic relation between pressure and density [11,81] is

$$\rho\nabla.\left(\frac{1}{\rho}\nabla p\right)-\frac{1}{c^2}\frac{\partial^2 p}{\partial t^2}=0 \qquad (2.1)$$

where p is the pressure, ρ is the density and c is the sound speed (in an ideal fluid). It is assumed in (2.1) that the acoustic disturbance is propagated without transporting mass and the gravitational effects are negligible [12]. In an ideal fluid the assumption is made that that density is constant in space, and then the standard form of the wave equation becomes

$$\nabla^2 p-\frac{1}{c^2}\frac{\partial^2 p}{\partial t^2}=0 \qquad (2.2)$$

In an ocean environment, underwater sound is produced by a forcing mechanism, either natural or artificial. In the presence of a sound source we include a forcing function $f(\mathrm{r},t)$ to obtain the inhomogeneous equation

$$\nabla^2 p(\mathbf{r},t)-\frac{1}{c(\mathbf{r})^2}\frac{\partial^2 p(\mathbf{r},t)}{\partial t^2}=f(\mathbf{r},t) \qquad (2.3)$$

where r in cylindrical coordinates is the location of the source in range, depth, and bearing. By taking the Fourier transforms of both sides of equation (2.3) we have the Helmholtz equation

$$\left[\nabla^2+k^2(\mathbf{r})\right]p(\mathbf{r},\omega)=f(\mathbf{r},\omega) \qquad (2.4)$$

where $\omega=2\pi f$ and $k(\mathbf{r})=\dfrac{\omega}{c(\mathbf{r})}$ is the wavenumber at the frequency ω and c(r) is the sound speed function.

Five methods that are in widespread use for practical solution of the wave equation are:

1. Ray theory
2. Wave-number integration
3. Parabolic equation
4. Finite differences/ finite elements
5. Normal modes

Ray theory is derived as the asymptotic limit (infinite frequency) solution to the wave equation assuming that the sound speed varies gradually on scales relative to actual source wave length. The limit is approached by dividing the medium into arbitrarily small layers and effectively results in ray refraction according to Snell's law. Advantages of ray theoretic solutions are that they can be rapidly computed, are highly intuitive, and are easily visualized. However, low frequency behavior such as diffraction effects are not intrinsically included. Since MFP is recommended for low frequency applications, the ray theoretic approach is very rarely used [1]. GAMARAY is an example of an available ray tracing code [13].

Wave-number integration is a direct numerical solution of the Green's function for the Helmholtz equation. It utilizes a fast Fourier transform to approximate the horizontal wavenumber spectrum, and is generally acknowledged to provide an exact solution for all frequencies. Important features of this approach include accurate near-field descriptions and the capability to accurately include the effect of elastic boundaries. However, the method is restricted to a range-independent environment, and the usage requires considerable experience. Range dependent solutions are available, but are extremely slow computationally. SAFARI and OASES are examples of available wave-number integration codes [14].

The parabolic equation method solves a parabolic equation which approximates the Helmholtz equation and assumes that the received field results from only a restricted cone of (shallow) source launch angles. Such an assumption is often justified for long range propagation where steep angles initially present in the source field are stripped off by repeated interactions with an absorbing or attenuating bottom. This method is gaining in popularity because it can more easily accommodate range-dependent environments, and is computationally efficient. The main disadvantage of the parabolic equation method is that it requires significant expertise on the part of the user [1,81].

Finite differences and finite elements are most often used when back-scattering from rough surfaces needs to be taken into account. They are also useful for environments with complex geometry. However, these methods are computationally expensive [1,81].

The normal mode methods are derived from the Helmholtz equation by first assuming a separable coordinate system (usually cylindrical) and subsequently expressing the solution as a finite sum of depth-dependent eigen-functions or resonant modes. These modes satisfy the local

boundary conditions and are analogous to the vibration modes of a string. Normal modes are relatively fast to compute and can be adapted to accommodate both compressional and shear waves. This method is essentially range independent, however it has been extended to include a range-dependent environment by allowing for either full mode coupling (where the modes can exchange energy) or the simpler adiabatic approach. The main advantage of the normal mode methods is the capability to provide highly accurate and rapidly computed low frequency fields. Moreover, these methods are more easily automated than other methods [1,11,81].

2.2. Normal mode solution

Assuming cylindrical symmetry of the propagating sound wave within a shallow water wave-guide, let us use a cylindrical coordinate system, $\mathrm{r} = (r, \varphi, z)$ and define the source located on the z-axis, $\mathrm{r}_0 = (0,0,z_0)$. The Laplacian operator for the Helmholtz equation satisfies the following

$$\nabla^2 = \frac{1}{r}\frac{\partial}{\partial r} r \frac{\partial}{\partial r} + \frac{1}{r^2}\frac{\partial^2}{\partial \varphi^2} + \frac{\partial^2}{\partial z^2} \tag{2.5}$$

Assuming that sound speed *c(z)* and density $\rho(z)$ depend only on depth *z,* we have for the Helmholtz equation (2.4) in cylindrical coordinates

$$\frac{1}{r}\frac{\partial}{\partial r}(r\frac{\partial p}{\partial r}) + \rho(z)\frac{\partial}{\partial z}(\frac{1}{\rho(z)}\frac{\partial p}{\partial z}) + \frac{\omega^2}{c^2(z)} = -2\frac{\delta(r)}{r}\delta(z - z_s) \tag{2.6}$$

Using the method of separation of variables let us substitute $\mathrm{p}(r,z) = \varphi(r) \times \psi(z)$ in the above equation to obtain two separate equations for range and depth. By including the boundary conditions for a pressure release interface at the sea surface and appropriate conditions for the sea bottom (for instance rigid bottom, penetrable bottom), we obtain a modal equation in the form of a Sturm-Liouville eigenvalue problem with homogeneous boundary conditions. The modal equation has an infinite number of eigenfunctions, generally called modes, $\psi_m(z)$. Each eigenfunction has a distinct eigenvalue in the form of horizontal propagation constant k_{rm}. An important feature of the modes is that they are orthogonal and form a complete set; i.e., any

continuous function can be represented as an infinite sum of normal modes. At large range from the source it can be shown that the solution of equation (2.6) has the form

$$p(r,z) = \frac{j\pi}{\rho(z_s)} \sum_{m=1}^{\infty} \psi_m(\mathrm{z_s})\psi_m(\mathrm{z})\mathrm{H}_0^{(1)}\left(k_{rm}r\right) \qquad (2.7)$$

where $H_0^{(1)}(r)$ is the *Hankel* function of the first kind.

2.3. ORCA

The normal mode code ORCA [15] is our primary numerical model because of its ease of use, versatility and computational speed. ORCA considers the compressional wave attenuation by making the wavenumber complex. It includes viscoelastic (lossy solid) media, thus shear speed and shear attenuation are considered. ORCA is designed such that the wave equation can be solved in an arbitrary number of layers with variations in compressional speed, density, shear speed, and attenuation for each layer. In this thesis, it is applied to range-independent shallow water environments.

2.4. Theoretical background of the Matched Field Processor

In this section the theoretical framework of popular classes of matched field processors is discussed. These classes are

1. Bartlett matched field processor family
2. Maximum likelihood based matched field processors
3. Bilinear matched field processors

Formulations are given for either deterministic or random sources that radiate either narrow band or wide band signals.

We are interested in theorems that specify conditions that guarantee a unique solution for source location or for environmental parameters. These conditions are highly dependent on the ocean modeling method and the specific model parameter. Since the ocean environment is very complicated and the role of ocean model parameters can not be fully incorporated in the model (there is no analytic form), we usually prove only the necessary part of the uniqueness. In order

to satisfy the sufficient part we should carefully set the bounds of parameter variations. The bounds are usually obtained from complementary information provided by other sources such as ground truth data for environmental parameter estimation.

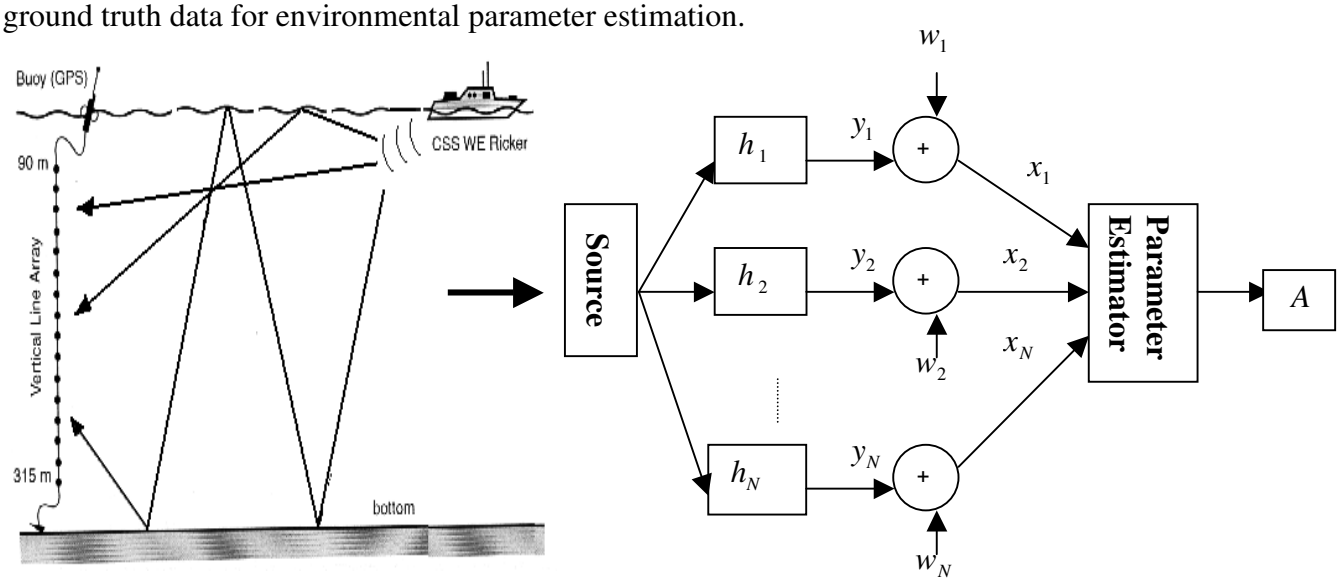

(a) (b)

Fig.2.1 (a) The geometry of an experiment for source localization or environmental parameter estimation using matched field processing (b) The multi-channel model of the experiment

The environment is modeled as a parallel set of linear transfer functions as shown in Fig. 2.1(b). The multi-channel system in the figure includes *N* linear transfer functions. The transfer function, h_i, corresponds to the paths traveled by acoustic waves from the ship to the i^{th} sensor (see Fig. 2.1 (a)), including interactions with ocean bottom and surface. It is assumed that the noise is additive and is spatially and temporally white, Gaussian and uncorrelated with the input signal.

We refer to *X, Y, W* and u as the measured, received, noise and source signal vectors, respectively, in the frequency domain. $H_i(f;A), i=1,2,...,N$ are the Fourier transforms of transfer functions h_i , $i=1,2,...,N$. The source generates either a deterministic or a random signal that can be narrow band or wide band (with *M* frequency components f_p , $p=1,\ldots,M$). The vector '*A*' corresponds to the set of source location or environmental parameters.

Based on the system block diagram shown in the Fig.2.1 the following equations are given:

$$X^{N\times M} = Y^{N\times M} + W^{N\times M} \tag{2.8}$$

$$Y^{N\times M} = H^{N\times M} D_u^{M\times M} \tag{2.9}$$

where

$$X = [X_{f_1}\ X_{f_2} \ldots X_{f_M}];\ Y = [Y_{f_1}\ Y_{f_2} \ldots Y_{f_M}];\ W = [W_{f_1}\ W_{f_2} \ldots W_{f_M}]$$

$$D_u = diag(\underbrace{u_{f_1}\ u_{f_2} \ldots u_{f_M}}_{M}), H = [H_{f_1;A}\ \ H_{f_2;A}\ \ldots\ H_{f_M;A}]$$

$$X_{f_i} = \left[x_1(f_i)\ x_2(f_i) \ldots . x_N(f_i)\right]^H, Y_{f_i} = \left[y_1(f_i)\ y_2(f_i) \ldots . y_N(f_i)\right]^H,$$

$$W_{f_i} = \left[w_1(f_i)\ w_2(f_i) \ldots . w_N(f_i)\right]^H,\ H_{f_{i;A}} = \left[H_1(f_i;A)\ H_2(f_i;A) \ldots . H_N(f_i;A)\right]^H$$

$(.)^H$ represents the Hermitian operator. The columns of the matrix H are linearly independent since each of them corresponds to a distinct frequency.

The measurement noise is assumed to be spatially and spectrally independent, circular Gaussian noise with zero mean having covariance matrix for each frequency component $C_{W_{f_i}}^{N\times N} = \sigma^2 I^{N\times N},\ i = 1,2,\ldots,N$.

2.4.1. Bartlett matched field processor family

The Bartlett matched field processor family is the most popular family used in the source localization and environmental parameters estimation. Some well-known MFPs like minimum variance, multiple constraint and matched mode processors are members of this family [1,16,17].

From equation (2.8), the covariance matrix of the measured signal for a deterministic source is

$$\begin{aligned} C_X = C_Y + C_W = HD_u D_u^H H^H + C_W = HD_{|u|^2} H^H + C_W \\ D_{|u|^2} = diag\left(\left|u_{f_1}\right|^2, \left|u_{f_2}\right|^2, \ldots, \left|u_{f_M}\right|^2\right) \end{aligned} \tag{2.10}$$

In the case of a random source, equation (2.10) becomes

$$\begin{aligned} C_X = C_Y + C_W = HE\left(D_u D_u^H\right)H^H + C_W = HD_{S_u} H^H + C_W \\ D_{S_u} = diag\left(S_u(f_1), S_u(f_2), \ldots, S_u(f_M)\right) \end{aligned} \tag{2.11}$$

where $S_u(f_i)$, $i = 1,2,\ldots, M$ is the power spectral density of the source at the ith frequency.

Equations (2.10) and (2.11) represent a relationship between the signal and noise subspaces of C_X and the column vectors of H based on the following theorem.

Theorem: There is a linear relationship between the eigenvectors of the received signal covariance matrix C_Y (which spans the signal subspace of C_X) and the non-zero columns of the transfer function matrix H if and only if $D_{|u|^2}$ is full rank.

Proof [18]: Let us form the singular value decomposition (SVD) of C_Y and use equation (2.11) to write

$$C_Y = U_Y \Lambda_Y U_Y^H = H D_{S_u} H^H \tag{2.12}$$

Let us define K as below

$$K = \Lambda_Y^{1/2} \Omega^H D_{S_u}^{-1/2} \tag{2.13}$$

where Ω can be any $M \times M$ unitary matrix given that $D_{|u|^2}$ is full rank. Substituting (2.13) in (2.12) we obtain following equation

$$\begin{aligned} C_Y &= U_Y \Lambda_Y U_Y^H = U_Y \Lambda_Y^{1/2} (\Lambda_Y^{1/2})^H U_Y^H = U_Y K D_{S_u}^{1/2} \Omega \Omega^H (D_{S_u}^{1/2})^H K^H U_Y^H \\ &= U_Y K D_{S_u} K^H U_Y^H = H D_{S_u} H^H \end{aligned} \tag{2.14}$$

Equation (2.14) implies the following linear relationship between the eigenvectors of C_Y (which span the signal subspace of C_X) and the columns of the transfer function matrix *H:*

$$U_Y K = H \tag{2.15}$$

The above theorem provides transfer functions with both sufficient and necessary conditions. However, for source localization and environmental parameter estimation, it only provides the necessary side of the proof for the parameter uniqueness.

The above theorem implies that:

1. The source signal should have non-zero components at all frequencies in the band in the sense that $D_{|u|^2}$ be full rank.
2. $H_i(f), i = 1,2,\ldots, N$ should not share common zeros at all frequencies in order to have a non-zero matrix U_Y.

The uniqueness conditions for random sources are the same as those conditions mentioned for the deterministic sources except that we have an expectation rather than a deterministic measure. For the random source case, the theorem implies that D_{S_u} should be full rank, so that the power spectral density (PSD) of the source should be non-zero over the frequency band. In reality, there is no way to measure C_Y, so that replacing it with C_X is inevitable. C_X is full rank with ordered eigenvalues as below:

$$\lambda_{s_1} \geq \lambda_{s_2} \geq .., \lambda_{s_T} \geq \lambda_{n_1} \geq \lambda_{n_2} = .. = \lambda_{n_{(N-T)}} = \lambda \qquad (2.16)$$

T: # of sources

Replacing C_Y with C_X gives an acceptable estimation result if the ratio $\frac{\lambda_{s_i}}{\lambda}$ is large enough for all $1 \leq i \leq T$.

We will describe two formulations derived from theorem 1 to estimate transfer functions based on the multiple signal classification (MUSIC) concept [19]. They are categorized as channel subspace (CS) methods in the blind system identification literature. In the first formulation we consider the fact that the space spanned by the columns of matrix *H* is orthogonal to the noise subspace of C_X. Therefore we have

$$\hat{H}_{f_i;A}^{MUSIC} = \arg\min_{\|H_{f_i;A}\|=1} \left\| H_{f_i;A}^H E_n \right\|^2 \quad , i = 1,2,\ldots, M \qquad (2.17)$$

where E_n is a matrix with columns from eigenvectors of the noise subspace of C_X.

In the above formulation it is assumed that the minimizing procedure results in the global minimum point. In the MFP literature, the inverse of equation (2.17) is known as the eigenvector processor [20]. Tolstoy [1] has commented that the eigenvector processor is not appropriate for estimating source or spectral intensities since it is seeking the zeros of (2.17), whereas we have shown theoretically that the processor gives us a unique answer if the conditions of theorem 1 are satisfied. The MUSIC algorithm has shown its power in the source localization for horizontal arrays, and there is a large body of work published on this technique, most of which has assumed plane wave fields and mutually uncorrelated sources [19,21]. The plane wave assumption is to assure that the sufficient part of the theorem is satisfied for source localization. Another processor using the same concept as MUSIC is called the approximate orthogonal processor (AOP) [22]. Fizell [22] has commented that the disadvantages of the AOP include its high false

alarm rate and its instability in the presence of noise. The instability comes from the inability to truly separate the signal subspace from the noise subspace when signal-to-noise ratio (SNR) is low. In this case, we can use model order estimators such as Akaike [23] or minimum description length (MDL) [24] to overcome this problem.

In the second formulation the projection of the column vectors of H onto the signal subspace of C_X is maximized. Thus we have

$$\hat{H}_{f_i;A}^{MUSIC} = \arg\max_{\|H_{f_i;A}\|=1} \left\| H_{f_i;A}^H E_y \right\|^2 \quad ,i = 1,2,\ldots, M \tag{2.18}$$

where E_y is a matrix with columns from eigenvectors of the signal subspace of C_X.

The above formulation is applicable to any vector located on the signal subspace of C_X including the received signal vector, i.e. $Y_{f_i;A}, i = 1,2,\ldots, M$ so that

$$\hat{H}_{f_i;A}^{Bartlett} = \arg\max_{\|H_{f_i;A}\|=1} \left| H_{f_i;A}^H Y_{f_i} \right|^2 \quad ,i = 1,\ldots, M \tag{2.19}$$

where Y_{f_i} is the received signal vector at the frequency f_i .

The equation (2.19) is known as the narrow band Bartlett matched field processor, for which the source location or environmental parameters are estimated from the transfer functions. In this case theorem 1 provides only the necessary part of the proof. The formulation can be extended to multiple frequencies using either a coherent estimation of frequencies [5],

$$\hat{H}_A^{Bartlett} = \arg\max_{\|H_{f_i;A}\|=1} \left| \sum_{f_i} H_{f_i;A}^H Y_{f_i} \right|^2 \quad ,i = 1,\ldots, M \tag{2.20}$$

or a non-coherent form [2],

$$\hat{H}_A^{Bartlett} = \arg\max_{\|H_{f_i;A}\|=1} \sum_{f_i} \left| H_{f_i;A}^H Y_{f_i} \right|^2 \quad ,i = 1,\ldots, M \tag{2.21}$$

For the Bartlett processor family, equations (2.20) and (2.21) are updated to the following equations to include random sources. For the coherent formulation we have

$$\hat{H}_A^{Bartlett} = \arg\max_{\|H_{fi}\|=1} \sum_{f_i} \sum_{f_j} \left(H_{f_i;A}^H E\left(Y_{f_i} Y_{f_j}^H \right) H_{f_j;A} \right) = \arg\max_{\|H_{fi}\|=1} \sum_{f_i} \sum_{f_j} \left(H_{f_i;A}^H C_{Y_{f_i,f_j}} H_{f_j;A} \right), i, j = 1,2,\ldots, M, \tag{2.22}$$

and for the non-coherent formulation,

$$\hat{H}_A^{Bartlett} = \arg\max_{\|H_{f_i}\|=1} \sum_{f_i} \left(H_{f_i;A}^H E\left(Y_{f_i} Y_{f_i}^H\right) H_{f_i;A} \right) = \arg\max_{\|H_{f_i}\|=1} \sum_{f_i} \left(H_{f_i;A}^H C_{Y_{f_i}} H_{f_i;A} \right), i = 1,2,\ldots,M, \quad (2.23)$$

where

$$C_{Y_{f_i}} = \left[S_{y_p,y_q}(f_i) \right]_{p,q=1,\ldots,N} \quad \text{, and} \quad C_{Y_{f_i,f_j}} = \left[S_{y_p,y_q}\left(f_i,f_j\right) \right]_{p,q=1,\ldots,N}.$$

$S_{y_p,y_q}(f_i)$ and $S_{y_p,y_q}\left(f_i,f_j\right)$ are the power spectral density and cross power spectral density of $y_p(f_i)$ and $y_q(f_i)$, respectively. In practice $C_{Y_{f_i}}$ and $C_{Y_{f_i,f_j}}, i,j = 1,2,\ldots,M$ are obtained using the periodogram technique [25].

As mentioned before, we have no access to the received signals experimentally, so use of the measured signals is inevitable. This suggests a sub-optimum formulation. In this case, assuming that the SNR is high enough, we find the maximum likelihood measure of the estimated transfer functions to be

$$\hat{H}_{f_i;A}^{Bartlett} \approx \arg\max_{\|H_{f_i;A}\|=1} \left(H_{f_i;A}^H C_{X_{f_i}} H_{f_i;A} \right), i = 1,\ldots,M \quad (2.24)$$

where $C_{X_{f_i}} = E\left(X_{f_i} X_{f_i}^H\right)$ and X_{f_i} is the measured signal vector at the frequency f_i.

The non-coherent formulation of the processor for a broadband signal is

$$\hat{H}_{f_i;A}^{Bartlett} \approx \arg\max_{\|H_{f_i;A}\|=1, i=1,\ldots,M} \sum_{i=1}^{M} \left(H_{f_i;A}^H C_{X_{f_i}} H_{f_i;A} \right), i = 1,\ldots,M \quad (2.25)$$

Although the above processor is quite advanced over conventional plane wave processors, it is not perfect because of its side-lobes and lack of resolution at the source location. This kind of processor (linear processor) has the least sensitivity to the mismatch between the model and the real environment.

In an effort to improve the Bartlett processor performance, the Minimum Variance (MV) processor has been developed. It has been designed to be optimum in the sense that the output noise power is minimized subject to the constraint that the signal be undistorted by the filter. The processor is defined as

$$\hat{H}_{f_i;A}^{MV} = \arg\max_{\|H_{f_i;A}\|=1} \frac{1}{\left(H_{f_i;A}^H C_{X_{f_i}}^{-1} H_{f_i;A} \right)}, i = 1,\ldots,M \quad (2.26)$$

There are two possible non-coherent formulations for wide-band MV processors. One adds up the denominator terms for different frequencies, giving the reciprocal of sums

$$\hat{H}_A^{MV} = \underset{\|H_{f_i;A}\|=1, i=1,2,\ldots,M}{\arg\max} \frac{1}{\sum_{i=1}^{M}\left(H_{f_i;A}^H C_{X_{f_i}}^{-1} H_{f_i;A}\right)} \tag{2.27}$$

The other formulation adds a term for each frequency, giving the sum of reciprocals

$$\hat{H}_A^{MV} = \underset{\|H_{f_i;A}\|=1, i=1,2,\ldots,M}{\arg\max} \sum_{i=1}^{M} \frac{1}{\left(H_{f_i;A}^H C_{X_{f_i}}^{-1} H_{f_i;A}\right)} \tag{2.28}$$

The reciprocal of sum formulation is closer to the non-coherent concept than is the second one. The reason is that in the reciprocal sum formulation the maximum point is obtained only if all denominator values corresponding to different frequencies have small values, while in the sum of reciprocal formulation the maximum point can be obtained if only one denominator (corresponding to one frequency) is small. We would expect the reciprocal of sum formulation to be more stable and accurate.

The covariance matrix of the received signal should be full rank, given that all conditions mentioned for the Bartlett processor are satisfied. Sometimes it may be necessary to diagonally load the matrix, i.e. add some small quantity to the diagonal. The performance of the MV processor degrades rapidly in the presence of error in the model estimates of the field as well as under mismatch conditions. This sensitivity requires that quantitative knowledge of the environmental parameters must be extraordinarily accurate. In addition, the propagation model used must also be highly accurate, a condition that is difficult to achieve if range and depth change rapidly [1]. The MV performance mimics that of the Bartlett processor in low signal-to-noise conditions if noise is temporally and spatially white Gaussian.

Daugherty and Lynch [26] have introduced a variable order processor similar in concept to the MV processor,

$$\hat{H}_{f_i;A}^{VOP} = \underset{\|H_{f_i;A}\|=1}{\arg\max} \frac{1}{\left(H_{f_i;A}^H C_{X_{f_i}}^{-\alpha} H_{f_i;A}\right)^{1/\alpha}}, i = 1,\ldots,M \tag{2.29}$$

where α is a variable coefficient. For $\alpha = 1$ we have the MV processor. The selection of α can change the sensitivity of the processor. A small value of α (smaller than one) gives a more robust processor to model mismatch.

In order to overcome the high sensitivity of the MV processor, Schmidt et al. [27] have introduced a multiple constraint (MC) processor. The principle behind the approach is to design a neighborhood response rather than a single point response, e.g. near the precise source range and depth, for which the signal is passed without distortion. The derivation of the MC processor is very similar to that of the MV processor, except that the constraint condition which optimized the response only at a single point is extended by a system of constraints imposed at L neighborhood points. Letting the vector d with L entries corresponding to constraints at L points, the processor is given by

$$\hat{H}_{f_i;A}^{MC} = \arg\max_{\|H_{fi;A}\|=1} \frac{d^H \left(H_{f_i;A}^H C_{X_{f_i}}^{-1} H_{f_i;A} \right)^{-1} d}{d^H \left(H_{f_i;A}^H H_{f_i;A} \right)^{-1} d} \;, i = 1, \ldots, M \tag{2.30}$$

For wide-band MC processors, the non-coherent formulation is given by

$$\hat{H}_A^{MC} = \arg\max_{\|H_{f_i;A}\|=1, i=1,2,\ldots,M} \sum_{i=1}^{M} \frac{d^H \left(H_{f_i;A}^H C_{X_{f_i}}^{-1} H_{f_i;A} \right)^{-1} d}{d^H \left(H_{f_i;A}^H H_{f_i;A} \right)^{-1} d} \tag{2.31}$$

Schmidt el al. suggest that the number of constraints be $L=2N_{dim}+1$, where N_{dim} is the number of dimensions or parameters in the problem [27].

The matched mode processor (MMP) proposed by Shang [28] operates in mode space in contrast to the Bartlett processor that operates based on signals recorded by hydrophones. The key advantage of this processor is that prior to processing, the data can be filtered to eliminate modes that degrade the localization, e.g., poorly modeled or noise dominated modes. The technique requires that the number of hydrophones N be greater than or equal to the number of effective modes L at the array range. The non-coherent wide-band MMP is given by

$$\hat{H}_A^{MMP} = \arg\max_{\|H_{f_i;A}\|=1, i=1,2,\ldots,M} \sum_{i=1}^{M} \left| \sum_{l=1}^{L} \hat{a}_l^* a_l \right|^2 \tag{2.32}$$

where a_l is the l^{th} modal excitation deduced from the data; i.e., $X_k(f_i) = \sum_{l=1}^{L} a_l(f_i)\psi_l(z_k, f_i)$, $i = 1,2,\ldots,M; k = 1,2,\ldots,N$ and $\hat{a}_l$ is the model prediction for the l^{th} modal

excitation, $H_k(f_i)=\sum_{l=1}^{L}\hat{a}_l(f_i)\psi_l(z_k,f_i)$, $i=1,2,...,M; k=1,2,...,N$ where N and M are the number of sensors in the array, and the number of frequency components, respectively. The performance of the processor is highly dependent upon the accuracy with which the mode excitation a_m can be inferred from the data, particularly for finite aperture vertical arrays that discretely sample the field. MMP and Bartlett processors are equivalent if the vertical array fully samples the effective modes composing the field at the array range, i.e. if all modes are used.

Resolution of the MMP is usually limited by the number of effective modes L seen at the array. An attractive feature of MMP is its potential for increased tolerance of modal errors relative to the Bartlett processor, especially for noise and interfering sources which often affect a different set of modes from those most strongly excited by the source. The performance can be improved by filtering out such degrading modes from the processor.

Richardson and Nolte [29] have proposed the optimum uncertain field processor (OUFP) as a generalization of MFP to address the problem of localizing an unknown source in an unknown or erroneously modeled environment. They incorporated *a priori* probabilistic environmental uncertainty to account for an unknown ocean parameter and subsequently compute the maximum *a posteriori* estimate of source position. They have shown that if the SNR is high and ocean parameterization is known, their processor reduces to the Bartlett MFP.

It is understood from the Bartlett MFP family that the covariance matrices involved in the formulations have both self (diagonal) and cross (off diagonal) terms. The diagonal terms do not contain phase information and consequently are not as sensitive as are the off diagonal terms. Performance degradation of the MFP is expected in the presence of noise.

Baggeroer et al. [16] incorporated a correlated ambient noise model into the source localization problem for the Bartlett and MV processors. Let us consider equation (2.10) in which C_W is now composed of ambient and either white or colored noise. Let σ_W^2 denote the mean-square noise level (at frequency f_i), so that $C_W=\sigma_W^2 Q$. Assuming that Q can be computed, we have

$$\hat{H}_{f_i;A}^{Bartlett}=\underset{\|H_{f_i;A}\|=1}{\arg\max}\left(H_{f_i;A}^H C_{y_{f_i}} H_{f_i;A}+\sigma_W^2 H_{f_i;A}^H Q H_{f_i;A}\right), i=1,\ldots,M \quad . \qquad (2.35)$$

For white noise we have $C_W = \sigma_W^2 I$, a constant that does not affect the estimator. In this case equation (2.35) obtains the simple form

$$\hat{H}_{f_i;A}^{Bartlett} = \arg\max_{\|H_{f_i;A}\|=1}\left(H_{f_i;A}^H C_{y_{f_i}} H_{f_i;A} + \sigma_W^2 I\right), i = 1,\ldots, M \ . \tag{2.36}$$

For the MV estimator we have

$$\hat{H}_{f_i;A}^{MV} = \hat{H}_{f_i;A}^{(N),MV} \frac{G(0)}{G(\gamma)}, i = 1,\ldots, M \ , \tag{2.37}$$

where $\hat{H}_{f_i;A}^{(N),MV}$ can be interpreted as the MV noise level at the estimated source location [1] and

$$G(\gamma) = 1 + \frac{E\left(|Y|^2\right)}{H_{f_i;A}^{(N),MV}}\left(1 - |\gamma|^2\right) \tag{2.38}$$

In this experiment $H_{f_i;A}^{(N),MV}$ is the MV noise level at the true source location and γ is a measure of the similarity between the replica and data fields with respect to the metric of the noise covariance. For $Q = I$, at the condition of best match between the replica and measured fields, $\gamma = 1$ and it follows from equation (2.37) we obtain $\hat{H}_{f_i;A}^{MV} \le H_{f_i;A}^{(N),MV} + E\left(|Y|^2\right)$. $H_{f_i;A}^{(N)MV}$ is the MV noise level so it is smaller than the Bartlett noise level at the source location; i.e., $H_{f_i;A}^{(N)MV} \le H_{f_i;A}^{(N),Bart} = \sigma_W^2$ so $\hat{H}_{f_i;A}^{MV} \le \hat{H}_{f_i;A}^{Bartlett} = E\left(|Y|^2\right) + \sigma_W^2$, i.e. the MV processor performance reaches Bartlett processor in the presence of noise.

2.4.2. Maximum Likelihood Matched field processor

The maximum likelihood matched field processor (MLMFP) is a classic estimator that is widely used in different parameter estimation problems where the probability density function (PDF) of the measured signal is known [30]. The concept of the MLMFP is to estimate source or environmental parameters such that *a posteriori* PDF of the measured signal is maximized. With Gaussian noise, maximum likelihood estimation is obtained by minimizing the difference between the received and the measured signals (least square criterion). In the coherent case the MLMFP has the following form:

$$\left(\hat{H}, \hat{u}\right)_{ML} = \arg\_zero_{H,u} \left\| Y^{N\times M} - H^{N\times M} D_u{}^{M\times M} \right\|^2 \tag{2.39}$$

By substituting the measured signal instead of the received signal, the above formulation can be rewritten

$$\left(\hat{H},\hat{u}\right)_{ML} = \arg\min_{H,u} E\left(\left\| X^{N\times M} - H^{N\times M} D_u{}^{M\times M} \right\|^2\right). \tag{2.40}$$

After solving equations (2.39) and (2.40), equations (2.41) and (2.42) are obtained:

$$\hat{H}_A^{ML} = \arg\_zero_H \left\| \left(I^{N\times N} - H\left(H^H H\right)^{-1} H \right) Y \right\|^2 \tag{2.41}$$

$$\hat{H}_A^{ML} = \arg\min_H \left(\left(I^{N\times N} - H\left(H^H H\right)^{-1} H \right) \underbrace{E(XX^H)}_{C_X} \left(I^{N\times N} - H\left(H^H H\right)^{-1} H \right)^H \right) \tag{2.42}$$

The corresponding theorems for uniqueness conditions are given in [30]. The MLMFP is an unstable when the condition number of the matrix $H^H H$ is large.

2.4.3. Bilinear matched field processor

The Bilinear processor (BMF) is formulated based on the mutual interaction of output signals,

$$X_{Bilinear}^{r\times M} = Y_{Bilinear}^{r\times M} + W^{r\times M} \tag{2.43}$$

$$Y_{Bilinear}^{r\times M} = H_{Bilinear}^{r\times M} D_{|u|^2}^{M\times M} \quad , \quad r = \frac{N(N-1)}{2} \tag{2.44}$$

$$X_{Bilinear}^{r\times M} = \left[X_{Bilinear,f_1}\, X_{Bilinear,f_2} \ldots X_{Bilinear,f_M} \right], X_{Bilinear,f_i} = \left[x_1(f_i)x_2^*(f_i) \ldots x_p(f_i)x_q^*(f_i) \ldots \right]^H,$$

$$Y_{Bilinear}^{r\times M} = \left[Y_{Bilinear,f_1}\, Y_{Bilinear,f_2} \ldots Y_{Bilinear,f_M} \right], Y_{Bilinear,f_i} = \left[y_1(f_i)y_2^*(f_i) \ldots y_p(f_i)y_q^*(f_i) \ldots \right]^H,$$

$$H_{Bilinear}^{r\times M} = \left[H_{Bilinear,f_1}\, H_{Bilinear,f_2} \ldots H_{Bilinear,f_M} \right], H_{Bilinear,f_i} = \left[H_1(f_i)H_2^*(f_i) \ldots H_p(f_i)H_q^*(f_i) \ldots \right]^H,$$

$$D_{|u|^2}^{M\times M} = diag(\left|u_{f_1}\right|^2, \ldots, \left|u_{f_M}\right|^2) \;;\; p = 1,\ldots,N; q = p+1,\ldots,N$$

where $W = [w_{nm}], m = 1,\ldots,M; n = 1,\ldots,r$ and w_{nm} is white, zero mean circular Gaussian noise.

Theorem 1 is also applicable to the BMF case, except that the noise and signal subspaces belong to the covariance matrix having a bilinear form for the measured signal; i.e.,

$$C_{X_{Bilinear}} = C_{Y_{Bilinear}} + C_W = H_{Bilinear} D_{|u|^2} D^H_{|u|^2} H^H_{Bilinear} + C_W = H_{Bilinear} D_{|u|^4} H^H_{Bilinear} + C_W . \quad (2.45)$$

The theorem implies that $D_{|u|^4}$ should be full rank, i.e. the source signal should have non-zero elements at each frequency in the signal bandwidth. It also assumes that the columns of $H_{Bilinear}$ do not share common zeros so that the linear relationship between the columns of $H_{Bilinear}$ and $C_{Y_{Bilinear}}$ is preserved. The MUSIC concept gives the following estimation equation

$$\hat{H}^{MUSIC}_{Bilinear,f_i} = \underset{\left\|H_{Bilinear,f_i}\right\|=1}{\arg\_zero} \left\| H^H_{Bilinear,f_i} E_n \right\|^2 \quad (2.46)$$

where E_n is a matrix with columns from eigenvectors of the noise subspace of $C_{X_{bilinear}}$.

Another formulation, obtained by maximizing the projection of $H_{Bilinear,f_i}$ onto the signal subspace of $C_{X,Bilinear}$ is

$$\hat{H}^{MUSIC}_{Bilinear,f_i} = \underset{\left\|H_{Bilinear,f_i}\right\|=1}{\arg\max} \left\| H^H_{Bilinear,f_i} E_y \right\|^2 \quad (2.47)$$

where E_y is a matrix with columns from eigenvectors of the signal subspace of $C_{X_{bilinear}}$.

Because $Y_{Bilinear,f_i}$ is located on the signal subspace, we can write

$$\hat{H}_{Bilinear,f_i} = \underset{\left\|H_{Bilinear,f_i}\right\|=1}{\arg\max} \left| H^H_{Bilinear,f_i} Y_{Bilinear,f_i} \right|^2 \quad (2.48)$$

$Y_{Bilinear,f_i}$ is the bilinear form of the received signal at the frequency f_i.

The above narrow band formulation can be extended to the wide band form, and the coherent form based on the MUSIC concept is given by following equation

$$\hat{H}^{Westwood}_{Bilinear} = \underset{\sum_{f_i}\left\|H_{Bilinear,f_i}\right\|=1}{\arg\max} \left| \sum_{f_i} \left(H^H_{Bilinear,f_i} Y_{Bilinear,f_i} \right) \right|^2 \quad (2.49)$$

For a random source, Westwood [3] substitutes $Y_{Bilinear,f_i}$ with the cross spectral density of the received signals (the expected value of $Y_{Bilinear,f_i}$).

The formulation for the non-coherent processor based on the least square concept is given by

$$\hat{H}^{Non-coherent}_{Bilinear} = \underset{\sum_{f_i}\left\|H_{Bilinear,f_i}\right\|=1}{\arg\max} \sum_{f_i} \left| H^H_{Bilinear,f_i} Y_{Bilinear,f_i} \right|^2 . \quad (2.50)$$

In practice we only have access to the received signals in the presence of added noise. In this case if the SNR is high the maximum likelihood measure of system transfer function is as follows

$$\hat{H}_{Bilinear,f_i} = \underset{\|H_{Bilinear,fi}\|=1}{\arg\max} \left(H^H_{Bilinear,f_i} C_{X_{Bilinear,f_i}} H_{Bilinear,f_i} \right)$$
$$C_{X_{Bilinear,f_i}} = E\left(X_{Bilinear,f_i} X^H_{Bilinear,f_i} \right), \tag{2.51}$$

and $X_{Bilinear,f_i}$ is the bilinear form of the received signal at the frequency f_i.

For the uniqueness conditions, the BMF has higher risk of having more than one solution for H, because of the bilinear structure of the processor having a non-linear relationship between $H_{Bilinear}$ and the system transfer functions. This is the case also from the necessary side of the theorem. The BMF has the advantage of being more sensitive to source or environmental parameters than is the Bartlett processor family since the self terms in the bilinear covariance matrix are removed. The BMF has a more complex formulation requiring more computation in comparison to the Bartlett processor family. In the derivation of the bilinear processors, we assume w_{nm} is white and Gaussian, but this assumption is generally not true in practice. Consequently the BMF is a sub-optimum estimation in comparison to the Bartlett processor family.

Chapter Three

Cross-relation Matched Field Processors, Theory and Formulation

In recent years methods based on second-order signal statistics have been considered extensively for blind system identification [18,31-36]. One of those methods is based on the cross-relation concept, a well-known characteristic of single-input multiple-output systems [37]. In blind system identification, the system parameter estimates are derived from output data only. The output data are generated from a system with known model architecture having unknown inputs. The model parameters are unknown and vary spatially in the environment. Applications can be found in various topics of signal processing including seismic [38,39], telecommunications [37], and image processing [40,41].

Different classes of blind identification techniques have been proposed to estimate either the system, the input source location parameters (inversion) or the source signal itself (communication). Extensions to the multiple-input multiple-output case based on second-order signal statistics are given in [42-44]. These techniques usually assume that

1. Channels have finite impulse response (FIR) structure
2. The number of channels and size of FIR transfer functions are known a priori
3. A sufficient number of output samples exist to obtain good channel parameter estimates
4. The input sequence is sufficiently complex
5. The channels are sufficiently distinct such that the channel Sylvester matrix [30] meets the full column rank condition.

The latter three assumptions belong to the set of identifiability conditions based on the assumption that a FIR structure is used. In practice, we often know the sinusoidal model of signal

propagation (provided by acoustic propagation modeling software such as ORCA), and the problem is to estimate the parameters that are unknown.

Adaptive matched field processing systems make use of ambient noise or signals of opportunity to learn the geoacoustic properties of a new environment. Such information is available by processing broadband noise radiated by passing ships. Ships are strong sources of underwater sound, the signal generally consisting of a combination of machinery noise along with propeller and hydrodynamic noise [45]. This kind of noise is a random signal, non-stationary with a complicated probability distribution function which characteristically produces continuous spectrum components and a set of line components [46,47]. The main part of propagated ship noise in water is the propeller noise, bursts of cavitation noise when the propeller blades move through the cavitation zone behind the vessel [18]. In chapter 5 we specify the characteristics of ship noise in more detail.

This chapter introduces a cross-relation (CR) based matched field processor technique for estimating the source location and environmental parameters in shallow water (section 3.1). The source is assumed to be broadband or narrow-band random noise. However the processor is applicable for broadband and narrow-band deterministic sources. The estimation formulas are derived for deterministic (section 3.2) and random sources (section 3.3) including non-stationary (NS) (sections 3.3.1), and wide sense stationary (WSS) (section 3.3.2) random sources. For time varying sources, formulations based on an evolutive spectrum concept are proposed to obtain the advantages of time-frequency analysis (section 3.4). For each of the above formulations, two estimation methods are proposed, a self-CR or a cross-CR, according to which channel output signal is used to construct the estimator. All the above formulations derive second order MFP.

We can extend the second-order cross-relation concept to higher order MFPs. It is known that the second order probability density function (PDF) cannot completely model the ship noise source, so it is believed that the ship noise has higher order (higher than 2) statistics. We propose a matched field processor based on the higher order cross-relation concept (section 3.5). The higher order characteristic of this kind of processor provides the ability of canceling the effect of Gaussian random sources (either white or non-white) since the third and some higher odd moments of Gaussian random signals are zero.

3.1 Cross-relation Concept

Let us consider the geometry of the measurement system in shallow water using a vertical linear array with N sensors. This system can be modeled by a multi-channel system consisting of N parallel linear transfer functions shown in Fig. 3.1. The transfer function h_i corresponds to the paths traveled by acoustic waves from the source to the i^{th} sensor, including interactions with ocean bottom and surface. It is assumed that the noise is additive and is spatially and temporally white, Gaussian and uncorrelated with the input signal. The cross-relation in equation (3.1) between the transfer function and measured signal at pairs of sensors follows from the linearity of the transfer functions:

$$\begin{cases} y_p(n) = h_p(n;\alpha) * S(n) \\ y_q(n) = h_q(n;\alpha) * S(n) \end{cases} \Rightarrow h_p(n;\alpha) * y_q(n) = h_q(n;\alpha) * y_p(n) \qquad (3.1)$$
$$p,q = 1,2,\ldots,N\,;\, p \neq q \quad ,n = 1,2,\ldots,L$$

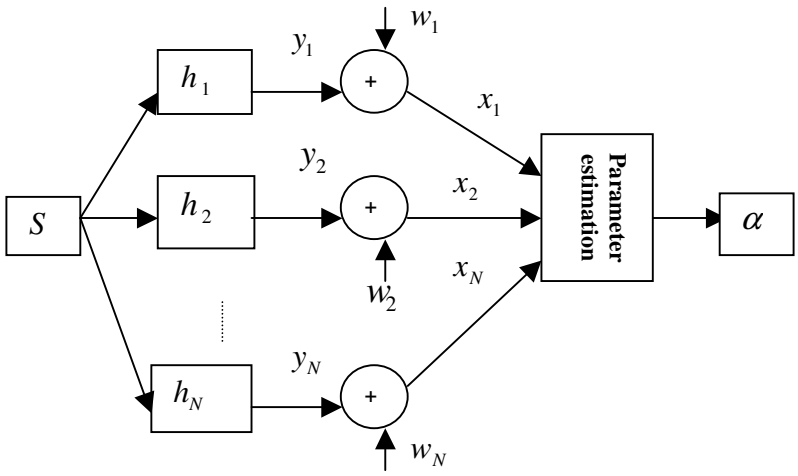

Fig. 3.1. The single-input multiple-output channel estimation

The above equation shows that the outputs of each channel pair are related by their channel responses. It gives a relationship such that, under certain identifiability conditions, we can identify multi-channel systems based on only channel outputs. This is why the method is referred as a blind identification technique. In this chapter we present a new derivation of this concept for random sources. The corresponding theorems and discussions are given for the deterministic sources in section 3.2 and for random sources in section 3.3.

3.2 Deterministic Sources

For the deterministic source, equation (3.1) can be rewritten in the following matrix form to solve for all channel responses simultaneously.

$$Yh = 0 \tag{3.2}$$

where

$$h = \left[h_1^T, h_2^T, \ldots, h_N^T\right]^T,\ h_p = \left[h_p(L-1), \ldots, h_p(0)\right]^T,\ p = 1,2,\ldots,N$$

$$Y = \left[\underbrace{Y_{1,2}^T, \ldots, \underbrace{Y_{p,q;p\neq q}^T}_{\frac{N(N-1)}{2}\ blocks}, \ldots, Y_{N,N-1}^T}\right]^T$$

$$Y_{p,q,p\neq q}^{\frac{M}{L}\times NL} = \left[\underbrace{0}_{\frac{M}{L}\times(p-1)L}\ \underbrace{Y_p}_{\frac{M}{L}\times L}\ \underbrace{0}_{\frac{M}{L}\times(q-p-1)L}\ \underbrace{-Y_q}_{\frac{M}{L}\times L}\ 0\right]$$

$$Y_p = \begin{bmatrix} y_p(0) & \ldots & y_p(L-1) \\ \ldots & \ldots & \ldots \quad \ldots \\ y_p(M-L-1) & \ldots & y_p(M-1) \end{bmatrix}$$

The above multi-channel system can be identified uniquely (to within a scalar) if and only if the null space dimension of the data matrix Y is one. This is a general necessary and sufficient condition for channel identification. Theorems have been presented in [37] that give explicit expressions and provide insight into the characteristics of the channels and input signal. These theorems imply that the blind identification problem has a unique solution if and only if:

1. The transfer functions $\{h_p(z)\}, p = 1,\ldots,N$ are coprime; i.e., they do not share any common roots
2. The linear complexity (a measurement of the diversity of a finite sequence [37]) of the source signal is greater than *2L+1* (for sufficient condition) and not less than *L+1* (for necessary condition)

The linear complexity can be described in the following way. Given finite input data $\{s(n)\}, n = 1,\ldots, M$, we define the *r*th-order Hankel matrix *S(r)* as follows:

$$S(r)=\begin{bmatrix} s(0) & \dots & s(r-1) \\ s(1) & \dots & s(r) \\ . & . & . \\ . & . & . \\ s(M-r-1) & \dots & s(M-1) \end{bmatrix}. \qquad (3.3)$$

Let p be the highest rank of the Hankel matrices $S(r), r=1,2,\dots,M,$ then the null space of a rank deficient Hankel matrix $S(r), (r>p)$ can be uniquely characterized by a pth-order polynomial:

$$a(z)=a(0)+a(1)z+\dots+a(p)z^{p}. \qquad (3.4)$$

The above equation has p roots, usually called *modes*. The number of modes is often referred to as the linear complexity of the sequence s(r), a measurement of diversity of a finite sequence $s(.)$.

The proof of the uniqueness theorem is given in the time domain [37], however it is easier to prove it in the frequency domain. We begin by writing equation (3.1) in frequency domain:

$$\begin{cases} Y_p(f_i)=H_p(f_i;A)S_{f_i} \\ Y_q(f_i)=H_q(f_i;A)S_{f_i} \end{cases} \Rightarrow H_p(f_i;A)Y_q(f_i)=H_q(f_i;A)Y_p(f_i) \qquad (3.5)$$
$$p,q=1,2,\dots,N \quad p\neq q \;;\; i=1,\dots,L \;;\; L\text{:\# of frequencies}$$

Let us rewrite (3.5) for all channels:

$$Y_F H_F = 0^{L\times L} \qquad (3.6)$$

$$Y_F^{2Lr\times L}=\left[\underbrace{Y_{1,2}^T,\dots,Y_{p,q,p\neq q}^T,\dots,Y_{N,N-1}^T}_{r=\frac{N(N-1)}{2}}\right]^T,\quad H_F^{2Lr\times L}=\left[\underbrace{H_{1,2},\dots,H_{p,q,p\neq q},\dots,H_{N,N-1}}_{r=\frac{N(N-1)}{2}}\right]^T$$
$$p=1,2,\dots,N \quad q=p+1,\dots,N$$

where

$$Y_{p,q}^{L\times 2L}=\begin{bmatrix} Y_p(f_1) & -Y_q(f_1) & 0 & 0 & & 0 & 0 \\ 0 & 0 & Y_p(f_2) & -Y_q(f_2) & \dots & 0 & 0 \\ 0 & 0 & 0 & 0 & \dots & 0 & 0 \\ 0 & 0 & 0 & 0 & \dots & 0 & 0 \\ 0 & 0 & 0 & 0 & \dots & Y_p(f_L) & -Y_q(f_L) \end{bmatrix}$$

$$H_{p,q}^{L\times 2L}=\begin{bmatrix} H_q(f_1,A) & H_p(f_1,A) & 0 & 0 & & 0 & 0 \\ 0 & 0 & H_q(f_2,A) & H_p(f_2,A) & ... & 0 & 0 \\ 0 & 0 & 0 & 0 & \ldots & 0 & 0 \\ 0 & 0 & 0 & 0 & \ldots & 0 & 0 \\ 0 & 0 & 0 & 0 & ... & H_q(f_L,A) & H_p(f_L,A) \end{bmatrix}$$

We first state the following lemma.

Lemma: The matrix H_F is full column rank if and only if for all the frequency band $f_i, i=1,2,\ldots,L$ the transfer functions $H_p(f_i;A), p=1,\ldots,N$ are not zero.

Proof: The proof of Lemma is straightforward since $H_p(f_i;A), p=1,\ldots,N$ are columns of H_F. The above lemma gives the same result that we had in the first condition given by [37]. Now we state the following theorem that gives the identifiability condition.

Theorem: The multi channel system (in frequency domain) is uniquely identified (up to a scalar) if and only if the null space dimension of Y_F is L while H_F is assumed to be full column rank (i.e., lemma is satisfied).

Proof: The proof of above theorem is straightforward and can be found in [49].

In order to have the null space dimension of Y_F equal to L, assuming the condition in the lemma is satisfied, $S_{f_i}, i=1,2,\ldots,L$ should be non-zero (see equation (3.1)). This implies that the source signal should be complex enough, another form of condition 2 given in [37]. The source can not be zero, a constant, or a single sinusoid if we are looking for transfer functions in a wide band frequency, for example.

The equation (3.6) is for the noise free case. For the case where channels are corrupted by noise the following matched field processor is proposed based on the least square criterion:

$$\hat{H}_F^{CR}=\underset{\|H_p(f;A)\|=1,\,p=1,\ldots,N}{\arg\min} E\left(\left\|X_F H_F\right\|^2\right) \qquad (3.7)$$

Here X_{CR} is matrix of the measured signal (see Fig. 3.1 or equation 2.9) and

$$X_F^{2Lr\times L}=\left[\underbrace{X_{1,2}^T,\ldots,X_{p,q,p\neq q}^T,\ldots,X_{N,N-1}^T}_{r=\frac{N(N-1)}{2}}\right]^T \quad p=1,2,\ldots,N \;\; q=p+1,\ldots,N$$

$$X_{p,q}^{L\times 2L}=\begin{bmatrix} X_p(f_1) & -X_q(f_1) & 0 & 0 & & 0 & 0 \\ 0 & 0 & X_p(f_2) & -X_q(f_2) & .. & 0 & 0 \\ 0 & 0 & 0 & 0 & \ldots & 0 & 0 \\ 0 & 0 & 0 & 0 & \ldots & 0 & 0 \\ 0 & 0 & 0 & 0 & ... & X_p(f_L) & -X_q(f_L) \end{bmatrix}$$

In matched field inversion, ensuring identifiability conditions for the transfer functions *h* does not guarantee (from sufficient side) a unique solution for the system or source parameters that we are seeking. As we mentioned in chapter 2, the sufficient conditions are highly dependent on the particular model for the ocean waveguide and the specific parameter. Since the ocean environment is very complicated and there is generally no exact analytic relationship between the model parameters and the acoustic field, ocean parameters can not be fully interpreted by the model (there is no analytic form), it is not practical to analytically determine the sufficiency. In order to reduce the non-uniqueness as much as possible we should carefully set the bounds of parameter variations. The bounds are usually obtained from complementary information provided by other sources such as ground truth data for environmental parameter estimation.

3.3 Random Sources

The estimation formulas are given for non-stationary (NS), and wide sense stationary (WSS) random sources. For each formulations two estimation methods are proposed, a self-CR or a cross-CR according to which channel output signal pair is used to construct the estimator.

3.3.1. Non-stationary Sources

Let us multiply both sides of equation (3.1) by the conjugate of $y_p(n_1)$ or $y_q(n_1)$ to produce the self-CR equation, or by $y_k(n_1), k=1,\ldots,N, k\neq p,q$ to produce the cross-CR equation, and then apply the expectation operator to this product. Here, n_1 is the time index; independent of *n*. The results are given in equation (3.8) for the self-CR estimator and equation (3.9) for the cross-CR estimator.

$$\begin{aligned} h_p(n;\alpha) * E\left(y_q(n)y_p^*(n_1)\right) &= h_q(n;\alpha) * E\left(y_p(n)y_p^*(n_1)\right) \\ h_p(n;\alpha) * R_{y_q,y_p}(n,n_1) &= h_q(n;\alpha) * R_{y_p}(n,n_1) \\ p,q &= 1,2,\ldots,N\,;\, p \neq q \end{aligned} \tag{3.8}$$

$$\begin{aligned} h_p(n;\alpha) * E\left(y_q(n)y_k^*(n_1)\right) &= h_q(n;\alpha) * E\left(y_p(n)y_k^*(n_1)\right) \\ h_p(n;\alpha) * R_{y_q,y_k}(n,n_1) &= h_q(n;\alpha) * R_{y_p,y_k}(n,n_1) \\ p,q &= 1,2,\ldots,N\,;\quad k = 1,\ldots,N\ ,\ k \neq p,q \end{aligned} \tag{3.9}$$

For the non-stationary source, the above equations can be rewritten in the following matrix form to solve for all channel responses simultaneously.

$$R_{y,self\_CR}(n_1)\,h = 0 \quad , \quad R_{y,cross\_CR}(n_1)\,h = 0 \tag{3.10}$$

where

$$h = \left[h_1^T, h_2^T, \ldots, h_N^T\right]^T,\ h_p = \left[h_p(L-1),\ldots,h_p(0)\right]^T\ ,\ p = 1,2,\ldots,N$$

$$R_{y,self\_CR}(n_1) = \left[\underbrace{R_{1,2}^T(n_1),\ldots,R_{p,q;p\neq q}^T(n_1),\ldots,R_{N,N-1}^T(n_1)}_{\frac{N(N-1)}{2}\ blocks}\right]^T$$

$$R_{y,cross\_CR}(n_1) = \left[\underbrace{R_{1,2,3}^T(n_1),\ldots,R_{p,q,k;k\neq p,q}^T(n_1),\ldots,R_{N,N-1,N-2}^T(n_1)}_{\frac{N(N-1)(N-2)}{3}\ blocks}\right]^T$$

$$R_{p,q;p\neq q}^{\frac{M}{L}\times NL}(n_1) = \left[\underbrace{0}_{\frac{M}{L}\times(p-1)L}\ \underbrace{R_{y_q,y_p}(n_1)}_{\frac{M}{L}\times L}\ \underbrace{0}_{\frac{M}{L}\times(q-p-1)L}\ \underbrace{-R_{y_p}(n_1)}_{\frac{M}{L}\times L}\ 0\right]$$

$$R_{p,q,k;k\neq p,q}^{\frac{M}{L}\times NL}(n_1) = \left[\underbrace{0}_{\frac{M}{L}\times(p-1)L}\ \underbrace{R_{y_q,y_k}(n_1)}_{\frac{M}{L}\times L}\ \underbrace{0}_{\frac{M}{L}\times(q-p-1)L}\ \underbrace{-R_{y_p,y_k}(n_1)}_{\frac{M}{L}\times L}\ 0\right]$$

$$R_{y_q,y_p}(n_1)=\begin{bmatrix} R_{y_q,y_p}(0,n_1) & \dots & R_{y_q,y_p}(L-1,n_1) \\ \dots & \dots & \dots \quad \dots \\ R_{y_q,y_p}(M-L-1,n_1) & \dots & R_{y_q,y_p}(M-1,n_1) \end{bmatrix}$$

$$R_{y_p}(n_1)=\begin{bmatrix} R_{y_p}(0,n_1) & \dots & R_{y_p}(L-1,n_1) \\ \dots & \dots & \dots \quad \dots \\ R_{y_p}(M-L-1,n_1) & \dots & R_{y_p}(M-1,n_1) \end{bmatrix}$$

The identifiability condition requires that the null space dimension of matrices $R_{y,self\_CR}$ and $R_{y,cross\_CR}$ should be one, while the vector h should be non-zero, implying that the $h_i, i=1,2,...,N$ should not share common zeros. To give more explicit expressions and provide more insight into the characteristics of the channels and the source signal (similar to what we had for deterministic sources but here we have a statistical sense), the following conditions are given:

1. The polynomials $\{h_p(z)\}, p=1,\dots,N$ are coprime or they do not share any common roots
2. The linear complexity of the expected value of the non-stationary source signal is greater than *2L+1* (for sufficient condition) and not less than *L+1* (for necessary condition)

As shown above, the cross-CR estimator only has signal cross-correlation components so in the presence of spatially white noises, this kind of estimator gives better performance than self-CR estimator which has both auto-correlation and cross-correlation terms.

For the case where channels are corrupted by noise, the following least-square estimators are proposed for the measured signal *x*:

$$P_{R,\alpha}^{self\_CR}=\sum_{n_1}\left\|R_{x,self\_CR}(n_1)h\right\|^{-1},\ P_{R,\alpha}^{cross\_CR}=\sum_{n_1}\left\|R_{x,cross\_CR}(n_1)h\right\|^{-1} \tag{3.11}$$

3.3.2 Wide Sense Stationary Sources

For wide sense stationary sources, equations (3.8) and (3.9) become

$$h_p(n;\alpha)*R_{y_q,y_p}(n-n_1)=h_q(n;\alpha)*R_{y_p}(n-n_1) \tag{3.12}$$

$$H_p(mF;\alpha)S_{y_q,y_p}(mF)=H_q(mF;\alpha)S_{y_p}(mF)$$

$$p,q=1,2,\dots,N\ ;\ p\neq q$$

$$h_p(n;\alpha)* R_{y_q,y_k}(n-n_1) = h_q(n;\alpha)* R_{y_p,y_k}(n-n_1) \tag{3.13}$$

$$H_p(mF;\alpha)S_{y_q,y_k}(mF) = H_q(mF;\alpha)S_{y_p,y_k}(mF)$$

$$p,q = 1,2,...,N;\ \ k = 1,...,N\ ,\ k \neq p,q$$

where $S_{y_p}(f)$ is the power spectral density of y_p and $S_{y_p,y_q}(f)$ is the cross power spectral density of y_p and y_q . The above equations can be written in the following matrix form to solve for all channel responses simultaneously:

$$S_{y,self\_CR}H = 0\ \ ,\ \ S_{y,cross\_CR}H = 0 \tag{3.14}$$

where

$$H = \left[H_1^T, H_2^T, ..., H_N^T\right]^T,\ H_p = \left[H_p(0), H_p(F), ..., H_p\left((L-1)F\right)\right]^T\ ,\ p = 1,2,...,N$$

$$S_{y,self\_CR} = \left[\underbrace{S_{1,2}^T, \ldots, S_{p,q;p\neq q}^T}_{\frac{N(N-1)}{2}\ blocks}, \ldots, S_{N,N-1}^T\right]^T$$

$$S_{y,cross\_CR} = \left[\underbrace{S_{1,2,3}^T, \ldots, S_{p,q,k;k\neq p,q}^T}_{\frac{N(N-1)(N-2)}{3}\ blocks}, \ldots, S_{N,N-1,N-2}^T\right]^T$$

$$S_{p,q;p\neq q}^{1\times NL} = \left[\underbrace{0}_{1\times(p-1)L}\ \ \underbrace{S_{y_q,y_p}}_{1\times L}\ \ \underbrace{0}_{1\times(q-p-1)L}\ \ \underbrace{-S_{y_p}}_{1\times L}\ \ 0\right]$$

$$S_{p,q,k;k\neq p,q}^{1\times NL} = \left[\underbrace{0}_{1\times(p-1)L}\ \ \underbrace{S_{y_q,y_k}}_{1\times L}\ \ \underbrace{0}_{1\times(q-p-1)L}\ \ \underbrace{-S_{y_q,y_k}}_{1\times L}\ \ 0\right]$$

$$S_{y_q,y_p} = \left[S_{y_q,y_p}(0)\ \ldots\ S_{y_q,y_p}\left((L-1)F\right)\right]\ ,\ S_{y_p} = \left[S_{y_p}(0)\ \ldots\ S_{y_p}\left((L-1)F\right)\right]$$

The identifiability condition is that the null space dimension of matrices $S_{y,self\_CR}$ and $S_{y,cross\_CR}$ should be one and that $H_i, i = 1,2,...,N$ should not be zero. To give more explicit expressions and provide more insights into the characteristics of the channels and the source signal, the following conditions are given:

1. For all the frequency band $f_i, i = 1,2,\ldots, M$, the transfer functions $H_p, p = 1,2,\ldots, N$ should not be zero.
2. In order to have the null space dimension of $S_{y,self\_CR}$ or $S_{y,cross\_CR}$ equal to one, assuming the condition mentioned in the item one is satisfied, the source spectral density function should be non-zero for all frequencies.

As shown above, the cross-CR estimator only has signal cross-spectrum density components, so in the presence of spatially white noise this kind of estimator performs better than the self-CR estimator which has both power spectral density and cross spectral density terms.

The unknown parameters are estimated by maximizing the following equations when the channels are corrupted by noise:

$$P_{S,\alpha}^{self\_CR} = \left\| S_{x,self\_CR} H \right\|^{-1}, \; P_{S,\alpha}^{cross\_CR} = = \left\| S_{x,cross\_CR} H \right\|^{-1} \tag{3.15}$$

The above equations can be rewritten in the following form to give a more explicit expression of the processors:

$$P_{\alpha}^{Self\_CR,Linear} = \frac{1}{\sum_{f_i} \sum_{p=1}^{N} \sum_{q=1, q\neq p}^{N} \left| S_{x_p}(f_i) H_{q;\alpha}(f_i) - S_{x_p,x_q}(f_i) H_{p;\alpha}(f_i) \right|^2} \tag{3.16}$$

$$P_{\alpha}^{Cross\_CR,Linear} = \frac{1}{\sum_{f_i} \sum_{p=1}^{N} \sum_{q=1, q\neq p}^{N} \sum_{r=1, r\neq p,q}^{N} \left| S_{x_r,x_p}(f_i) H_{q;\alpha}(f_i) - S_{x_r,x_q}(f_i) H_{p;\alpha}(f_i) \right|^2} \tag{3.17}$$

3.4. Time-Frequency Matched Field Processor

Time-frequency representations (TFR) of signals map a one-dimensional signal of time, *x(t)*, into a two-dimensional function of time and frequency, $T_x(t, f)$. The values of the TFR surface above the time-frequency plane give an indication as to which spectral components are present at specific times.

TFRs have been applied to analyze, modify, and synthesize time-varying signals. Three-dimensional plots of TFR surfaces have been used as pictorial representations enabling a signal processor to analyze how spectral components of a signal or system vary with time [50-52]. TFRs are divided into two major groups, linear and quadratic (bilinear). The short-time Fourier transform (STFT), Gabor transform, and the time-frequency version of the wavelet transform (WT) are members of linear TFR group. All linear TFRs satisfy the superposition or linearity principle which states that if *x(t)* is a linear combination of some signal components, then the TFR of *x(t)* is the same linear combination of the TFRs of each of the signal components. The Wigner distribution and ambiguity function are the most important members of the energetic and correlative interpretations of the quadratic group, respectively [50]. The Wigner distribution (equation (3.18)) and ambiguity function (equation (3.19)) are given respectively as

$$W_{x,y}(t,f)=\int_{\tau} x(t+\frac{\tau}{2})y^{*}(t-\frac{\tau}{2})e^{-j2\pi f\tau}d\tau=\int_{v} X(f+\frac{v}{2})Y^{*}(f-\frac{v}{2})e^{j2\pi vt}dv \qquad (3.18)$$

$$A_{x,y}(\tau,v)=\int_{t} x(t+\frac{\tau}{2})y^{*}(t-\frac{\tau}{2})e^{-j2\pi vt}dt=\int_{v} X(f+\frac{v}{2})X^{*}(f-\frac{v}{2})e^{j2\pi vt}dv \qquad (3.19)$$

The Wigner distribution and ambiguity function are dual in the sense that they are a Fourier transform pair:

$$A_{x,y}(\tau,v)=\int_{t}\int_{f} W_{x,y}(t,f)e^{-j2\pi(vt-\tau f)}dtdf \qquad (3.20)$$

For random signals, the expectation of the above formula is considered. In this case, the Wigner distribution is called an *evolutive spectrum*. For the energetic TFR, we seek to combine the concepts of the instantaneous power $p_x(t)=|x(t)|^2$ and the spectral energy density $P_x(f)=|X(f)|^2$, while in the correlative TFR representation, we seek to combine the temporal correlation $r_x(\tau)=\int_t x(t+\tau)x^{*}(t)d\tau$ and the spectral correlation $R_X(v)=\int_f X(f+v)X^{*}(f)df$.

Two prominent examples of the energetic form are the spectrogram and the scalogram, defined as the squared magnitudes of the STFT and WT, respectively. Two fundamental classes of energetic TFRs, are the classical Cohen class and affine class [50]. The Cohen class includes all time-frequency shift-invariant, quadratic TFRs in which the shift of a signal in time and/or frequency results in a corresponding shift in the TFR by the same time delay and /or modulation

frequency. Every member of the Cohen class is interpreted as a 2-D filtered Wigner distribution (an evolutive power spectrum for a random signal) [50]; i.e.,

$$T_x \in \textit{Cohen class} \Leftrightarrow T_x(t,f) = \iint_{t',f'} \psi_T(t-t', f-f')W_x(t',f')dt'df' \tag{3.21}$$

where $W_x(t,f)$ is the Wigner distribution of *x(t)*. Each member of Cohen's class is associated with a unique, signal-independent kernel function $\psi_T(t,f)$.

The affine class includes all energetic, quadratic TFRs which preserve time scaling and time shift. Any TFR which is an element of the affine class can be derived from the Wigner transform by means of an affine transformation [50]; i.e.,

$$T_x \in \textit{Affine class} \Leftrightarrow T_x(t,f) = \iint_{t',f'} \chi_T(f(t-t'), \frac{f'}{f})W_x(t',f')dt'df' \tag{3.22}$$

where $\chi_T(\alpha,\beta)$ is a two-dimensional kernel function. The scalogram is the most famous member of this group.

Let us now derive a time-frequency based matched field processor. We multiply both sides of the Fourier transform of equation (3.1) by $y_p^*(n_1T)e^{j2\pi n_1 mTF}$ or $y_q^*(n_1T)e^{j2\pi n_1 mTF}$ for the self-CR case, and by $y_k^*(n_1T)e^{j2\pi n_1 mTF}$, $k=1,\ldots,N, k\neq p,q$, for the cross-CR case and then apply the expectation operator to produce

$$H_p(mF;\alpha)\underbrace{E\left(Y_q(mF)y_p^*(n_1T)e^{j2\pi n_1 mTF}\right)}_{RD_{y_q,y_p}(mF,n_1T)} = H_q(mF;\alpha)\underbrace{E\left(Y_p(mF)y_p^*(n_1T)e^{j2\pi n_1 mTF}\right)}_{RD_{y_p}(mF,n_1T)} \tag{3.23}$$

$$p,q = 1,2,\ldots,N;\ p\neq q$$

$$H_p(mF;\alpha)\underbrace{E\left(Y_q(mF)y_k^*(n_1T)e^{j2\pi n_1 mTF}\right)}_{RD_{y_k,y_q}(mF,n_1T)} = H_q(mF;\alpha)\underbrace{E\left(Y_p(mF)y_k^*(n_1T)e^{j2\pi n_1 mTF}\right)}_{RD_{y_k,y_p}(mF,n_1T)} \tag{3.24}$$

$$p,q,k = 1,2,\ldots,N;\ p\neq q \textit{ and } k\neq p,q$$

where, RD_{y_p} is *self-Rihaczek* distribution of y_p and RD_{y_k,y_q} is *cross-Rihaczek* distribution of y_p and y_q [50,53]. This distribution is a bilinear time-frequency distribution and a member of the Cohen class [50]. The *self-Rihaczek* distribution and *cross-Rihaczek* distribution have the following relationship with the ambiguity function [50]:

$$RD_x(t,f) = \int_\tau \int_\upsilon \left[e^{j\pi\tau\upsilon} A_x(\tau,\upsilon) \right] e^{j2\pi(t\upsilon - f\tau)} d\tau d\upsilon$$
$$RD_{x,y}(t,f) = \int_\tau \int_\upsilon \left[e^{j\pi\tau\upsilon} A_{x,y}(\tau,\upsilon) \right] e^{j2\pi(t\upsilon - f\tau)} d\tau d\upsilon \quad (3.25)$$

where $A_x(\tau,\upsilon)$ is the ambiguity function of *x(t)* and $A_{x,y}(\tau,\upsilon)$ is the cross-ambiguity function of *x(t)* and *y(t)*.

The relationship between the ambiguity function and the evolutive spectrum is given in (3.20). The *Rihaczek* distribution has the following properties of bilinear time-frequency representation:

1. Time shift: $RD_{\tilde{x}}(t,f) = RD_x(t-t_0,f)$ *for* $\tilde{x}(t) = x(t-t_0)$
3. Frequency shift: $RD_{\tilde{x}}(t,f) = RD_x(t,f-f_0)$ *for* $\tilde{x}(t) = x(t)e^{j2\pi f_0 t}$
4. Time marginal: $\int_f RD_x(t,f)df = |x(t)|^2$
5. Frequency marginal: $\int_t RD_x(t,f)dt = |X(f)|^2$
6. Time moments: $\int_t \int_f t^n RD_x(t,f)dtdf = \int_t t^n |x(t)|^2 dt$
7. Frequency moments: $\int_t \int_f f^n RD_x(t,f)dtdf = \int_f f^n |X(f)|^2 df$
8. Time-frequency scaling: $RD_{\tilde{x}}(t,f) = RD_x(at,\frac{f}{a})$ *for* $\tilde{x}(t) = \sqrt{|a|}x(at)$
9. Finite time support: $RD_x(t,f) = 0$ for *t* outside $[t_1,t_2]$ if *x(t)=0* outside $[t_1,t_2]$
10. Finite frequency support: $RD_x(t,f) = 0$ for *f* outside $[f_1,f_2]$ if *X(f)=0* outside $[f_1,f_2]$
11. Moyal's formula (unitarity): $\left(RD_{x_1,y_1}(t,f), RD_{x_2,y_2}(t,f)\right) = (x_1,x_2)(y_1,y_2)^*$
12. Convolution: $RD_{\tilde{x}}(t,f) = \int_{t'} RD_h(t-t',f)RD_x(t',f)dt'$ *for* $\tilde{x}(t) = \int_{t'} h(t-t')x(t')dt'$
13. Multiplication: $RD_{\tilde{x}}(t,f) = \int_{f'} RD_h(t,f-f')RD_x(t,f')df'$ *for* $\tilde{x}(t) = h(t)x(t)$

Equations (3.23) and (3.24) can be rewritten in the following matrix forms to solve for all channel responses simultaneously:

$$RD_{y,self\_CR}(n_1)H = 0 \ , \ RD_{y,cross\_CR}(n_1)H = 0 \quad (3.26)$$

where

$$H=\left[H_1^T,H_2^T,\ldots,H_N^T\right]^T,\ H_p=\left[H_p(0),H_p(F),\ldots,H_p\left((M-1)F\right)\right]^T,\ p=1,2,\ldots,N$$

$$RD_{y,self\_CR}(n_1)=\left[\underbrace{RD_{1,2}^T(n_1),\ldots,RD_{p,q;p\neq q}^T(n_1),\ldots,RD_{N,N-1}^T(n_1)}_{\frac{N(N-1)}{2}\ blocks}\right]^T$$

$$RD_{y,cross\_CR}(n_1)=\left[\underbrace{RD_{1,2,3}^T(n_1),\ldots,RD_{p,q,k;k\neq p,q}^T(n_1),\ldots,RD_{N,N-1,N-2}^T(n_1)}_{\frac{N(N-1)(N-2)}{3}\ blocks}\right]^T$$

$$RD_{p,q;p\neq q}^{1\times NM}(n_1)=\left[\underbrace{0}_{1\times(p-1)M}\ \underbrace{RD_{y_q,y_p}(n_1)}_{1\times M}\ \underbrace{0}_{1\times(q-p-1)M}\ \underbrace{-RD_{y_p}(n_1)}_{1\times M}\ 0\right]$$

$$RD_{p,q,k;k\neq p,q}^{1\times NM}(n_1)=\left[\underbrace{0}_{1\times(p-1)M}\ \underbrace{RD_{y_q,y_k}(n_1)}_{1\times M}\ \underbrace{0}_{1\times(q-p-1)M}\ \underbrace{-RD_{y_p,y_k}(n_1)}_{1\times M}\ 0\right]$$

$$RD_{y_q,y_p}(n_1)=\left[RD_{y_q,y_p}(0,n_1T)\quad\ldots\quad RD_{y_q,y_p}\left((M-1)F,n_1T\right)\right]$$

$$RD_{y_p}(n_1)=\left[RD_{y_p}(0,n_1T)\quad\ldots\quad RD_{y_p}\left((M-1)F,n_1T\right)\right]$$

The identifiability condition requires that the null space dimension of matrices $RD_{y,self\_CR}$ and $RD_{y,cross\_CR}$ should be one and that the vector H be non-zero, i.e. $H_p, p=1,2,\ldots,N$ should not be zero for all frequencies. To give more explicit expressions and provide more insights into the characteristics of the channels and the source signal (similar to what we had for deterministic sources but here we have a time-frequency sense of input signal), the following conditions are given:

1. For all the frequency band $f_i, i=1,2,\ldots,M$, the transfer functions $H_p, p=1,2,\ldots,N$ should not be zero.
2. In order to have the null space dimension of $RD_{y,self\_CR}$ or $RD_{y,cross\_CR}$ equal to one, assuming the condition mentioned in the item one is satisfied, the *Rihaczek* distribution of the source $RD_s(n_1,f_i), i=1,2,\ldots,L$ should be non-zero for all time indices n_1. This implies that the source signal should be complex enough in the time-frequency sense.

As shown above, the cross-CR estimator only has signal cross-correlation components so, in the presence of spatially white noises, this kind of estimator performs better than the self-CR estimator which has both auto-correlation and cross-correlation terms.

For channels corrupted by noise, the following least square estimators are proposed:

$$P_{RD,\alpha}^{self\_CR} = \sum_{n_1} \left\| RD_{x,self\_CR}(n_1)H \right\|^{-1},\ P_{RD,\alpha}^{cross\_CR} == \sum_{n_1} \left\| RD_{x,cross\_CR}(n_1)H \right\|^{-1} \qquad (3.27)$$

3.5. Higher Order Matched Field Processors

The higher-order statistics have been applied in many diverse fields such as sonar, radar, and seismic signal processing in data analysis and system identification [54-56]. Specific higher order statistics, known as cumulants, and their associated Fourier transforms, known as polyspectra, reveal not only amplitude information but also phase information. This is important because, as is well known, second-order statistics (such as auto-correlation) are phase blind.

Cumulants, on the other hand, are blind to any kind of Gaussian process; thus they can handle colored Gaussian measurement noise automatically, whereas correlation-based methods can not. Cumulant-based methods boost the signal-to-noise ratio when signals are corrupted by Gaussian measurement noise. Regarding the process distribution we can choose the appropriate cumulant to reach our goals. For example, if a random process is symmetrically distributed as are Laplace, uniform, Gaussian, and Bernoulli-Gaussian distributions, then its third-order cumulant equals zero. Thus in order to obtain a non-zero process we should use a fourth-order cumulant. For non-symmetric distributions such as exponential, Rayleigh, and k-distributions, the third order cumulant is not zero. Ship noise has a complex distribution with statistics higher than second order, so a matched field processor based on higher order statistics will let us use more information in the data. This matter will be discussed further in chapter 5.

Higher-order statistics are applicable when we are dealing with non-Gaussian processes. Many real world applications are truly non-Gaussian. The greatest drawbacks to the use of higher-order statistics are that they require longer data records and much more computation than do correlation-based methods. Longer data lengths are needed in order to reduce the variance associated with estimating the higher-order statistics from real data using sample averaging techniques.

Let $v=[v_1,v_2,...,v_k]^T$ and $x=[x_1,x_2,...,x_k]^T$ where x denotes a collection of random variables. The *kth*-order cumulant of these random variables is defined as the coefficient of $(v_1,v_2,...,v_k)$ in the Taylor series expansion of the cumulant-generating function [54]; i.e.,

$$K(v)=\ln E\left(e^{jv'x}\right) \tag{3.28}$$

The *kth*-order cumulant is defined in terms of its joint moments of orders up to *k* and vice versa. The moment-to-cumulant formula is

$$C_x(I)=\sum_{\bigcup_{p=1}^{q} I_p=I}(-1)^{q-1}(q-1)!\prod_{p=1}^{q}m_x(I_p) \tag{3.29}$$

where $\bigcup_{p=1}^{q} I_p = I$ denotes summation over all partitions of set *I*. Set *I* contains the indices of the components of vector *x*. The partition of the set *I* is the unordered collection of nonintersecting nonempty sets I_p such that $\bigcup_{p=1}^{q} I_p = I$ where q is the number of partitions sets I_p. The term $m_x(I_p)$ represents the moment of the partition x corresponding to set I_p, i.e. $m_x(I_p)=E\left(x_1x_2...x_p\right)$. As examples, for zero-mean real random variables, the second-, third-, and fourth-order cumulants are given by

$$cum(x_1,x_2)=E\left(x_1x_2\right),\ cum(x_1,x_2,x_3)=E\left(x_1x_2x_3\right) \tag{3.30}$$

$$cum(x_1,x_2,x_3,x_4)=E\left(x_1x_2x_3x_4\right)-E\left(x_1x_2\right)E\left(x_3x_4\right)-E\left(x_1x_3\right)E\left(x_2x_4\right)-E\left(x_1x_4\right)E\left(x_2x_3\right) \tag{3.31}$$

The cumulant-to-moment formula is:

$$m_x(I)=\sum_{\bigcup_{p=1}^{q} I_p=I}C_x(I_p) \tag{3.32}$$

The most important properties of cumulants are:

1. If $\lambda_i, i=1,2,...,k$, are constants, and $x_i, i=1,2,...,k$ are random variables, then

$$cum(\lambda_1x_1,...,\lambda_kx_k)=\left(\prod_{i=1}^{k}\lambda_i\right)cum(x_1,...,x_k) \tag{3.33}$$

2. Cumulants are symmetric in their arguments
3. Cumulants are additive in their arguments, i.e.

$$cum(x_0+y_0,z_1,...,z_k)=cum(x_0,z_1,...,z_k)+cum(y_0,z_1,...,z_k) \tag{3.34}$$

4. If α is a constant, then $cum(\alpha+z_1,z_2,...,z_k)=cum(z_1,...,z_k)$

5. If the random variables $\{x_i\}$, $i=1,\ldots,k$ are independent of the random variables $\{y_i\}$, $i=1,\ldots,k$ then
$$cum(x_1+y_1,\ldots,x_k+y_k)=cum(x_1,\ldots,x_k)+cum(y_1,\ldots,y_k) \tag{3.35}$$
If $\{y_i\}, i=1,\ldots,k$ is taken from Gaussian (colored or white) and $k\geq 3$ then $cum(y_1,\ldots,y_k)=0$. This makes the higher-order statistics more robust to additive measurement noise than correlation, even if the noise is colored.
6. If a subset of the k random variables $\{x_i\}, i=1,\ldots,k$ is independent of the rest, then $cum(x_1,\ldots,x_k)=0$
7. Cumulants of an independent, identically distributed random sequences are delta functions

In many practical applications we are given data and want to calculate cumulants from the data. Cumulants involve expectations, and as in the case of correlation they can not be computed in an exact manner from real data; they must be approximated in much the same way that the correlation is approximated. Cumulants are approximated by replacing expectations by sample averages.

Now, we derive a matched field processor based on higher-order statistics by multiplying both sides of equation (3.1) by a subset of $Y_k(F), k=1,\ldots,N, k\neq p,q$, and then apply the expectation operator to this product to produce a *T*-order cross-relation equation ($T\leq N$):

$$\begin{gathered} H_p(F;\alpha)E\left(Y_q(F)Y_r(F)\ldots Y_{r+T-2}(F)\right)=H_q(F;\alpha)E\left(Y_p(F)Y_r(F)\ldots Y_{r+T-2}(F)\right) \\ H_p(F;\alpha)m_Y(I_q)=H_q(F;\alpha)m_Y(I_p) \\ p,q,r=1,2,\ldots,N;\ p\neq q\ ,\ MFP\ order:T \\ I_q=\{q,r,r+1,\ldots,r+T-2\},\ I_p=\{p,r,r+1,\ldots,r+T-2\} \end{gathered} \tag{3.36}$$

If we replace moments by cumulants in equation (3.32) we obtain

$$H_p(F;\alpha)\left(\sum_{\cup_{r=1}^{s} I_r=I_p} C_{Y(F)}(I_r)\right)=H_q(F;\alpha)\left(\sum_{\cup_{r=1}^{s} I_r=I_q} C_{Y(F)}(I_r)\right) \tag{3.37}$$

The above equations can be written in the following matrix form to solve for all channel responses simultaneously:

$$CUM_Y H=0 \tag{3.38}$$

where

$$H=\left[H_1^T,H_2^T,...,H_N^T\right]^T,\ H_p=\left[H_p(0),H_p(F),...,H_p\left((L-1)F\right)\right]^T,\ p=1,2,...,N$$

$$CUM_Y=\left[\underbrace{cum^T_{1,2,...,T},\ldots,cum^T_{p,q,k_1,...,k_{T-2}},\ldots}_{\binom{N}{T}\ blocks}\right]^T$$

$$cum^{1\times NL}_{p,q,k_1,...,k_{T-2}}=\left[\underbrace{0}_{1\times(p-1)L}\ \underbrace{cum_{Y_p,Y_{k_1},...,Y_{k_{T-2}}}}_{1\times L}\ \underbrace{0}_{1\times(q-p-1)L}\ \underbrace{-cum_{Y_p,Y_{k_1},...,Y_{k_{T-2}}}}_{1\times L}\ 0\right]$$

$$cum_{Y_p,Y_{k_1},...,Y_{k_{T-2}}}=\left[\sum_{\cup_{r=1}^{s}I_r=I_p}C_{Y_p(0),Y_{k_1}(0),...,Y_{k_{T-2}}(0)}(I_r)\ ...\ \sum_{\cup_{r=1}^{s}I_r=I_p}C_{Y_p((L-1)F),Y_{k_1}((L-1)F),...,Y_{k_{T-2}}((L-1)F)}(I_r)\right]$$

The identifiability condition is that the null space dimension of matrix CUM_Y should be one and $H_p, p=1,2,...,N,$ should not be zero. To give more explicit expressions and provide more insights into the characteristics of the channels and the source signal, the following conditions are given (based on theorem (page 30)):

1. For all the frequency band $f_i, i=1,2,\ldots,M$, the transfer functions $H_p, p=1,2,...,N,$ should not zero.
2. In order to have the null space dimension of CUM_Y equal to one, and, assuming the condition mentioned above is satisfied, the source *T*-order moment should be non-zero for all frequencies.

For the case where channels are corrupted by noise, the least-square estimator, referred to as high-order cross-relation based MFP, is

$$P^{H\_CR}_{Y,\alpha}=\left\|CUM_Y H\right\|^{-1} \qquad (3.39)$$

The above equations can be rewritten in the following form to give a more explicit expression of the processors:

$$P_{Y;\alpha}^{H\_CR}=\frac{1}{\sum_{p}\sum_{q}\ldots\sum_{m}\left|H_p(F;\alpha)E\left(Y_q(F)Y_m(F)\ldots Y_{m+T-2}(F)\right)-H_q(F;\alpha)E\left(Y_p(F)Y_m(F)\ldots Y_{m+T-2}(F)\right)\right|^2}$$

$$=\frac{1}{\sum_{p}\sum_{q}\ldots\sum_{m}\left|H_p(F;\alpha)m_Y(I_q)-H_q(F;\alpha)m_Y(I_p)\right|^2}=\frac{1}{\sum_{p}\sum_{q}\ldots\sum_{m}\left|H_p(F;\alpha)\sum_{\cup_{r=1}^{s}I_r=I_p}C_{Y(F)}(I_r)-H_q(F;\alpha)\sum_{\cup_{r=1}^{s}I_r=I_q}C_{Y(F)}(I_r)\right|^2} \tag{3.40}$$

$$I_q=\{q,m,m+1,\ldots,m+T-2\},\ I_p=\{p,m,m+1,\ldots,m+T-2\}$$

where *p, q, m, r* are not equal numbers chosen from set *{1,2,…,N}*. The MFP's order is *T*. Let us consider the third order case as follows:

$$P_{Y,\alpha}^{H\_CR}=\frac{1}{\sum_{p}\sum_{q}\sum_{m}\sum_{r}\left|H_p(F;\alpha)E\left(Y_q(F)Y_m(F)Y_r(F)\right)-H_q(F;\alpha)E\left(Y_p(F)Y_m(F)Y_r(F)\right)\right|^2}$$

$$=\frac{1}{\sum_{p}\sum_{q}\sum_{m}\sum_{r}\left|H_p(F;\alpha)cum\left(Y_q(F)Y_m(F)Y_r(F)\right)-H_q(F;\alpha)cum\left(Y_p(F)Y_m(F)Y_r(F)\right)\right|^2} \tag{3.41}$$

In the case of a true match, we write the output signals in terms of transfer function and source signal (as given in equation (3.1)),

$$P_{Y,\alpha}^{H\_CR}=\frac{1}{\left|cum\left(s^3(F)\right)\right|^2\sum_{p}\sum_{q}\sum_{m}\sum_{r}\left|H_p(F;\alpha)H_q(F)H_m(F)H_r(F)-H_q(F;\alpha)H_p(F)H_m(F)H_r(F)\right|^2} \tag{3.42}$$

For zero-mean Gaussian random sources (white or non-white) we have $cum\left(s^3(F)\right)=2\sigma^2\bar{s}=0$. The Gaussian source cannot be localized since its 3rd order cumulant is zero and does not satisfy the second part of identifiability condition. This provides MFP the ability of concentrating on non-Gaussian sources such as radiated noise from passing ships.

The effect of zero mean spatially white non-Gaussian interference is canceled since each output signal does not appear more than once in the cumulants.

For the mismatch case, we consider the following. Let us assume that a mismatch exists in the true source location or an environmental parameter has occurred. The cross-relation term (equation (3.36)) takes the form

$$CR_{pq}=E(s^T)H_m(F)\ldots H_{m+T-2}(F)\left(\underbrace{H_p(F;\alpha)H_q(F)-H_q(F;\alpha)H_p(F)}_{\mu_{pq}}\right) \tag{3.43}$$

For parameters with low sensitivity to the pressure field, there is no significant change in the amplitude of the transfer function. In this case we mainly focus on the transfer function phase.

Moreover, let us assume that the array length is small enough in comparison to the water depth so with good approximation we can assume that the amplitudes of the transfer functions appearing in the formulation are the same. Equation (3.43) can be simplified to

$$\left|CR_{pq}\right| \approx \left|E(s^T(F))\right|\left|H(F)\right|^{T-1}\left|\mu_{pq}\right| \tag{3.44}$$

By substituting equation (3.44) in the MFP formulation (equation (3.40)) we have:

$$P_{Y,\alpha}^{H\_CR} = \frac{1}{M(T)\left|H(F)\right|^{2(T-1)}\left|E(s^T(F))\right|^2 \sum_p \sum_q \left|\mu_{pq}\right|^2} \tag{3.45}$$

where M(T) is a constant multiplier that shows the number of CR terms in the MFP formulation. For an array with N sensors we have $M(T) = \binom{N-2}{T-1}$.

To obtain a simpler equation, let us assume that the deviation due to the mismatch is independent of the sensors *p* and *q*:

$$P_{Y,\alpha}^{H\_CR} \approx \frac{1}{M(T)\left|H(F)\right|^{2(T-1)}\left|E(s^T(F))\right|^2 \binom{N}{2}\left|\mu\right|^2} \tag{3.46}$$

Now, let us define the MFP sensitivity. The sensitivity function *S* is defined as

$$S = \left[S_1, S_2, \ldots, S_q\right] \tag{3.47}$$

where

$$S_i = \left|\frac{\partial P_{Y,\alpha}^{H\_CR}}{\partial \alpha_i}\right| ; i = 1, \ldots, q \tag{3.48}$$

The sensitivity function from equation (3.46) becomes

$$S_i^T \approx \frac{2}{M(T)\left|H(F)\right|^{2(T-1)}\left|E(s^T(F))\right|^2 \binom{N}{2}\left|\mu\right|^3} \frac{\partial \mu}{\partial \alpha_i} \tag{3.49}$$

To see how the MFP sensitivity changes with increasing the order from *T* to *T+1* we obtain

$$S_i^{T+1} = \frac{M(T)\left|E(s^T(F))\right|^2}{M(T+1)\left|H(F)\right|^2\left|E(s^{T+1}(F))\right|^2} S_i^T = \frac{T\left|E(s^T(F))\right|^2}{\left|H(F)\right|^2\left|E(s^{T+1}(F))\right|^2 (N-T-1))} S_i^T \tag{3.50}$$

The transfer functions norms represent the transmission loss from the source to the vertical array sensors. The loss is generally high because of the high ocean attenuation, so the transfer functions are small. This fact increases the sensitivity function to larger values for higher order MFP; however in order to calculate the sensitivity function we need to know the relative value of moments.

Chapter Four

Phase Regulated Back Wave Propagation Technique, Concept and Formulation

In this chapter we consider the concept of back wave propagation (BWP) as an inversion method to estimate ocean geoacoustic parameters in experiments for which the source location is known. A phase-regulation technique is introduced to increase the sensitivity of the method for geoacoustic model parameters having low sensitivity. We also address the case of data consisting of signal plus additive noise. We show theoretically that we can increase the sensitivity by a factor α using the phase regulation procedure. We also show that the spatial resolution of signal energy that is concentrated by BWP at the known source position is increased when α increases. This leads us to define a criterion based on the spatial distribution of signal energy around the true source location. The criterion is formulated based on the spatial variance of the back-propagated pressure field in a window around the known source location. We also propose a multi-step search process to avoid using a complicated multi-dimensional search process.

Inversion results from both simulations and experimental data are given in chapter 6. The real data were taken from the Pacific Shelf experiment carried out in shallow water off the West Coast of Vancouver Island in the Northeast Pacific Ocean. That experiment is described in chapter 5.

4.1 Back wave propagation concept

Matched field inversion (MFI) techniques have been used in ocean acoustic tomography to estimate model parameters of the real ocean environment. These techniques maximize or minimize objective functions when the measured acoustic pressure field is optimally matched with the modeled field (replica). Matched field processors are members of the blind system

identification class (see chapter 3), and well-known processors such as the Bartlett, Matched Mode, Minimum Variance, and Multiple Constraints processors have been applied to data obtained using multi-sensor arrays in the ocean (see chapter 2).

The back wave propagation (BWP) concept is based on the reciprocity and superposition properties of the ocean wave-guide which state that the measured pressure fields can be considered as sources for an array of transmitters; i.e., the conjugate of the measured field at the array is weighted by the range and back propagated by the array. Because the ocean field is a passive environment and if the geometry of the transmit array is the same as the experimental geometry, then it can be shown that only for the true ocean environmental parameters does the back-propagated wave field converge to the location of the source. In Fig.4.1 the scheme of forward and backward propagation is given.

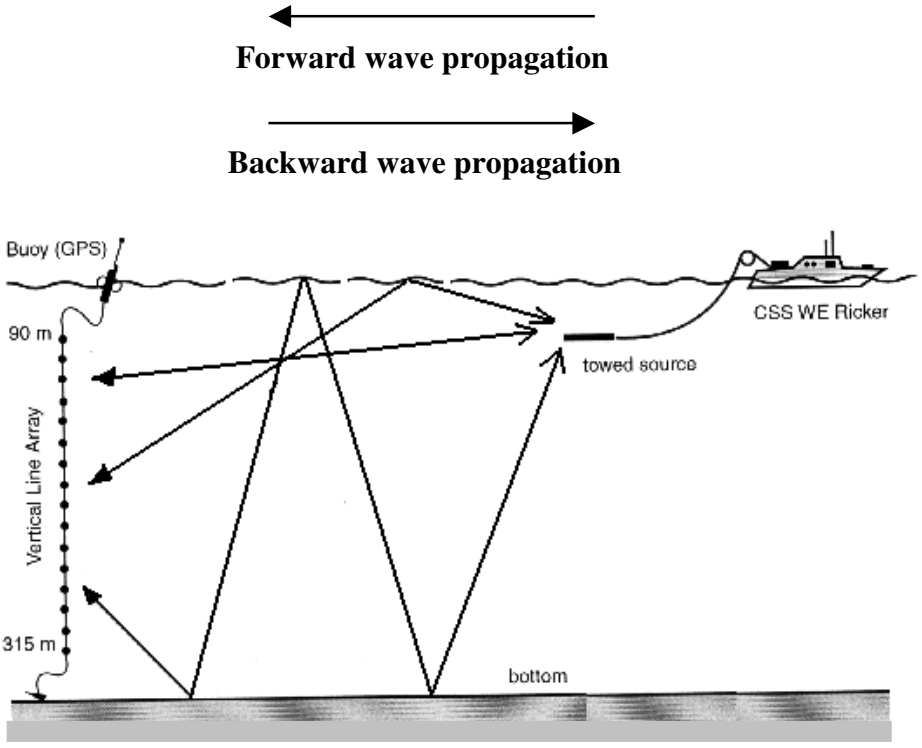

Fig.4.1. Forward and backward propagation scheme

A parabolic equation (PE) based back wave propagation model was originally suggested by Tappert et al. [57]. However, since then the technique has received relatively little attention. Collins et al. [58] and Thomson et al. [59] have shown the use of BWP for source localization in

range dependent environments. In this chapter we develop an inversion method based on BWP for estimating the properties of the waveguide. A post processing phase regulation technique is derived to improve the performance of the method for estimating low sensitivity parameters.

For some inversion problems it is known that with conventional estimation methods there is weak sensitivity of the pressure field measurements to environmental parameters such as shear speed, shear attenuation, and density. In contrast the phase regulated BWP technique has the advantage of being adapted to the environmental conditions. In this procedure we vary a sensitivity factor α that enhances the phase changes due to model and environmental mismatch. By appropriately choosing values of α we can estimate environmental parameters to a required accuracy. The theory of this concept is presented in section 4.2. In practice, however, we are limited in choosing arbitrarily high values for α because of noise effects. In section 4.3 we discuss the effects of noise on the sensitivity value and source location estimation.

In section 4.4 we introduce a criterion for estimating the best match of model parameters with those of the real ocean environment. The criterion minimizes the spatial variance of the back- propagated signal energy in the vicinity of the source location.

A significant disadvantage of MFI methods is the computationally complex search method which are difficult to realize in practice. To overcome this difficulty, we propose a procedure based on appropriate choice of sensitivity factor and environmental parameters in a multi-step search process that approximates a D-dimensional searching process with a T d-dimensional searching processes where $D=Td$ and $T<D$. This approximation is usually achieved by classifying environmental parameters into three sets high, medium and low sensitivity with respect to the sensitivity of the pressure field to them and choosing an appropriate value of α for each set. This procedure is discussed in section 4.5.

4.2 Phase regulated back wave propagation

The BWP concept implies that the fields received at an array of N sensors can be used as sources. The pressure field used as the source in the back propagation step is the conjugate of the measured field $P^*(r_c, z_k)$, $k = 1,\ldots,N$ obtained in the forward propagation step but weighted by

the range. The back-propagated field at location (r,z) for a range independent environment can be expressed using normal modes [11,81]

$$P_b(r,z,\gamma)=\sum_{k=1}^{N}\frac{j(r_c-r)^{\frac{1}{2}}P_f^*(r_c,z_k,\gamma)}{4\rho(z_k)}\sum_{m=1}^{M}\Psi_m(z_k)\Psi_m(z)H_0^{(1)}(k_{rm}(r_c-r)) \qquad (4.1)$$

$\gamma=[\gamma_1,\gamma_2,\ldots,\gamma_q]$ is a vector which contains both the environmental and the source parameters, $\rho(z)$ is the depth dependent density function, $H_0^{(1)}(r)$ is Hankel function (type 1, order 0), $\Psi_m(z)$ is the m^{th} eigenfunction (mode) and k_{rm} is m^{th} eigenvalue of the m^{th} mode. Let us define the function $R_k(r,z,\gamma)$, the pressure signal measured at a point (r,z) weighted by the range parameter,

$$R_k(r,z,\gamma)=\frac{j(r_c-r)^{\frac{1}{2}}P_f^*(r_c,z_k,\gamma)}{4\rho(z_k)}\sum_{m=1}^{M}\Psi_m(z_k)\Psi_m(z)H_0^{(1)}(k_{rm}(r_c-r)) \qquad (4.2)$$

If we substitute (4.2) into (4.1) then we can write the back-propagated field as

$$P_b(r,z,\gamma)=\sum_{k=1}^{N}\left|R_k(r,z,\gamma)\right|e^{j\phi_k(r,z,\gamma)} \qquad (4.3)$$

It can be shown that the maximum values of $P_b(r,z,\gamma)$ occur whenever $\phi_k(r,z,\gamma)\approx 0\ ;k=1,\ldots,N.$

To evaluate how the pressure signal changes with changes in the parameters; we introduce the s*ensitivity vector,*

$$S=\left[S_1,S_2,\ldots,S_q\right] \qquad (4.4)$$

$$S_i=\left|\frac{\partial P_b(r,z,\gamma)}{\partial\gamma_i}\right|;i=1,\ldots,q \qquad (4.5)$$

Substituting (4.3) into (4.5), we obtain

$$S_i=\left|\sum_{k=1}^{N}\left(\frac{\partial\left|R_k(r,z,\gamma)\right|}{\partial\gamma_i}e^{j\phi_k(r,z,\gamma)}+j\frac{\partial\phi_k(r,z,\gamma)}{\partial\gamma_i}\left|R_k(r,z,\gamma)\right|e^{j\phi_k(r,z,\gamma)}\right)\right| \qquad (4.6)$$

It has been shown that in some cases the changes in the signal pressure relative to changes in a particular environmental parameter are small [60]. In order to overcome this problem we introduce a phase enhanced technique wherein we amplify the phase changes arising from environmental mismatch by the s*ensitivity factor* α. By multiplying the phase function $\phi_k(r,z,\gamma)$ in (4.3) by α we obtain

$$P_b^{\alpha}(r,z,\gamma) = \sum_{k=1}^{N} \left|R_k(r,z,\gamma)\right| e^{j\alpha\phi_k(r,z,\gamma)} \tag{4.7}$$

For this new expression we calculate the sensitivity

$$S_i^{\alpha} = \left| \sum_{k=1}^{N} \left(\frac{\partial \left|R_k(r,z,\gamma)\right|}{\partial \gamma_i} e^{j\alpha\phi_k(r,z,\gamma)} + j\alpha \frac{\partial \phi_k(r,z,\gamma)}{\partial \gamma_i} \left|R_k(r,z,\gamma)\right| e^{j\alpha\phi_k(r,z,\gamma)} \right) \right| \tag{4.8}$$

In the case of low sensitivity to an environmental parameter, the expressions in (4.6) and (4.8) are close to zero. We can approximate them by

$$S_i \approx \left| \sum_{k=1}^{N} \left(j \frac{\partial \phi_k(r,z,\gamma)}{\partial \gamma_i} \left|R_k(r,z,\gamma)\right| e^{j\phi_k(r,z,\gamma)} \right) \right| \tag{4.9}$$

$$S_i^{\alpha} \approx \left| \sum_{k=1}^{N} \left(j\alpha \frac{\partial \phi_k(r,z,\gamma)}{\partial \gamma_i} \left|R_k(r,z,\gamma)\right| e^{j\alpha\phi_k(r,z,\gamma)} \right) \right| \tag{4.10}$$

In the BWP technique the mismatch between the selected model parameters and their actual values can be evaluated by assessing the spatial resolution of the back-propagated signal that is focused near the source. Actually these points refer to the places where $\phi_k(r,z,\gamma) \approx 0 \; ; k = 1,\ldots,N$. At these points S_i *and* S_i^{α} take the form

$$S_i \approx \left| \sum_{k=1}^{N} \left(j \frac{\partial \phi_k(r,z,\gamma)}{\partial \gamma_i} \left|R_k(r,z,\gamma)\right| \right) \right| \tag{4.11}$$

$$S_i^{\alpha} \approx |\alpha| \left| \sum_{k=1}^{N} \left(j \frac{\partial \phi_k(r,z,\gamma)}{\partial \gamma_i} \left|R_k(r,z,\gamma)\right| \right) \right| = |\alpha| S_i \tag{4.12}$$

The sensitivity of BWP is increased by the sensitivity factor α. In principle by appropriately choosing α we can estimate environmental parameters to a required resolution.

Applying the phase factor also changes the spatial resolution of the focused energy points; i.e., it concentrates the back-propagated signal that is focused near the source. We can show this by calculating the derivative of $P_b^{\alpha}(r,z,\gamma)$ with respect to the displacement vector $\vec{u} = (r,z)$ at the focused energy points:

$$\frac{\partial P_b^{\alpha}(\vec{u},\gamma)}{\partial \vec{u}} = \sum_{k=1}^{N} \left(\frac{\partial \left|R_k(\vec{u},\gamma)\right|}{\partial \vec{u}} e^{j\alpha\phi_k(\vec{u},\gamma)} + j\alpha \frac{\partial \phi_k(\vec{u},\gamma)}{\partial \vec{u}} \left|R_k(\vec{u},\gamma)\right| e^{j\alpha\phi_k(\vec{u},\gamma)} \right) \tag{4.13}$$

The fact that the signal pressure norm changes little with changes in location relative to the effect of the phase changes allow us to rewrite equation (4.13) as

$$\frac{\partial P_b^{\alpha}(\vec{u},\gamma)}{\partial \vec{u}} \approx \alpha \sum_{k=1}^{N} \left(j \frac{\partial \phi_k(\vec{u},\gamma)}{\partial \vec{u}} \left| R_k(\vec{u},\gamma) \right| e^{j\alpha\phi_k(\vec{u},\gamma)} \right) \tag{4.14}$$

At focused points $(\phi_k(r,z,\gamma) \approx 0 \; ; k = 1,\ldots,N)$ we obtain

$$\frac{\partial P_b^{\alpha}(\vec{u},\gamma)}{\partial \vec{u}} \approx \alpha \sum_{k=1}^{N} \left(j \frac{\partial \phi_k(\vec{u},\gamma)}{\partial \vec{u}} \left| R_k(\vec{u},\gamma) \right| \right) \approx \alpha \frac{\partial P_b(\vec{u},\gamma)}{\partial \vec{u}} \tag{4.15}$$

The effect of noise on these relations is considered next.

4.3 Noise effects

Because of background noise, we are limited in choosing arbitrarily high values for α. Let us assume that the noise effect appears in the form of an additive random phase with a uniform distribution having a depth dependent mean equal to $\phi_{k,0}$ and variance d_k. The total field with noise is then

$$P_f^{'n'}(r_c, z_k, \gamma) = P_f(r_c, z_k, \gamma) e^{j\phi_{nk}} \tag{4.16}$$

If we substitute (4.16) into (4.3) and using the fact that $E\{e^{j\phi_{nk}}\} = 2\frac{\sin(d_k)}{d_k} e^{j\phi_{0,k}}$, we can write the back-propagated field as

$$\begin{aligned} E\{P_b(r,z,\gamma)\} &= \sum_{k=1}^{N} \left| R_k(r,z,\gamma) \right| e^{j\phi_k(r,z,\gamma)} E\left\{ e^{j\phi_{nk}} \right\} \\ &= 2\sum_{k=1}^{N} \left| R_k(r,z,\gamma) \right| \frac{\sin(d_k)}{d_k} e^{j\phi_{0,k}} e^{j\phi_k(r,z,\gamma)} \end{aligned} \tag{4.17}$$

The maximum value of $E\{P_b(r,z,\gamma)\}$ occurs whenever

$$\left(\phi_k(r,z,\gamma) + \phi_{0,k} \right) \approx 0 \; ; k = 1,\ldots,N \tag{4.18}$$

The meaning of (4.18) is that noise causes a distortion in the phase function that results in a bias in the source location estimation. When incorporating the phase factor α we have

$$E\left\{P_b^{\alpha}(r,z,\gamma)\right\} = 2\sum_{k=1}^{N}\left|R_k(r,z,\gamma)\right|\frac{\sin(\alpha d_k)}{\alpha d_k}e^{j\alpha\phi_{0,k}}e^{j\alpha\phi_k(r,z,\gamma)} \qquad (4.19)$$

The sensitivity factor α does not have a significant effect on the source localization estimate since the zeros of equation (4.18) are not affected by α.

Following the procedure used to obtain equation (4.11), the sensitivity function (equation (4.17)) in the presence of noise becomes (α=1)

$$S_i \approx 2\left|\sum_{k=1}^{N}\left(j\frac{\partial\phi_k(r,z,\gamma)}{\partial\gamma_i}\frac{\sin(d_k)}{d_k}\left|R_k(r,z,\gamma)\right|\right)\right|, \qquad (4.20)$$

Assuming that $\phi_{k,0}$ is small enough that the bias imposed on the source location is negligible. Equation (4.20) indicates that the phase variation due to the background noise has considerable effect on the sensitivity function. The sensitivity nulls occur for $d_k = n\pi$, *n=integer* for all *k*. For $\alpha \neq 1$, equations (4.12) and (4.19) show that the sensitivity for $\phi_{k,0}$ small is

$$S_i^{\alpha} \approx 2\alpha\left|\sum_{k=1}^{N}\left(j\frac{\partial\phi_k(r,z,\gamma)}{\partial\gamma_i}\frac{\sin(\alpha d_k)}{\alpha d_k}\left|R_k(r,z,\gamma)\right|\right)\right|. \qquad (4.21)$$

From equation (4.21) we see that for the α-enhanced phase the sensitivity amplification is modified by the phase variation. For very small phase variance d_k we have $\frac{\sin(\alpha d_k)}{\alpha d_k} \approx 1$ and obtain the same results as for the noiseless case.

4.4 A spatial variance measure for BWP best match

The essence of the BWP technique is the convergence of back propagated waves at the true source location if the environmental model parameters are exactly matched. There is an energy distribution around the source when a mismatch occurs. This fact leads us to consider the energy distribution of the back-propagated field near the source as a criterion to determine the best match. A measure of field distribution is obtained by calculating the field spatial variance with respect to true source location in a window around the source. Its value is minimized when most of signal energy concentrates at the source point, i.e., where a true match occurs.

Let us define $f(r,z)$, $|r-r_0| \le \frac{N}{2}$, $|z-z_0| \le \frac{M}{2}$ as the energy in an $M \times N$ window around the true source location $S(r_0,z_0)$ where $\|f\| = 1$ (see Fig.4.2).

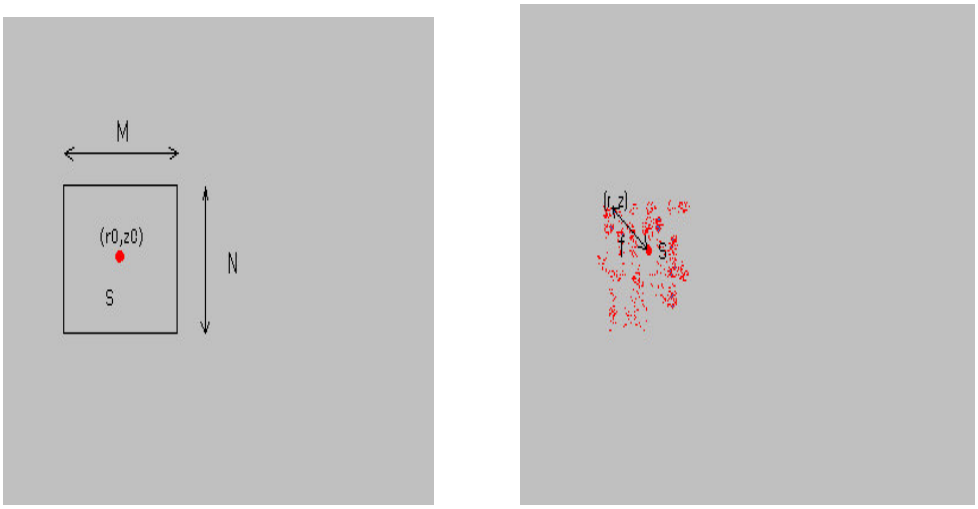

(a) (b)

Fig.4.2. (a) The convergence of back propagated wave energy for true environmental parameter (high spatial variance) and (b) in the case of mismatch (low spatial variance)

The criterion is to minimize the spatial variance of the back-propagated field energy with respect to the true source location. If we denote $f(r,z) = \frac{\left|P_b^{\alpha}(r,z,\gamma)\right|^{\beta}}{\left\|P_b^{\alpha}(r,z,\gamma)\right\|_F^{\beta}}$ as the distance probability density function, the criterion can be interpreted as the mean square distance from the true source location. $\|.\|_F$ denotes the Frobenius norm.

$$BWP_{criterion} = \frac{1}{MN} \sum_{m=-M/2}^{M/2} \sum_{n=-N/2}^{N/2} d^2(r,z) f(r,z)$$

$$where \qquad (4.16)$$

$$d(r,z) = \sqrt{(r-r_0)^2 + (z-z_0)^2}$$

We refer to the above criterion as the BWP focal function.

4.5 An efficient multi-step search procedure

A direct way to find the best estimates of D unknown environmental parameters is to use a D-dimensional grid search among possible parameter values. This search is computationally expensive. We can reduce the D-dimensional search space to the T successive d-dimensional

search space ($D=Td$ where $T<D$) by exploiting the fact that the pressure field has different sensitivity with respect to these parameters. For example, the pressure field is most sensitive to the water depth even for small sensitivity factors while for a small sensitivity factor α, the field is only weakly sensitive to changes with respect to other environmental parameters such as compressional speed and density changes. A block diagram of the search procedure is shown in Fig. 4.3.

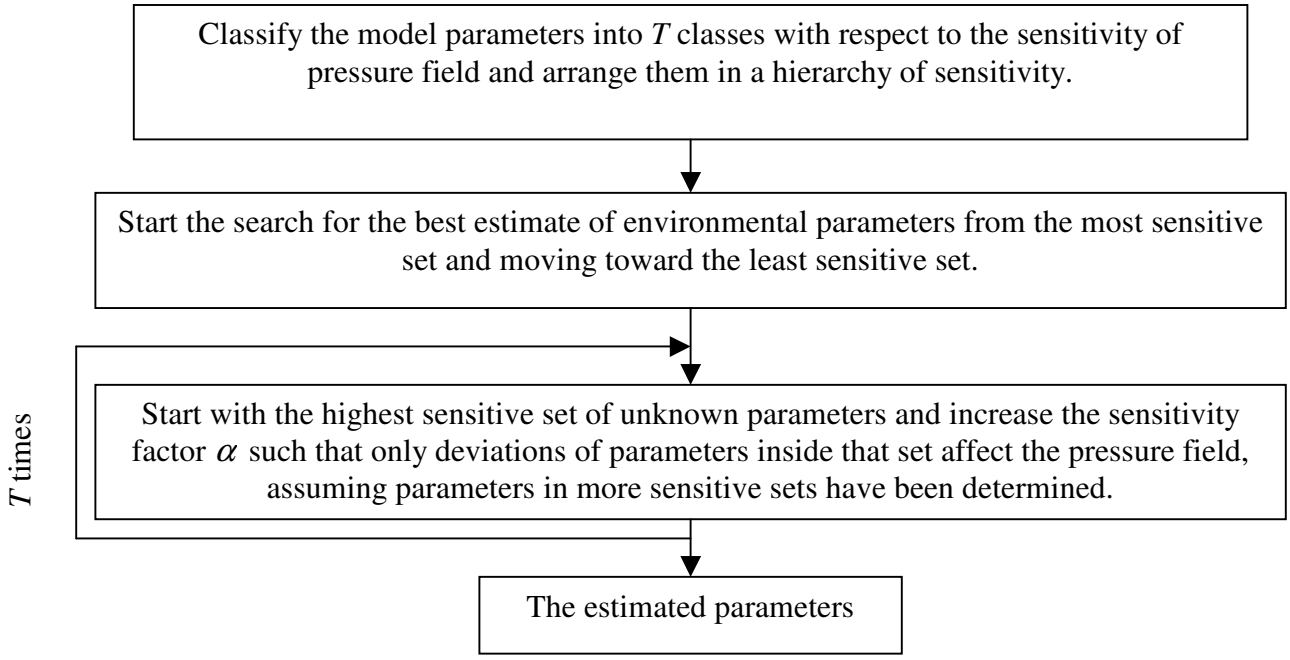

Fig.4.3. A block diagram of multi-steps search process

In summary we first adjust the high sensitivity parameters such as water depth. In the next step we search among potential values of medium sensitivity parameters such as compressional speed using a higher value of α. For this value of α the sensitivity to very low sensitivity parameters such as density remains low. At the last step we increase the sensitivity factor to a higher value to adjust the low sensitivity parameters. This gives a three-step technique. We can increase the steps by more precisely categorizing the environmental parameters. The simulation and experimental results are given in chapter 4.6.

Chapter Five

Source Localization, Simulation and Experiment

This chapter presents an evaluation of cross-relation matched field processors for source localization and compares their performance with that for other MFPs. The evaluation is conducted using both simulations and experimental data. Environmental parameters are assumed known in the simulations, and for the real data we rely on values obtained from seismic ground truth data in the region of experiment. The simulation environment described in section 5.1 is designed to approximate the conditions at the experimental site of the Pacific Shelf sea trial conducted on September 1993 in a region close to Vancouver Island, BC, Canada. We make use of data from a deterministic source (in the form of CW tones) and a random source (ship signal) received by a vertical linear array. An overview of ship signal specifications is given in this section.

The simulation results are given in section 5.2 for two types of broadband sources. At first we consider a random source generator to simulate a ship signal. After adding measurement noise to data, the performance of two different kinds of cross-relation MFP (self and cross) is compared with that for the representatives of major MFP classes, i.e. Bartlett, MV, and Westwood matched field processors. In a subsection (5.2.2), we apply a novel time-frequency MFP (section 3.4) to data generated by a known broadband chirp signal in an environment that contains other random sources (such as wind noise, ocean waves, ship noises, and etc.). We use the signature of the chirp signal in a preprocessing step to restore the chirp content of the received signal. This approach does not preclude the idea of using blind system identification techniques because we are blind with respect to the other random sources. We show the performance of time-frequency MFP in recovering the chirp source location from only a single pulse, and compare the performance with that of other MFPs. Conventional MFPs have overlooked the use of the chirp source in the presence of strong correlated noises. Because the chirp signal is a wide-band signal, it overlaps in frequency with other correlated noises; the

overlap normally precludes recovering of the chirp signal using processors formulated in the frequency domain.

Time-frequency MFPs (TF-MFP) are used in seismic, sonar and radar applications where the chirp signal is an essential part of wide band inversion experiments.

The last section of this chapter provides the results obtained from processing the data from the experiment. We evaluate the performance of cross-relation MFPs for source localization using the ship data and compare both resolution of the main peak and side-lobe level with those of other processors. We then apply a higher-order MFP and compare its source localization performance with that obtained from conventional MFPs. The higher-order MFP is helpful for environments where there is Gaussian interference, either coherent (or colored) that may come from a single source, or white such as measurement noise. Conventional MFPs are insensitive to the higher order statistical content of the ship signal, so cannot use the complete information embedded in the data. Although the analysis is conducted for a surface ship, the results can be extended to other kind of vessels such as submarines and other random point sources.

5.1. Pacific Shelf Experiment

The ship noise and continuous-wave (CW) data were obtained using a multi-element vertical array (MEVA) that was deployed on September 1993 in shallow water off the West coast of Vancouver Island in the Northeast Pacific Ocean. Fig.5.1 shows the location of the experiment. This location was selected in order to take advantage of drilling results obtained during the ocean drilling program (ODP), Cascadia Margin Leg 146 [61].

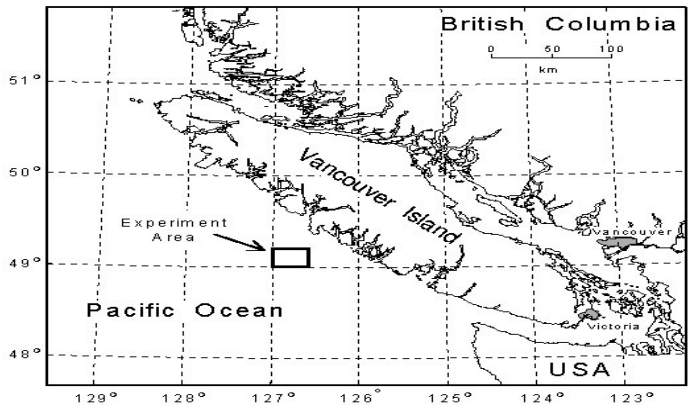

Fig.5.1 The location of the experiment is shown with respect to the south-western coastline of British Columbia, Canada

The CSS W.E. RICKER, a medium size merchant ship, was the source ship that transmitted a multi-frequency continuous-wave (CW) towed source. The CFAV ENDEAVOUR, another medium size merchant ship, collected acoustical data from the vertical linear array (VLA). The source and receiver positions were obtained from GPS (global positioning system) data that were recorded every two minutes at the source ship and the array. The source to receiver ranges were determined with maximum error of 200 m. These range estimates were within 100 m of the ranges determined from the CFAV ENDEVOUR's radar data for the array surface buoy and source ship. The source ship's track and receiver's position from 905 hrs to 1242 hrs on September 13, 1993 is shown in Fig. 5.2. The array system is shown in Fig. 5.3.

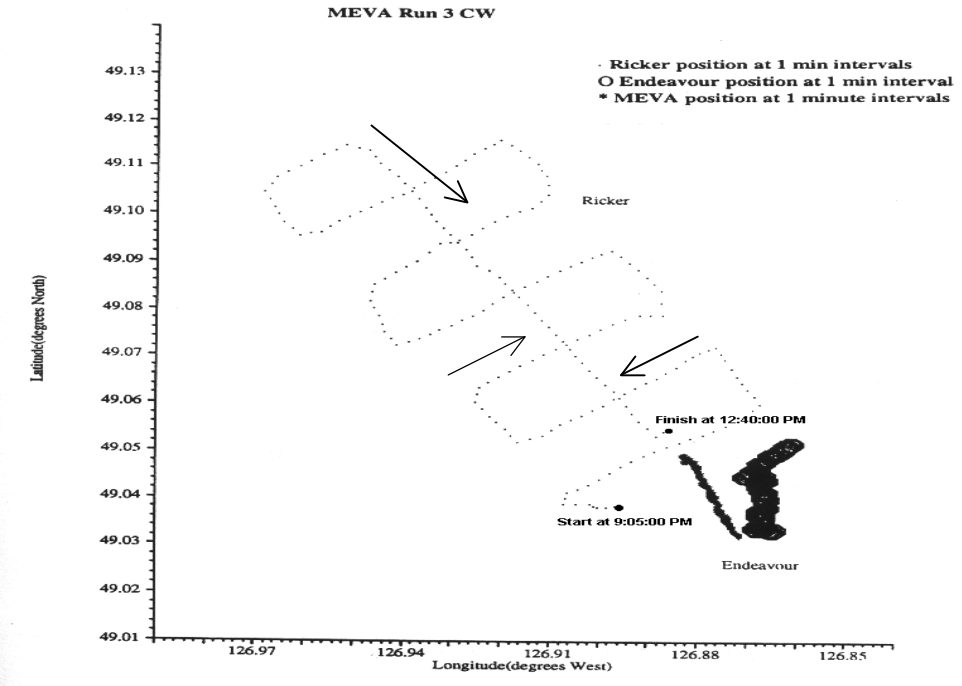

Fig. 5.2 Towed track from 905 hrs to 1240 hrs with indicated target (MEVA run 3 trial)

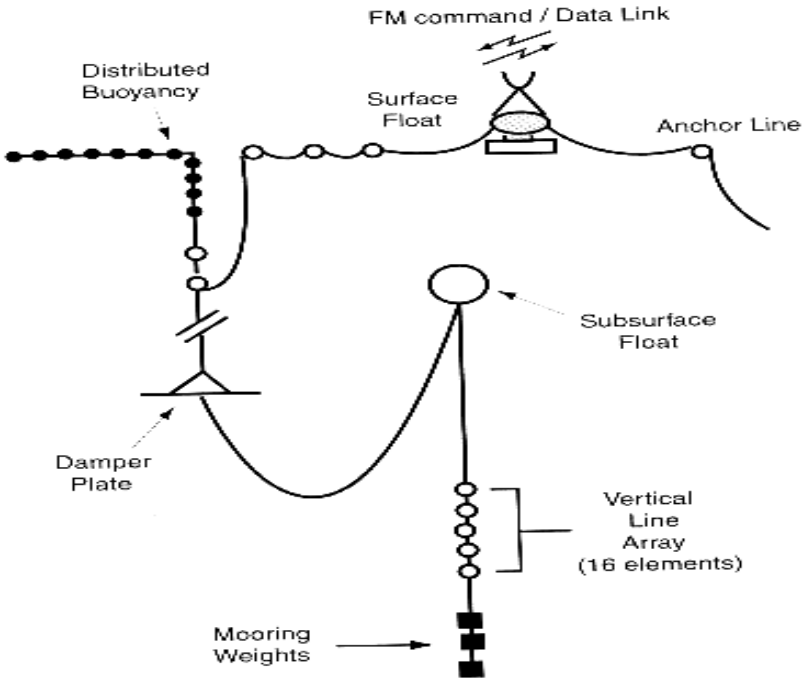

Fig. 5.3 MEVA 3 – Vertical line array configuration

The VLA was suspended from a surface float that was anchored by a line to the bottom and restricted its motion to a radius of about 1 km. Mechanical isolation from the sea surface motion was achieved by a two-stage suspension system consisting of the distributed buoyancy and a damper plate, and a subsurface float that was connected by a neutrally buoyant cable of about 20-m in length. The natural frequency of the first stage was designed to be well below the sea surface swell and wave frequencies. The VLA consists of a 16-element filled array with 15 m spacing. The top hydrophone was at a depth of 90 m and the bottom at 315 m, with a total aperture of 225 m. According to Tolstoy [1], optimal MFP results using a linear processor are obtained for hydrophone spacing $\Delta_{hp} \leq \lambda$, and for an array that spans as much of the water column as possible. This will provide a more complete sample of the spatial variation of the acoustic field and thus improve the MFP localization [1].

The hydrophones, which had a sensitivity of –191 dB *re:* $1V / \mu Pa$, were enclosed with pre-amplifiers in 0.5-m sections of 7.6-cm-diam oil filled PVC hose. Modules consisting of the hydrophone enclosure and a selected length of cable were connected to construct a desired array

aperture. The hydrophone data were filtered, amplified, and digitized at 1500 samples/s with a 12-bit A/D at an underwater electronic unit located at the top of the VLA. The digital data were also transmitted over the RF link from the surface float to the ship, and subsequently recorded on exabyte tape. Power for the system was supplied by wet and dry cell batteries which were contained in a sealed box at the base of the surface float. The system could operate for a period of 5 days before recharging was necessary.

The position of the VLA in Fig. 5.2 was intended to remain at a fixed location but strong currents in the region caused it to drift. This drifting may have been due to tidal currents and was at most ~25m for the data analyzed here, based on the recorded GPS position. There was also some evidence from data collected at a nearby site, that upwelling occurred near the time of the experiment [62]. Commonly associated with upwelling are coastal currents and a water column with greater range-dependent sound-speed characteristics.

Three CW tones at 45, 70, and 72 Hz were transmitted from a source towed by CSS Ricker along the track shown in Fig. 5.2. The source depth was approximately 30m, but the exact depth was not known due to a failure of a depth sensor on the source. The tones served as beacons to calibrate the methods for source localization developed in this thesis.

5.1.1. Oceanographic conditions

5.1.1.1. Bathymetric Database

Erroneous bathymetry data have a significant impact on matched field source localization. Bathymetric data off the coast of Vancouver Island were found to be quite limited for the experimental site. A ”Geological Survey of Canada” chart, Davis et al. [63], shows well-defined contours, but digitized information is not available. Therefore, a bathymetric database, specific to the MEVA experiment was constructed using various sources of echo-sounding data [64]. The final result is shown in Fig. 5.4. The area in which MEVA 3 was conducted is shown by a dotted box.

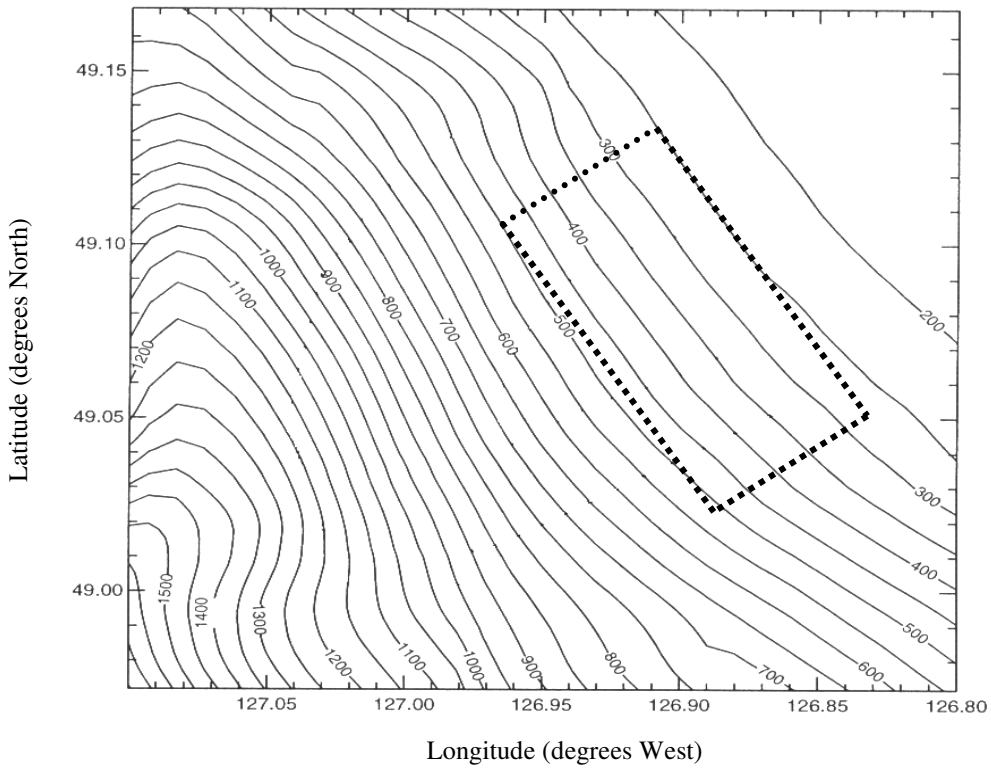

Fig. 5.4 Contour chart for experimental region. The dotted box shows the region in which MEVA 3 was conducted

5.1.1.2. Geoacoustic data

The determination of the geoacoustic properties of the experimental region was accomplished using various inversion methods described in reports by Hannay [65], Hanny and Chapman [9], and Chapman et al. [66], and by refining model parameters via a simple grid-search in matched field localization [64]. We apply our inversion method to a portion of data for which the propagation was approximately range independent. The layered structure of the ocean bottom along the selected ship track along the 400m contour is shown in Fig. 5.5. The detailed geoacoustic information is given in Table 5.1 [64].

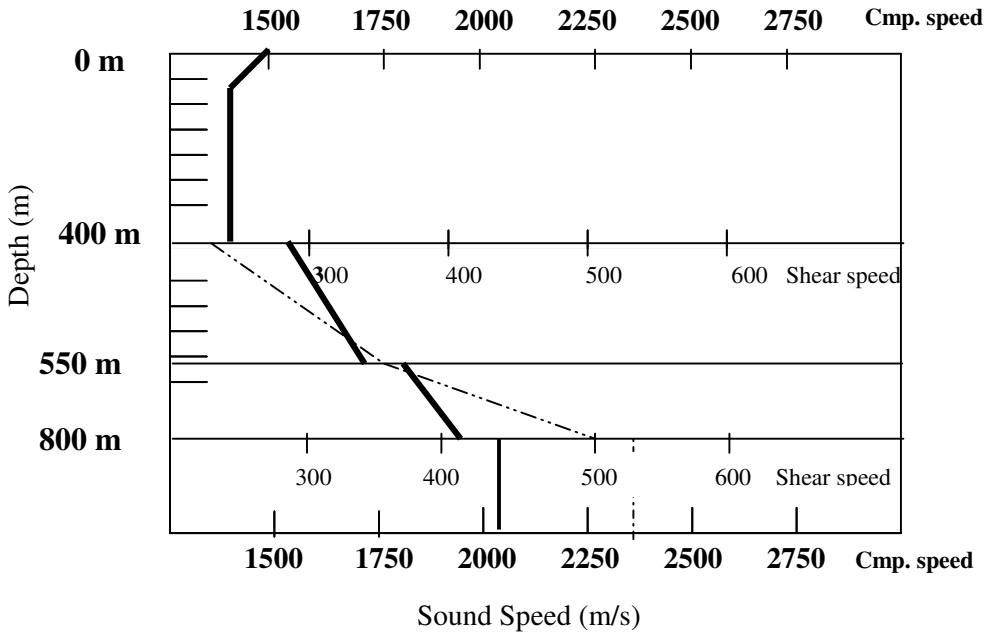

Fig 5. The sound speed profiles used in the environmental model. The shear speed, C_s (dot-dashed) and the compressional speed, C_p (dark and solid) are shown on the three lower abscissa scales

Table 1. Geoacoustic properties based on [64]

Sediment	**Depth (m)**	**C_p (m/s)**	**C_s (m/s)**	$\alpha_p\,(dB/\lambda^{-1})$	$\alpha_s\,(dB/\lambda^{-1})$	$\rho\,(g/cm^3)$
Sand-silt	0-150	1550-1700	100-350	0.2	0.5	1.6
Layer 2	150-300	1800-1950	350-500	0.2	0.5	1.8
Basement	(350+)	2100	550	0.2-10	0.5-10	2.1

5.1.1.3. Sound speed profile

Changes in sound speed profile can have a profound effect on sound transmission, particularly the changes that occur within the surface layer. The speed is susceptible to daily and local changes such as solar heating, wind and currents. Urick [45] showed that the changes of temperature over a 24 hour period can range up to 5 degree Celcius. Such a variation can contribute up to 10 m/s variability in the sound speed profile. In addition there are factors other

than temperature that contribute to sound speed profile variation such as currents, wind mixing, and geographical location.

Over the entire period of the experiment (from 10 Sept to 18 Sept 93) 19 sound speed profiles were collected. For the data considered here, the sound speed profile measured immediately before the experiment is shown in Fig. 5.6.

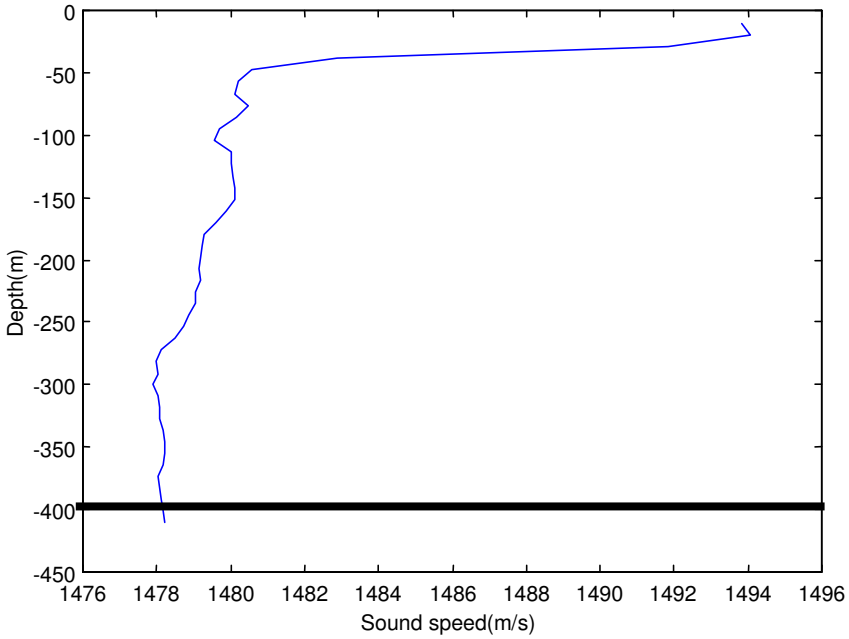

Fig. 5.6 Sound speed profile for MEVA 3 trial

5.1.2 Vessel noise specification

Average ambient ocean noise power spectra are given in Fig. 5.7 for different conditions of shipping and wind speed [45]. In the infrasonic region below 20 Hz, only a single line is drawn, since the wind speed dependence is slight and uncertain. The “heavy shipping” curve is used for locations near the shipping lanes while the “light shipping” curve is appropriate for locations remote from ship traffic. The “shipping” curves show dominant power in the band between 20 Hz and 300 Hz.

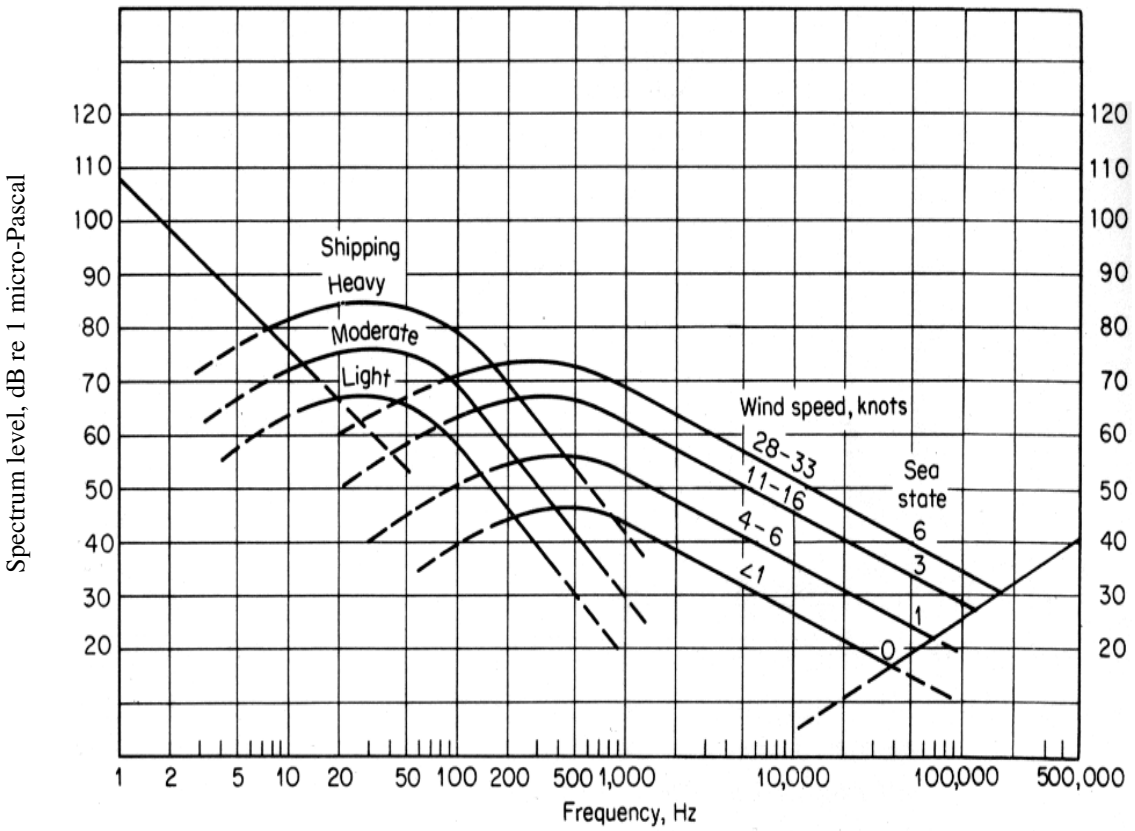

Fig. 5.7 Average ocean ambient noise spectra [45]

The radiated signal of ships and submarines consisting of a mixture of tones and a continuous spectra that is due to different sources of signal, and can be categorized into three groups [45]: machinery signals, propeller signals, and hydrodynamic signals that originates in the irregular flow of water past the vessel.

Machinery signal comes from mechanical vibration of the many and diverse parts of a moving vessel. This vibration is coupled to the sea via the hull of the vessel. These vibrations originate with 1) unbalanced rotating parts such as out-of-round shafts or motor armatures, 2) repetitive discontinuous parts such as gear teeth, armature slots, and turbine blades, 3) reciprocating parts such as the explosion in cylinders of reciprocating engines, 4) cavitation and turbulence in the fluid flow in pumps, pipes, valves, and condenser and discharges, and 5) mechanical friction. The first three sources produce a line-component spectrum in which the signal is dominated by tonal components at the fundamental frequency and harmonics of the vibration-producing process, and the other two give a continuous spectrum. Because of the

various machinery components in the vessel, the harmonic structure of the radiated signal is complex. The line component of the spectrum is irregular and variable, giving rise to a non-stationary, broadband signal.

Although the propeller is a part of the propulsion machinery of a vessel, the propeller signal is different from the machinery signal with respect to both its origin and frequency spectrum. The machinery signal originates inside the vessel and transmits to the water through the hull at various sites along the hull, whereas the propeller signal originates outside the hull. The source of the propeller signal is principally the signal of cavitation induced by the rotating propellers. When a propeller rotates in water, regions of low or negative pressure are created at the tips and on the surface of the propeller blades. If these negative pressures become high enough, physical rupture of the water takes place and cavities in the form of minute bubbles begin to appear. These bubbles collapse a short time later, either in the turbulent stream or up against the propeller itself and in so doing emit a sharp pulse of sound. The sound produced by a great many of such collapsing bubbles is a loud “hiss” that dominates the high frequency end of the ship signal spectrum. Since the cavitation signal consists of a large number of random small bursts caused by bubbles collapsing, it has a continuous spectrum. At high frequency its spectral level decreases with frequency at the rate of 6 dB/octave. There is a peak in the spectrum of cavitation signal which, for ships and submarines, usually occurs within the frequency decade 100 to 1000 Hz. The location of the peak in the spectrum shifts to lower frequencies at higher speed and at lesser depths. There are many factors other than speed and depth that affect the propeller signal [45]. A damaged propeller generates stronger signal than an undamaged one. The signal is stronger during turns and acceleration than during uniform cruising. “Singing” propellers generate strong tones between 100 and 1000 Hz as a result of resonant excitation of the propeller by vortex shedding. The sound made by a singing propeller is very intense and can be heard at long distance. The propeller signal is not radiated uniformly in all directions. Signal intensity is weaker in the fore-and-aft directions than abeam, probably because of screening by the hull in the forward direction and by the wake at the rear. The propeller signal is known to be amplitude-modulated and to contain propeller beats, or periodic increase of amplitude, occurring at the rotation speed of the propeller shaft, or at the propeller blade frequency equal to the shaft frequency multiplied by the number of blades. The propellers of surface ships cavitate strongly at

normal operating speeds. Their low-frequency radiated signal spectrum is dominated by the blade-rate series of line components at the propeller blade frequency and its harmonics.

The hydrodynamic signal originates in the irregular and fluctuating flow of fluid past the moving vessel. The pressure fluctuations called flow signal are associated with the irregular flow and may be radiated directly as sound to a distance, or may excite some portions of the vessel into vibration. This kind of signal is a normal characteristic of flow of a viscous fluid and occurs in connection with smooth bodies without protuberances or cavities. Like Helmholtz resonators, cavities may be excited by the fluid flow across their openings, in the manner that a bottle can be made to sing by blowing over its opening. Other kinds of hydrodynamic signals are the roar of the breaking bow and stern waves of a moving vessel, and the signal originating at the intake and exhaust of the main circulating water system. Under normal circumstances the hydrodynamic signal is likely to be only a minor contributor to radiated signal, however under some exceptional conditions where a structural member is excited into a resonance, the hydrodynamic signal becomes a dominant source.

In our research, we consider medium size merchant ships, such as the CSS W. E. Ricker, as the sound source in matched field localization and inversion. The major acoustic source on merchant vessels is propeller cavitation, whose spectrum is a combination of continuous and line components [46]. The line components consist of a set of harmonically related tones having fundamental frequency equal to the propeller blade rate.

A report given in [47] assigns 50 merchant ships' signals into three ship classes: passenger/ferries, cargo ships, and tankers. The data show considerable variations in spectra for different ships even within one class. The aggregate of 50 ship spectra along with their mean is given in Fig. 5.8. Ross [48] has proposed a formulation to estimate the mean spectral level from the rate and number of ship's propeller blades. The estimated mean is shown by the dashed line. The means and variances of three different ship classes are shown in Fig. 5.9 and 5.10, respectively. The data show considerable variations in the ships' spectra from either frequency content or ship class. This fact generally favors the use of broadband MFP in processing ship radiated signals.

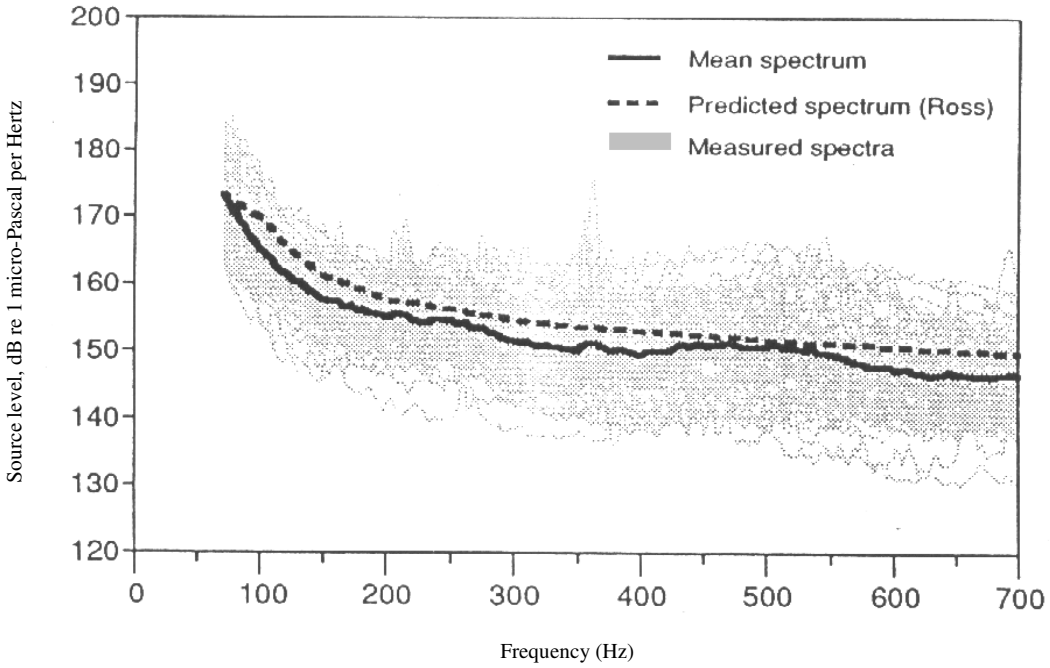

Fig. 5.8 An aggregate of 50 individual sources spectra, the aggregate mean source spectrum and a predicted source spectrum (dotted curve) [47]

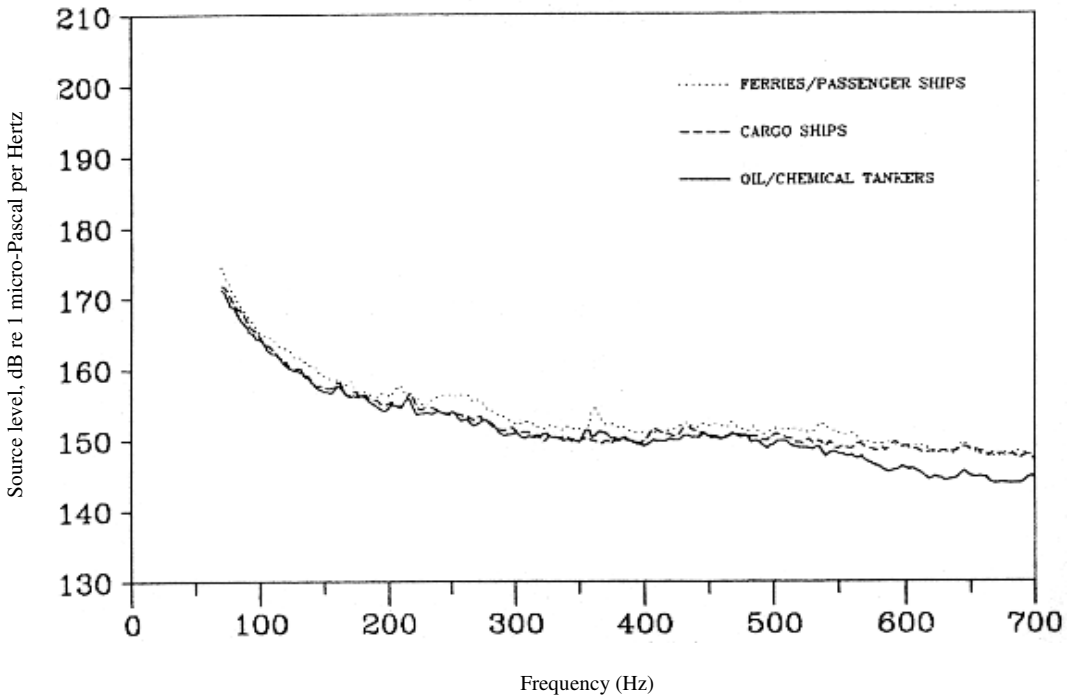

Fig. 5.9 Mean source spectra for three different ship classes [47]

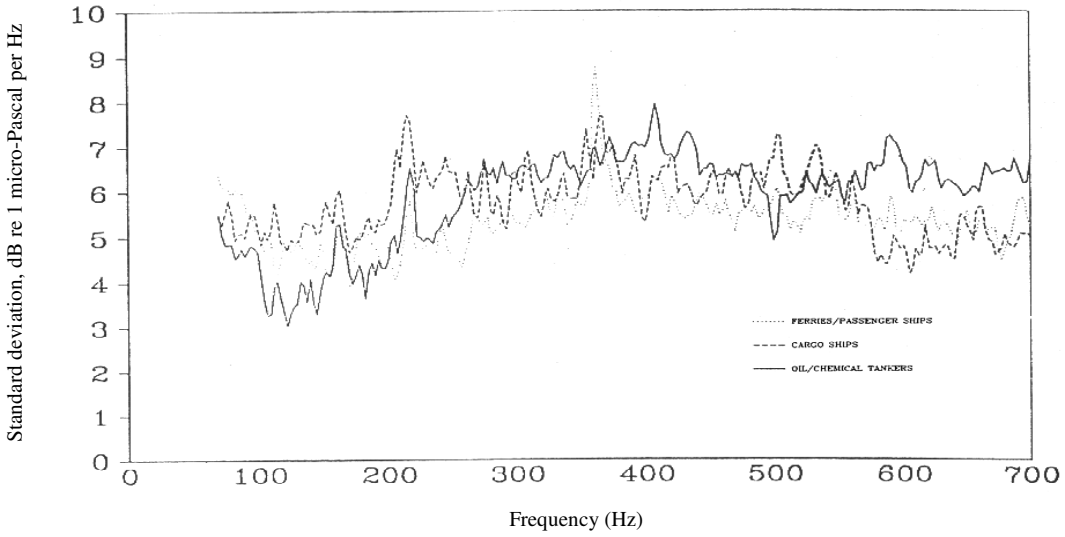

Fig. 5.10 The standard deviation curves for three different ship classes [47]

It has not entirely established if the second order statistics of a ship signal are adequate to completely represent the signal. In section 5.3 higher order statistics of ship signals will be examined for source localization information content. For that case we use a higher order matched field processor for source localization. In order to use the non-stationary form of a matched field processor, we need to know the probability density function (PDF) of the ship signal. However, the PDF of ship signal has not been reported in the literature

5.2. Simulation results

In this section two simulations are conducted to evaluate the performance of CR based matched field processors for source localization in comparison with other processors. The replica or modeled fields used in the simulation are calculated using the Westwood normal mode model, ORCA [15]. The simulation conditions including array specifications and environmental properties that are the same as those mentioned for the experiment (see section 5.1).

In the first simulation the CR-MFP formulation for wide sense stationary sources is compared with other processors in the presence of measurement noise. The second simulation is devoted to time-frequency (TF) CR-MFP. We demonstrate localization for a frequency varied

pulse generator (such as chirp signal) in the presence of other correlated random sources such as ship, ocean waves, and wind noise. We introduce a novel TF filtering procedure that concentrates on a chirp pulse source.

In both simulations we consider a broadband processing scheme. The transmission loss for the simulated environment is shown in Fig. 5.11 for 10 Hz, 70 Hz, 130 Hz, 190 Hz, and 250Hz.

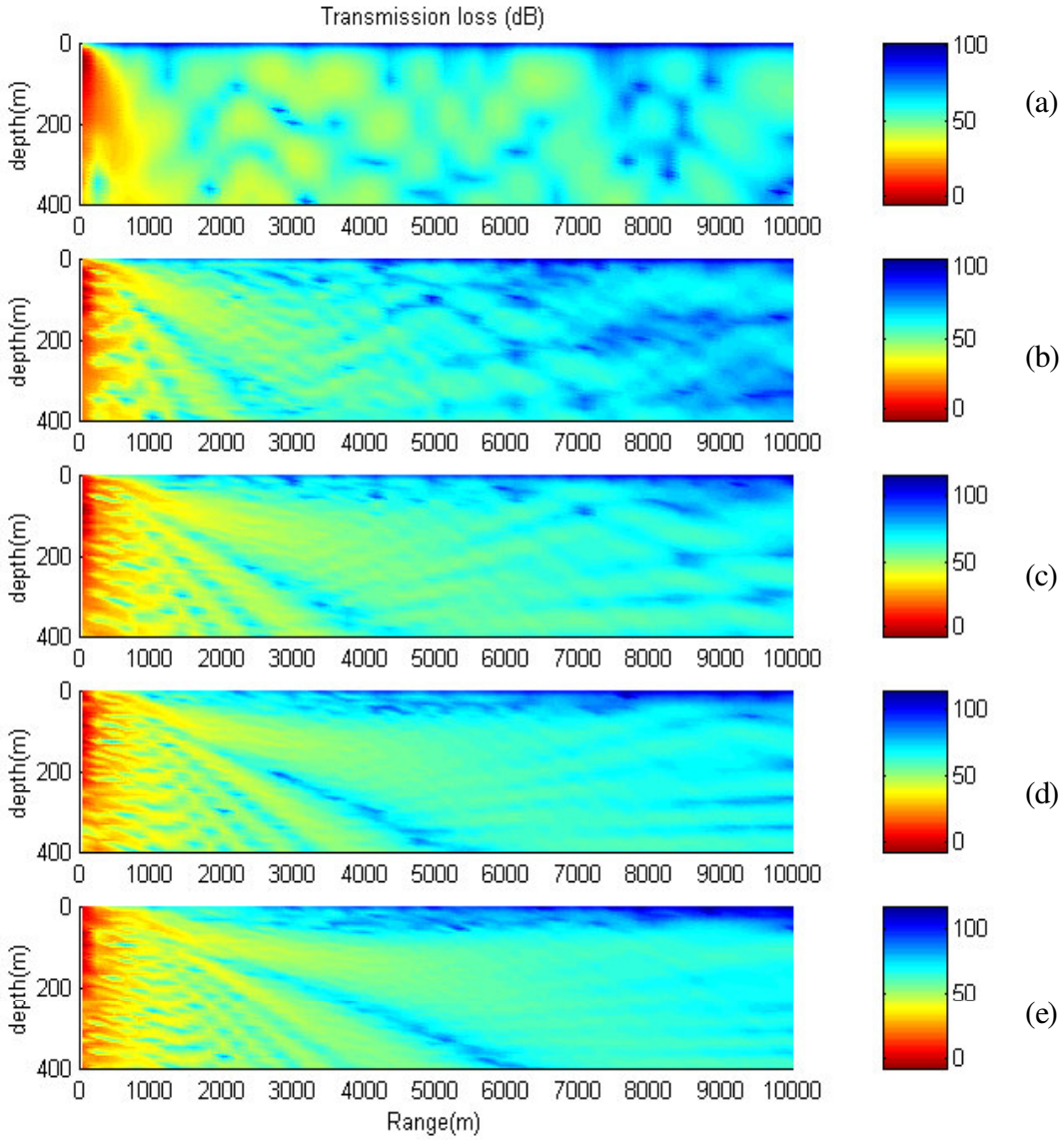

Fig. 5.11 Transmission loss at frequencies: (a)10 Hz (b)70 Hz (c)130 Hz (d)190 Hz (e)250 Hz

5.2.1. Wide sense stationary (WSS) sources

The simulated source propagates a colored wide band, WSS, Gaussian random signal sampled at the rate of 240 Hz. A slice of the signal in the time domain and its spectrum are shown in Fig. 5.12.

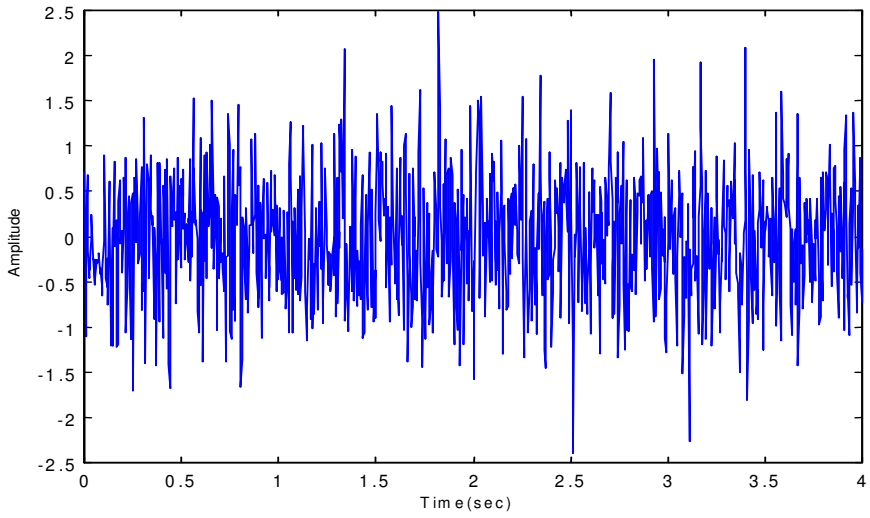

(a)

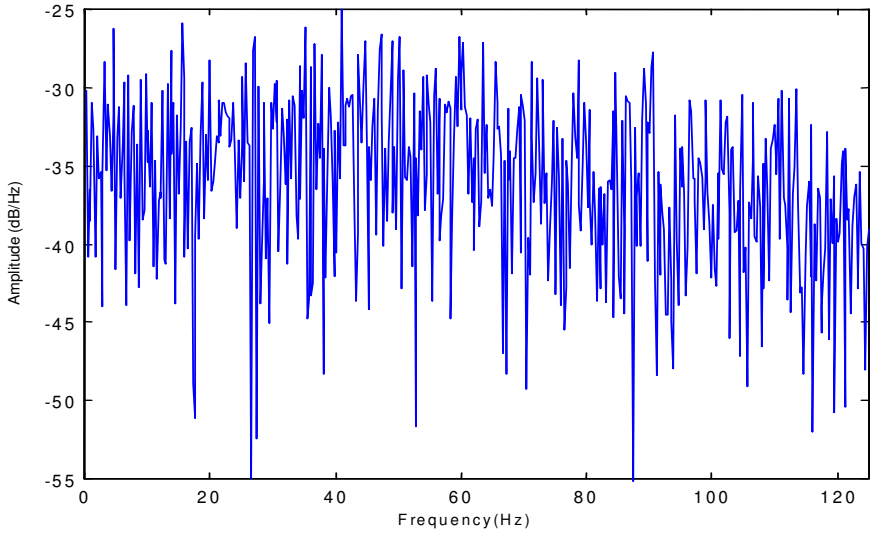

(b)

Fig. 5.12. (a) A slice of source signal in time domain and (b) in frequency domain

The source depth is 106 m and its distance from the array is 3.6 km. The frequency range is between 40 Hz and 100 Hz with resolution 3 Hz. Transfer functions in time domain that

correspond to paths traveled by the acoustic waves from the source to the sensors on the array are shown in Fig. 5.13. The frequency domain transfer function from the source to the first sensor is shown in Fig. 5.14.

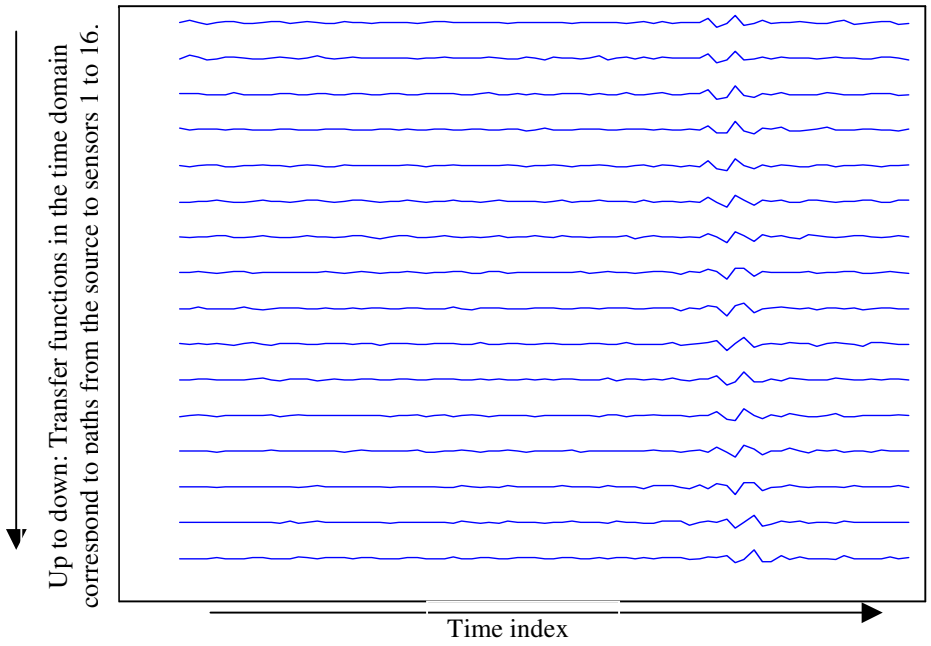

Fig. 5.13. Transfer functions in time domain

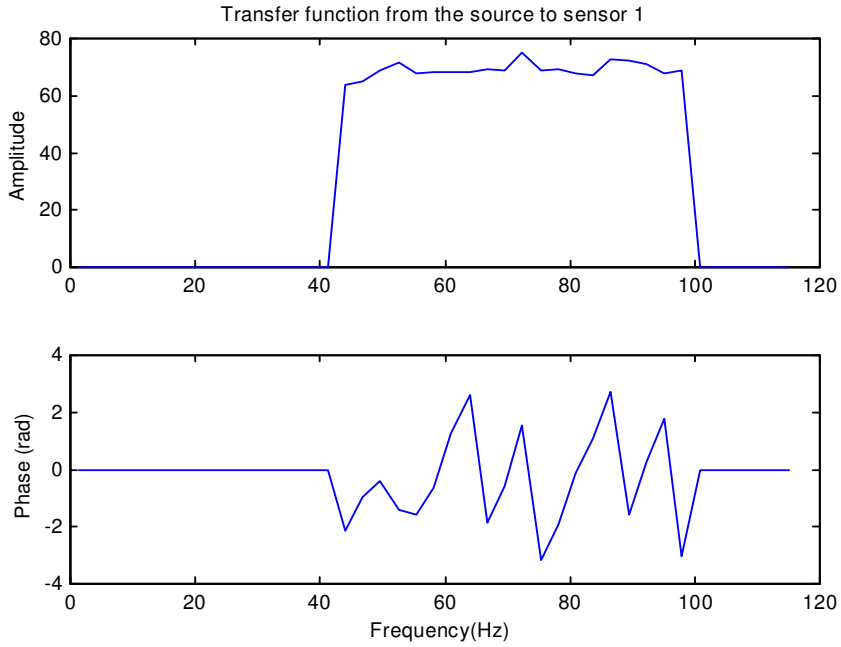

Fig. 5.14. Transfer function correponds the path from the source to the first sensor in frequency domain (a) amplitude (b) phase

In the first step spatially and temporally white Gaussian random measurement noise is added to the signals at the receivers to obtain a signal-to-noise ratio (SNR) of 20 dB. The noise is uncorrelated with the source signal. The performance analysis is carried out by comparing the source location resolution and side lobe level for the following MFPs: the Bartlett and MV version one (2.27) and two (2.28) processors as representatives of the linear MFP family; the Westwood MFP as the representative of bilinear MFP; and the CR-based MFPs (self-CR and cross-CR). In order to estimate the covariance matrix components (spectra and cross spectra) of data at the receivers, we use the periodogram technique [25] with FFT size points of 80, obtained from averaging 2 minutes data. The periodogram is a biased estimator whose estimation error variance approaches zero when the number of data averages approaches infinity for either the spectrum or cross spectrum. For 20 dB SNR, averaging over 2 minutes of data will give adequate data spectrum estimation. A block diagram of the procedure is shown in Fig. 5.15.

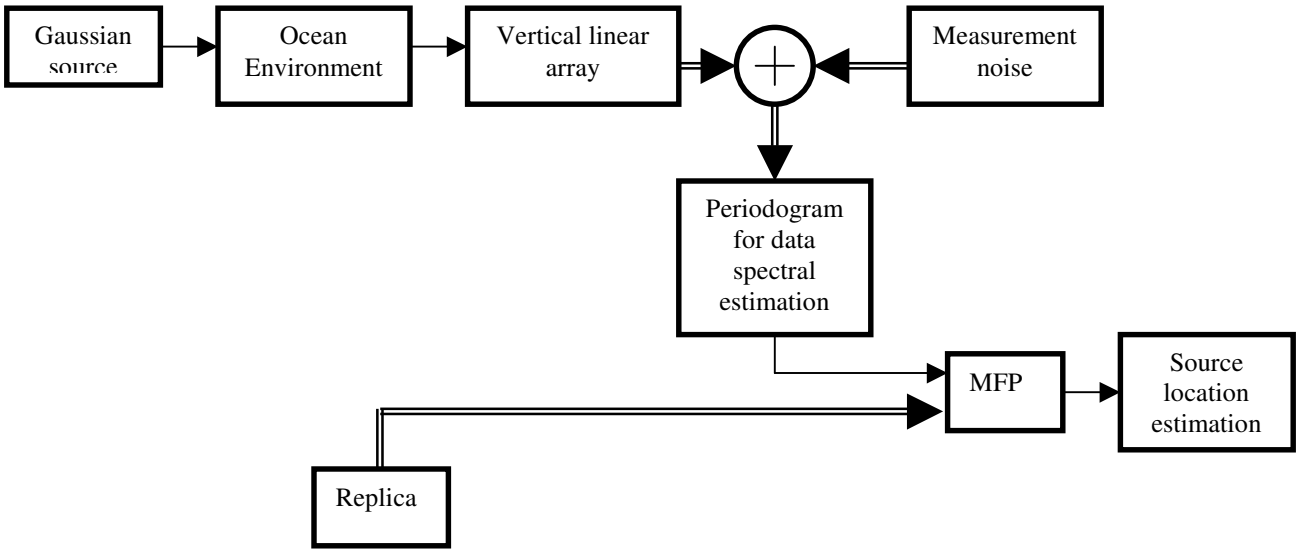

Fig. 5.15 The block diagram of simulation procedure

The ambiguity functions of different processors are shown in Figs 5.16 through 5.21. The grid search spans the range from 50 m to 10 km with a resolution of 110 m, and the depth spans 1 m to 400 m with a resolution of 20 m.

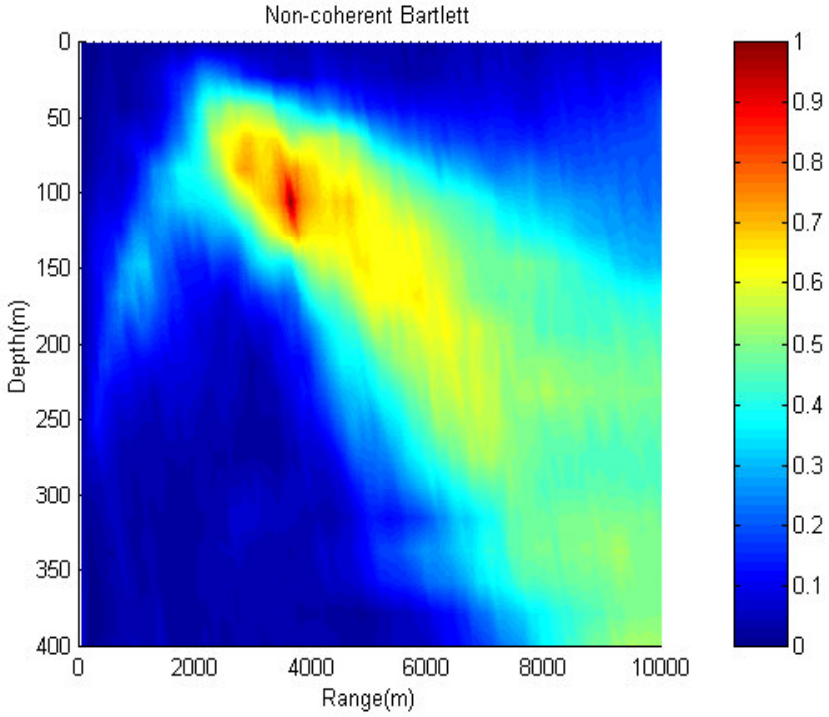

Fig. 5.16. Ambiguity surface for Bartlett processor

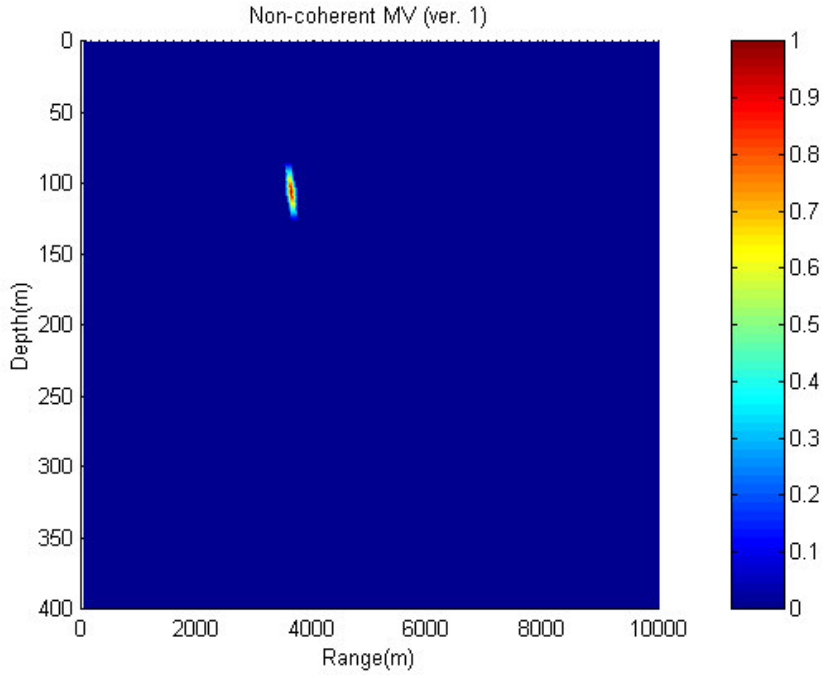

Fig. 5.17. Ambiguity surface for MV processor (version one)

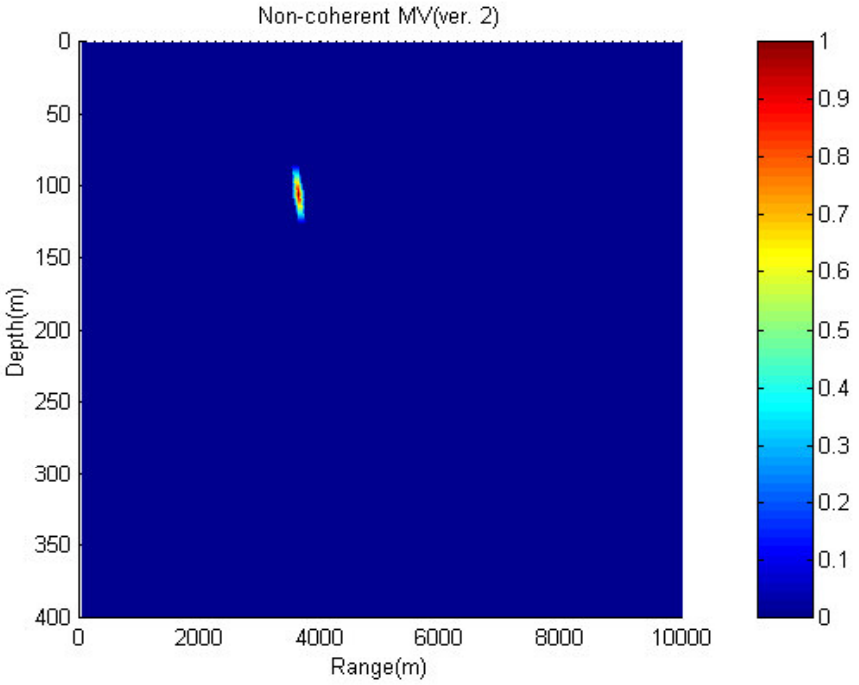

Fig. 5.18 Ambiguity surface for MV processor (version two)

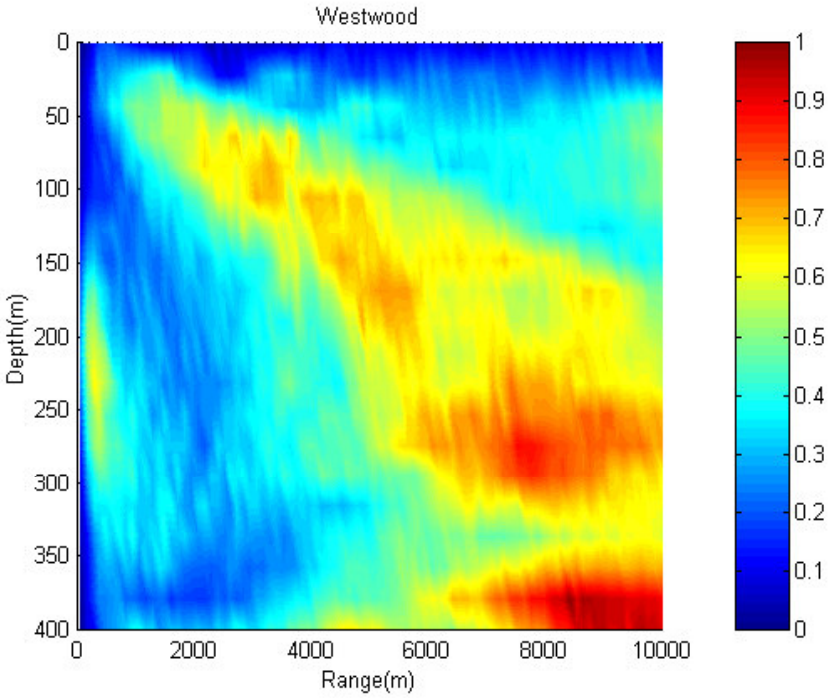

Fig. 5.19 Ambiguity surface for Westwood processor

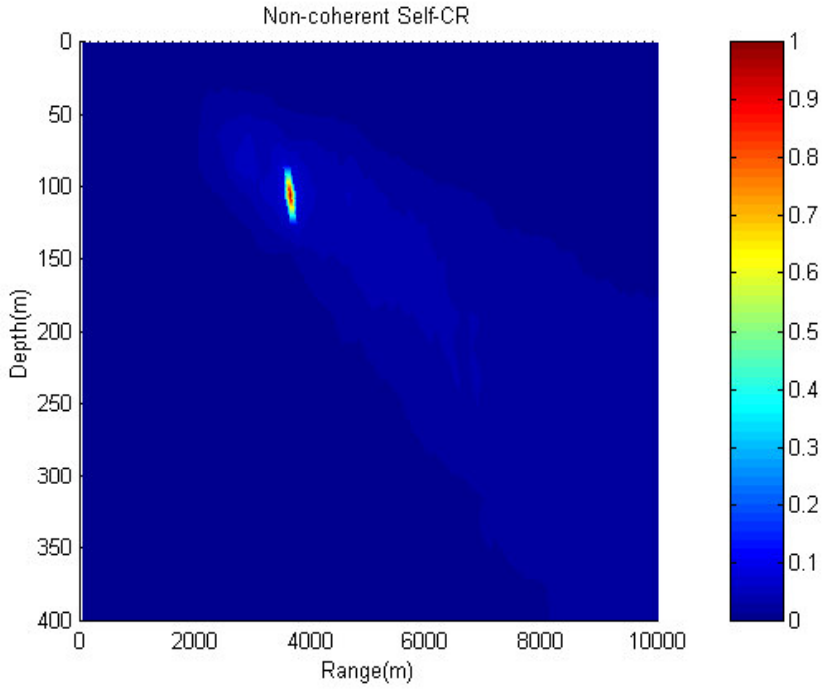

Fig. 5.20 Ambiguity surface for self-CR processor

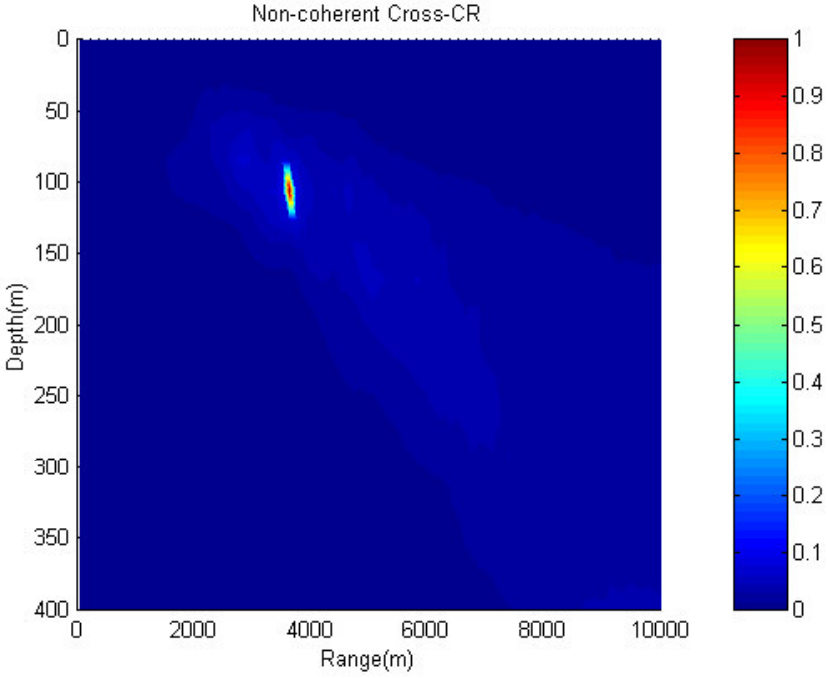

Fig. 5.21 Ambiguity surface for cross-CR processor

The figures demonstrate that all estimators except the Westwood MFP have detected the true source location. The reason for the poor performance of Westwood processor may be that the spectrum of the source noise is not flat as required for the Westwood MFP. The cross-CR, self-CR, and MV (both versions) give superior performance with respect to resolution and side lobe levels.

Cross sections of the ambiguity surface in range for a depth of 106 m, and in depth for a range of 3.6 km are shown in Figs 5.22 and 5.23, respectively. We can see lower side lobe levels and sharper main lobes around the source location for CR-based and MV MFPs in comparison to that for the Bartlett processor. MV-MFPs give lower side-lobe level and narrower main lobe beam in comparison with those for CR-MFPs. Both versions of MV-MFP give nearly identical results since the processing is conducted in a controlled simulation benchmark. At the first glance this result may suggest superior performance for the MV processor in comparison with that of other MFPs. However it is well known that the MV processor is highly sensitive to mismatch [1], and its performance with real data is limited, unless great care is taken.

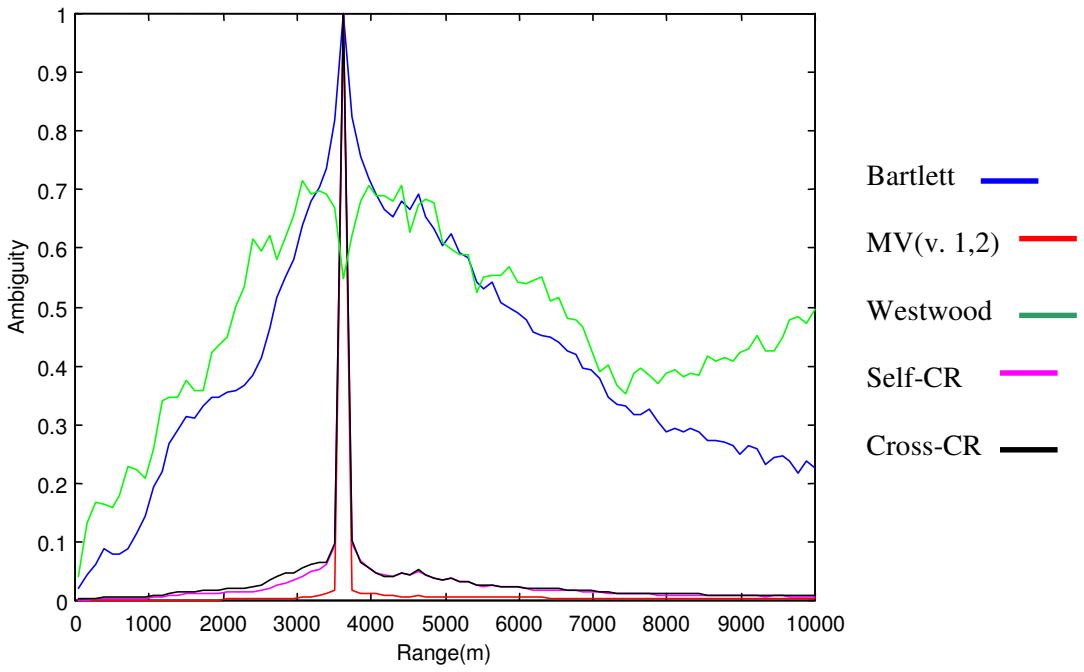

Fig. 5.22 Performance of the different MFPs in range for a depth of 106 m

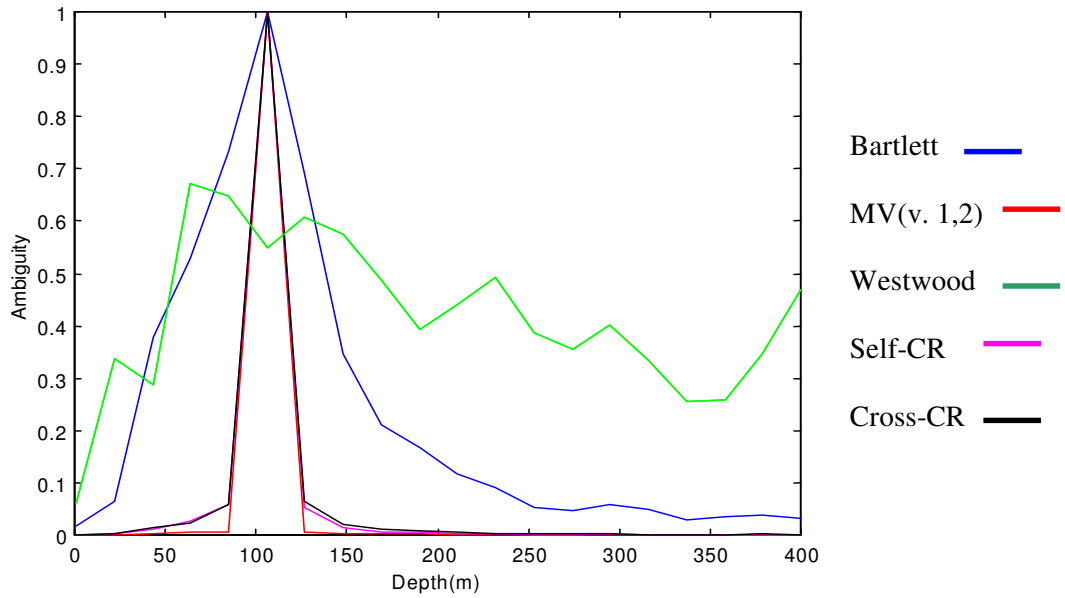

Fig. 5.23 Performance of the different MFPs in depth for a range of 3.6km

In the second step, we evaluate the localization performance for a SNR of -20dB. In this case, we use a periodogram with 80 FFT points and averaging on 5.5 minutes of the received data. This increase up to a factor of two compared to the previous time frame is necessary for proper estimation of covariance matrix elements. The ambiguity functions of the different processors are shown in Figs 5.24 through 5.29.

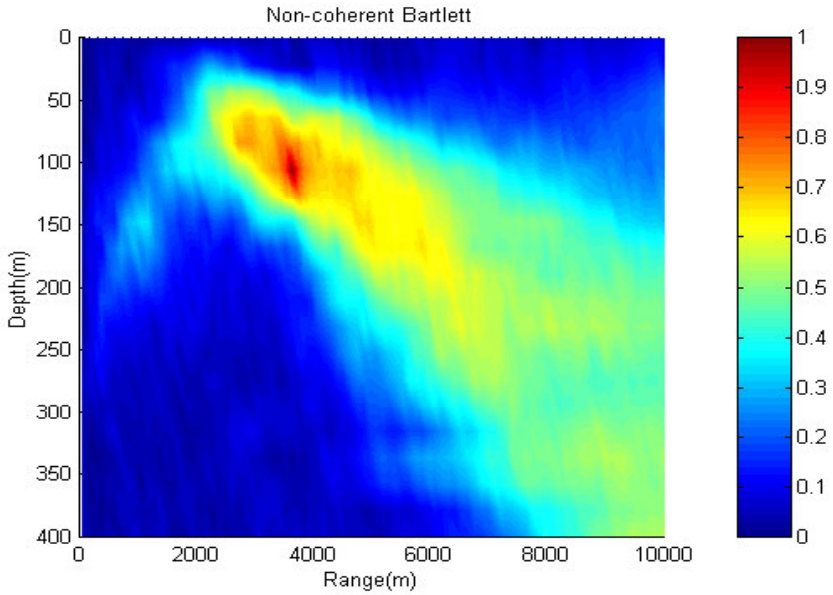

Fig. 5.24 Ambiguity surface for Bartlett processor (SNR=-20dB)

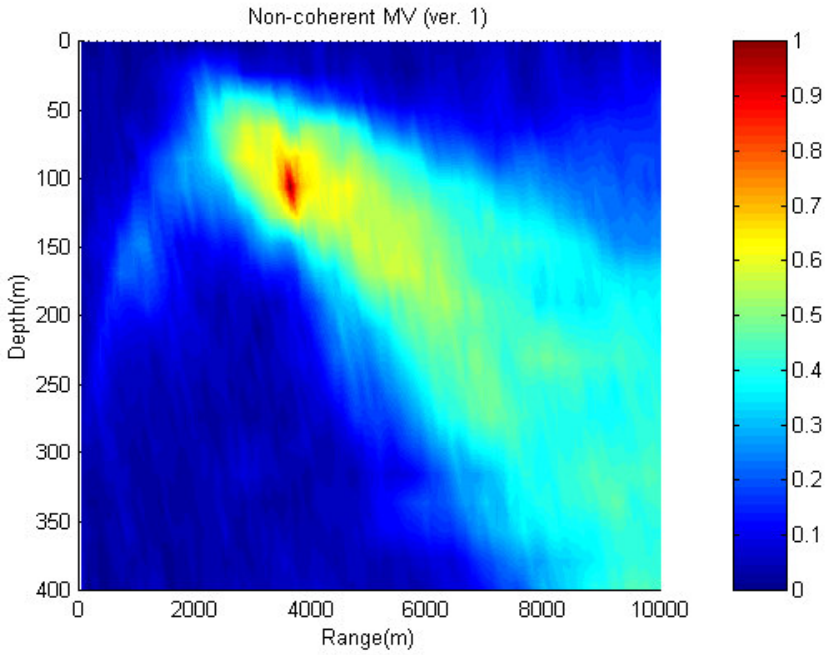

Fig. 5.25 Ambiguity surface for MV processor, version one (SNR=-20dB)

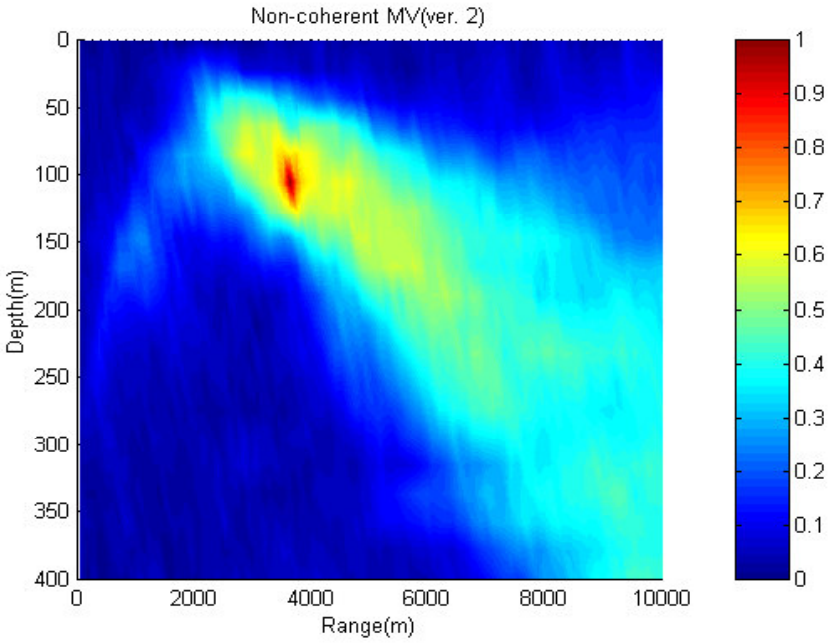

Fig. 5.26. Ambiguity surface for MV processor, version two (SNR=-20dB)

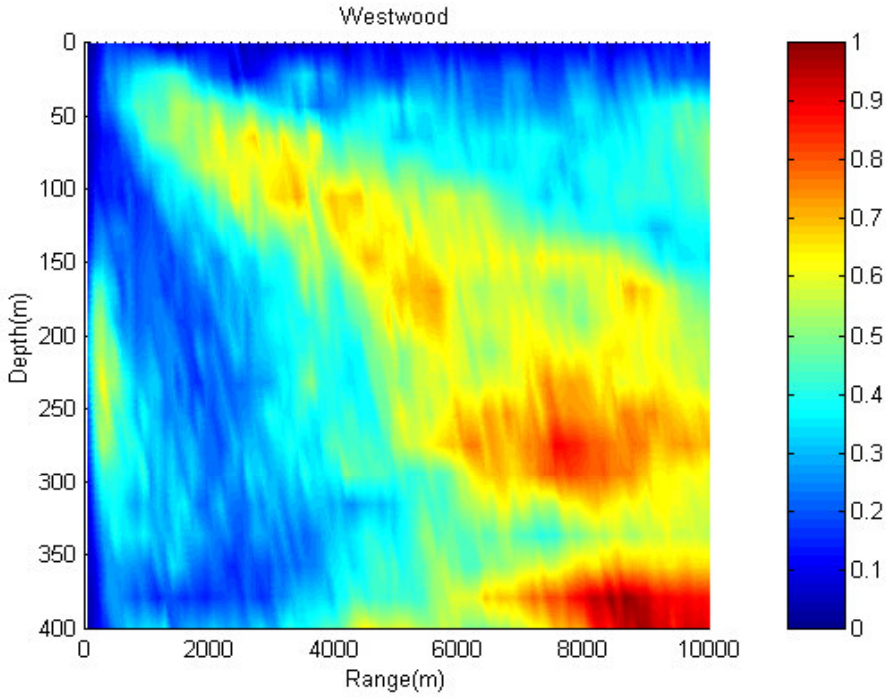

Fig. 5.27. Ambiguity surface for Westwood processor (SNR=-20dB)

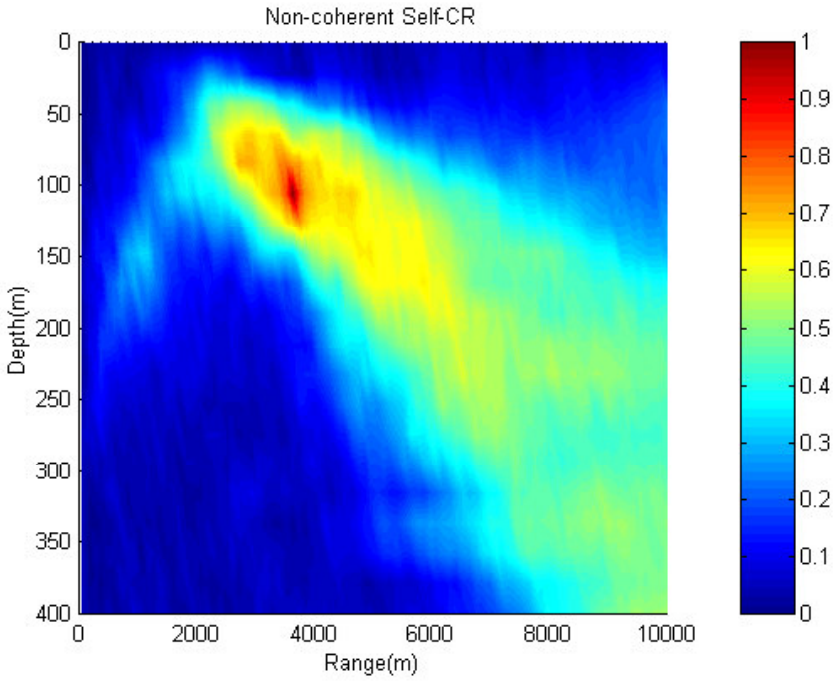

Fig. 5.28. Ambiguity surface for self-CR processor (SNR=-20dB)

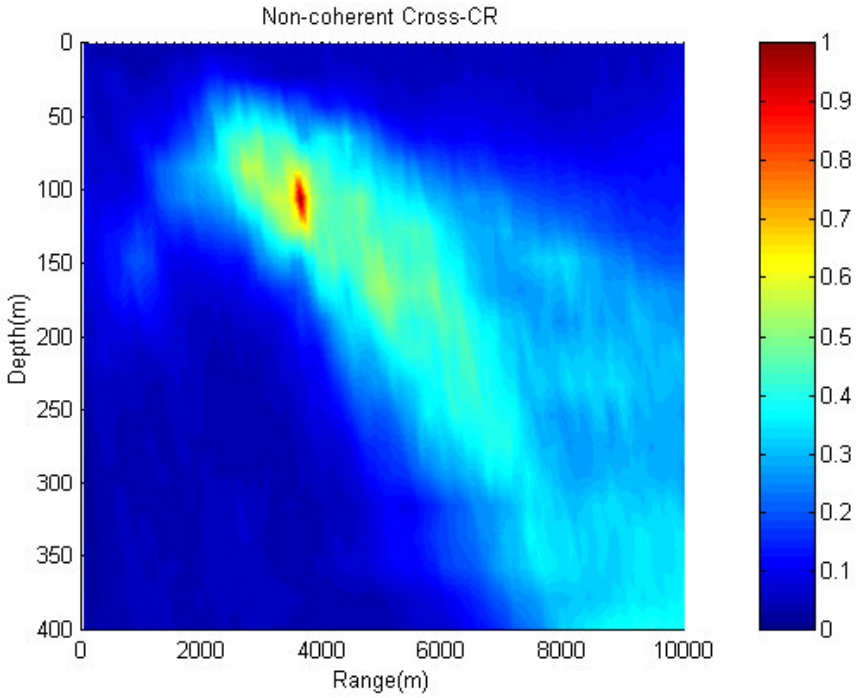

Fig. 5.29 Ambiguity surface for cross-CR processor (SNR=-20dB)

The figures demonstrate that all estimators except the Westwood MFP have detected the true source location. The cross-CR gives superior performance with respect to resolution and side lobe levels since it makes use of only cross-spectrum components and consequently the measurement white noise is canceled. The Bartlett and MV estimators (both versions) show nearly the same performance as each other. This result was discussed in the chapter 2 in the context of received random data that are contaminated by white measurement noise. For this case the MV-MFP performance is degraded sharply and approaches the Bartlett performance. Self-CR gives a performance close to that of the Bartlett because of the effect of white noise that contaminates the self-spectrum elements.

Cross sections of the ambiguity surface in range for a depth of 106 m, and in depth for a range of 3.6 km are shown in Figs 5.30 and 5.31, respectively. We can see lower side lobe levels and sharper main lobes around the source location for cross-CR MFP in comparison to that for other processors. Both versions of MV-MFP give results nearly identical to those of the Bartlett processor since the processing is conducted in a controlled simulation benchmark.

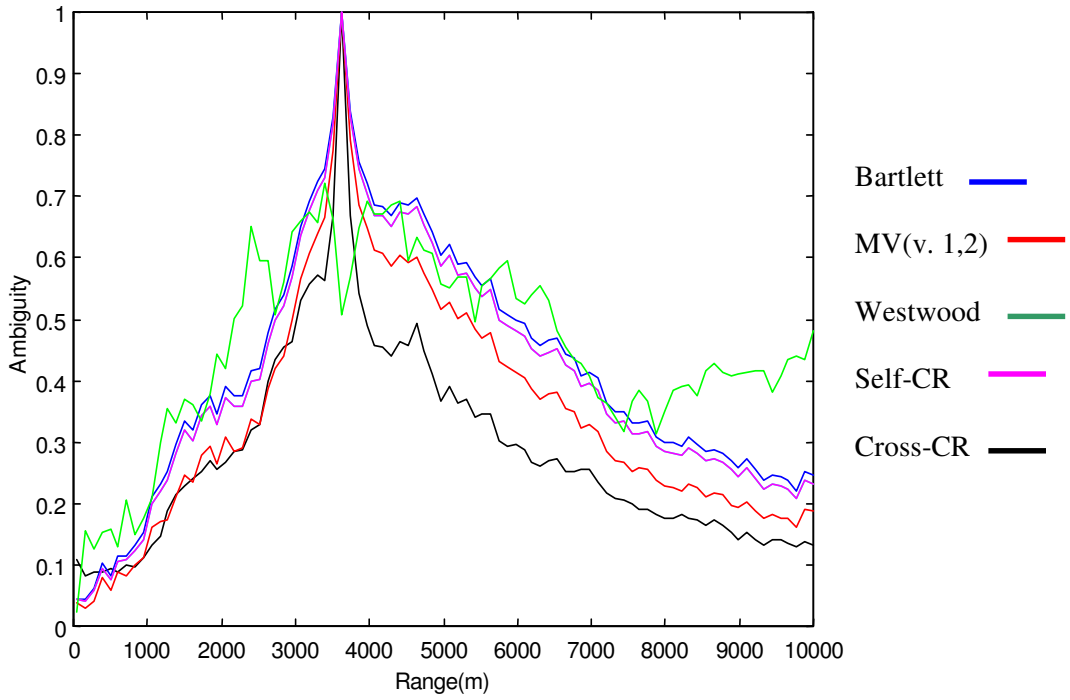

Fig. 5.30 Performance of the different MFPs in range for a depth of 106m

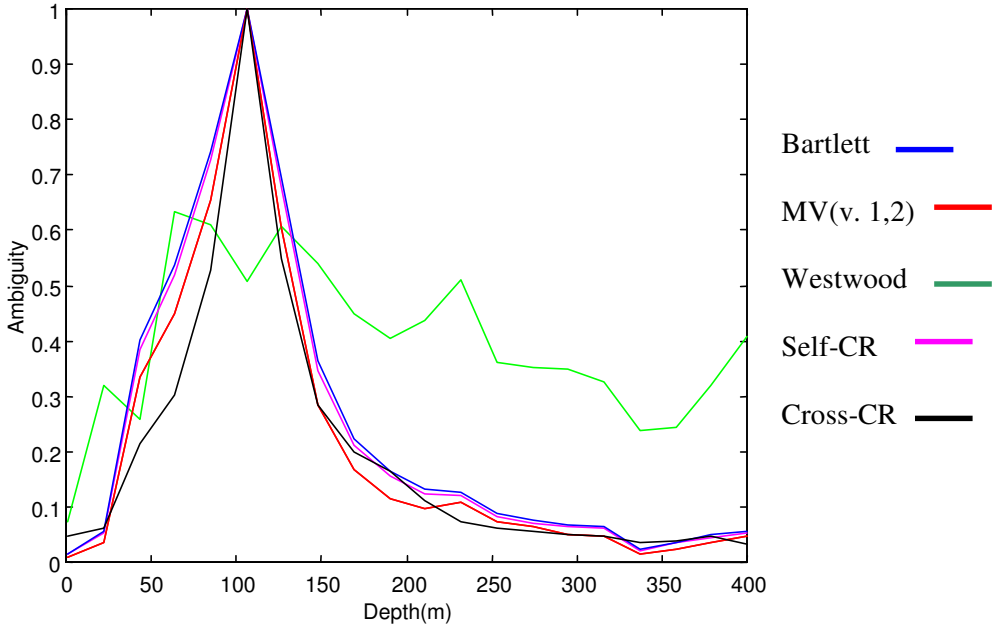

Fig. 5.31 Performance of the different MFPs in depth for a range of 3.6km

5.2.2. Time-Frequency MFP for time varying sources

Broadband time-varying pulses such as chirp signals are widely used in seismic applications to determine the layered earth structure, and in radar to achieve high range resolution. The various MFPs which have been developed rely on arbitrary frequency components of source signals. However, chirp and other time-varying source signals posses a specific signature in time-frequency space. In chapter 3 we introduced a novel MFP based on the time-frequency distribution (TFD). The known signature of a time-varying source can be evaluated in TFD space for MF localization in an environment that contains correlated interference such as ship noise, ocean waves, and wind sound. We describe an approach for designing a signal dependent TF filter that preferentially passes only the known chirp signal. The filter is constructed in ambiguity function (AF) space for convenience. The time-frequency MFP is categorized as a "blind" processor since we have no information regarding the interference that may appear as correlated noise at the receiver. Recall that white noise can be removed by using the cross-CR formulation that contains only cross spectrum of the measured signals in its structure (see equation 3.8). In this section, we demonstrate the performance of the TF processor using a simulation.

In the simulation two sources are considered. The first one propagates a chirp pulse sampled at 120 Hz. The chirp source depth is 93 m and its distance to the array is 1.42 km. Another source generates Gaussian noise with nearly the same power as the chirp source (its standard deviation is 0.8). The noise source depth is 298 m and its distance to the array is 7.5 km. The frequency range is between 1 Hz and 60 Hz with resolution 3 Hz. The grid search for source localization spans the range from 50 m to 9 km with resolution of 150 m, and depth from 1 m to 400 m with the resolution of 10 m. The schematic form of the simulated experiment is given in Fig. 5.32.

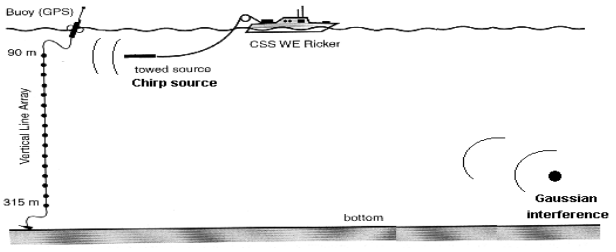

Fig.5.32 The schematic form of simulation for time-frequency MFP

The chirp signal in the time domain and its spectrum are shown in Figs 5.33 and 5.34, respectively. The Rihaczek distribution of the chirp pulse for the TFD and AF spaces are given in Figs 5.35 and 5.36, respectively. The figures show the linear variation of the signal in both spaces and imply an important signature with which to build the appropriate filter.

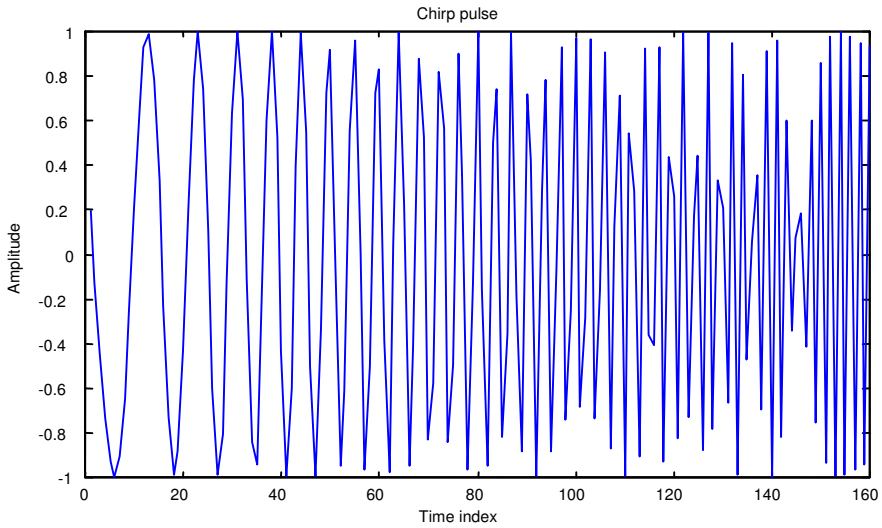

Fig. 5.33 Chirp pulse in time domain

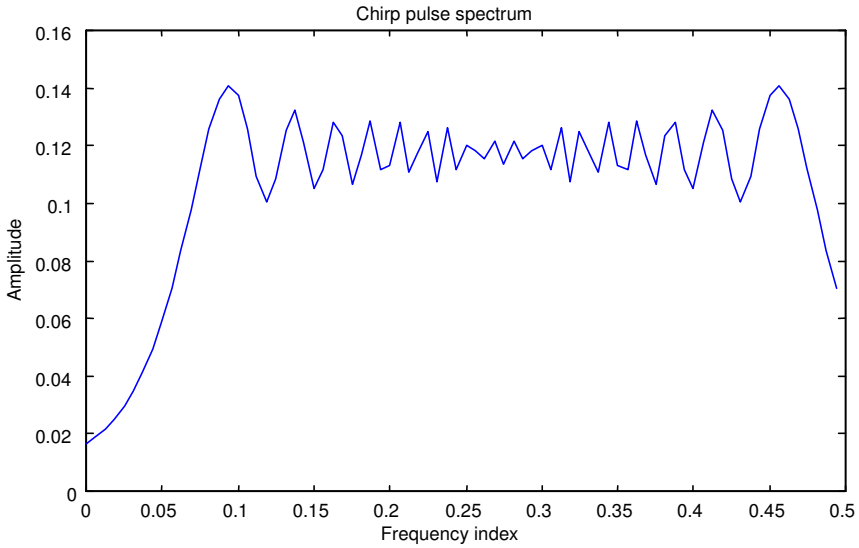

Fig. 5.34 Chirp pulse spectrum (normalized frequency)

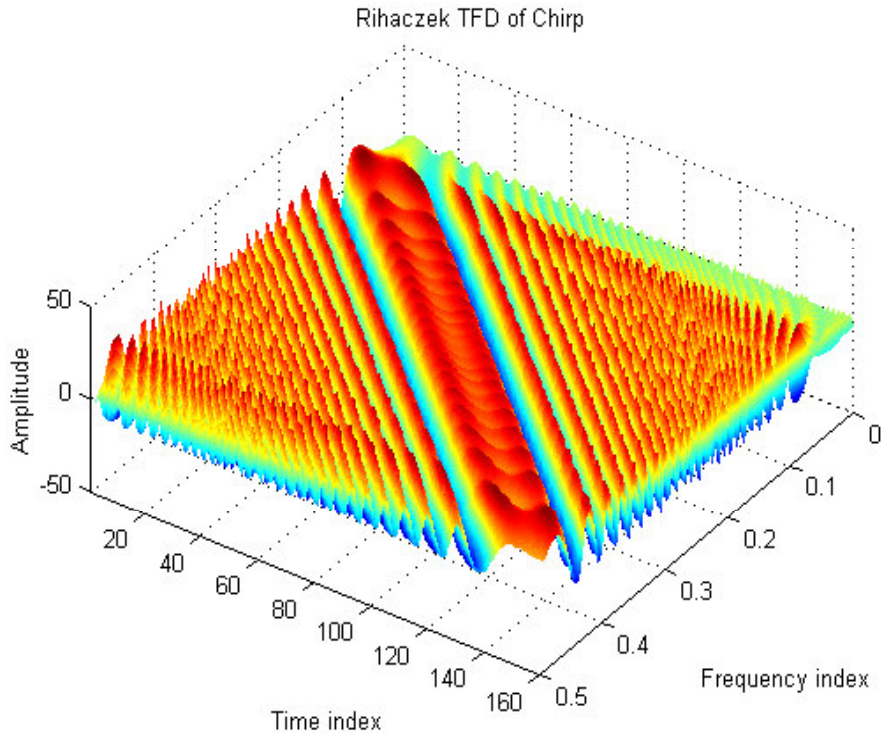

Fig. 5.35 Rihaczek TFD of chirp signal

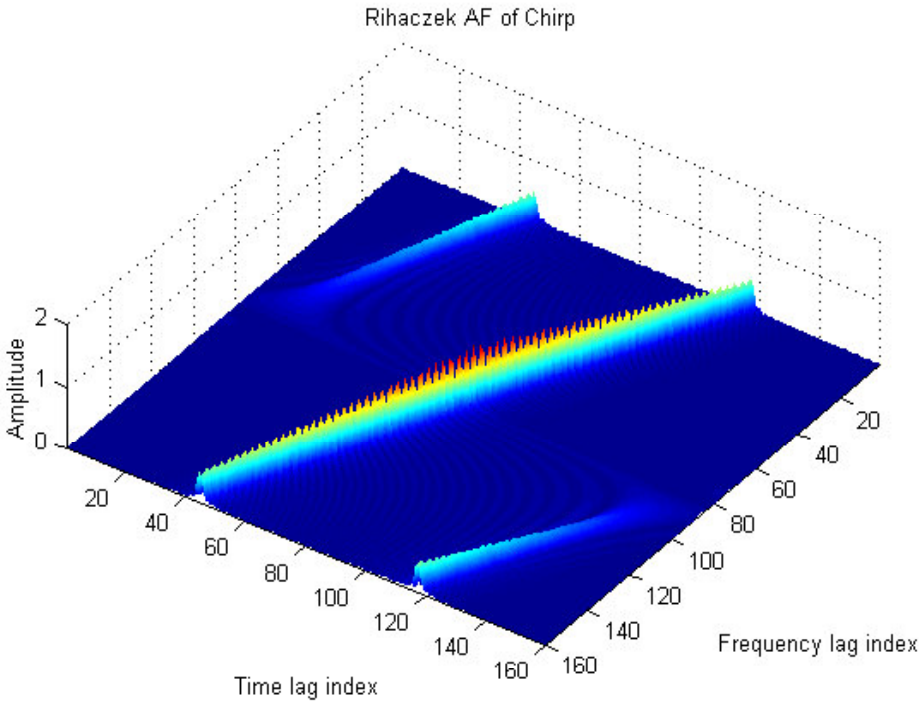

Fig. 5.36 Rihaczek AF of chirp signal

A time sample of noise generated by a Gaussian interference and its spectrum are shown in Figs 5.37 and 5.38, respectively. There is no structured signature in the Rihaczek distribution of the Gaussian interfering noise in either of the TFD or AF spaces (see Figs 5.39 and 5.40). In fact we can see that the noise energy is distributed uniformly throughout the TFD and AF spaces (except at the origin for the AF display where the white Gaussian interference is maximally correlated with itself at zero lag).

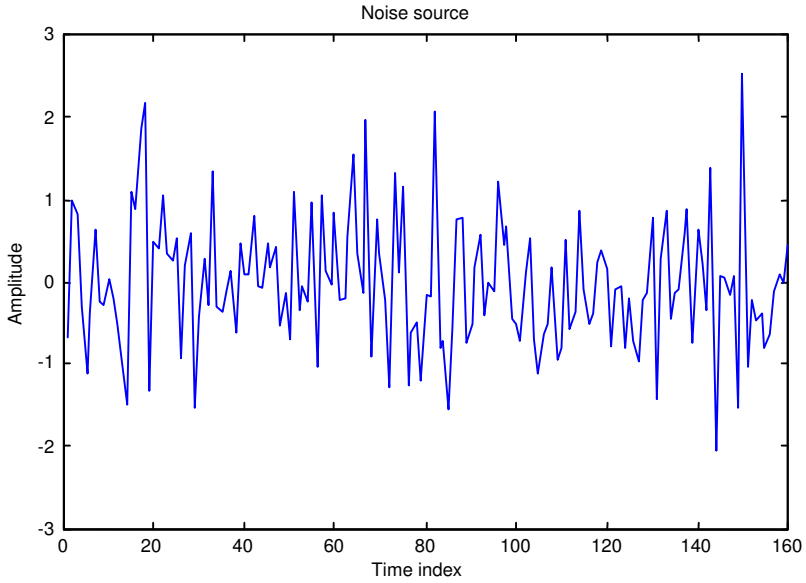

Fig. 5.37. Gaussian interference in time domain

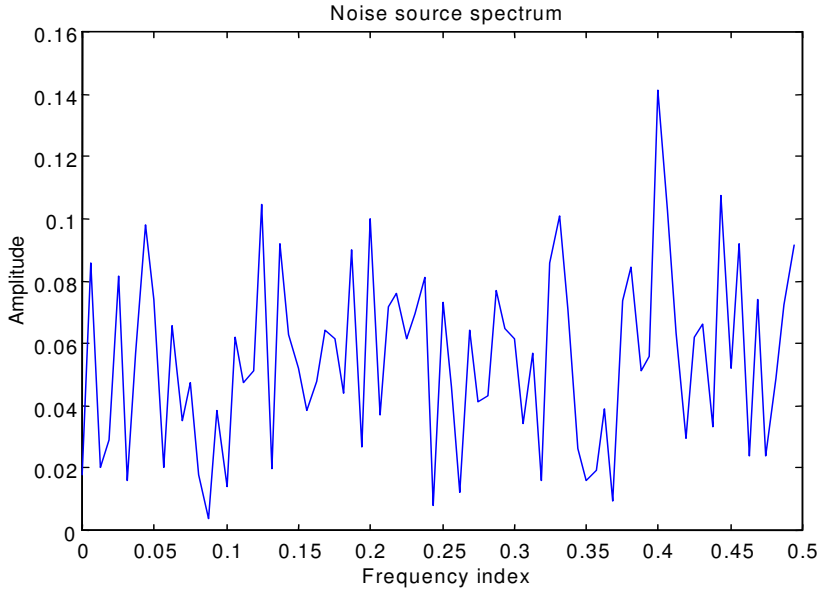

Fig. 5.38 Gaussian interference spectrum (normalized frequency)

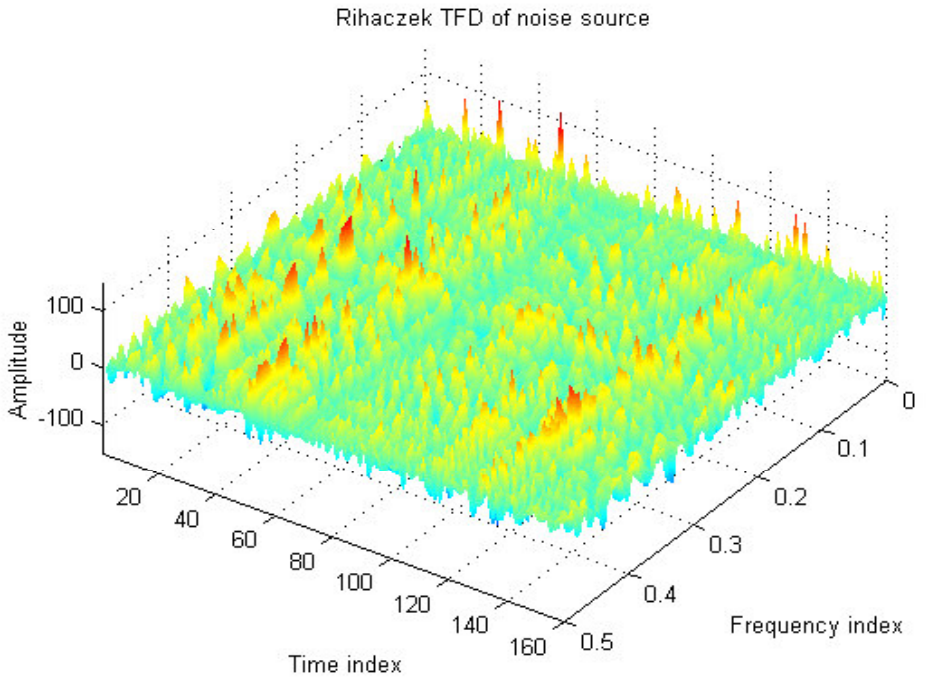

Fig. 5.39. Rihaczek TFD of Gaussian interference

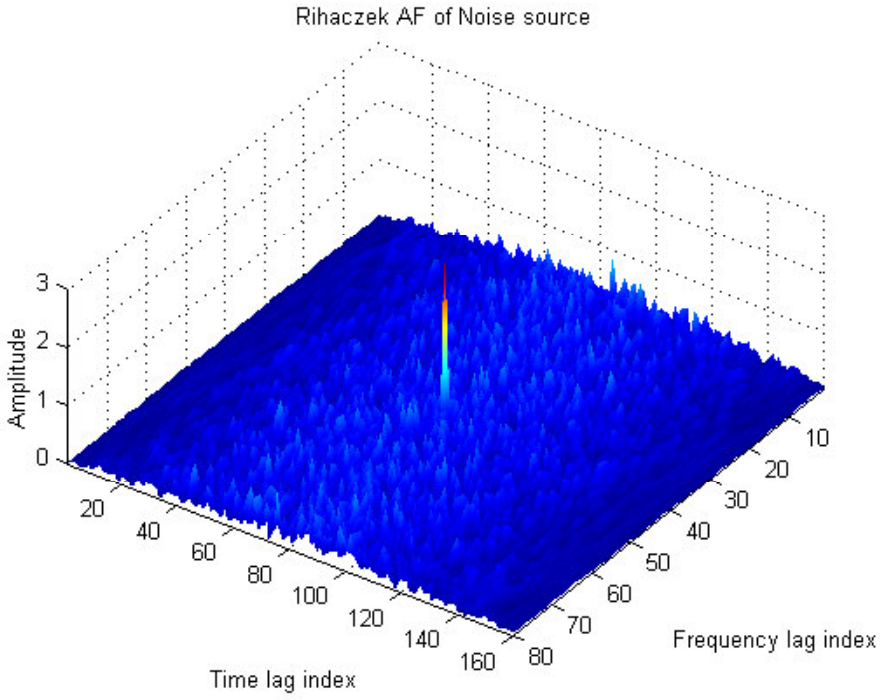

Fig. 5.40 Rihaczek AF of Gaussian interference

At the receiver we have the correlated form of Gaussian interference. However, it is evident that in the TFD space the correlated form of Gaussian interference does not possess a specific signature that is related to the chirp signature. This fact gives us the opportunity of filtering out the correlated interference by using an appropriate TFD filter. There is no way to separate the chirp signal from the correlated interference using either the time or the frequency domain alone, since both signals have overlapped components. In order to use the straightforward singular value decomposition (SVD) based techniques such as MUSIC (multi signal classification) [19], it is required that the sources be uncorrelated (although resolution reducing methods have been developed for the correlated sources [67]). This assumption is not generally satisfied. For this reason, TF filtering is an alternative way to extract a chirp signal from a received data sample that is contaminated by correlated noise.

Several techniques have been proposed for the time-frequency kernel (filter) design. Most of them rely on a constant filter shape such as Bessel, Butterworth, exponential, and cone kernels with parameters adapted to the signal of interest [68,69,70,71,72]. These constant kernels are applicable for a limited class of signals. In order to overcome this limitation, Baraniuk and Jones proposed an optimal kernel based on the Cohen' class. This filter adapts to each signal, and so offers good performance for a large class of signals [73]. A fast algorithm has been developed for finding the optimum kernel, allowing the computation of the signal-dependent TFD with a time complexity on the same order as for a fixed kernel distribution [74]. An adaptive form of the above optimum kernel has been given in [75].

In this section we consider a simple form of the above optimum kernel design to shape a mask in AF space which can pass the chirp signal while excluding the major part of the correlated interference. We propose the design in AF space for three reasons. First, the multiplicative operation of the kernel in the AF space is conceptually and mathematically simple. Second, signals with known signatures such as chirps, can be separated in AF space from other interferences that have no special signature. Moreover it is appropriate for removing cross-component elements (due to the bilinear form of Rihaczek distribution [50]) Third, computation of the signal-dependent TFD is efficient in AF space (see equation (3.20) in chapter 3).

The mask has a simple structure with abrupt amplitude change from one to zero, causing the TFD result to show ringing. The mask is designed such that it passes more than 90% of the

chirp signal energy. The shape of the mask in AF space is shown in Fig. 5.41. Another distortion comes from the sub-sampling of the TFD space for use in TF-MFP (to decrease the complexity of computation). This will help us to evaluate the performance of different MFPs in the presence of distortion. A block diagram of the simulation procedure is shown in Fig. 5.42.

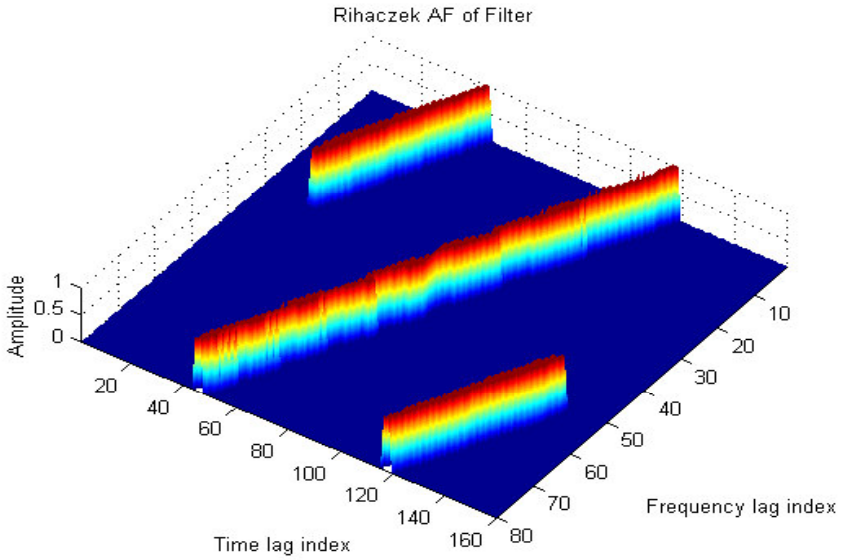

Fig. 5.41 Rihaczek AF of mask

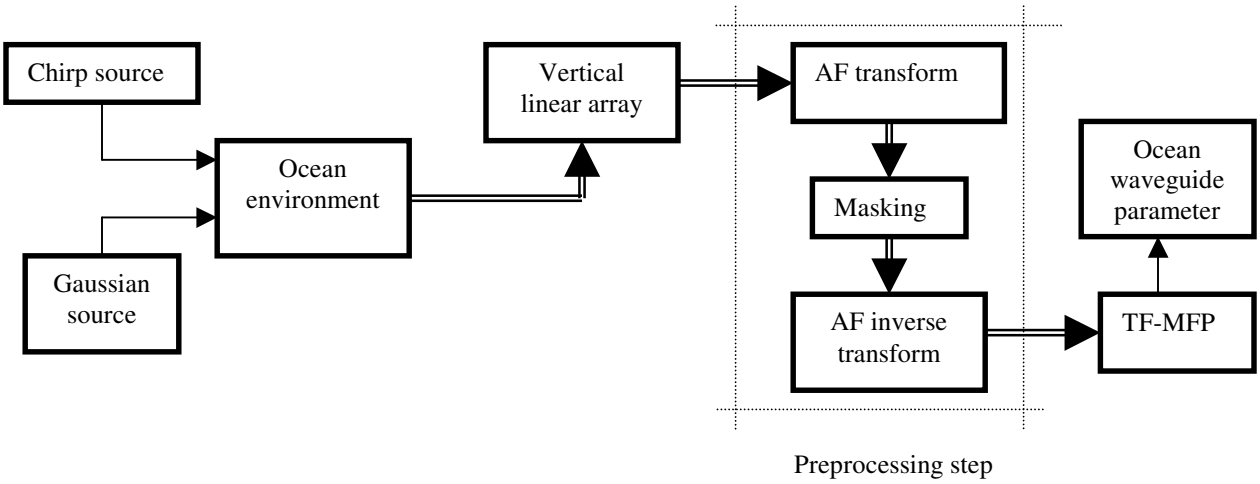

Fig. 5.42 A block diagram of simulation procedure

In the next step we apply the above mask to the received signals. To show how the mask works we examine the received signals at sensors 1 and 15, shown in Fig. 5.43. The self-Rihaczek distributions of sensor 1 data in the TFD and AF spaces are shown in Figs 5.44 and 5.45,

respectively. The figures clearly show how the chirp signal is evident in a signal contaminated by a powerful correlated noise.

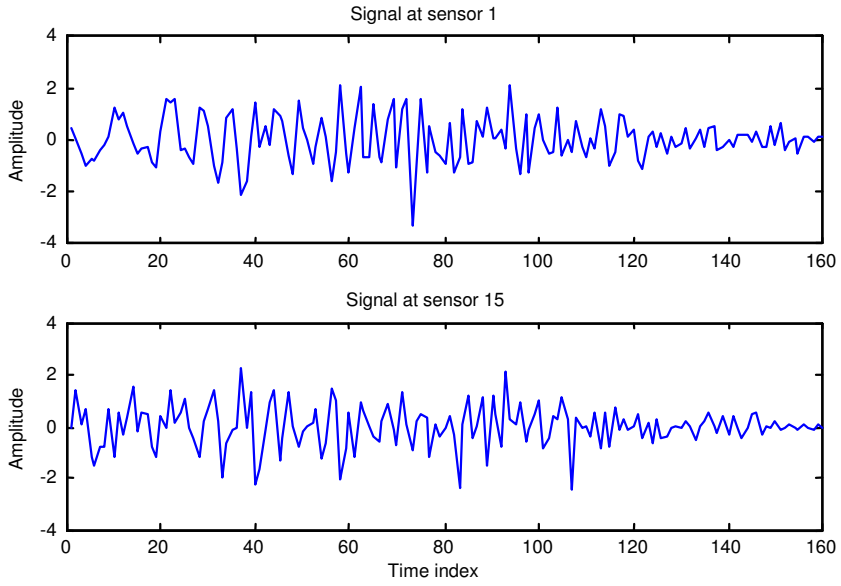

Fig. 5.43 The received signals at the (a) sensor 1 and (b) sensor 15

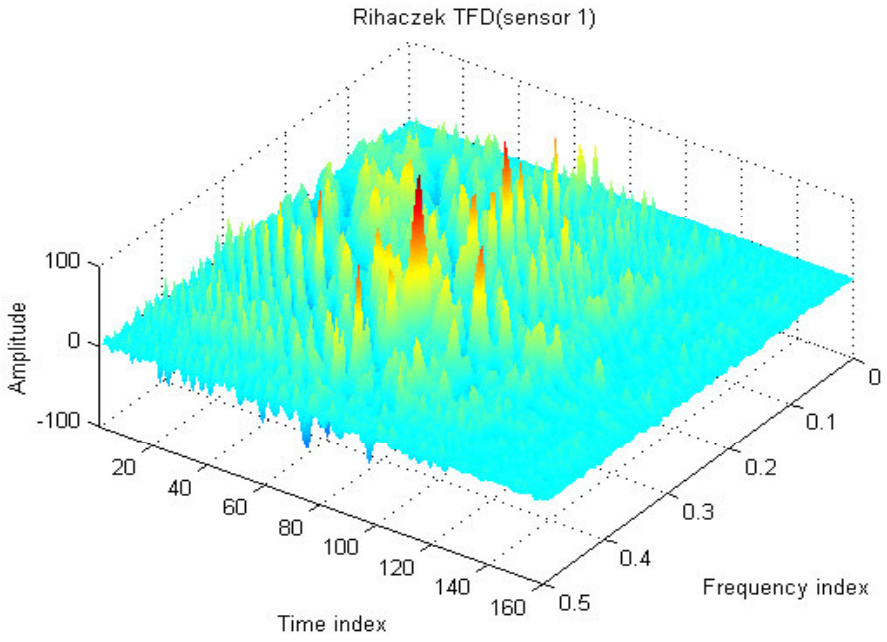

Fig. 5.44 Self-Rihaczek TFD of data at sensor 1

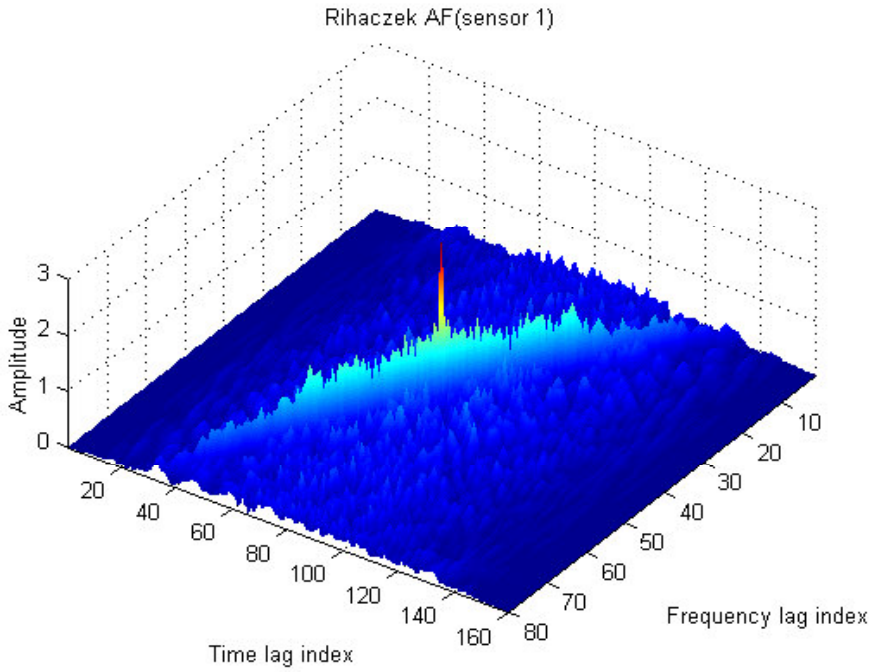

Fig. 5.45 Self-Rihaczek AF of data at sensor 1

Now, we apply the mask to the above AF space. The results in AF and TFD spaces are shown in Figs 5.46 and 5.47, respectively. Fig. 5.47 shows that the chirp signature emerges from noisy signal in TFD space after applying the mask.

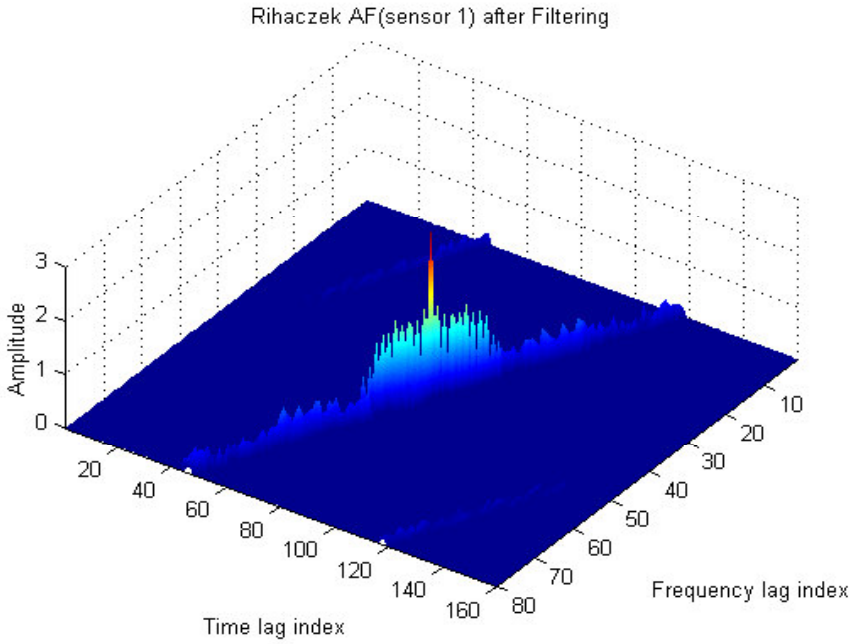

Fig. 5.46. Self-Rihaczek AF of data at sensor 1 after applying mask

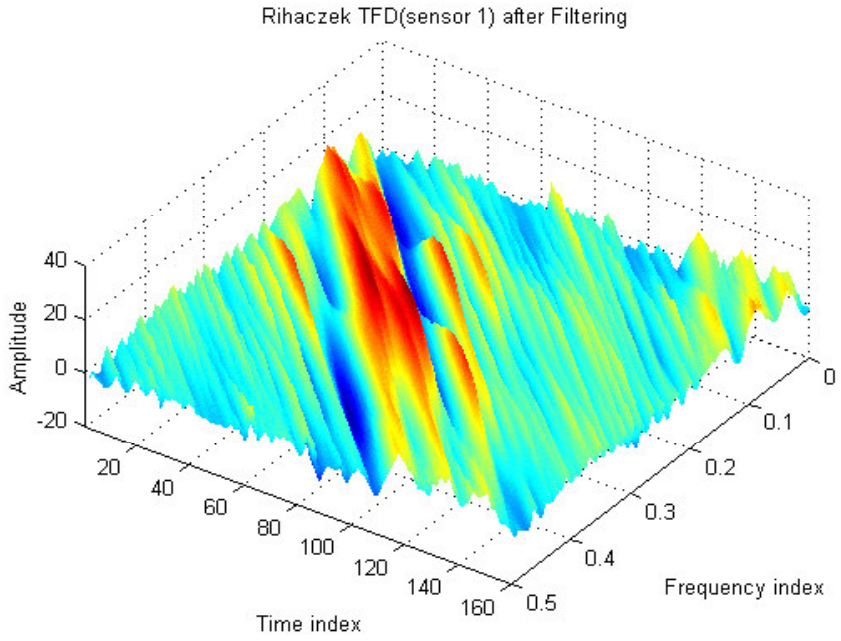

Fig. 5.47 Self-Rihaczek TFD of data at sensor 1 after applying mask

To see the effect on TF-MFP we repeat the above procedure but this time for the cross-Rihaczek case where two signals, from sensor one and fifteen, are involved in the process. The cross-Rihaczek distribution of sensors one and fifteen in TFD and AF spaces are shown in Figs 5.48 and 5.49, respectively.

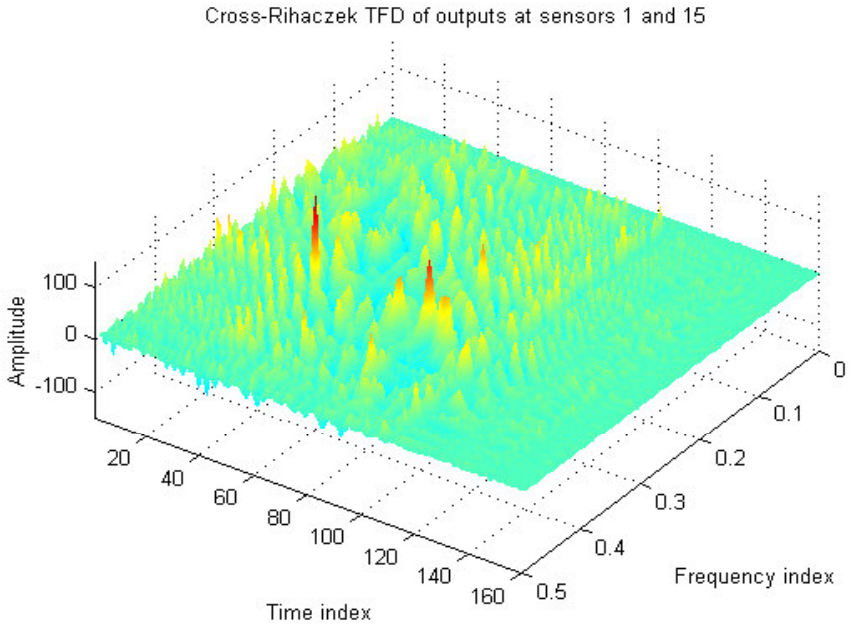

Fig. 5.48 Cross-Rihaczek TFD of signals at sensors 1 and 15

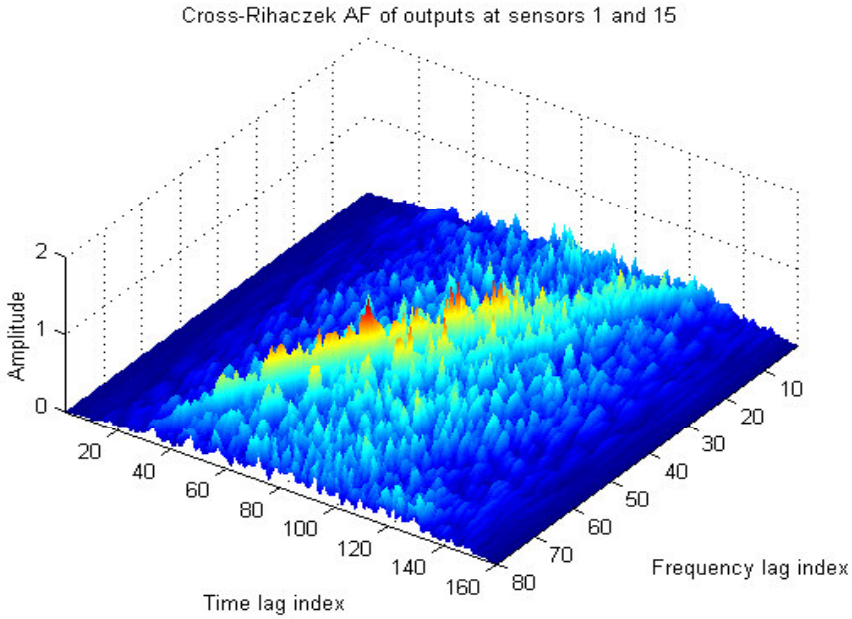

Fig. 5.49 Cross-Rihaczek AF of signal at sensors 1 and 15

The figures clearly show that the chirp signal is evident in a signal contaminated by a powerful correlated noise. There are more peaks in the AF space due to the effect of multiple transfer functions in the cross-Rihaczek formulation. Now, we preprocess by applying the mask in the AF space. The results in AF and TFD spaces are shown in Figs 5.50 and 5.51, respectively. Fig. 5.51 shows that the chirp signature emerges from the noisy data in TFD space after applying the mask.

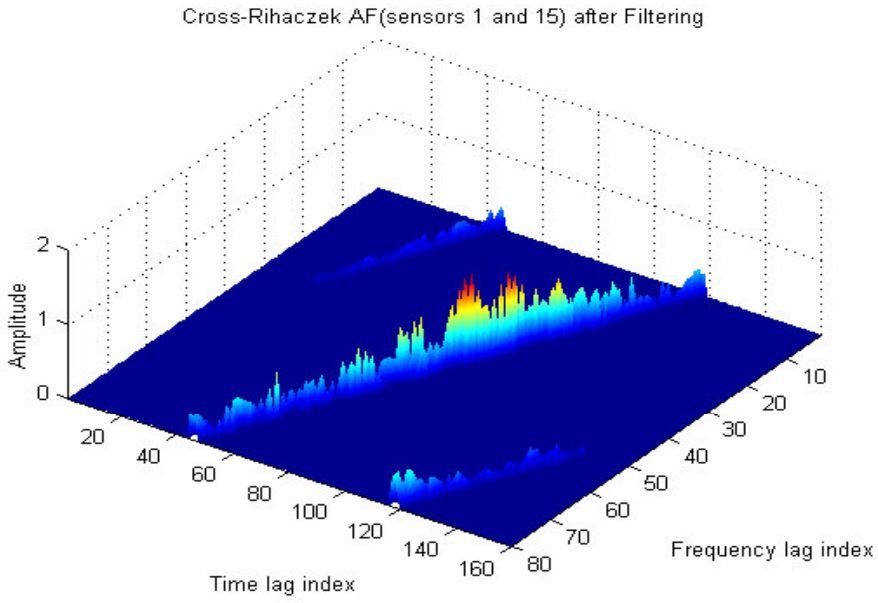

Fig. 5.50 Cross-Rihaczek AF of signal at sensors 1 and 15 after masking

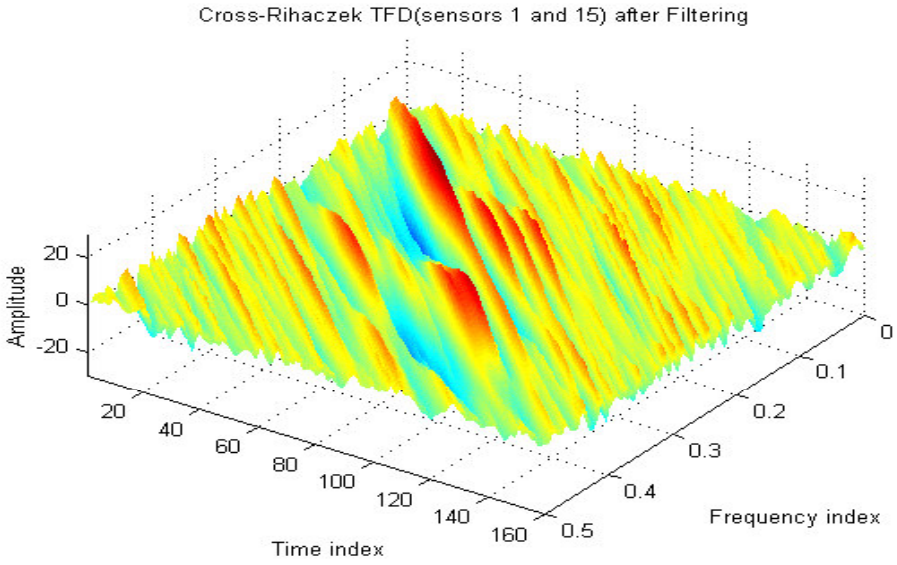

Fig. 5.51 Cross-Rihaczek TFD of signals at sensors 1 and 15 after masking

Now we use the preprocessed data in TF-MFP, and compare the performance of TF-MFP with other MFPs. In order to decrease the computational complexity, we sub-sample by a factor of 4 in both frequency and time. For conventional MFPs we use sub-sampling of 4. The ambiguity surfaces of the Bartlett processor for Gaussian noise sources with standard deviations (STD) of 0.8 and 0.95 are shown in Figs 5.52 and 5.53, respectively. The ambiguity surfaces of MV (version one and two) are given in Figs 5.54, and 5.55, respectively.

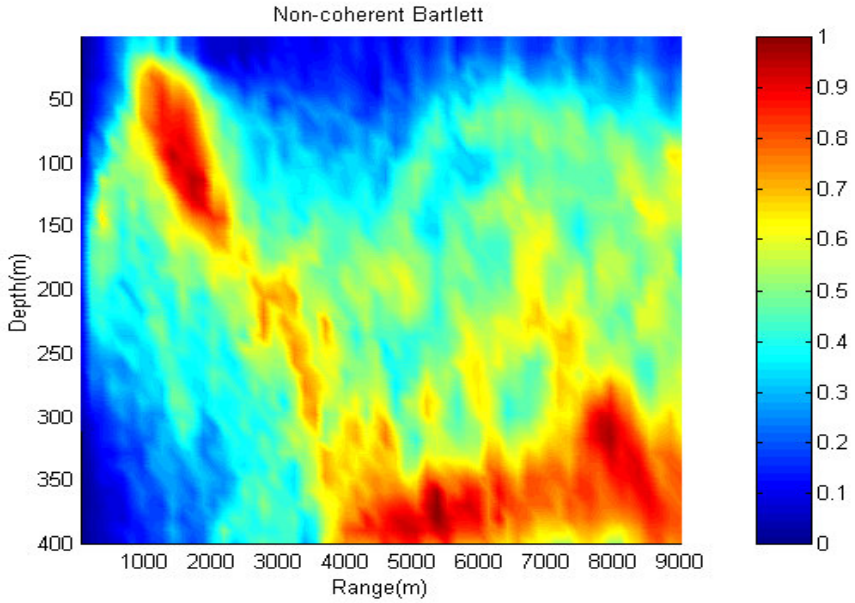

Fig. 5.52 Ambiguity surface for Bartlett processor (Gaussian interference STD=0.8)

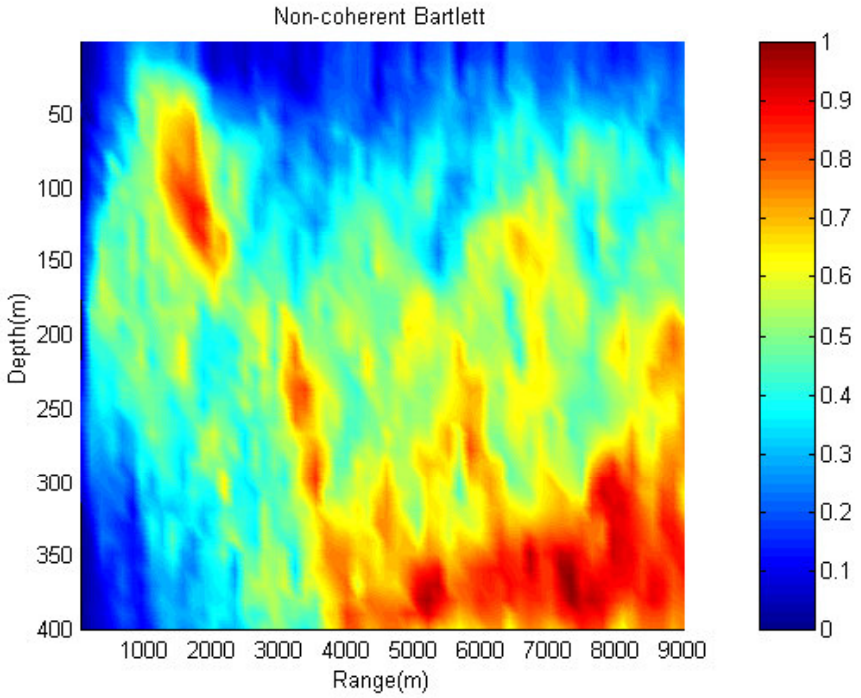

Fig. 5.53 Ambiguity surface for Bartlett processor (Gaussian interference STD=0.95)

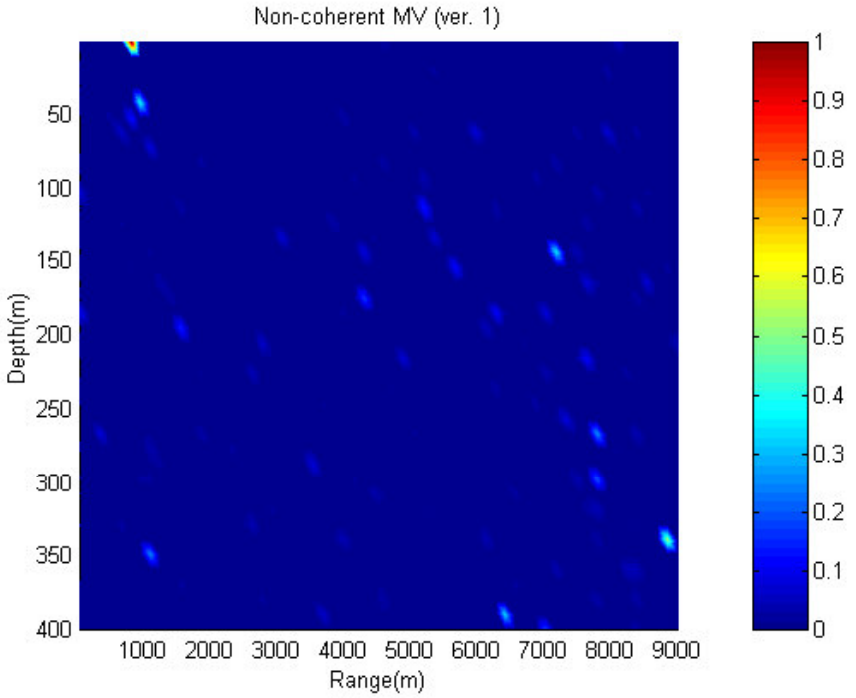

Fig. 5.54 Ambiguity surface for MV processor (version one, Gaussian interference STD=0.8)

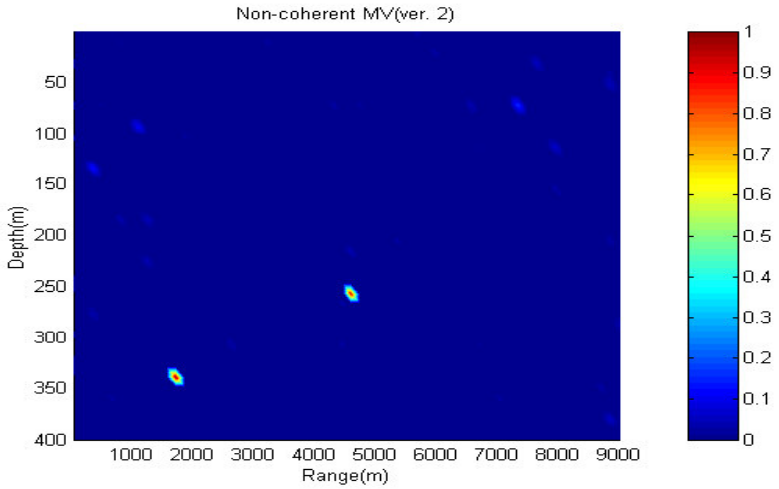

Fig. 5.55 Ambiguity surface for MV processor (version two, Gaussian interference STD=0.8)

For a Gaussian noise source with standard deviation of 0.85 the Bartlett processor has localized both the chirp source and Gaussian interference. However there are several false detections in the ambiguity surface. Moreover, the Bartlett processor fails to show a focused point at the true chirp source location. For a standard deviation of 0.95, the Bartlett processor fails to localize the chirp source. Due to the high sensitivity to mismatch for the MV processors, and to the distortion that come from sub-sampling both versions of MV have failed to localize both sources and show false sources.

Westwood's ambiguity surface is given in Fig. 5.56 for a standard deviation of 0.8. It shows a source that is close to the chirp source range but at a depth around 60m, far from the true chirp source depth. For a Gaussian interference with standard deviation of 0.95 (see Fig. 5.57), the Westwood processor fails to localize either sources.

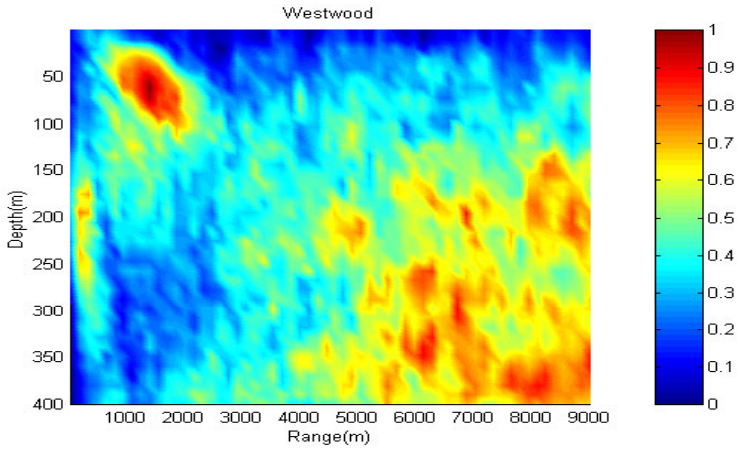

Fig. 5.56 Ambiguity surface for Westwood processor (Gaussian interference STD=0.8)

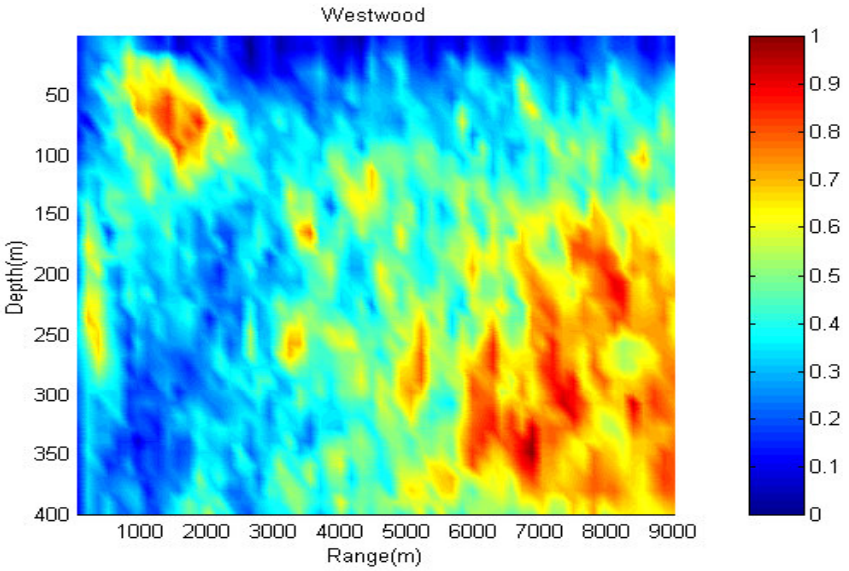

Fig. 5.57 Ambiguity surface for Westwood processor (Gaussian interference STD=0.95)

Because they do not utilize TF features, both the self-CR and cross-CR processors fail to localize the chirp source, as shown in Figs 5.58 and 5.59, respectively. They show a few false sources, while the Gaussian interference is successfully localized.

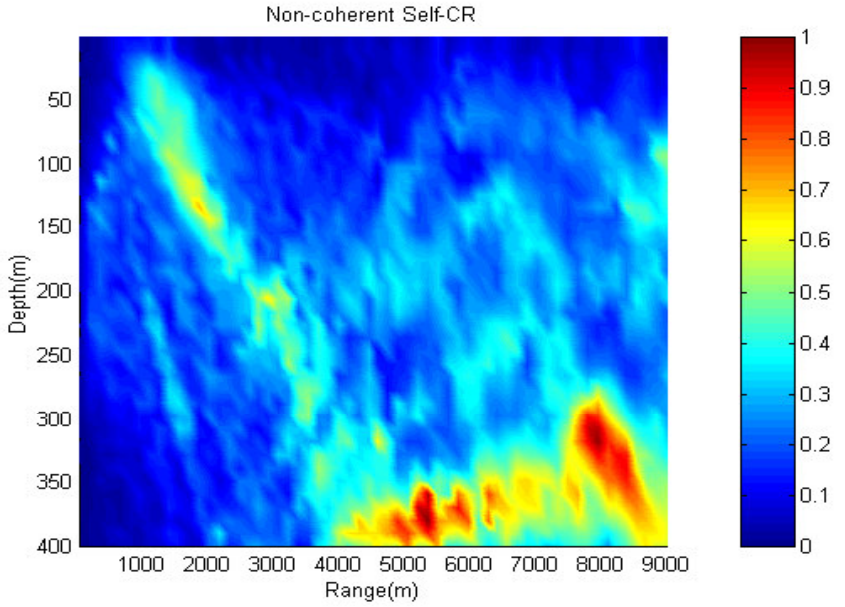

Fig. 5.58 Ambiguity surface for self-CR processor (Gaussian interference STD=0.8)

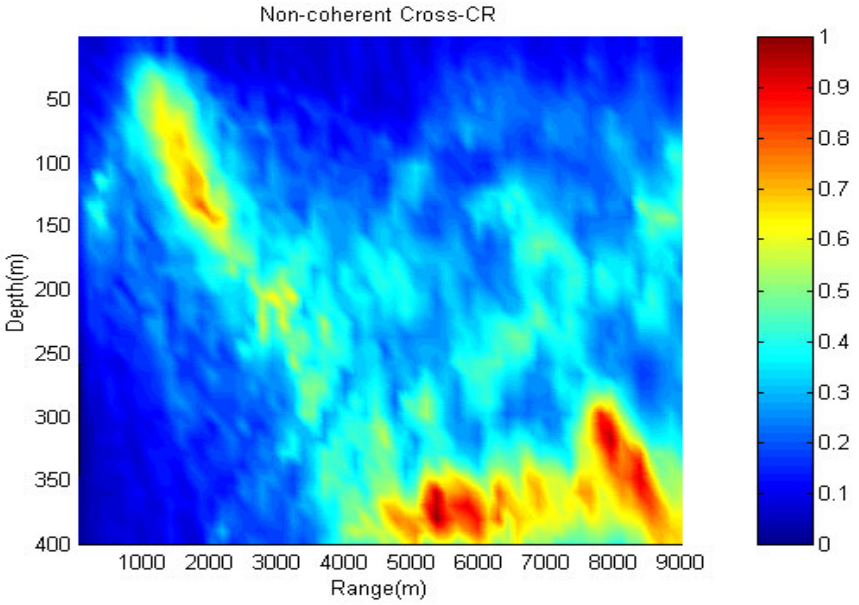

Fig. 5.59 Ambiguity surface for cross-CR processor (Gaussian interfernce STD=0.8)

The result is significantly different for TF-MFP. With the pre-process masking, both versions of TF-MFP (self-CR and cross-CR) successfully localized the chirp source (Gaussian interference with STD=0.8). The effect of the Gaussian interference is cancelled by the preprocessing masking step described above. The ambiguity surfaces for the self TF-MFP and cross TF-MFP are shown in Figs 5.60 and 5.61, respectively.

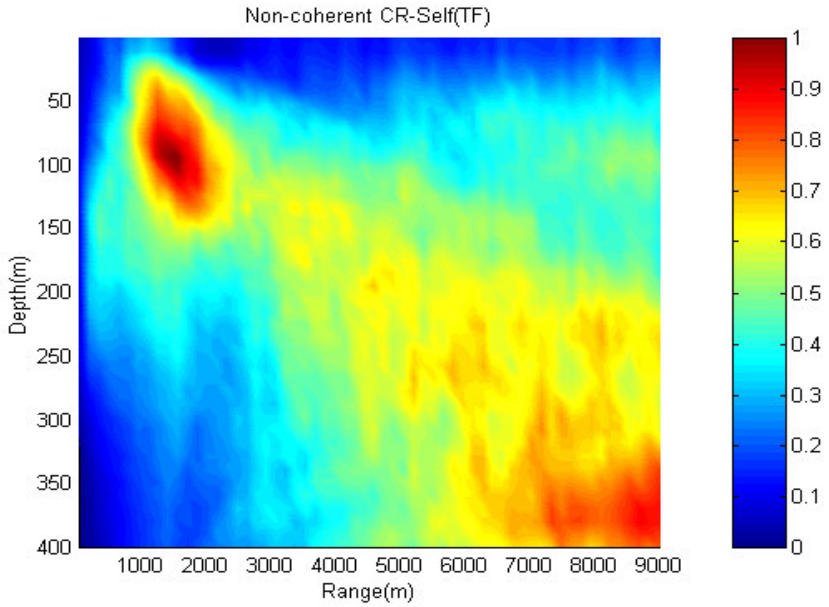

Fig. 5.60 Ambiguity surface for self-CR TF-MFP (Gaussian interference STD=0.8)

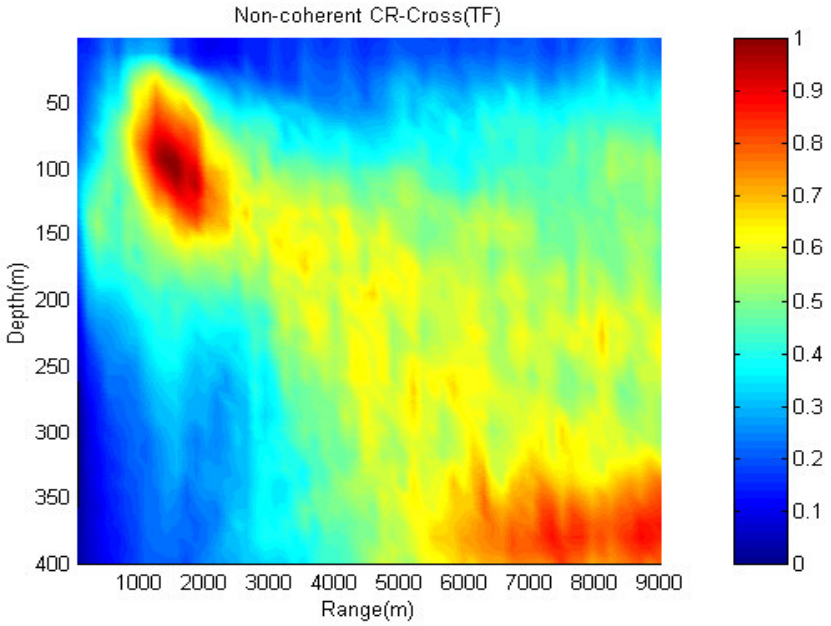

Fig. 5.61 Ambiguity surface for cross-CR TF-MFP (Gaussian interference STD=0.8)

With a more powerful Gaussian interference (STD=0.95), the cross-CR TF-MFP (Fig. 5.63) shows greater canceling of the effect of correlated noise than does self-CR TF-MFP (Fig. 5.62). Moreover, because the cross-CR TF-MFP is constructed with only cross terms it also has the advantage of canceling the white measurement noise.

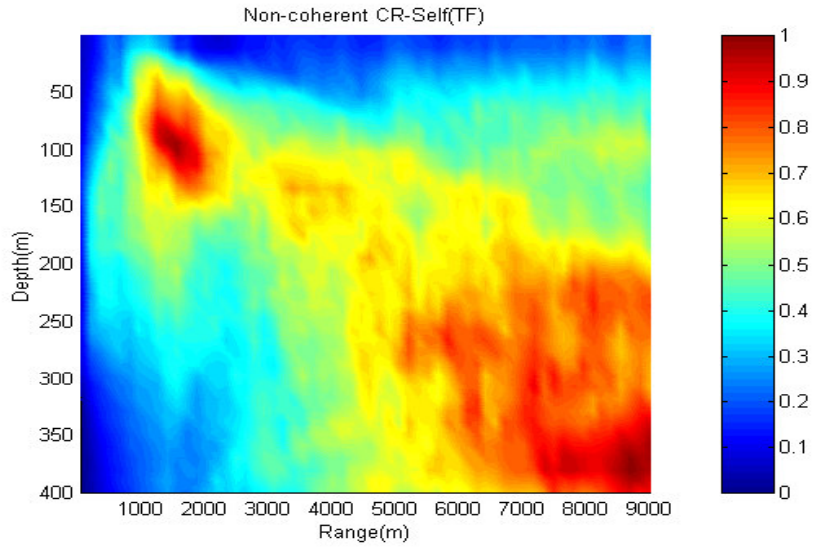

Fig. 5.62 Ambiguity surface for self-CR TF-MFP (Gaussian interference STD=0.95)

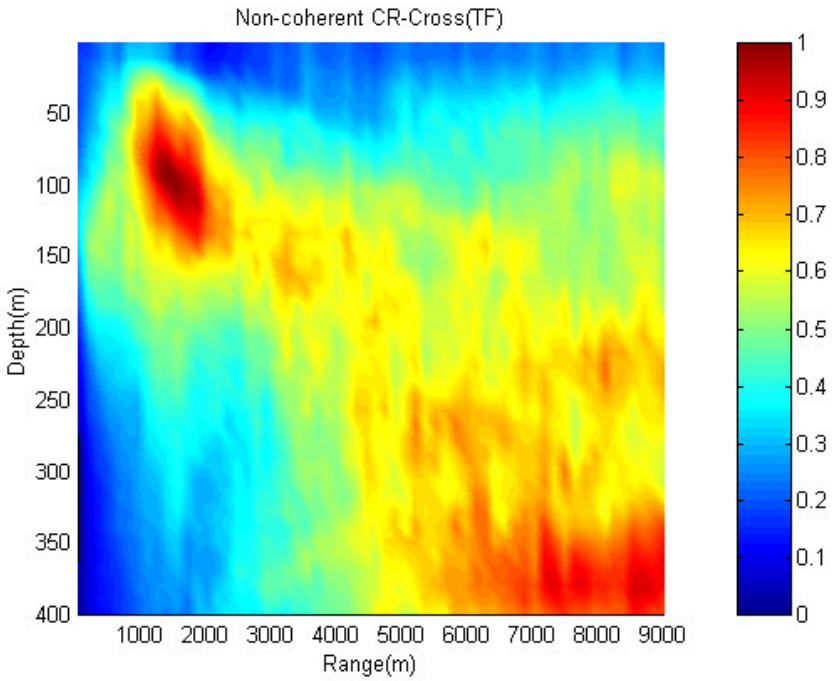

Fig. 5.63 Ambiguity surface for cross-CR TF-MFP (Gaussian interference STD=0.95)

5.3. Experimental results

In this section we consider source localization using both the tonal data and radiated ship data from the MEVA3 track. The tonal signals and the ship data are considered separately to demonstrate the performance of the MFPs for narrow band and broadband signals. In the first part of the section, we evaluate the performance of the second order CR-MFPs and compare it with that for the other MFPs. In the second part the higher order MFP is considered in order to examine the use of higher order information content of ship data in source localization. The replica or modeled fields used in experiments are calculated using the Westwood normal mode model, ORCA [15]. The experimental conditions including array specifications and environmental properties were described in section 5.1.

We consider a section of the track where the bathymetry between the source ship and the array satisfies the range independence assumption. At this point, the recorded range between the

array and the ship is 3.33 km with a bearing of 153.30 degrees. The positions of the ship and the array are shown in Fig. 5.64.

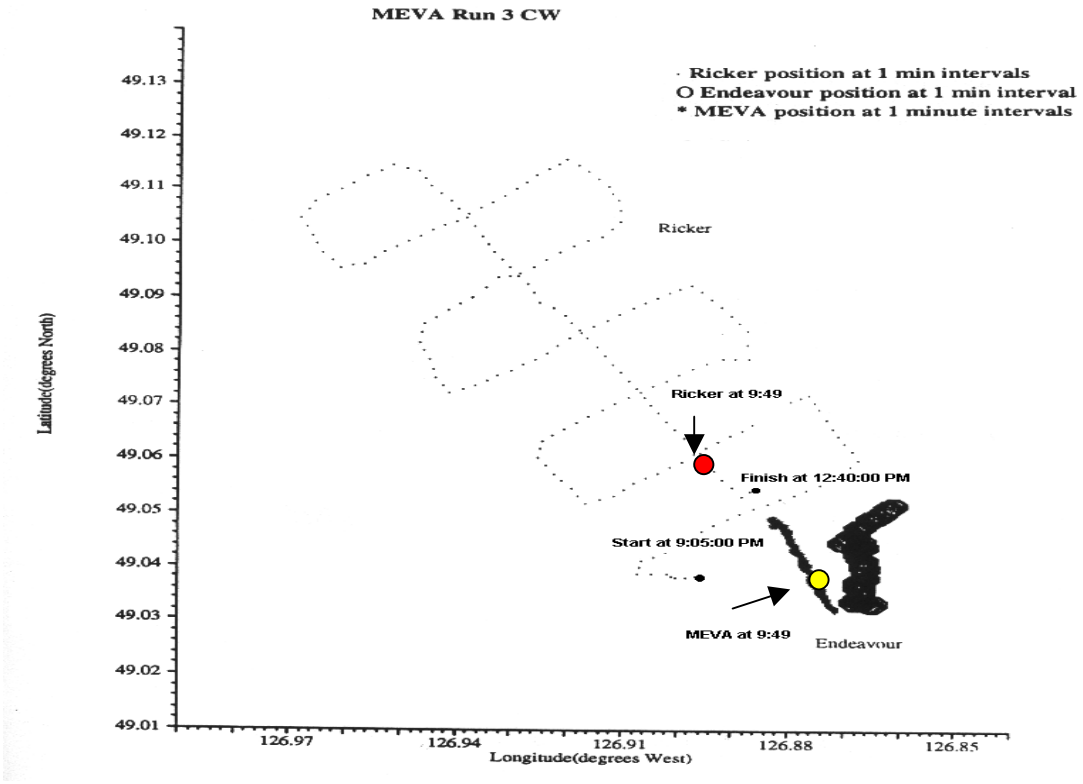

Fig. 5.64 The position of Ricker and array on the MEVA3 trial track at 9:49pm

5.3.1 Second order based MFPs

The source signals include the tonal signals at 45 and 70 Hz transmitted from the towed source and ship data generated by CSS. Ricker. The sampling frequency is 1500 Hz and since the bandwidth of the anti-aliasing filter is around 750 Hz, the original discrete data were sub-sampled by a factor of 2. For both the tonal signals and ship data, we use the periodogram technique averaging over 40 time samples to estimate signal spectra and cross-spectra. A time slice of sensor 16's data is shown in Fig. 5.65(a), and the corresponding spectrum is shown in Fig. 5.65(b).

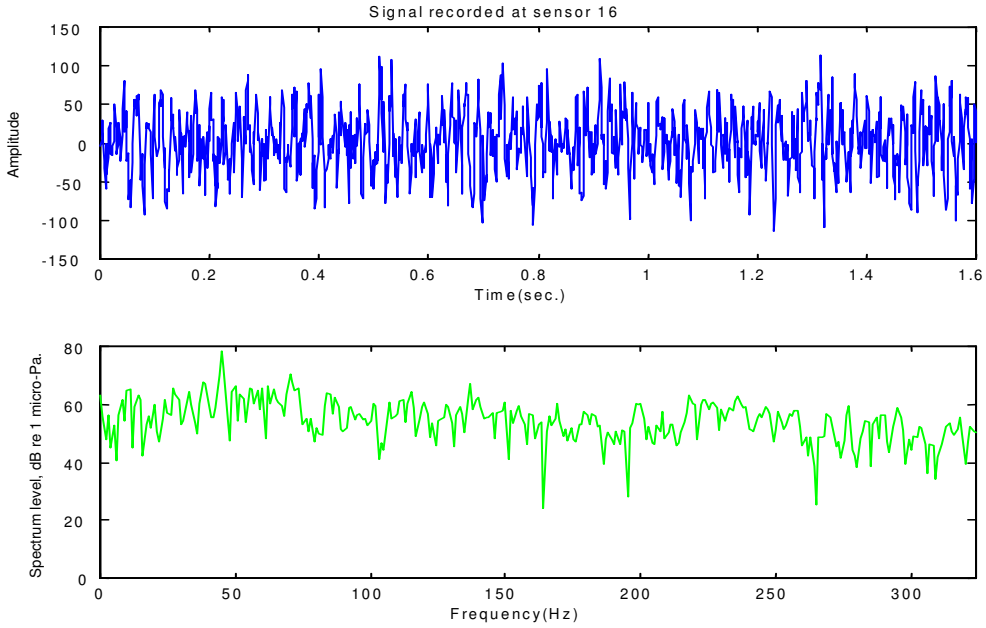

Fig. 5.65 A slice of sensor 16's data in (a) time and its (b) spectrum

5.3.1.1 Continuous wave (CW) sources

For the 45 Hz CW data, the ambiguity surfaces of the Bartlett, MV, CR-MFPs, and Westwood processors are given in Figs 5.66, 5.67, 5.68, 5.69, and 5.70, respectively. The grid search spans a range from 50 m to 10 km with resolution of 110 m, and depth from 1 m to 400 m with a resolution of 10 m.

The figures demonstrate that MFPs other than MV and Westwood have detected the true source location. The cross-CR and self-CR give superior performance in comparison with the Bartlett processor with respect to resolution and side lobe levels. Ambiguity surfaces localize the source at a range of 3.63 km and a depth of 31 m. The range is about 300 m different from the range indicated by GPS. However, for a range grid resolution of 110 m, this difference is within the range error due to the GPS uncertainties for the position of the ship and the array (200 m), and the uncertainty of the distance of the source from the ship (50-70 m). Mismatch in the geoacoustic model may also be a source of error, since at 45Hz acoustic waves can penetrate relatively deep into the bottom. The depth value (31 m) for the towed source is reasonable

according to the experimental design, however there is no value documented for the source depth in the MEVA3 report.

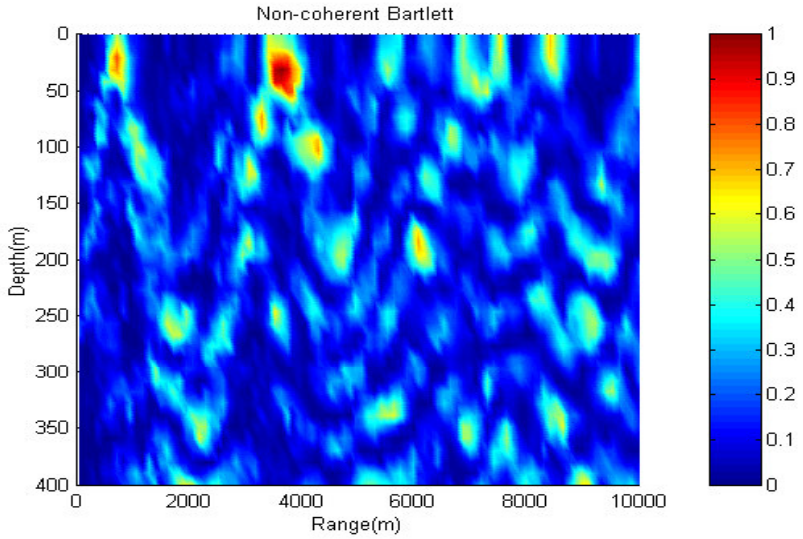

Fig. 5.66 Ambiguity surface for Bartlett processor (45Hz data)

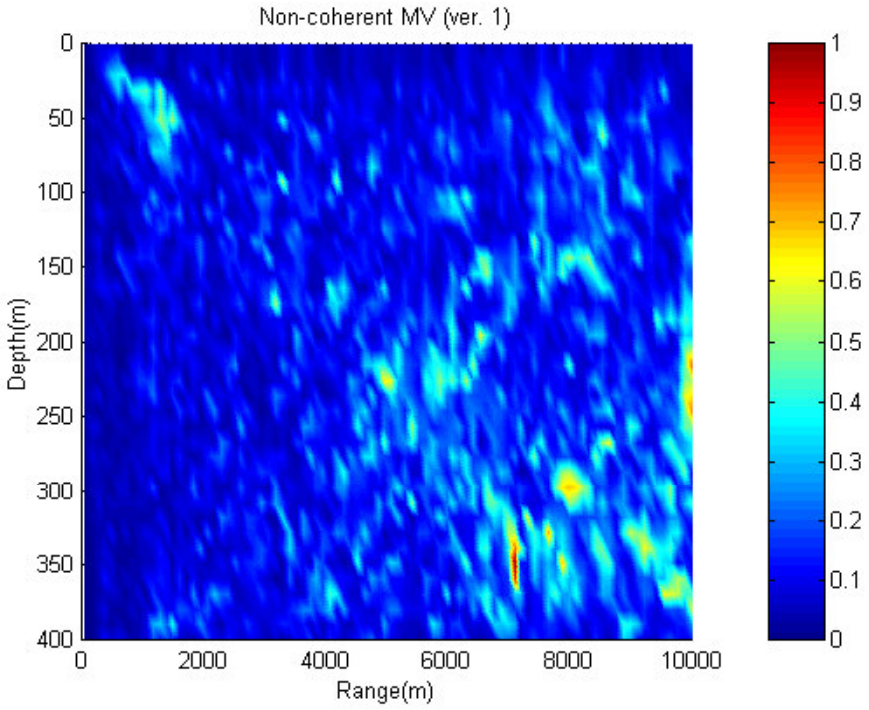

Fig. 5.67 Ambiguity surface for MV processor (45Hz data)

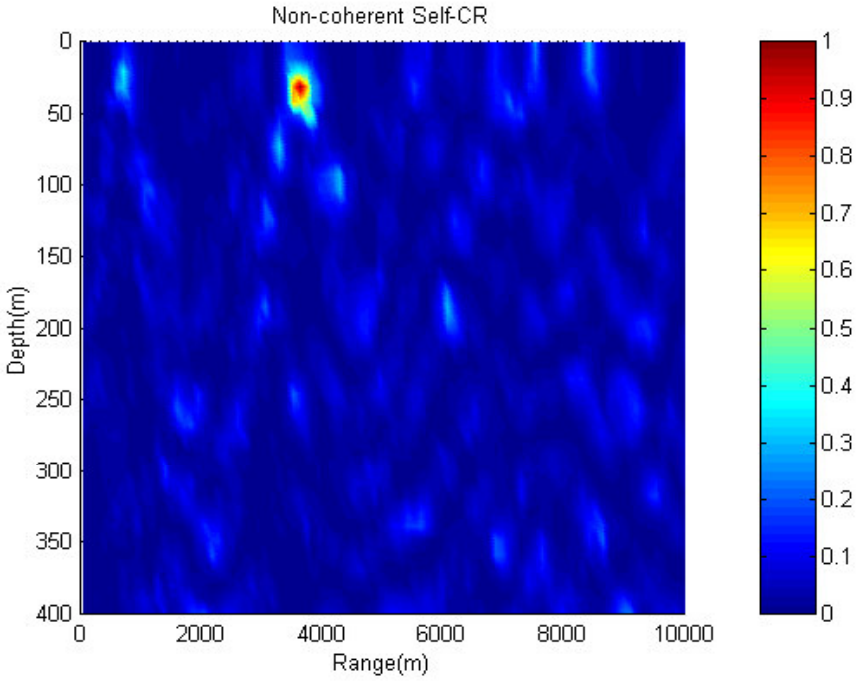

Fig. 5.68 Ambiguity surface for self-CR processor (45Hz data)

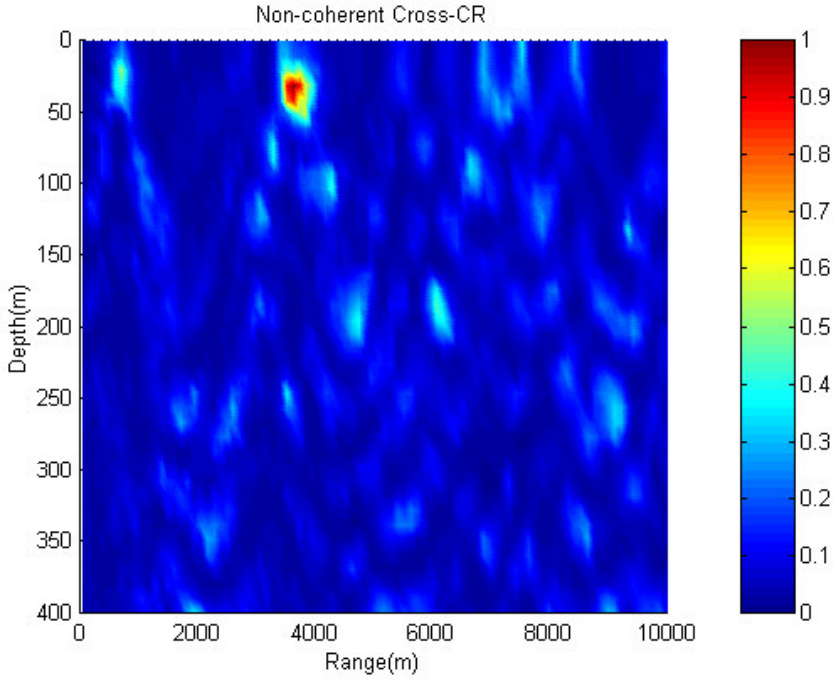

Fig. 5.69 Ambiguity surface for cross-CR processor (45Hz data)

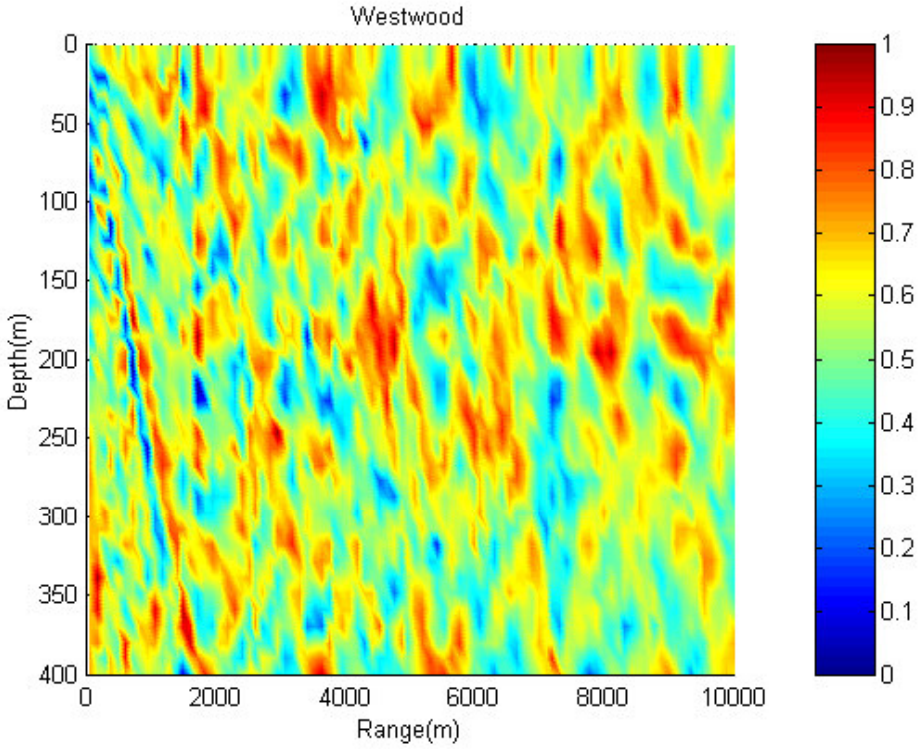

Fig. 5.70 Ambiguity surface for Westwood processor (45Hz data)

Cross sections of the ambiguity surface in range for a depth of 31 m, and in depth for a range of 3.63 km are shown in Figs 5.71 and 5.72, respectively. We can see lower side lobe levels and sharper main lobes at the source location for CR-based MFPs in comparison to that for the Bartlett processor. To discuss this behavior, we first consider the self-CR and Bartlett processors. Both contain self-term components. The result that the side lobe levels for the self-CR (Fig. 5.68) are significantly low shows that the level of spatially white noise is not strong at 45Hz. Referring to Fig. 5.66 the side lobe levels are significantly higher for the Bartlett processor. Since spatially white noise is not strong, the higher side lobe levels are due to model mismatch. Comparison of the two figures indicates that the self-CR is significantly more robust than the Bartlett to model mismatch. The self-CR MFP shows better performance in main lobe width and side lobe level than that for the cross-CR MFP (Fig. 5.69) in this environment with low spatially white noise. The reason is likely due to the phase distortion due to mismatch between the model and the environment. The cross-CR MFP is more sensitive to phase distortion than is the self-CR because of its formulation that only includes cross-term components whereas the self-CR includes both self-term (spectral magnitudes) and cross-term components.

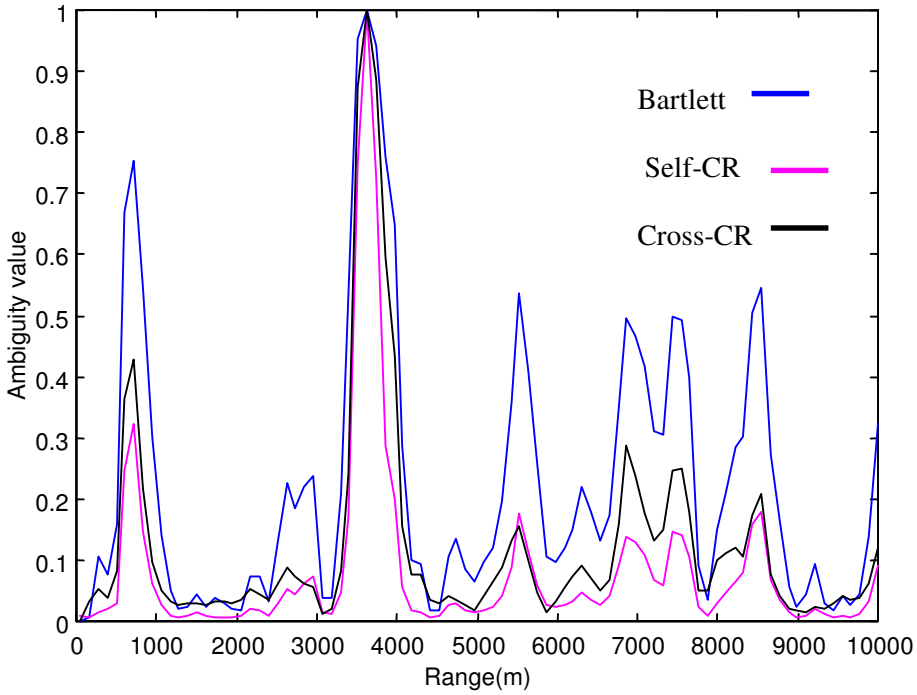

Fig. 5.71 Performance of the different MFPs in range for a depth of 31m

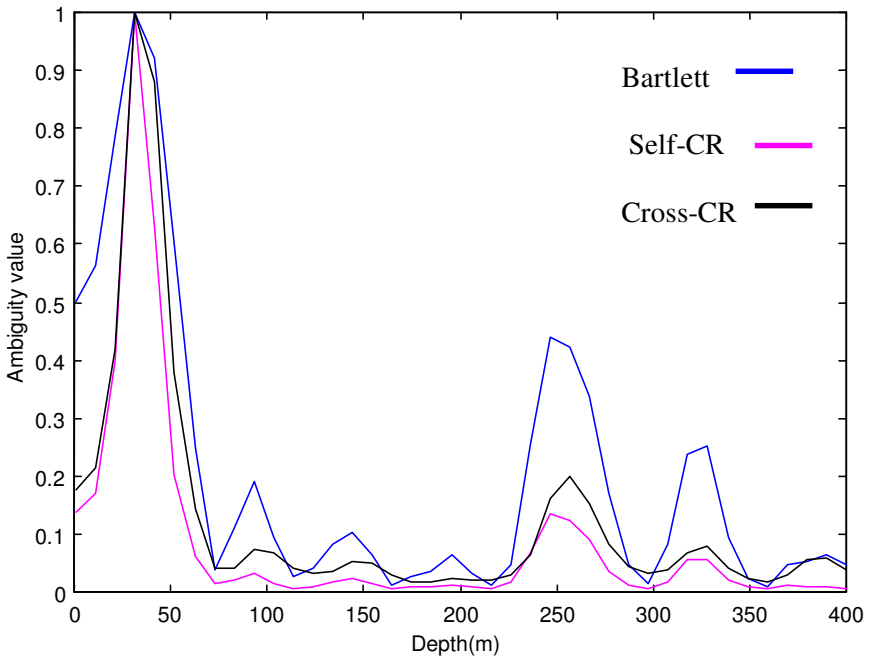

Fig. 5.72 Performance of the different MFPs in depth for a range of 3.63km

For the 70Hz CW data the ambiguity surfaces for the Bartlett, MV, CR-MFPs, and Westwood processor are shown in figures 5.73, 5.74, 5.75, 5.76, and 5.77, respectively. The grid search dimension is the same as that for the 45 Hz experiment.

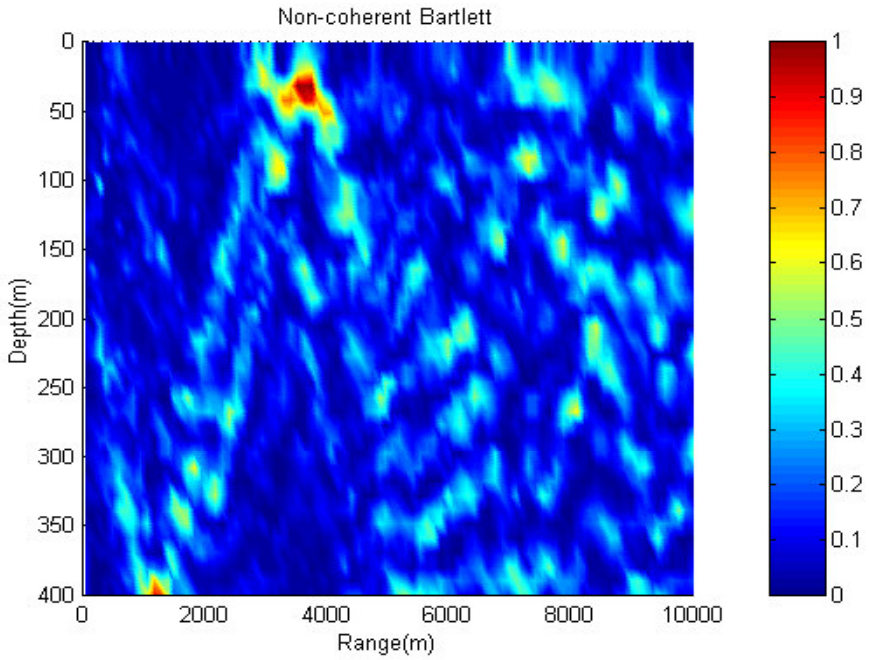

Fig. 5.73 Ambiguity surface for Bartlett processor (70 Hz data)

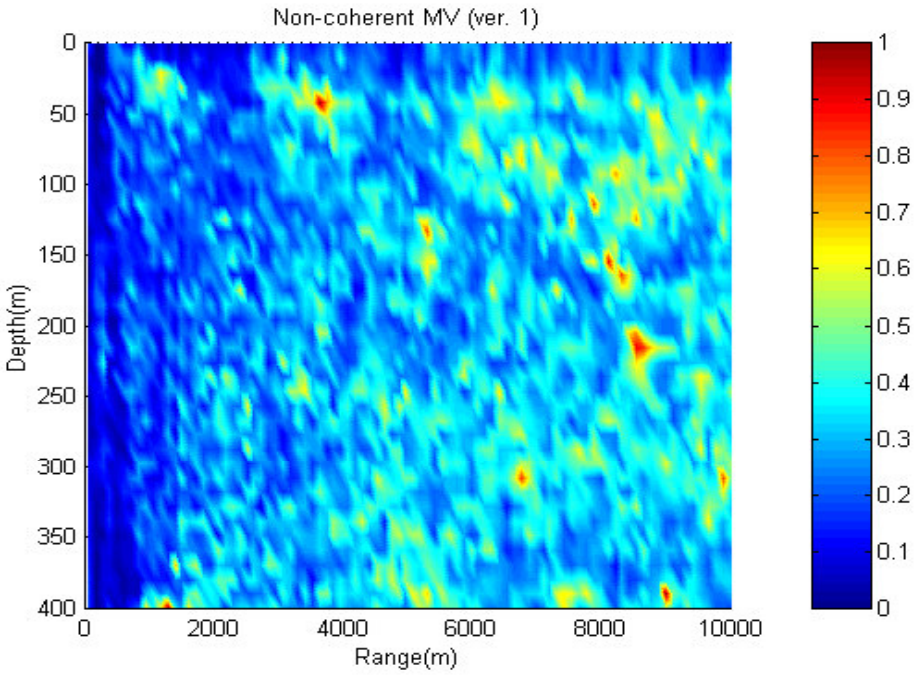

Fig. 5.74 Ambiguity surface for MV processor (70 Hz data)

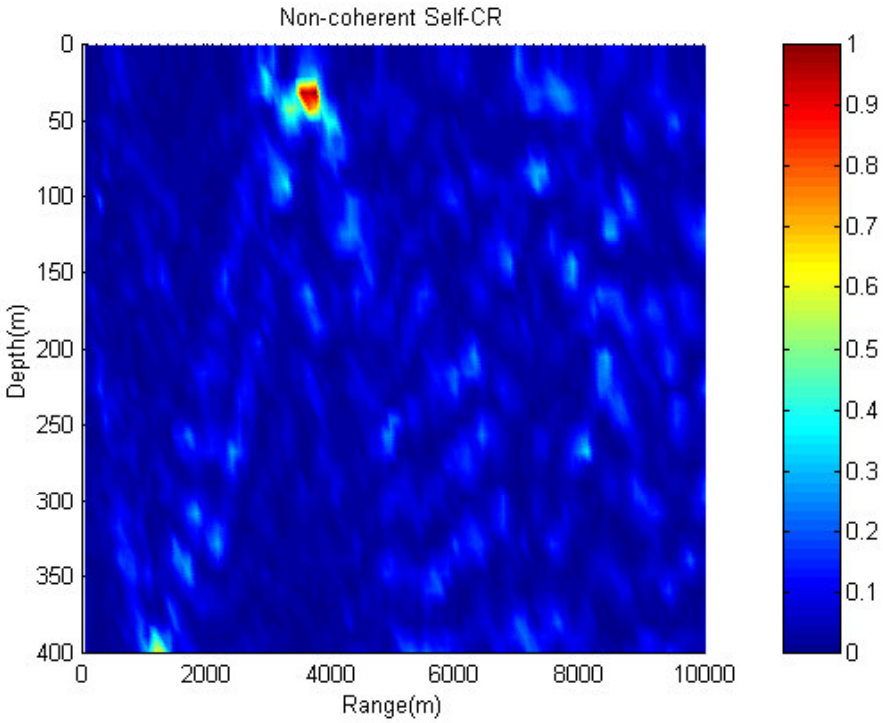

Fig. 5.75 Ambiguity surface for self-CR processor (70 Hz data)

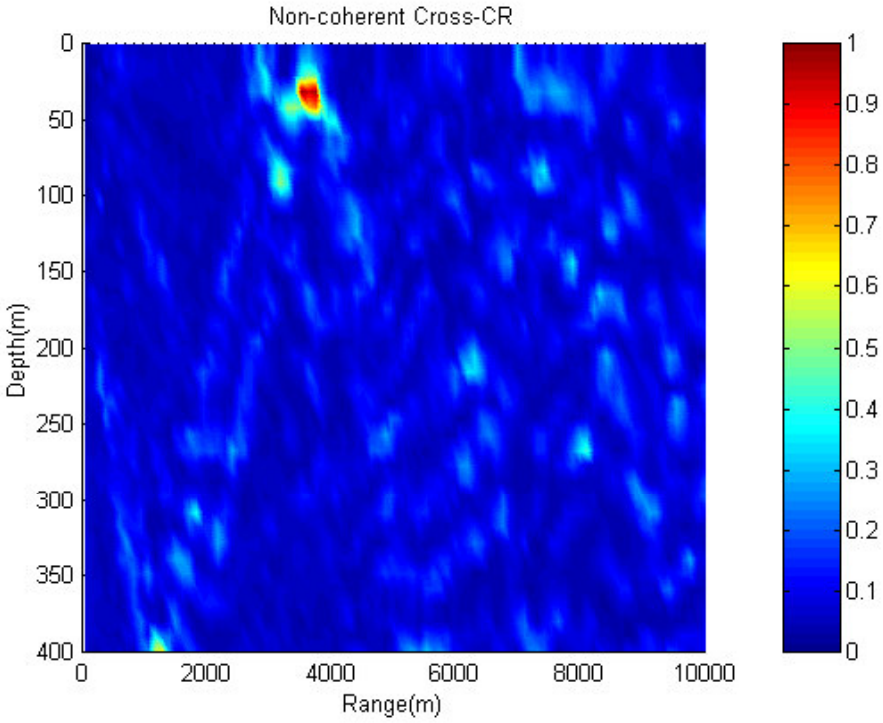

Fig. 5.76 Ambiguity surface for cross-CR processor (70 Hz data)

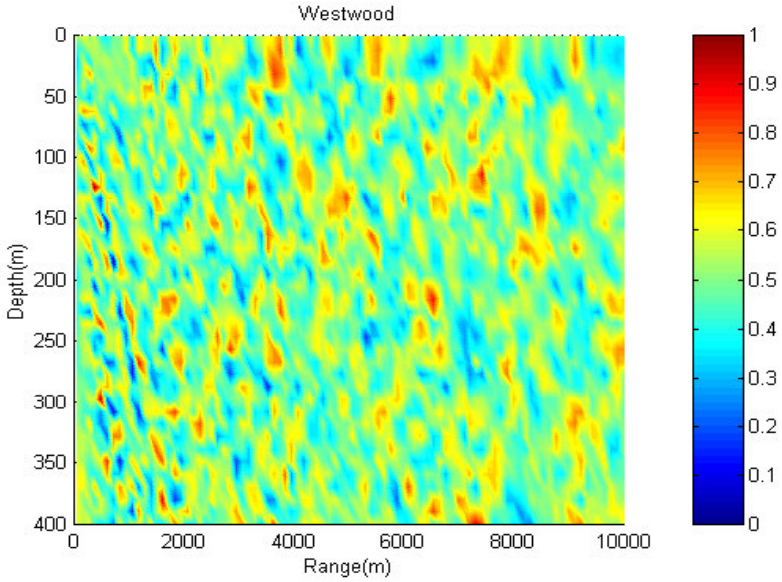

Fig. 5.77 Ambiguity surface for Westwood processor (70 Hz data)

The figures demonstrate that except for the MV and Westwood processors, the other MFPs have detected the true source location. The cross-CR and self-CR give superior performance in comparison to the Bartlett processor with respect to resolution and side lobe levels. Ambiguity surfaces localize the source at a range of 3.52 km and depth of 31 m. The estimated source range is closer to the GPS value than the estimate for the 45 Hz data. This may be due in part to a lesser impact of environmental mismatch in the geoacoustic model. At 70 Hz, the penetration into the ocean bottom is relatively shallow compared to that for 45 Hz.

Cross sections of the ambiguity surface in range for a depth of 31 m, and in depth for a range of 3.52 km are shown in Figs 5.78 and 5.79, respectively. We can see lower side lobe levels and sharper main lobes around the source location for CR-based MFPs in comparison to those for the Bartlett processor. To discuss this behavior, we first consider the self-CR and Bartlett processors. Both contain self-term components. The result that the side lobe levels for the self-CR (Fig. 5.75) are significantly low shows that the level of spatially white noise is not strong at 70 Hz. Referring to Fig. 5.73 the side lobe levels are significantly higher for the Bartlett processor. Since spatially white noise is not strong, the higher side lobe levels are due to model mismatch. Comparison of the two figures indicates that the self-CR is significantly more robust than the Bartlett to model mismatch. The self-CR MFP shows better performance in main lobe

width and side lobe level than that for the cross-CR MFP (Fig. 5.76) in this environment with low spatially white noise. The reason is likely due to the phase distortion from mismatch between the model and the environment, similar to the results from the 45-Hz data.

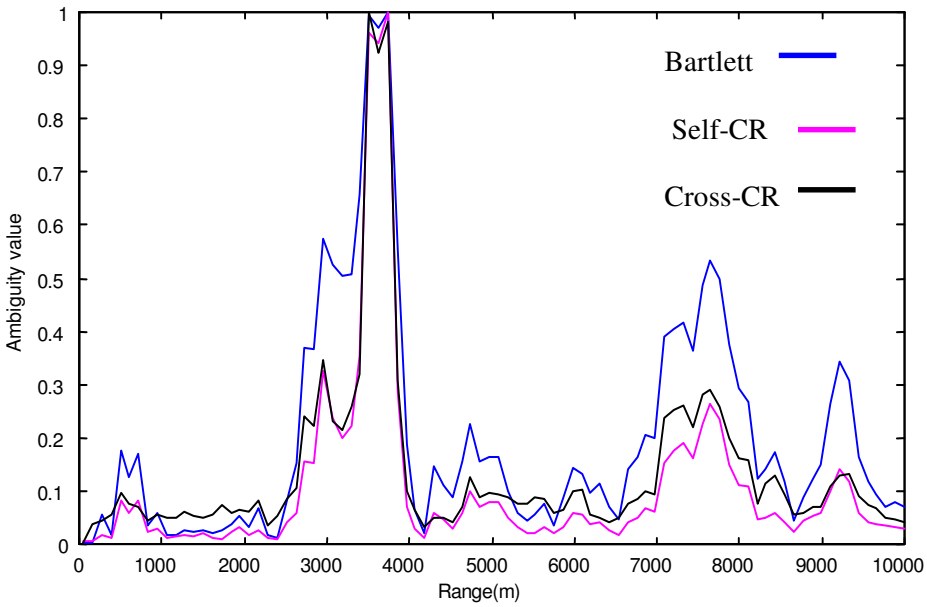

Fig. 5.78 Performance of the different MFPs in range for a depth of 31m (70 Hz data)

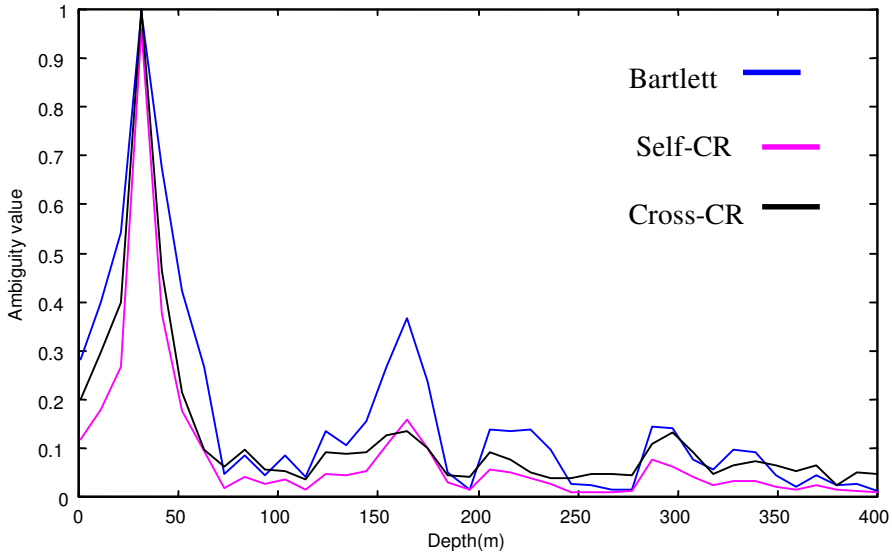

Fig. 5.79 Performance of the different MFPs in depth for a range of 3.52km (70 Hz)

5.3.1.2 Ship noise

For localization with the radiated ship signal, the signal spectrum is divided into three bands, 1-40 Hz, 73-133 Hz, and 150-270 Hz in order to eliminate the CW tones at 45 Hz and 70 Hz. We also null the spectral components at and around the tonal harmonics; i.e., at 90 Hz, 135 Hz, 140-Hz, 180 Hz, 210 Hz, 225 Hz, and 270 Hz before MF processing. However, the effect of the transmitted tones can not be fully cancelled especially in the second band (73-133 Hz) since the source generator is not an ideal source and does not give pure sine waveforms at specified frequencies. The analysis is carried out using the second band, 73-133 Hz, and the third band, 150-270 Hz, to decrease the effect of low frequency interfering noise from other ships in the transportation route near the experimental area.

In order to reduce the complexity of computation, we consider a resolution of 2 Hz for the second band and 4 Hz for the third band to obtain 30 spectral components in each band.

For the second band (73-133 Hz) highlighted in Fig. 5.80, the ambiguity surface of the Bartlett, MV (versions one and two), CR-MFPs, and Westwood processor are given in Figs 5.81, 5.83, 5.84, 5.85, 5.87, and 5.89, respectively. In order to give a precise understanding of localized sources, we enlarge the neighborhood region around the identified sources for the Bartlett, self-CR, and cross-CR MFPs as shown in Figs 5.82, 5.86, and 5.88, respectively. The grid search dimensions are the same as for the 45 Hz and the 70 Hz tones.

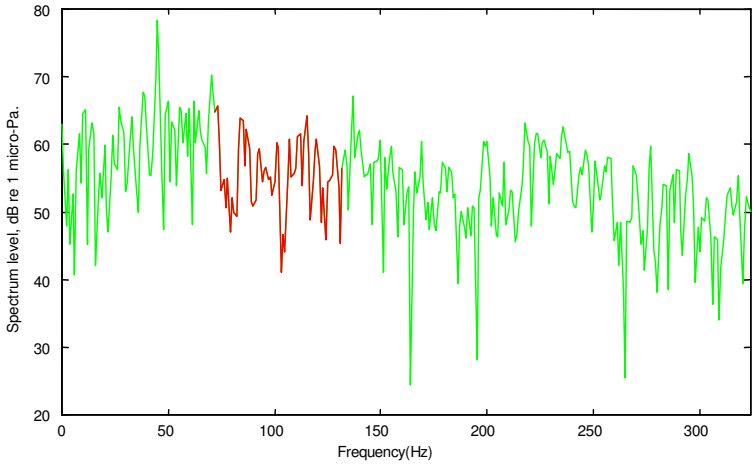

Fig. 5.80 The second band of ship data, 73-133Hz, highlighted by red color

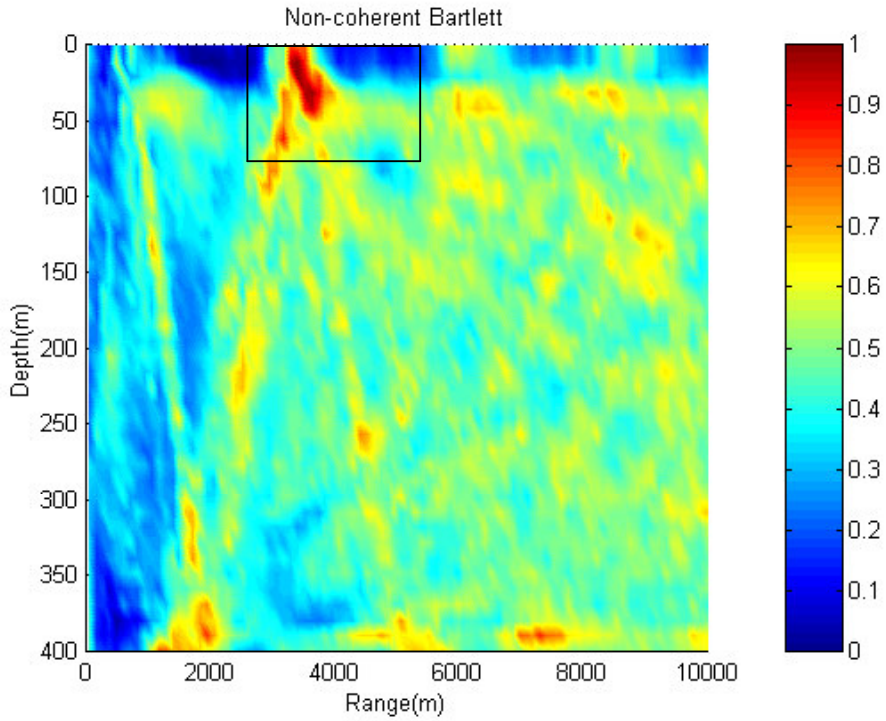

Fig. 5.81 Ambiguity surface for Bartlett processor (73-133Hz)

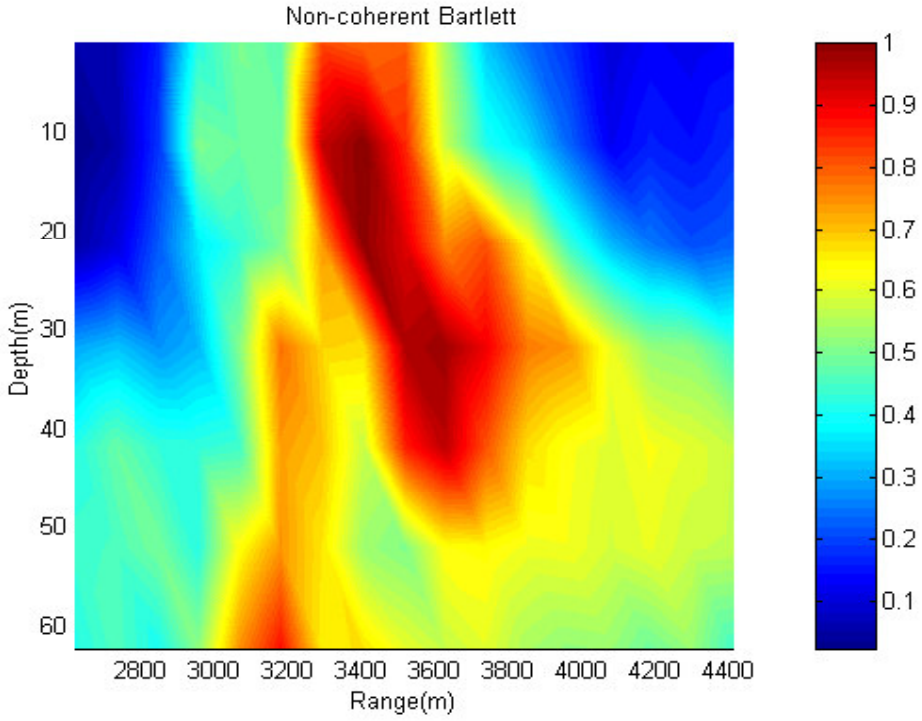

Fig. 5.82 Ambiguity surface for Bartlett processor (73-133Hz), the enlarged part around the identified source

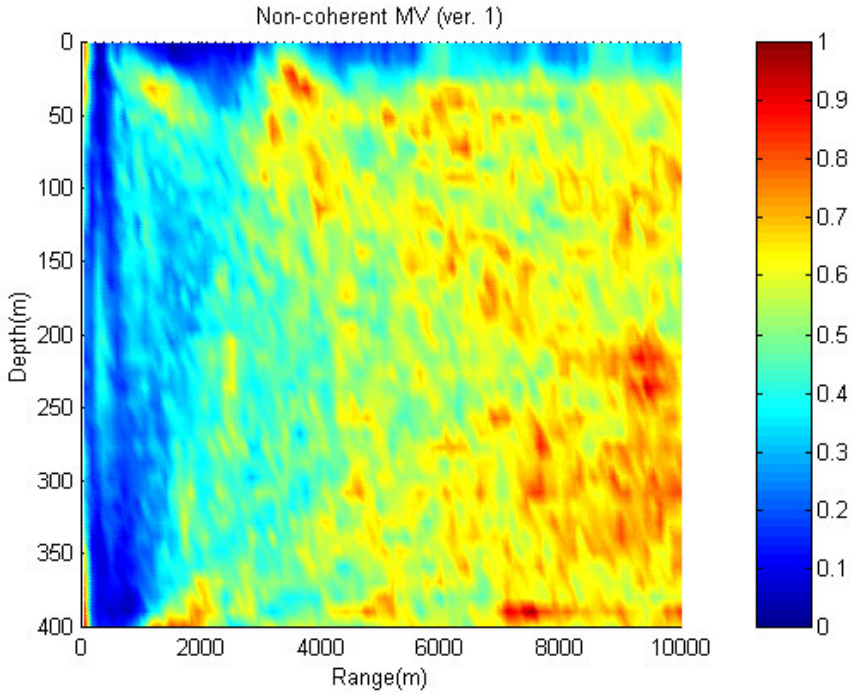

Fig. 5.83 Ambiguity surface for MV processor, version 1 (73-133Hz)

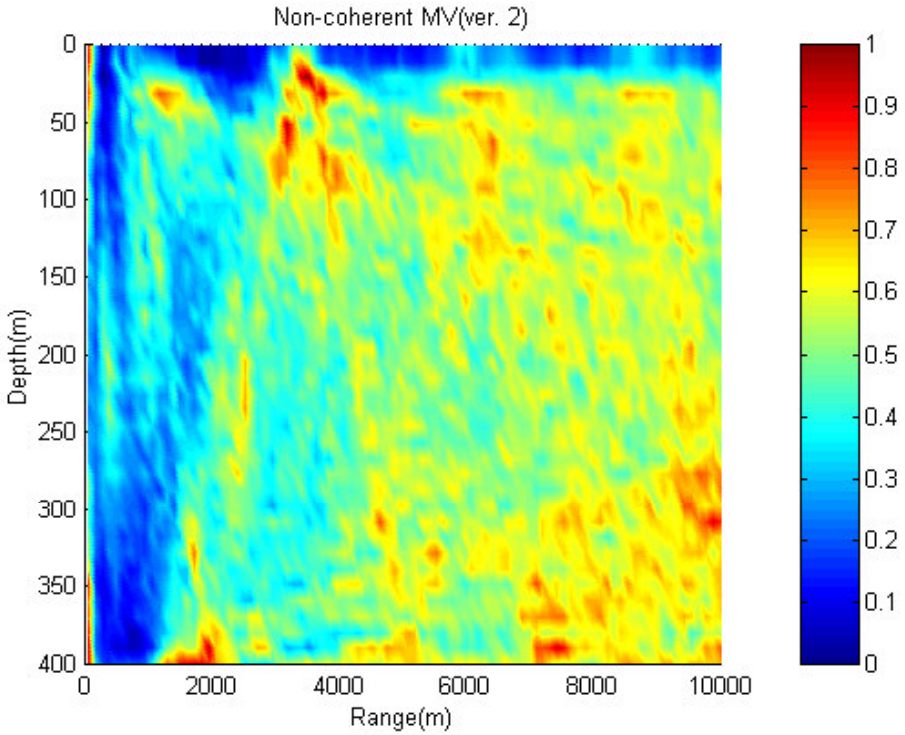

Fig. 5.84 Ambiguity surface for MV processor, version 2 (73-133Hz)

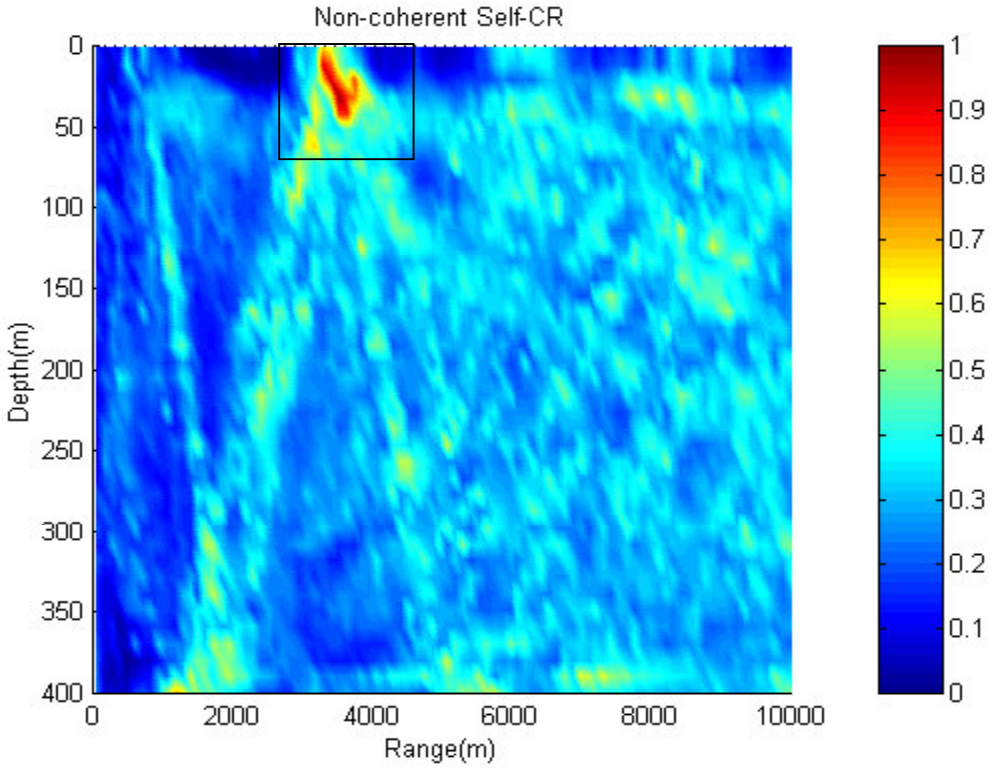

Fig. 5.85 Ambiguity surface for self-CR processor (73-133 Hz)

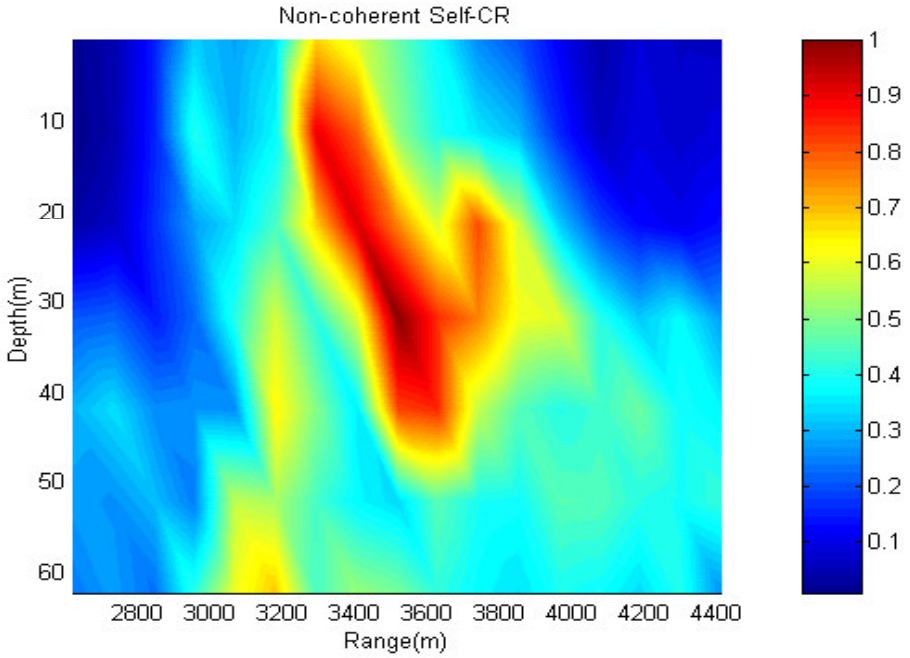

Fig. 5.86 Ambiguity surface for self-CR processor (73-133 Hz), the enlarged part around the identified source

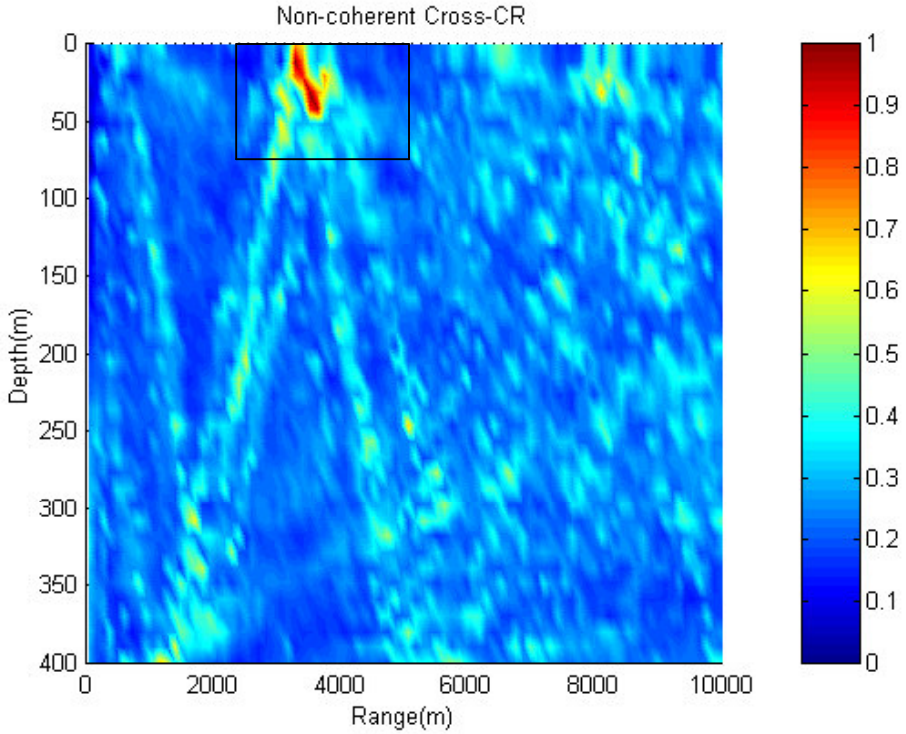

Fig. 5.87. Ambiguity surface for cross-CR processor (73-133 Hz)

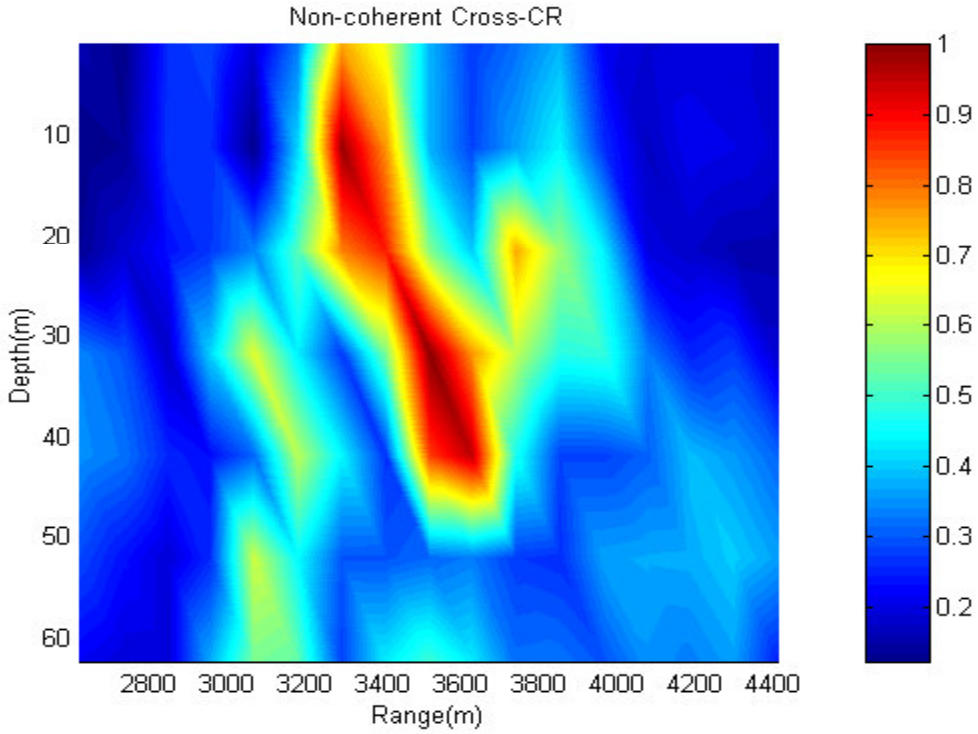

Fig. 5.88 Ambiguity surface for cross-CR processor (73-133 Hz), the enlarged part around the source

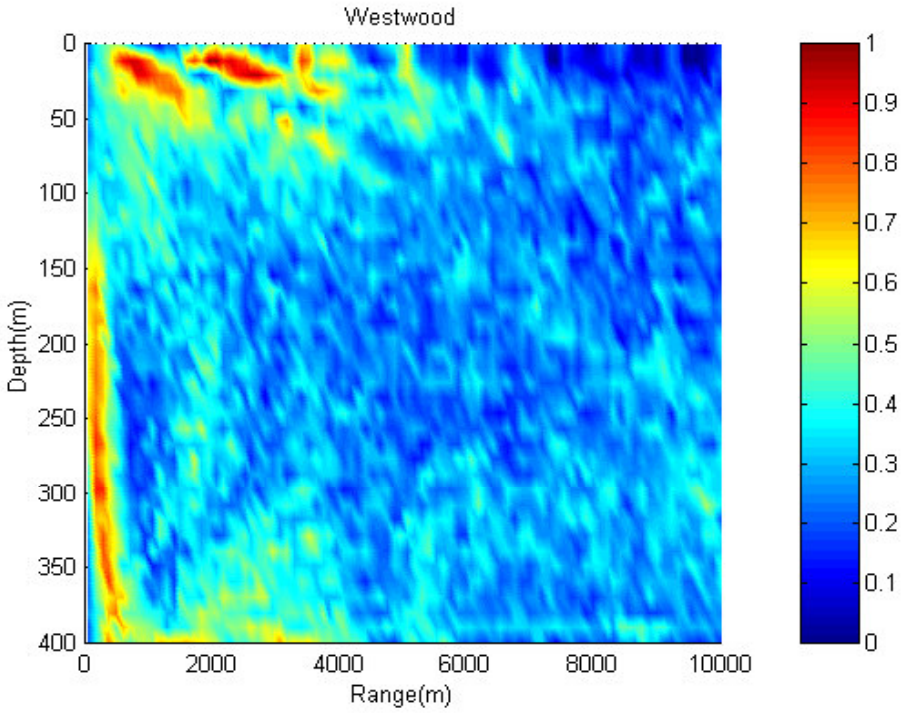

Fig. 5.89 Ambiguity surface for Westwood processor (73-133Hz)

The cross-CR has clearly localized both the ship and the towed source. The appearance of the CW source in the ambiguity surface is due to incomplete cancellation of the harmonics of the towed source in the second band. The Bartlett processor has localized the source, but with poor resolution. The main peak includes both the towed source and ship. The CR based MFPs give considerable improvement in side-lobe level reduction and sharpness of the main lobe width in comparison with that for the Bartlett MFP. The self-CR shows both CW and ship locations, but with a weak value at the ship location. The cross-CR successfully shows both ship and CW locations with strong ambiguity values. It localizes the ship at a range of 3.35km, very close to that indicated by GPS. The ship depth is estimated around 10m while we expect to have it exactly on the ocean surface. The error can be due to the poor depth resolution of the ambiguity surface and possible mismatches in the geoacoustic model. The MV-MFPs (both versions) give poor side-lobe levels. The ambiguity surfaces indicate strong levels at various locations other than the ship or CW source locations. The reason is due to the high sensitivity of MV processors to model mismatch [1]. However, the version two MV gives better performance regarding side-lobe-level than that for version one MV. The Westwood MFP has failed to localize both sources.

The reason may the non-flat spectrum of ship data, failing the requirement for the Westwood MFP.

For the third band, 150-270 Hz, highlighted in Fig. 5.90, the ambiguity surfaces of the Bartlett, MV (both versions), CR-MFPs, and the Westwood processor are given in Figs 5.91, 5.93, 5.95, 5.97, 5.99, and 5.101, respectively. In order to give better visualization of source localization, we enlarge the neighborhood around the identified sources for Bartlett, MV (both versions), self-CR, and cross-CR MFPs as shown in Figs 5.92, 5.94, 5.96, 5.98 and 5.100, respectively. The grid search dimensions are the same as for the 45 Hz and 70 Hz data.

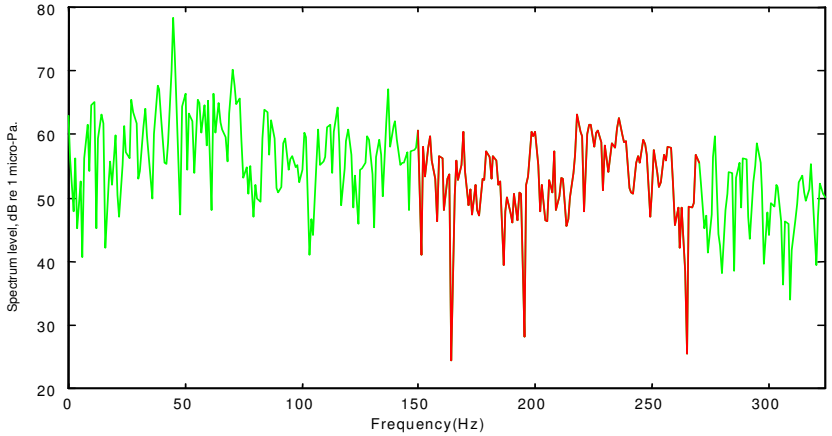

Fig. 5.90. The third band of ship data, 150-270 Hz, highlighted by red color

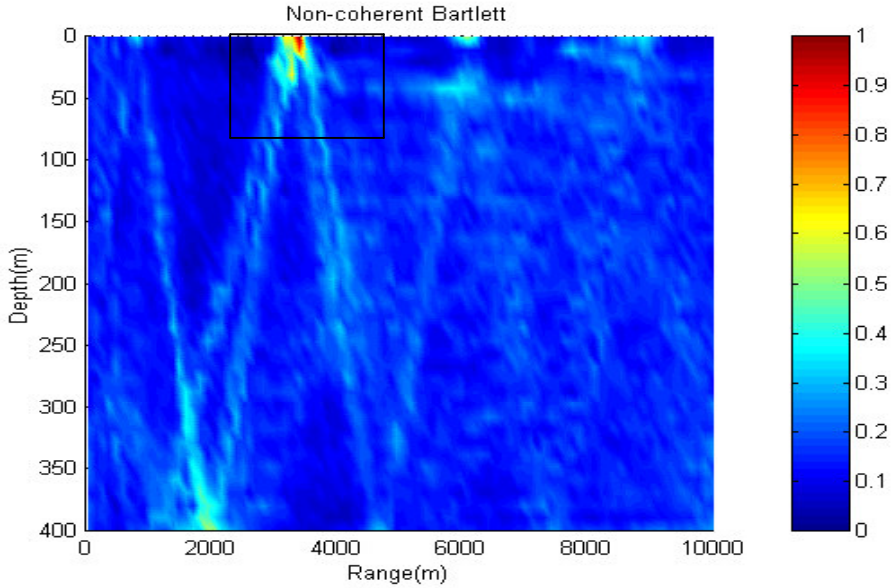

Fig. 5.91 Ambiguity surface for Bartlett processor (150-270 Hz)

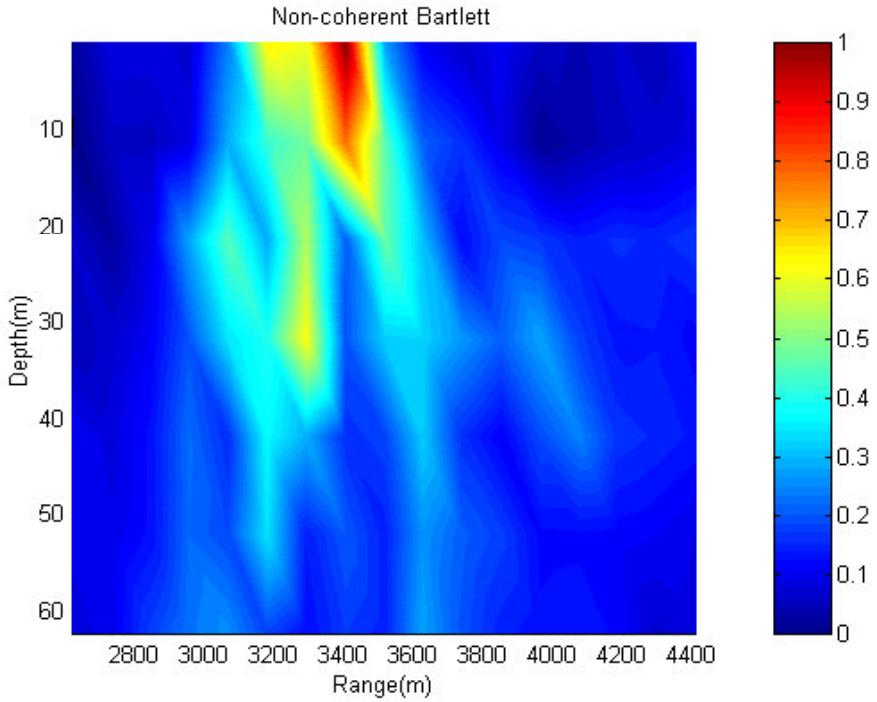

Fig. 5.92 Ambiguity surface for Bartlett processor (150-270 Hz), the enlarged part around the source

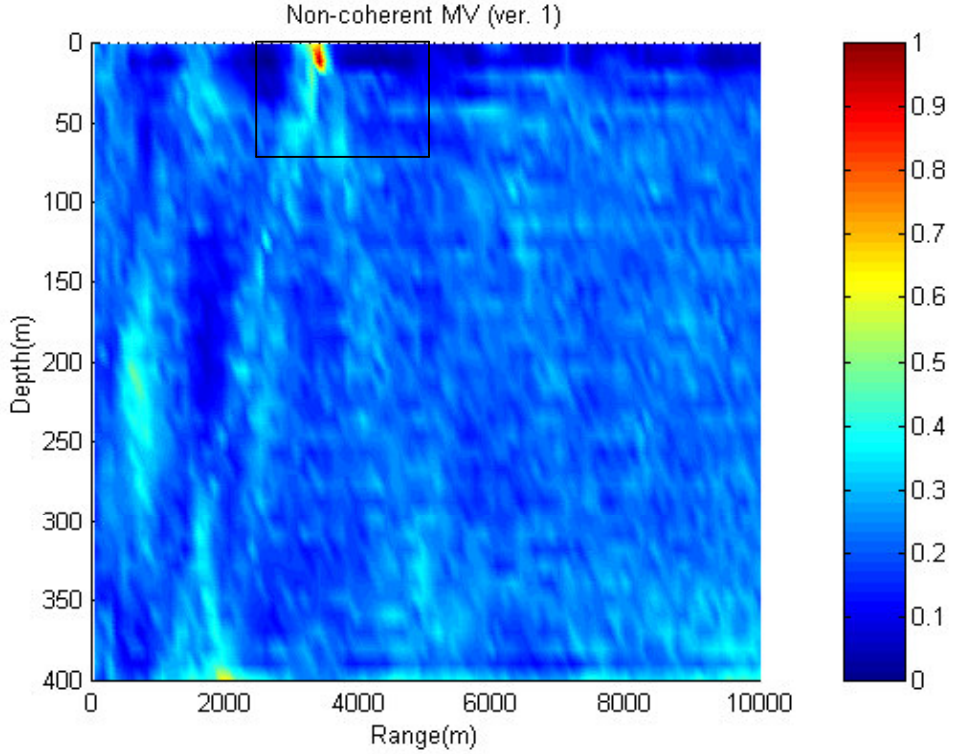

Fig. 5.93 Ambiguity surface for MV processor, version one (150-270 Hz)

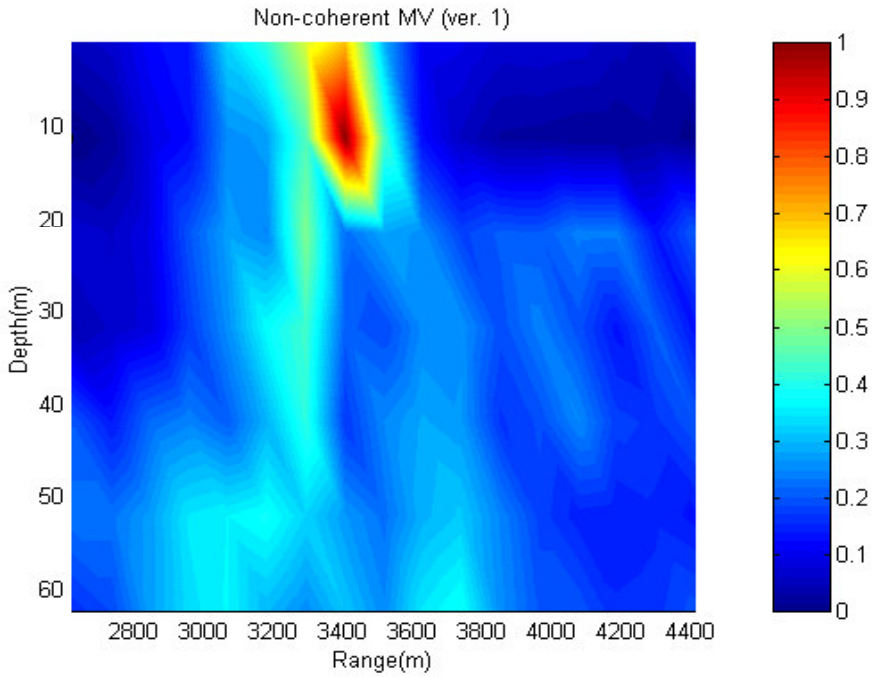

Fig. 5.94 Ambiguity surface for MV processor, version one (150-270 Hz), the enlarged part around the source

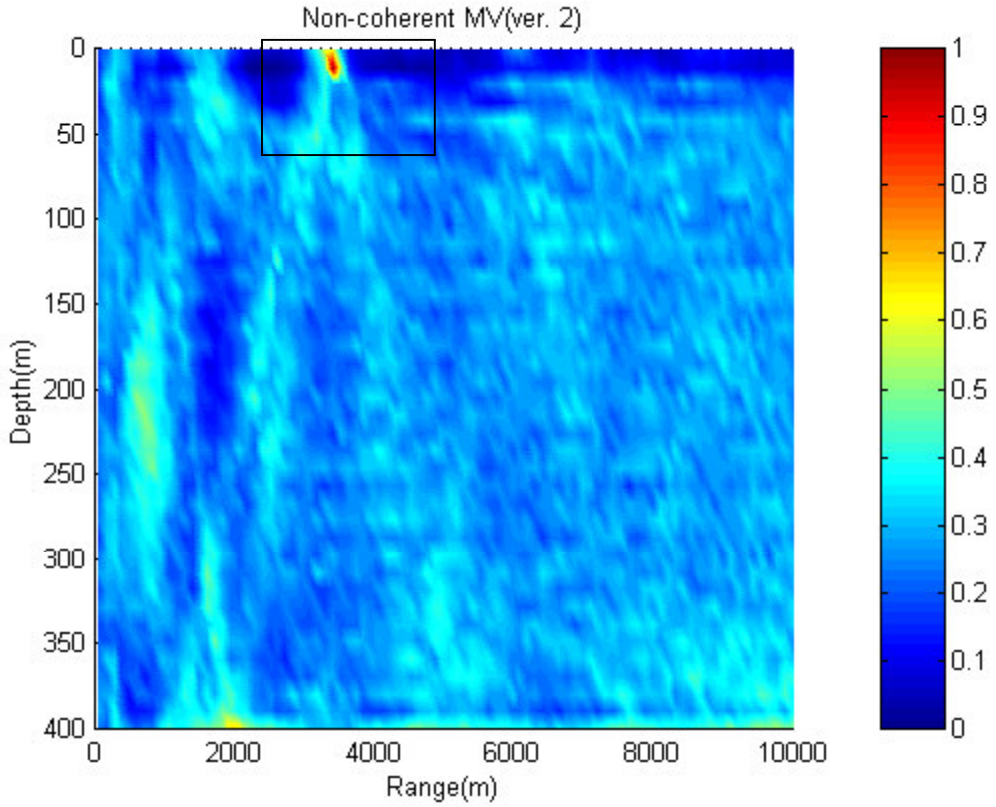

Fig. 5.95 Ambiguity surface for MV processor, version two (150-270 Hz)

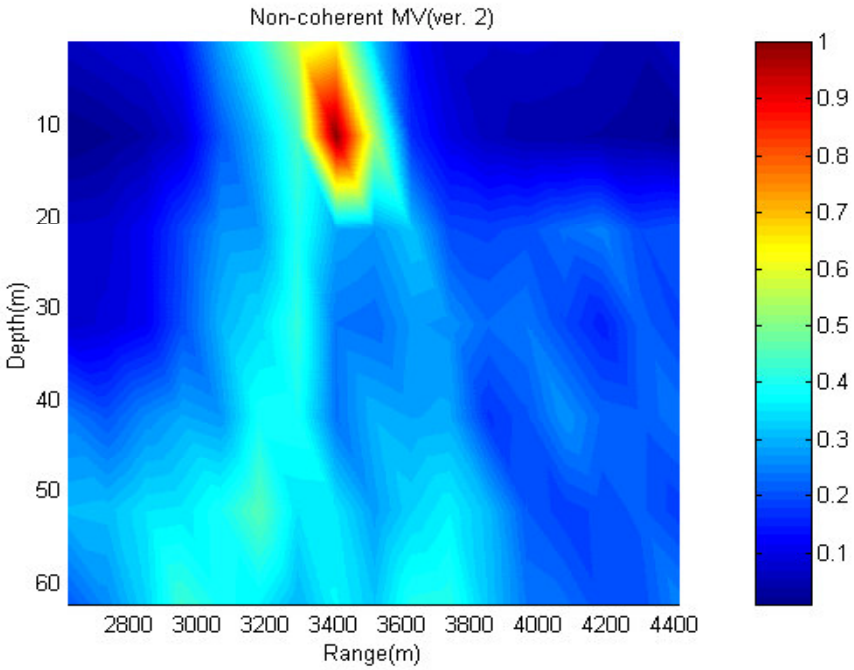

Fig. 5.96 Ambiguity surface for MV processor, version two (150-270 Hz), the enlarged part around the source

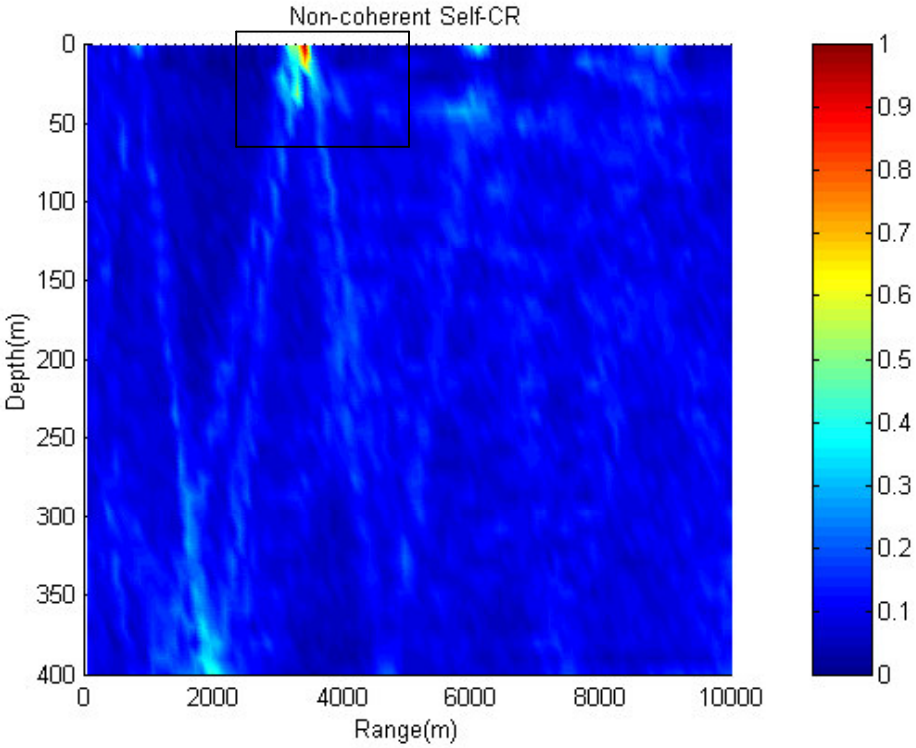

Fig. 5.97 Ambiguity surface for self-CR processor (150-270 Hz)

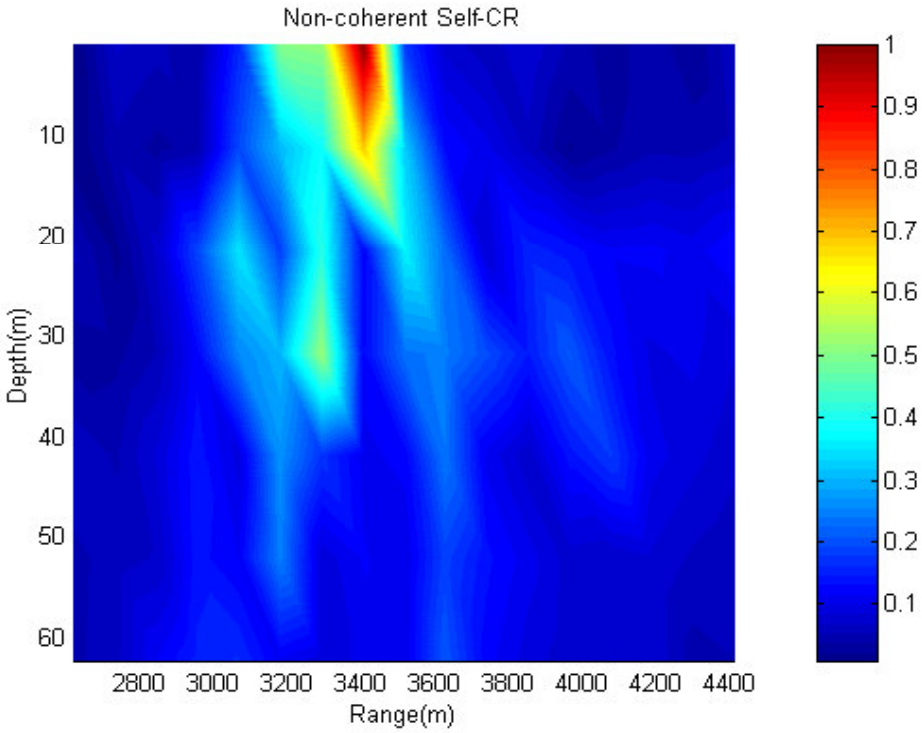

Fig. 5.98 Ambiguity surface for self-CR processor (150-270 Hz), the enlarged part around the source

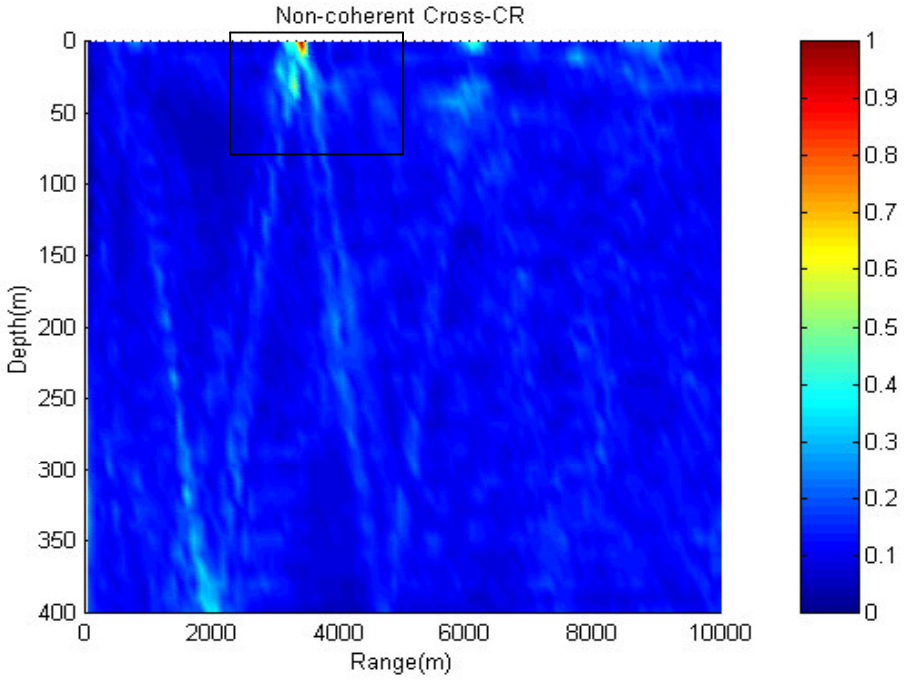

Fig. 5.99 Ambiguity surface for cross-CR processor (150-270 Hz)

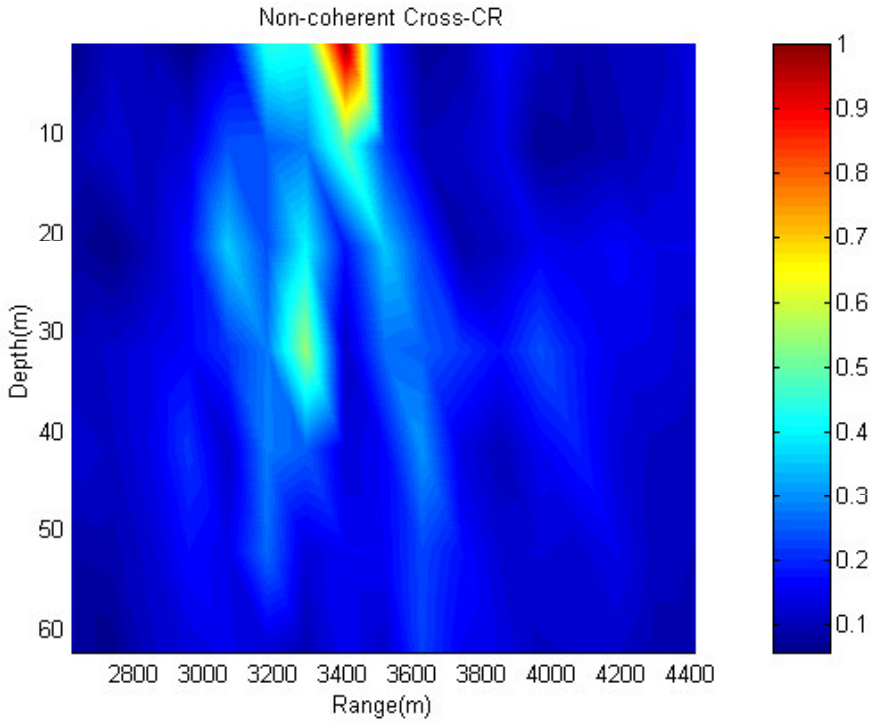

Fig. 5.100 Ambiguity surface for cross-CR processor (150-270 Hz), the enlarged part around the source

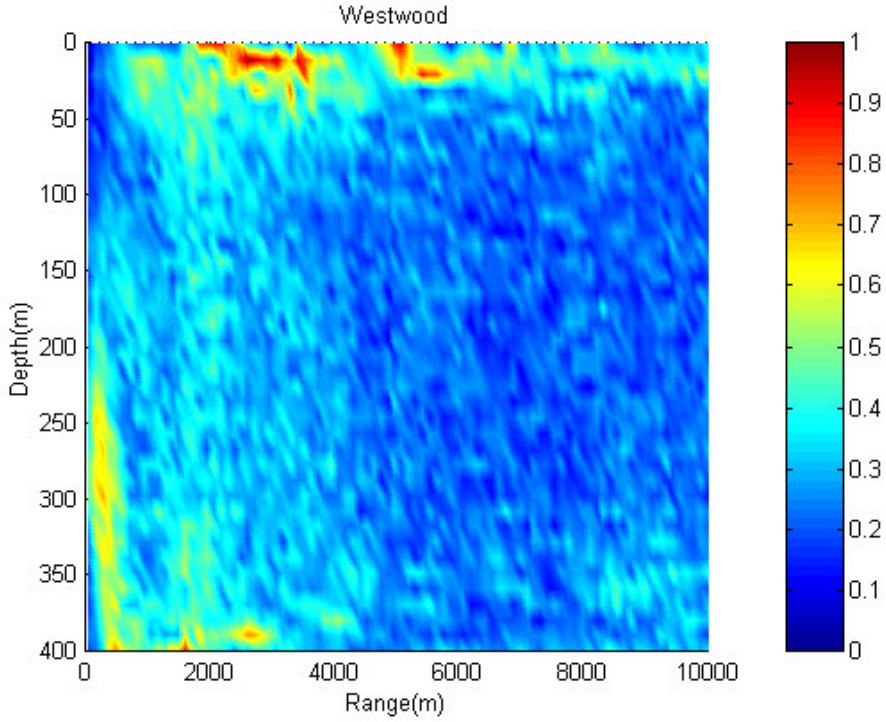

Fig. 5.101 Ambiguity surface for Westwood processor (150-270 Hz)

All processors except the Westwood processor have found the true source location, at a range of 3.35km, almost the same as by GPS, and on the ocean surface. The Bartlett and CR-MFPs give lower side-lobe-levels than those for MV-MFPs. The reason for better performance by Bartlett and MV processors in comparison to their results for the lower frequency band is likely due to the limited penetration depth in the ocean bottom at the higher frequencies in the 150-270 Hz band, where the interaction with the ocean bottom is restricted within a few wavelengths at the seafloor. Since the water depth is accurately known, the higher frequency data are less sensitive to the model mismatch. The second version of MV gives higher side-lobe-level than that for the first version of MV. The cross-CR shows slightly better performance than that for other processors with respect to the side-lobe-level and main lobe width. Again, the Westwood MFP has failed to localize sources.

5.3.2. Higher-order matched field processor

In this section we apply the higher order cross relation based MFP to localize the ship using the radiated ship data from the MEVA3 track (Fig. 5.64). The ship position from GPS data was at a range of 3.33km with a bearing of 153.27 degree to the VLA location. The analysis is carried out over 73-133 Hz with resolution 2 Hz and 150-270 Hz with resolution of 4 Hz. The replica or modeled fields used in the analysis is calculated using ORCA.

For frequency band 73-133 Hz, the 3^{rd} and 4^{th} order cross-CR MFPs are shown in Figs 5.102 and 5.103, respectively. The 3^{rd} order MFP shows a strong peak at the ship position with sidelobes around the CW source position. The 4^{th} order MFP shows a weak value at the ship position. This fact suggests that the 4^{th} order component of ship noise is not as strong as its 2^{nd} order (see Figs 5.82, 5.86, and 5.88 for Bartlett, self-CR, and cross-CR MFPs, respectively) and 3^{rd} order components in the frequency band 73-133 Hz for the MEVA3 trial. .

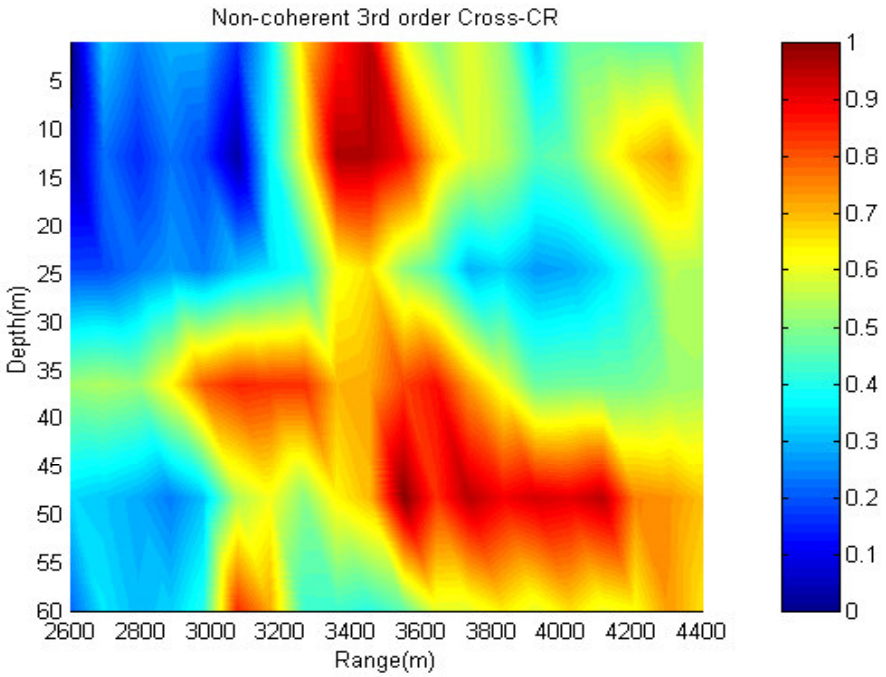

Fig. 5.102 Ambiguity surface for 3rd order cross-CR processor (73-133 Hz)

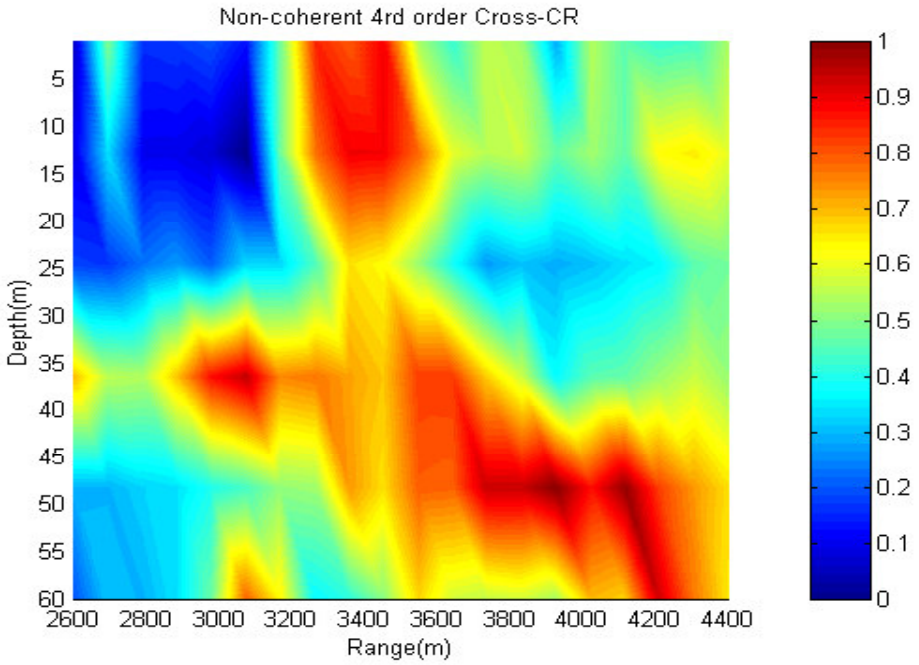

Fig. 5.103. Ambiguity surface for 4th order cross-CR processor (73-133 Hz)

For the higher frequency band of 150-270Hz, the 3rd and 4th order cross-CR MFPs are shown in Figs 5.104 and 5.105, respectively. Both figures show strong peaks at the ship position. This fact

indicates that the ship has strong component for not only second order but also third and fourth order in frequency band 150-270 Hz in comparison with other sources in the environment.

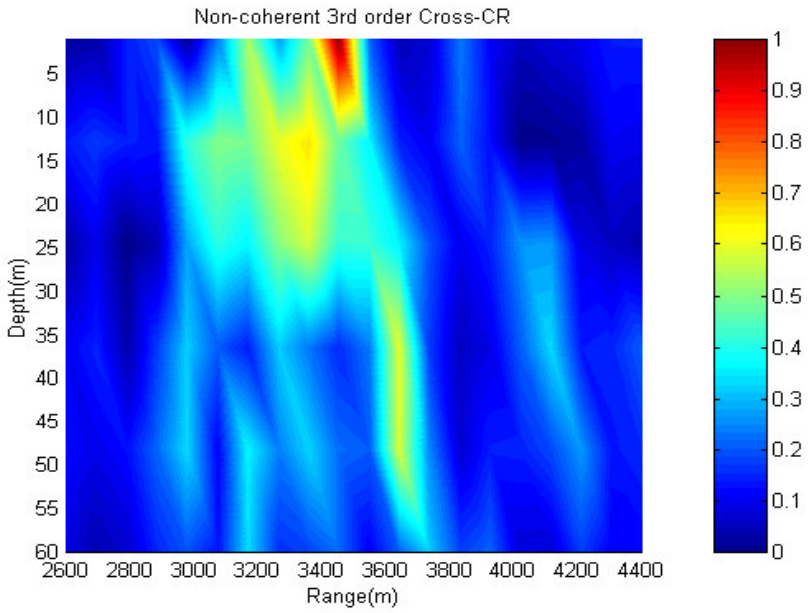

Fig. 5.104. Ambiguity surface for 3rd order cross-CR processor (150-270 Hz)

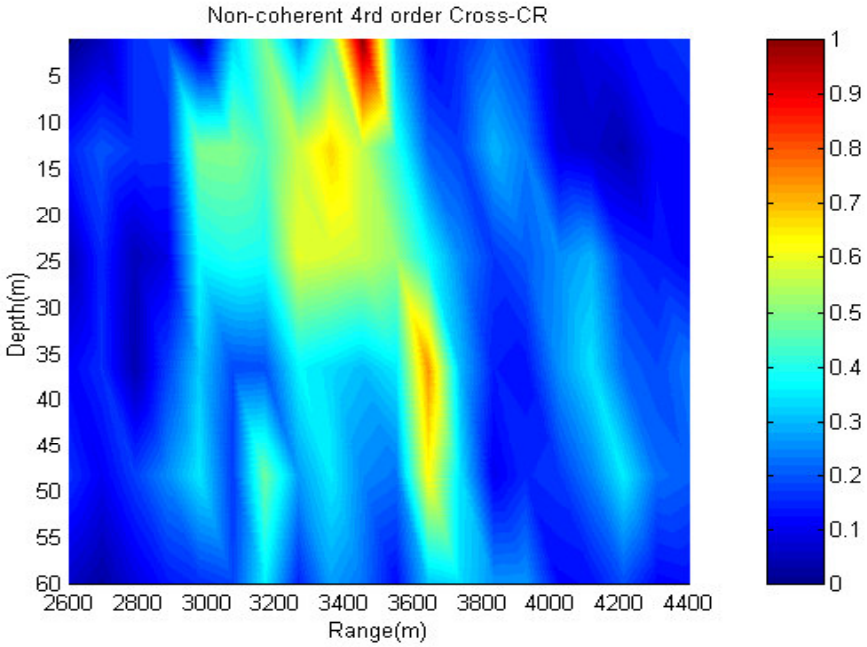

Fig. 5.105. Ambiguity surface for 4th order cross-CR processor (150-270 Hz)

Chapter Six

Geoacoustic parameter estimation, Simulation and experiment

Matched field processing has been applied to a wide variety of inverse problems in underwater acoustics [1,76]. Geoacoustic properties of the ocean bottom have been estimated by matched field inversion using acoustic field data for specific experimental geometries [77,78]. Although target localization can be carried out for an arbitrary array geometry, geoacoustic inversions have generally been done using vertical line arrays that provide a measure of the depth profile of the field in the water.

The components of the matched field inversion method include a geoacoustic model, a propagation model for calculating the acoustic field at the receiver, a cost function based on a matched field processor for asserting specific models, and an efficient search algorithm for searching the model parameter space. The inversion proceeds by specifying a set of geoacoustic models, and then searching the model parameter space to obtain the best correlation between measured and modeled acoustic fields. The practical application of the inversion depends in part on having an efficient method for searching the space of ocean bottom models.

The first investigations were carried out using continuous wave (CW) signals [6,7]. However, the use of broadband signals has been considered. Hermand and Gerstoft [8] analyzed multi-tone CW data and observed that the inversion results at single frequencies were inconsistent across the band. An incoherent average over the band was essential for producing stable geoacoustic estimates that were in agreement with ground truth data. The same erratic behavior of estimates from single frequency inversion was observed by Tolstoy [1] in her analysis of spectral components of explosive charge data, using a high resolution matched field processor. In light of these difficulties, Hannay and Chapman [9] applied a fully coherent (in frequency and space) matched field processor to the analysis of their experiment data from explosive charges. This procedure is similar to the waveform matching approach used in

seismology. The results indicated improved performance for the coherent processor over single frequency estimates. In a related study, Deane and Buckingham [10] have investigated the use of broadband noise from the sea surface in geoacoustic estimation. In this method the coherence of sea surface ambient noise measured at vertically separated sensors is used to invert properties of the sediment in shallow water. Although these studies are primarily at high frequencies (1-20 kHz), the use of background noise as the sound source is a significant result.

Successful inversion requires that the experimental geometry be accurately known. However, there is usually some degree of uncertainty in the measurement of the variables that define the experimental arrangement. In general, the inversion performance is more sensitive to mismatch in some parameters such as water depth, water sound speed, array tilt, but is relatively insensitive to parameters such as shear wave speed in ocean layers and density.

A central issue in broadband matched field inversion is the speed and efficiency of the algorithm, since replica fields must be calculated at many frequencies in the band. The search algorithm plays an important role in this issue. A straight forward way to find the best estimates of the unknown environmental parameters is to use a multidimensional grid search among possible parameter values. This search is computationally expensive, and more efficient nonlinear methods such as simulated annealing or genetic algorithms are favored. In simulated annealing the search is initiated with random values for the parameters chosen from the imposed parameter bounds; the inversion then proceeds through a series of iterations involving random perturbations of the model parameters, as a control parameter analogous to the temperature is reduced. Perturbations that decrease the cost function are accepted unconditionally. Those that increase the cost function are accepted conditionally; with probability of acceptance given by the Boltzmann distribution [79]. Genetic algorithms are based on an analogy with biological evolution. An initial population is selected randomly from all possible model parameter vectors, and the fitness of each member is computed. Through a set of evolutionary steps the initial population evolves in order to become more fit. An evolutionary step consists of selecting a parental distribution from the initial population, based on the individual's fitness. The parents are then combined in pairs; operators are applied to these pairs to form a set of children. Traditionally crossover and mutation operators have been used. Finally the children replace a

fraction of the initial population to obtain a more fit population. A description of genetic algorithm applied to the seismoacoustic parameter estimation problem is given in [6,80].

All above mentioned algorithms require a multidimensional search among the environmental parameters. We can reduce a multidimensional search to successive searches with lower dimensions by exploiting the fact that the pressure field has different sensitivities with respect to different environmental parameters. In the back wave propagation technique, we accomplish the successive search by changing the sensitivity factor in which the most sensitive environmental parameters are first estimated and then less sensitive parameters are estimated (see chapter 4). For the case where broadband sources are considered as the sound source, we can significantly reduce the search space by classifying geoacoustic parameters based on acoustic wave penetration in the ocean bottom with respect to frequency. In this procedure we first estimate environmental parameters of upper layers using high frequencies that primarily sample the sea floor environment, and then estimate parameters of deeper layers using lower frequencies.

For simplicity we use a grid search to show the efficiency of the successive search process compared to the multidimensional search process. The more sophisticated search processes such as simulated annealing and genetic algorithm can be used in the reduced dimension spaces to improve search efficiency.

In section 6.1 we consider simulation and experimental results for inversion using the back wave propagation technique. We estimate values for three model parameters, including water depth, compressional speed at the base of sediment (second) layer and the density of the sediment layer. These parameters can be classed as examples of high, medium and weak sensitivity to the ocean field.

A broadband inversion using the cross relation matched field processor (see section 3.3.2) is then considered in section 6.2. The inversion uses the ship radiated noise as a sound source to estimate the water depth, upper compressional speed of the first layer, and first layer thickness.

For both simulations and experimental results the waveguide used for the inversions presented in this chapter is that of the Pacific Shelf experiment described in chapter 5. The replica or modeled fields are calculated using the normal mode model, ORCA [15].

6.2. Back wave propagation, simulation and experiment results

6.1.1 Simulation results

In this section we present results of the analysis of data from a continuous wave (CW) source which was at a depth of 25 m and towed along an arc of a distance of 5.6 km from the vertical array, the same position of the true source in real data that will be used in section 6.1.2. The geoacoustic model is shown in Fig. 6.1.

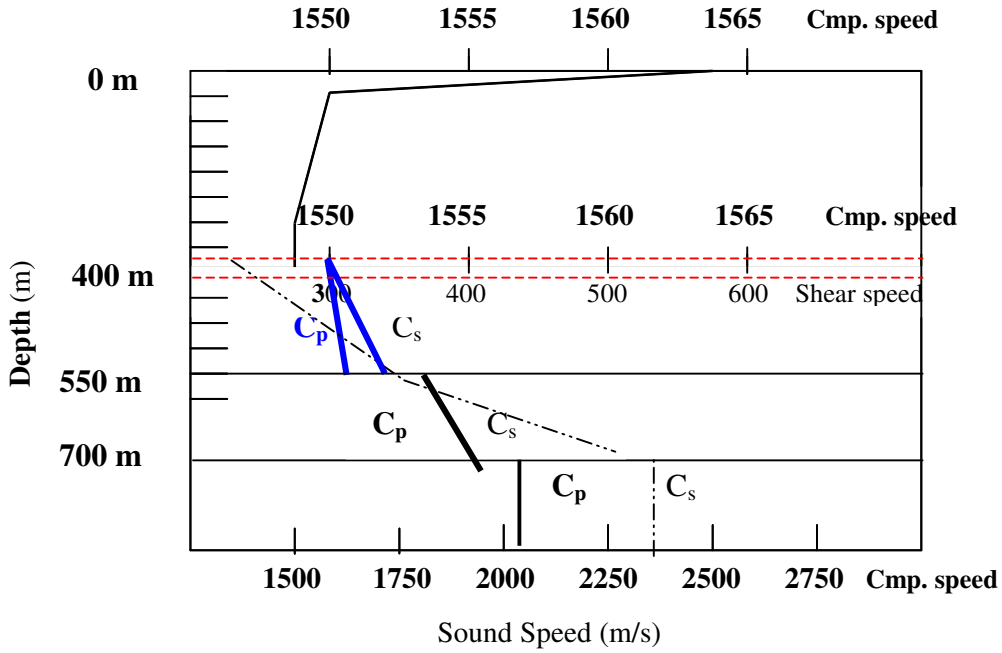

Fig 6.1 The sound speed profiles used in the environmental model. The shear speed, C_s (dot-dashed) and the compressional speed, C_p (dark and solid) are shown on the three lower abscissa scales

We estimate values for three of the model parameters including water depth (its uncertainty is shown with dashed red line), compressional speed at the base of the first sediment layer (shown with dashed blue line) and the density of the sediment layer. The bounds for the values of these parameters and the nominal values of the other fixed parameters were obtained from the literature [60]. These parameters can be classed in terms of high, medium and weak sensitivity to the ocean field. The true values for the water depth was 395 m, for the sediment compressional speed, 1692 m/s, and for the density, 1.5 gm/cm^{-3}. The SNR=20dB and the source emitted a tone at 45 Hz.

In Fig. 6.2 the 45-Hz ambiguity surface obtained using the BWP technique with nominal values of the adjustable environmental parameters is shown over the full range-depth search space. The value of α is equal to one. The peak of the ambiguity surface is located at the true source position.

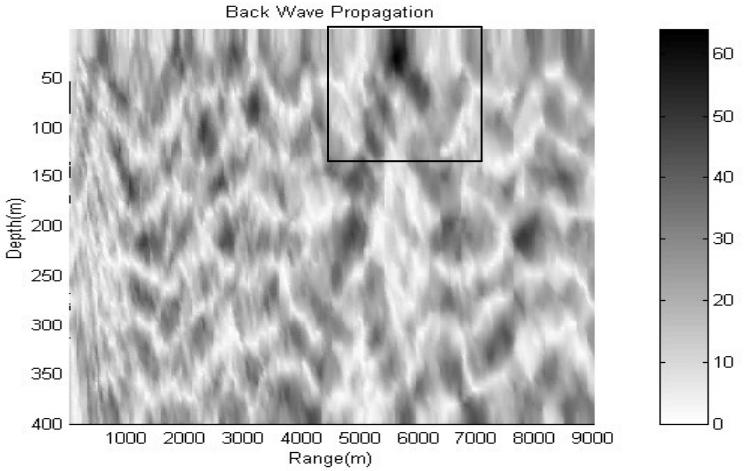

Fig.6.2 The 45-Hz ambiguity surface obtained from BWP technique on full range-depth space with α=1

A direct way to find the best estimates of the three unknown environmental parameters is to use a 3-dimensional grid search among possible parameter values. This search is computationally expensive. If the parameters are not strongly correlated, we can reduce the 3-dimensional search to three 1-dimensional searches by exploiting the fact that the pressure field has different sensitivity with respect to the parameters. The pressure field is most sensitive to the water depth, while for α=1 the field is only weakly sensitive to changes with respect to compressional speed and density changes. We first estimate the water depth and then search among potential values of compressional speed, using a value of α=2. For this value of α the sensitivity to density remains low. At the last step we increase the sensitivity factor to α=4 to estimate the density. This three-step technique is efficient computationally and effective in providing realistic estimates. We use the focal function as the best match criterion (see chapter 4).

We start the procedure by defining a window around the source location from ranges between 4.5 km and 7 km and depths between 1 m and 100 m. The search over water depth values between 350 m and 440 m with a resolution of 5 m is shown in Fig. 6.3. The sharpest focus of the main peak is obtained for a depth of 395 m, as indicated by the minimum in the normalized

BWP focal function curve. The BWP ambiguity surface with the adjusted water depth (395m) is shown in Fig. 6.4.

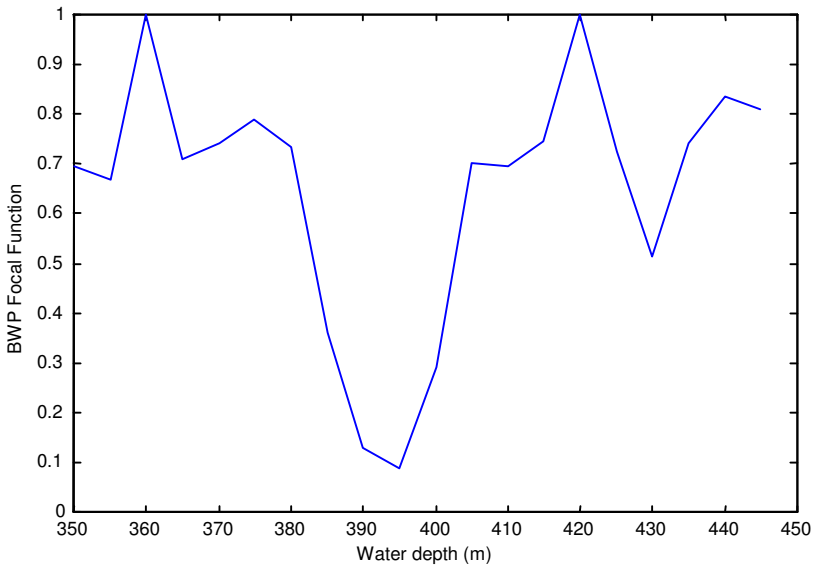

Fig. 6.3 The BWP focal function for different water depth values between 350 m and 440 m with resolution 5 m (α=1)

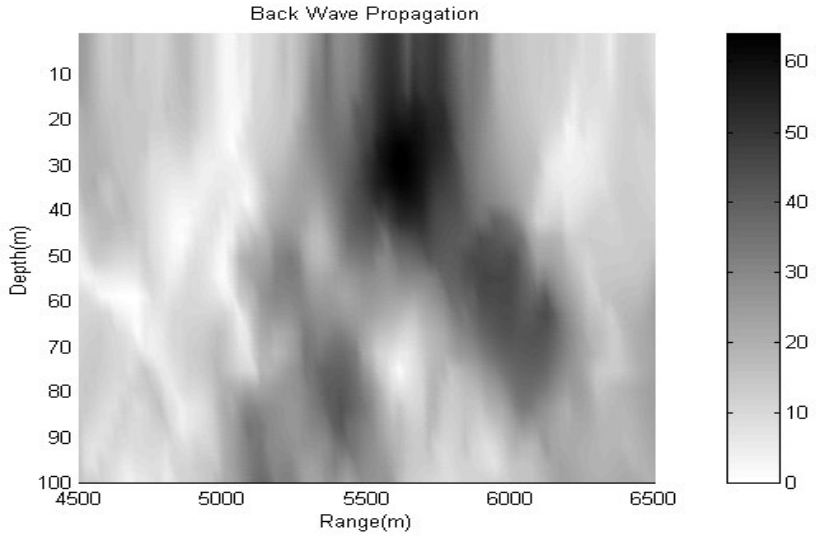

Fig.6.4 The 45-Hz ambiguity surface obtained from BWP technique on a window around the source location with α=1 after adjusting water depth

In the next step, we change compressional speed from 1680 m/s to 1715 m/s with 2 m/s resolution, using α=2. The normalized BWP focal function shows a minimum value at 1692-

m/s. The curve (solid line) is shown in Fig. 6.5, where we also have shown the result for α=1. This curve shows small change with respect to speed, and justifies our assumption in using the sequential search procedure. The BWP ambiguity surface with the adjusted water depth and compressional speed is shown in Fig. 6.6. It shows a more concentrated energy point around true source location, a result that we showed in the chapter 4

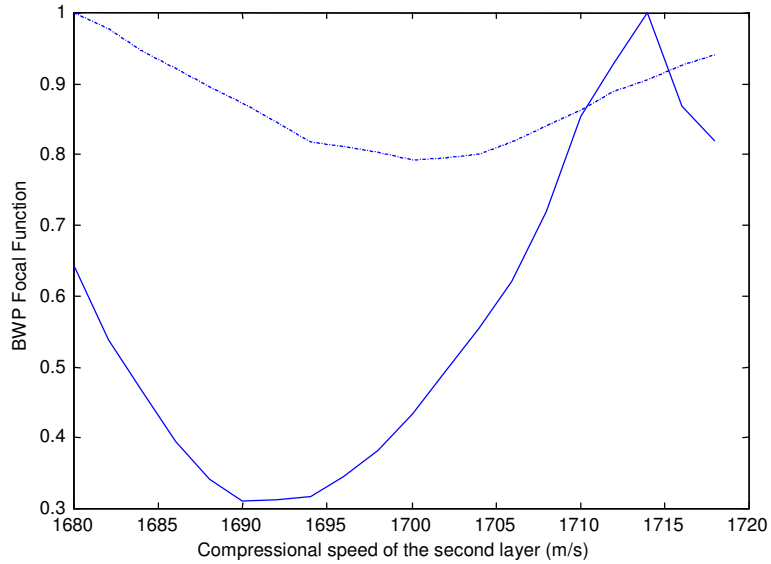

Fig. 6.5 The BWP focal function for different compressional speed values between 1680 m/s and 1715 m/s with resoution 2 m/s with α=2 (solid) and α=1 (dashed)

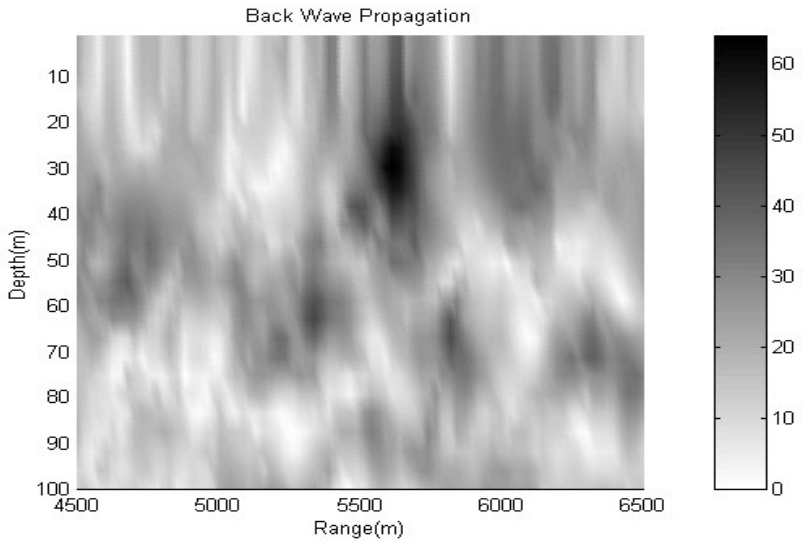

Fig. 6.6 The 45-Hz ambiguity surface obtained from BWP technique on a window around the source location with α=2 after adjusting water depth and compressional speed

In the final step we change the density value from 1.15 g/cm^{-3} to 2.1 g/cm^{-3} with 0.05 g/cm^{-3} resolution with α=4. The normalized BWP focal function shows a minimum value at 1.5 g/cm^{-3}. This result (solid line) is shown in Fig. 6.7, where we also have shown BWP focal function changes for α=2 (dash-dot line) and α=1 (dotted line). These curves show small changes with respect to density changes, as required for the sequential search procedure. The inversion was successful in recovering the true values for each of the parameters that were searched and the BWP ambiguity surface with the adjusted water depth and compressional speed and density values is shown in Fig. 6.8. It shows a highly concentrated energy point around true source location.

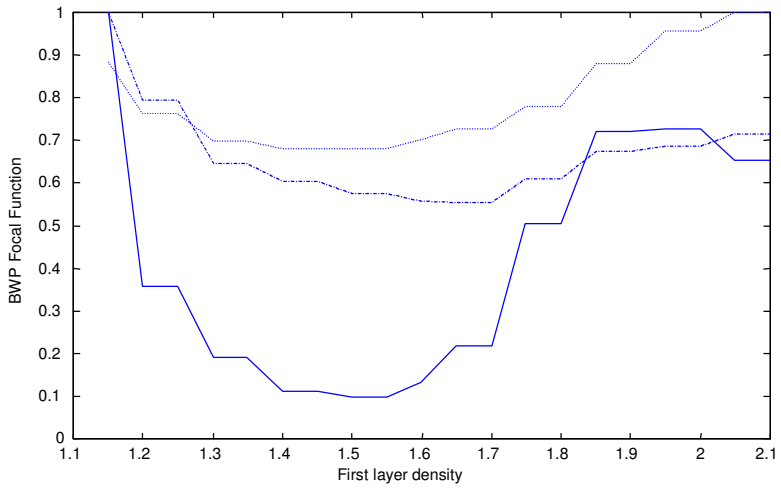

Fig. 6.7. The BWP criterion for different density values between 1.15 g/cm^{-3} to 2.1 g/cm^{-3} with 0.05 g/cm^{-3} resolution α=4 (solid) and α=1 (dotted) and α=2 (dash-dot line)

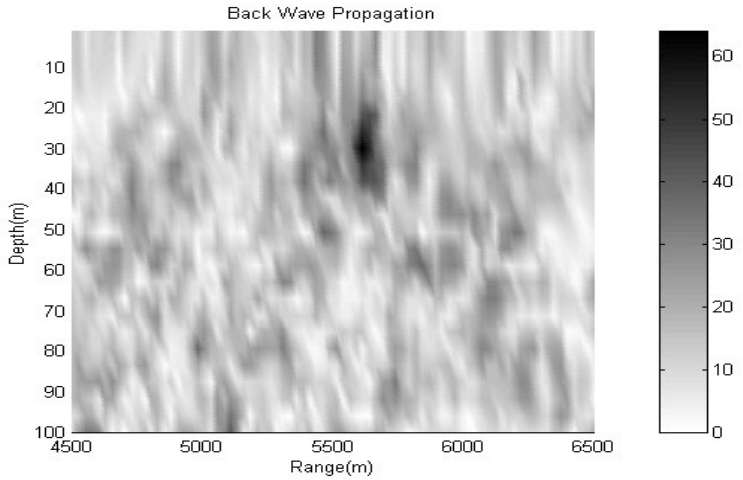

Fig. 6.8 The 45-Hz ambiguity surface obtained from BWP technique on a window around the source with α=4 with adjusted water depth and compression speed and density.

6.1.2 Experimental results

In this section we apply the phase regulated BWP to data collected in shallow water off Vancouver Island, BC, Canada, well known as trial MEVA3 (see chapter 5).

We present results of the analysis of real data from a continuous wave (CW) source which was towed at a depth of 25 m along an arc of a distance 5.6 km from the array. The source and receiver positions were recorded by GPS (global position system), which has an error of ~100 m. The CW source emitted a tone at 45 Hz and the data were collected at a sampling rate of 1500 Hz. The geoacoustic model is shown in Fig. 6.1. We follow the same procedure as we did in simulation to estimate the unknown environmental parameters including water depth, compressional speed at the base of the second layer and the density of the sediment layer. These parameters are the same parameters as we investigated in the simulation. In Fig. 6.9 the 45-Hz ambiguity surface with nominal values of the adjustable environmental parameters is shown. The value of α is equal to one. The peak of the ambiguity surface is located close to the true source position. However, the ambiguity surface shows higher side-lobe level than that in the simulation due to mismatch between model and environmental parameters.

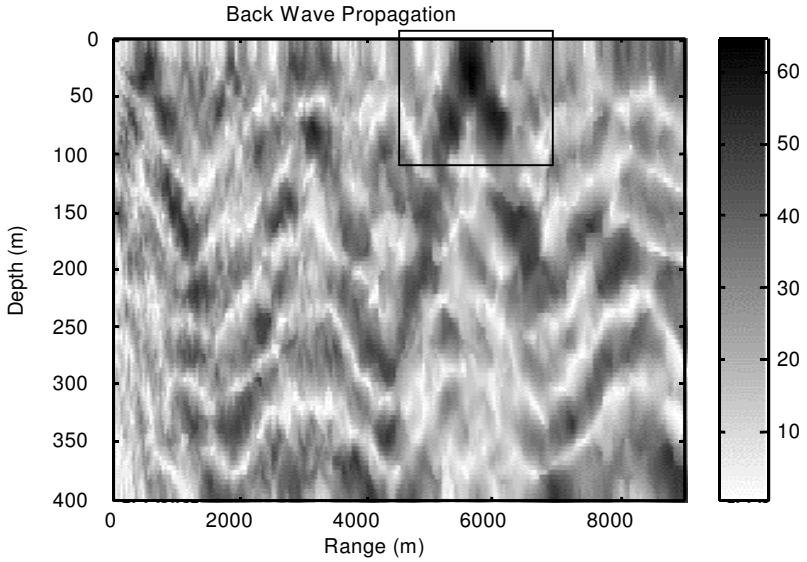

Fig.6.9. The 45-Hz ambiguity surface obtained from BWP technique on full range-depth space with α=1

We start the procedure by searching over water depth values between 350 m and 440 m with a resolution of 5 m is shown in Fig. 6.10. We use the focal function as the best match criterion (see

chapter 4). The sharpest focus of the main peak is obtained for a depth of 395 m, as indicated by the minimum in the normalized BWP focal function curve. The minimum point is higher than the corresponding minimum point for the simulation (see Fig. 6.3) due to mismatch between model and environmental parameters for the MEVA3 trial site. The BWP ambiguity surface with the adjusted water depth (395 m) is shown in Fig. 6.11, with higher side-lobe level than that in simulation (see Fig. 6.4).

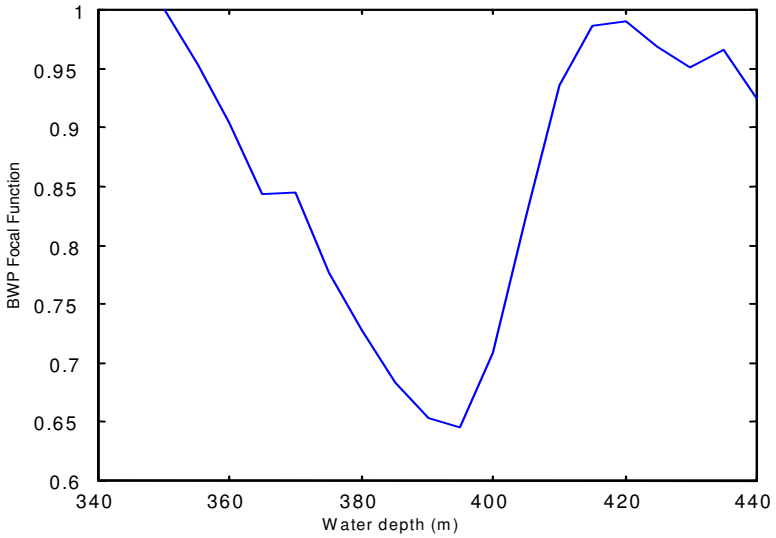

Fig. 6.10 The BWP focal function for different water depth values between 350 m and 440 m with resolution 5 m (α=1)

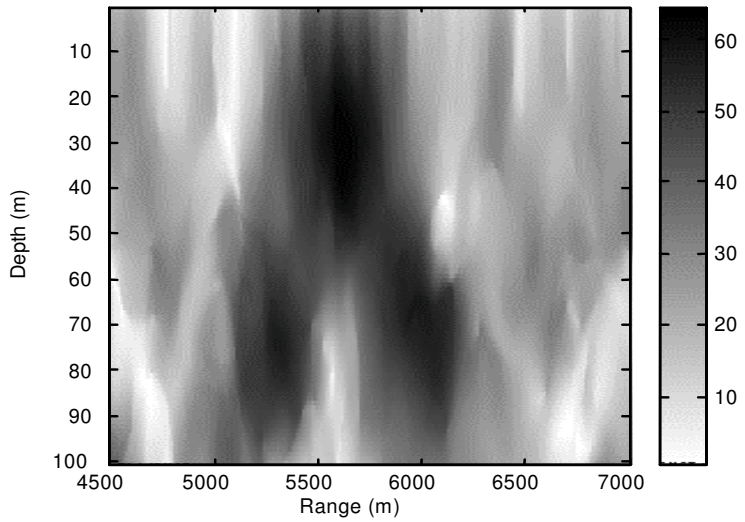

Fig. 6.11 The 45-Hz ambiguity surface obtained from BWP technique on a window around the source location with α=1 after adjusting water depth

Now, we change compressional speed from 1680 m/s to 1710 m/s with 2 m/s resolution, using α=2. The normalized BWP focal function shows a minimum value at 1692 m/s. The curves are shown in Fig. 6.12 for α=2 (solid line) and α=1 (dotted line). The BWP ambiguity surface with the adjusted water depth and compressional speed is shown in Fig. 6.13 with higher side-lobe level than that from the simulation.

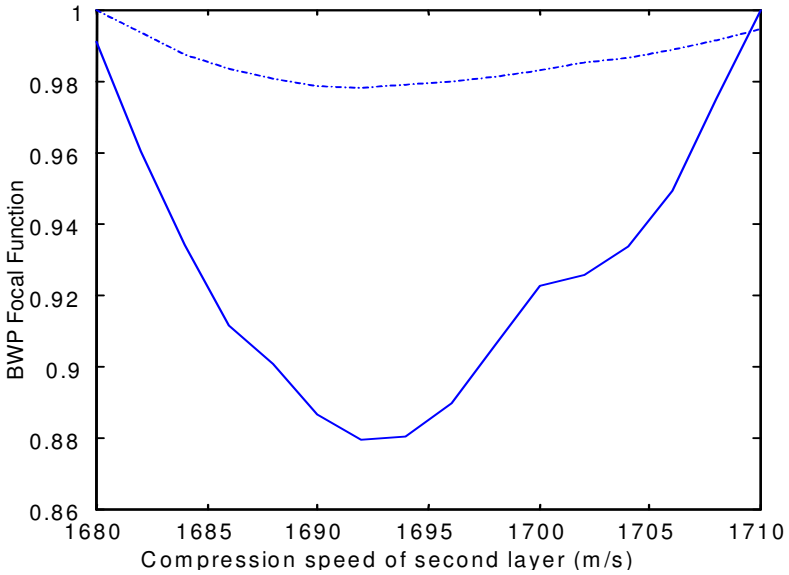

Fig. 6.12. The BWP focal function for different compressional speed values between 1680 m/s and 1710 m/s with resoution 2 m/s with α=2 (solid) and α=1 (dotted)

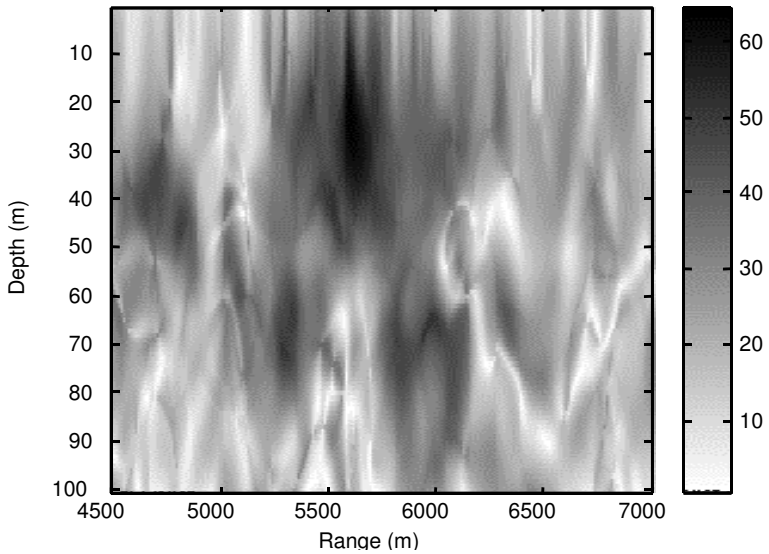

Fig. 6.13. The ambiguity surface with α=2 after adjusting water depth and compressional speed

We change the density value from 1.35 g/cm^{-3} to 1.9 g/cm^{-3} with 0.05 g/cm^{-3} resolution with α=4. The normalized BWP focal function shows a minimum value at 1.5 g/cm^{-3}. The curves for α=4 (solid line), α=2 (dashed line), and α=1 (dotted line) are shown in Fig. 6.14. The ambiguity surface with the adjusted parameters is shown in Fig. 6.15.

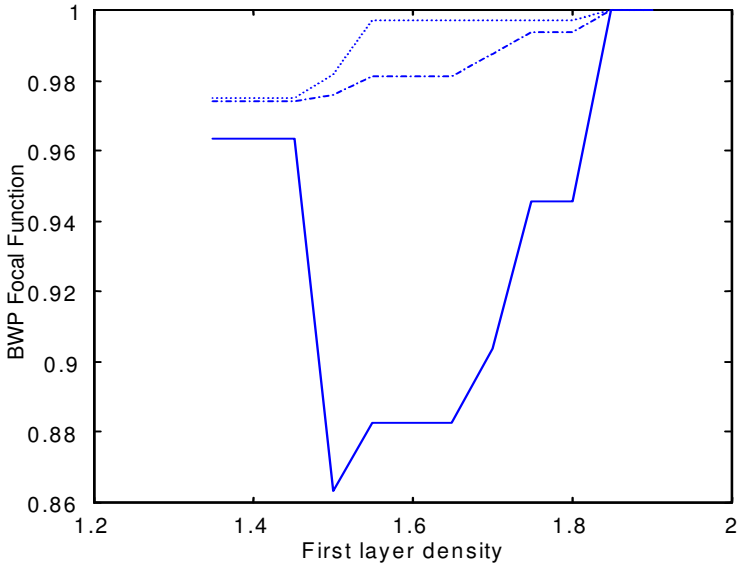

Fig. 6.14 The BWP criterion for different density values between 1.35 g/cm^{-3} to 1.9 g/cm^{-3} with 0.05 g/cm^{-3} resolution α=4 (solid) and α=1 (dotted) and α=2 (dash-dot line)

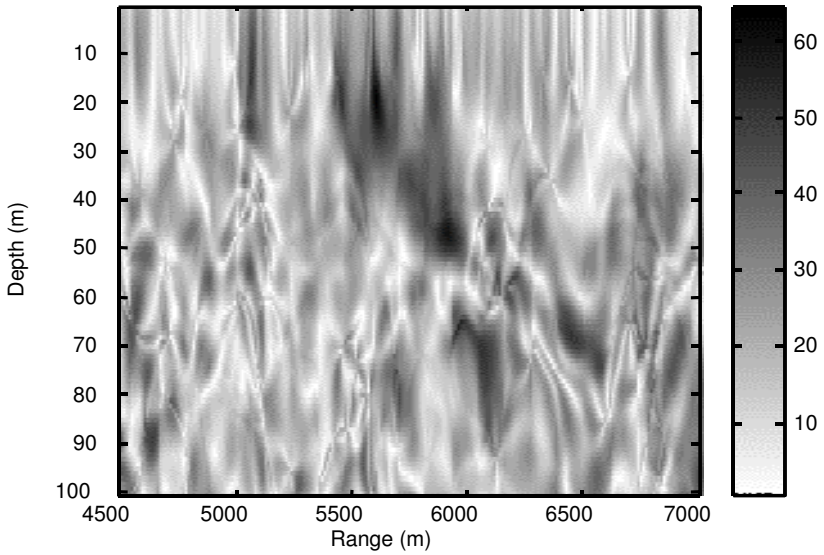

Fig. 6.15 The 45-Hz ambiguity surface obtained from BWP technique on a window around the source with α=4 with adjusted water depth and compression speed and density.

6.3 Broadband inversion using the cross-relation based matched field processor

In this section we apply a broadband inversion procedure to data collected in shallow water off Vancouver Island, BC, Canada (MEVA3 trial), using the cross relation MFP. We present results of the analysis of real data from a ship that was located at an arc of a distance 3.3 km from the array. The geoacoustic model is shown in Fig. 6.16.

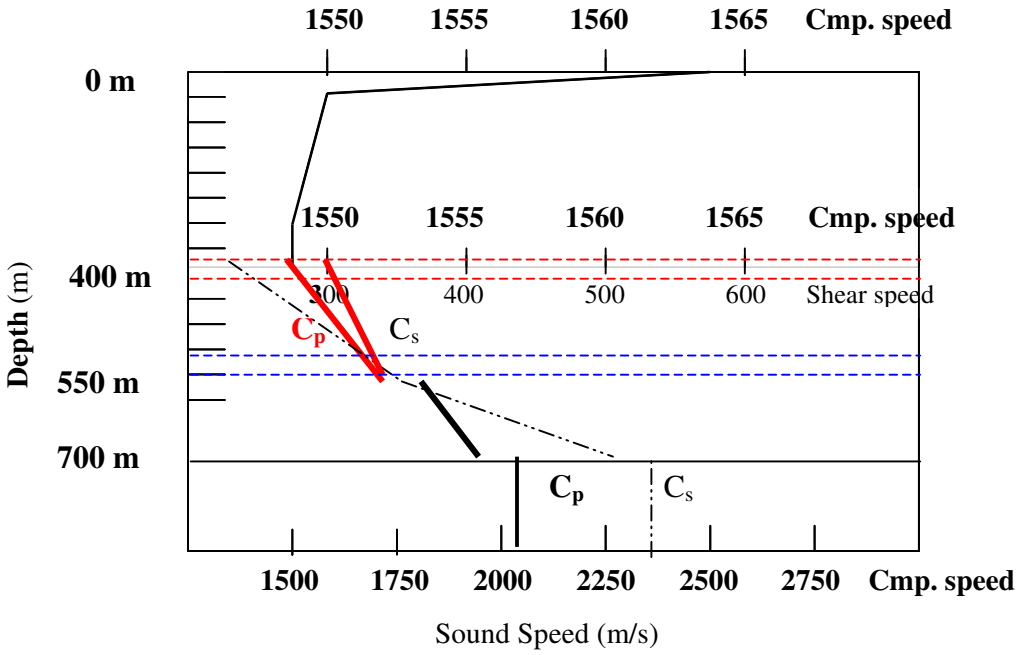

Fig. 6.16. The sound speed profile used in the environmental model. The shear speed C_s (dot-dashed) and the compressional speed C_p (solid) are shown on the three lower abscissa scales

We estimate values for three of the model parameters including water depth (its uncertainty is shown with dashed red line), compressional speed at the top of the first layer of sediment (shown by the bold dashed red line) and the first layer thickness (shown with the dashed blue line). The bounds for the values of these parameters and the values of the other fixed parameters were obtained from the literature [60]. The inversion uses the broadband ship noise as the sound source. We can reduce the dimension of the search space by classifying the unknown geoacoustic parameters based on the acoustic wave penetration in the ocean bottom with respect

to frequency. We first estimate the water depth and upper compressional speed of the first layer using the frequency band 190-270 Hz and then estimate the first layer thickness using the frequency band 73-133 Hz in a two-step process. We compare results obtained using the focal function criterion for the best match with those obtained using a criterion which searches for the maximum value of the ambiguity function at the source location.

In Fig. 6.17 the ambiguity surface for the 190-270 Hz band with nominal values of the adjustable environmental parameters is shown.

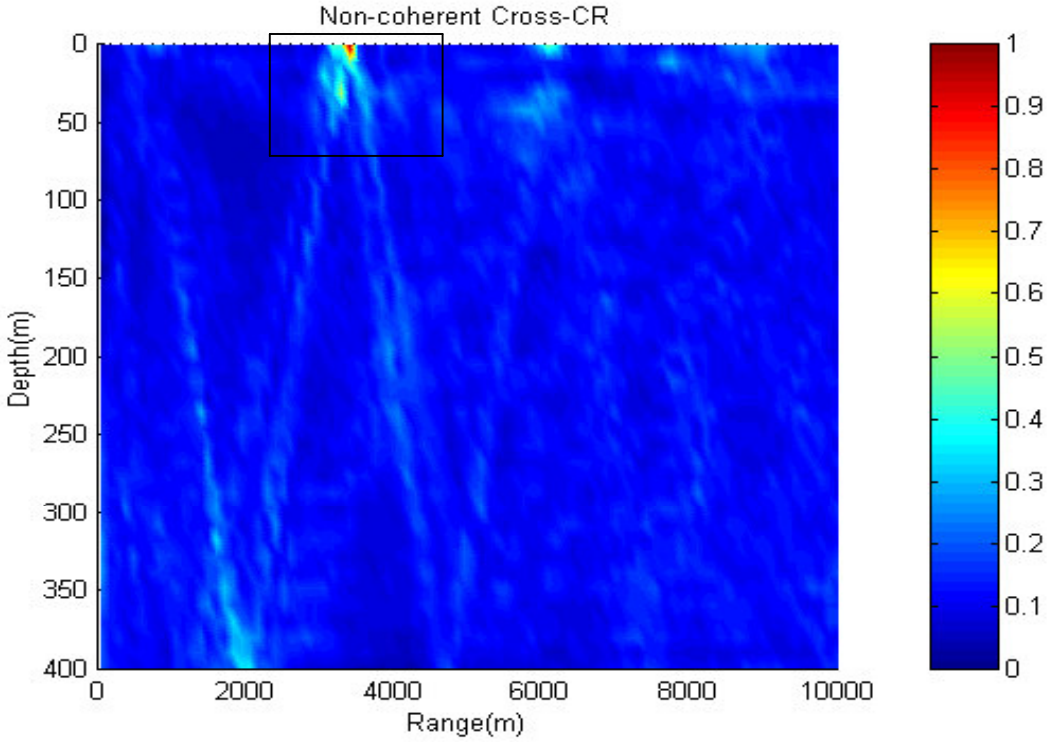

Fig.6.17 The 190-270-Hz ambiguity surface obtained from cross CR-MFP n full range-depth space with nominal parameter values

We search the values for the water depth and upper compressional speed of the first layer among 30 possible search points. The two-dimensional search ranges are 370-420 m with resolution of 10m for the water depth, and 1510-1590 m/s with resolution of 20 m/s for the compressional speed. For a window around the source location from ranges between 3 km and 4 km and depths between 1 m and 60 m, the result is shown in Fig. 6.18.

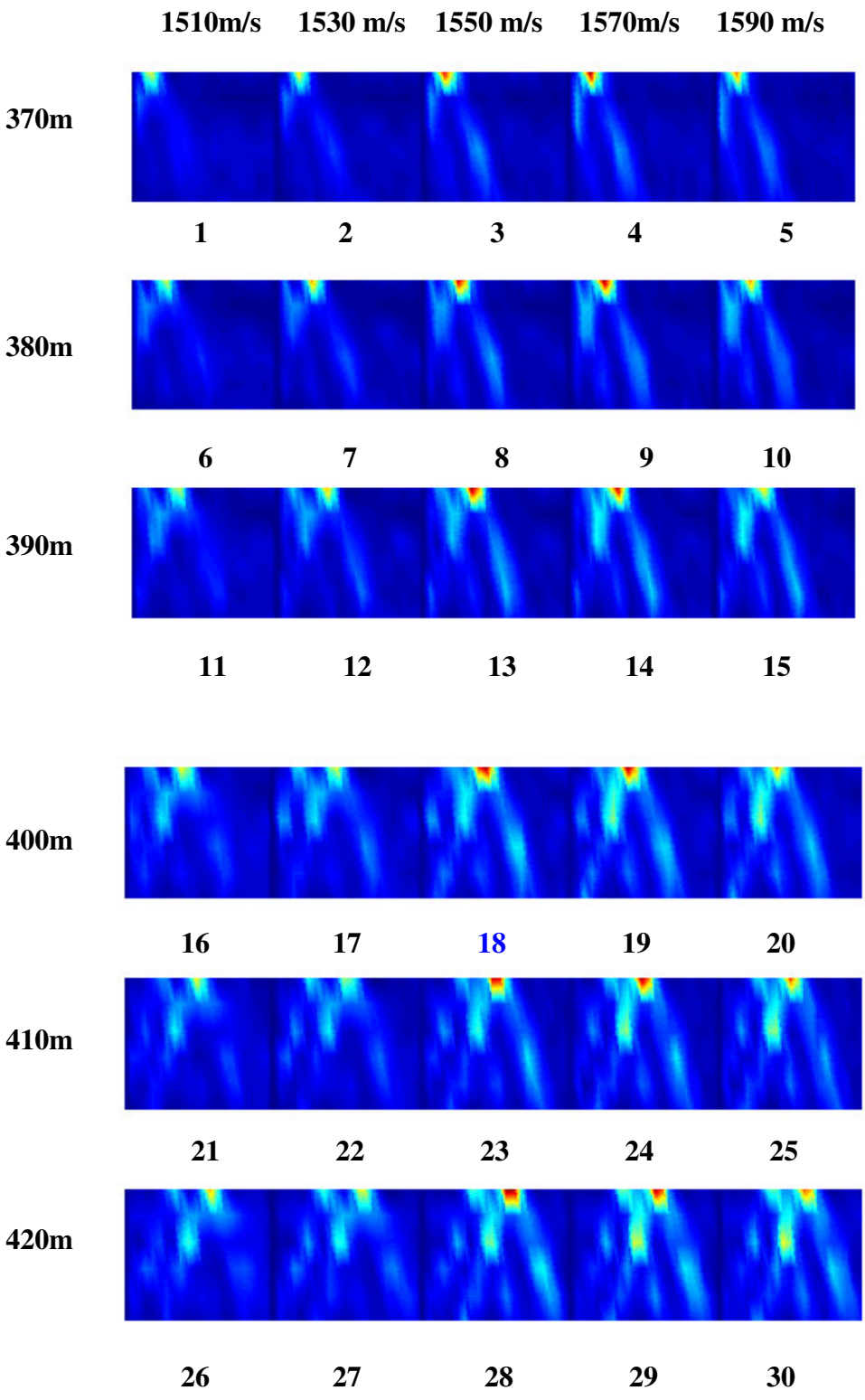

Fig.6.18. The 190-270-Hz ambiguity surface at a window around true source location for 30 search points for water depth and upper compressional speed of the first layer of sediment

The focal function and ambiguity values at the source position are shown in Figs 6.19 and 6.20, respectively for 30 search points. Both criteria show the minimum at point 18 that corresponds to water depth of 400 m and compressional speed of 1550 m/s. The estimated water depth is close to the value obtained from BWP technique, i.e. 395 m, that was obtained using a different data set corresponding to a greater range of 5.6 km along the experimental track. The estimated compressional speed is close to the value obtained by ground truth data that is 1550 m/s from a seismic experiment in the region [60].

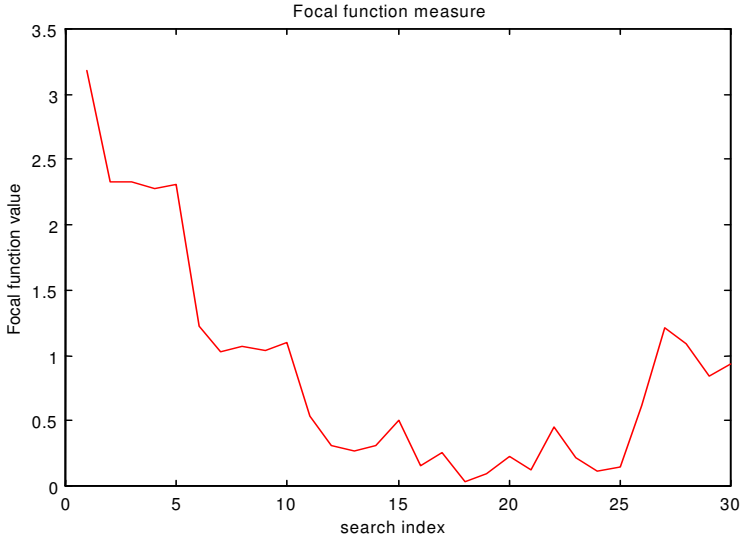

Fig. 6.19 The focal function with respect to search index for water depth and the upper compressional speed of the first layer

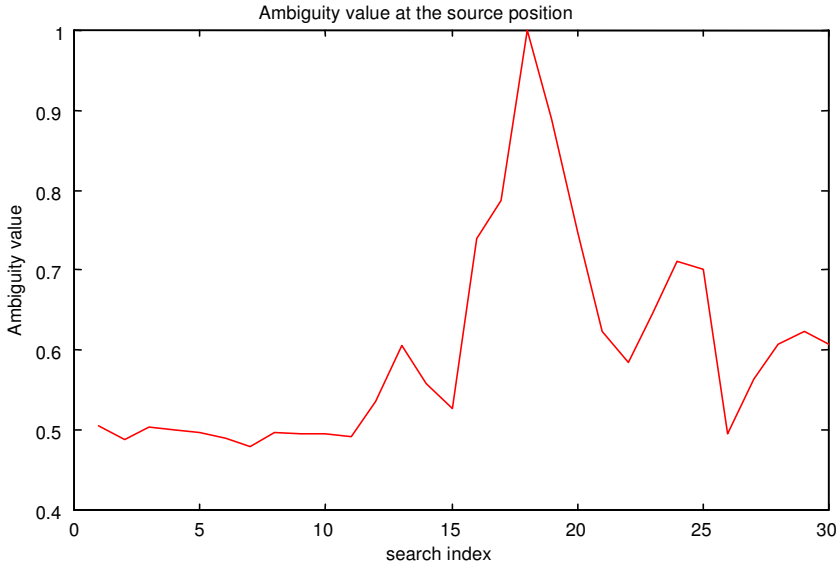

Fig. 6.20 The ambiguity value at the source location with respect to search index for water depth and the upper compressional speed of the first layer

The variation of the first layer thickness has little effect on the pressure field in the frequency band 190-270 Hz and consequently on matched field processor. In order to show this fact, we search the first layer thickness from 50 m to 250 m with a resolution of 10 m in frequency band of 190-270 Hz. For a window around the source location from ranges between 3 km and 4 km and depths between 1 m and 60 m, the result is shown in Fig. 6.21.

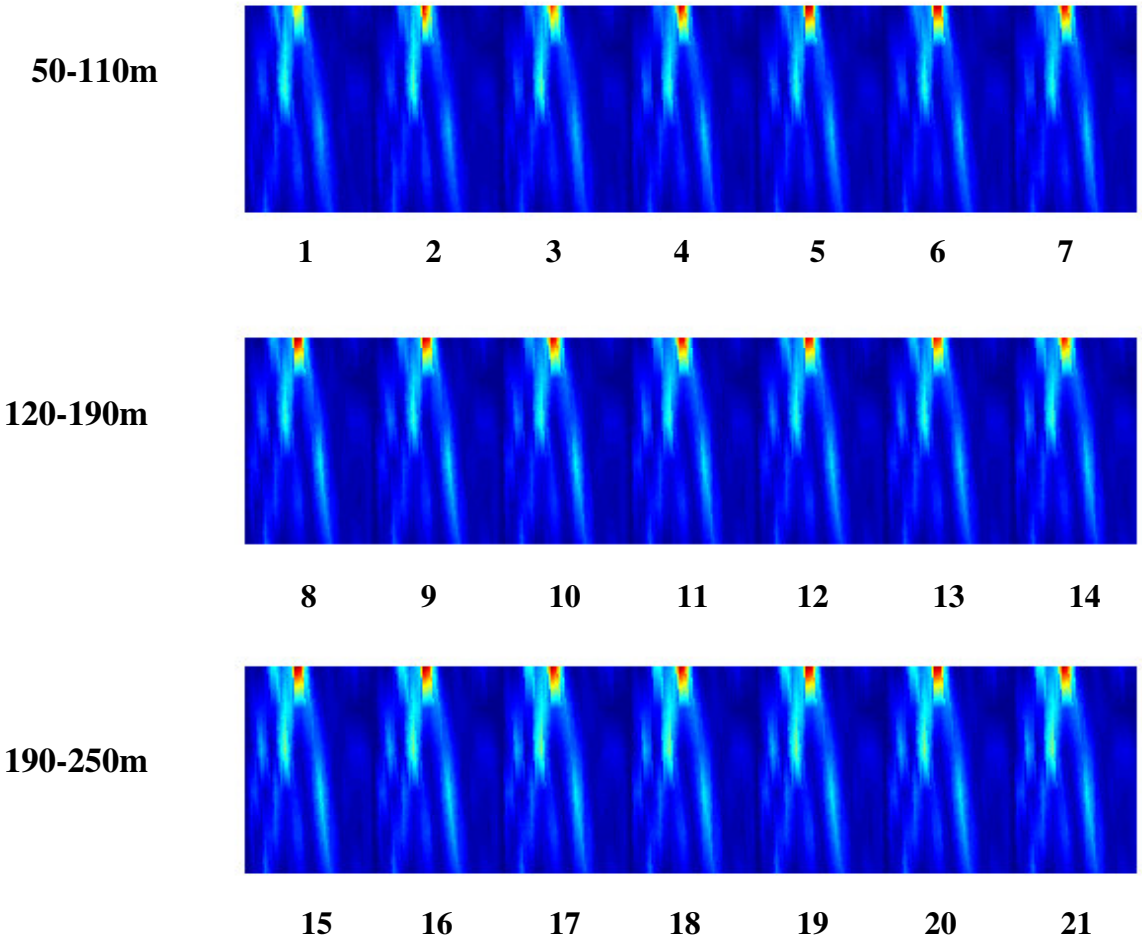

Fig.6.21. The 190-270-Hz ambiguity surface at a window around true source location for 21 search points for the first layer thickness

The focal function and ambiguity value at source location for 21 search points are shown in Figs 6.22 and 6.23, respectively. The focal function varies from 0.2 to 0.6, indicating that the

ambiguity surface changes insignificantly with respect to first layer thickness at higher frequency. Neither is there a significant change in the ambiguity value at the source location.

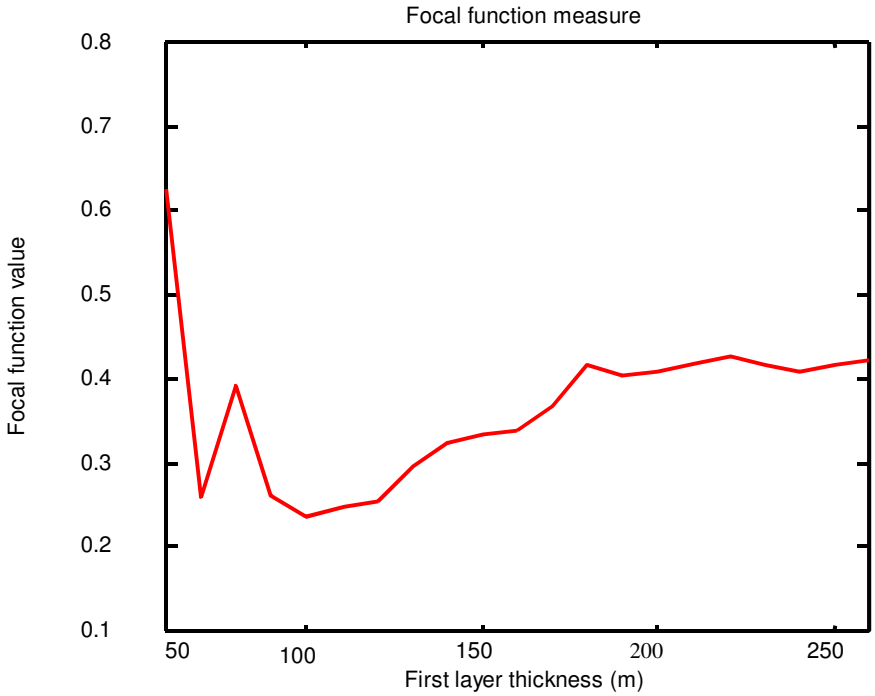

Fig. 6.22 The focal function for the first layer thickness

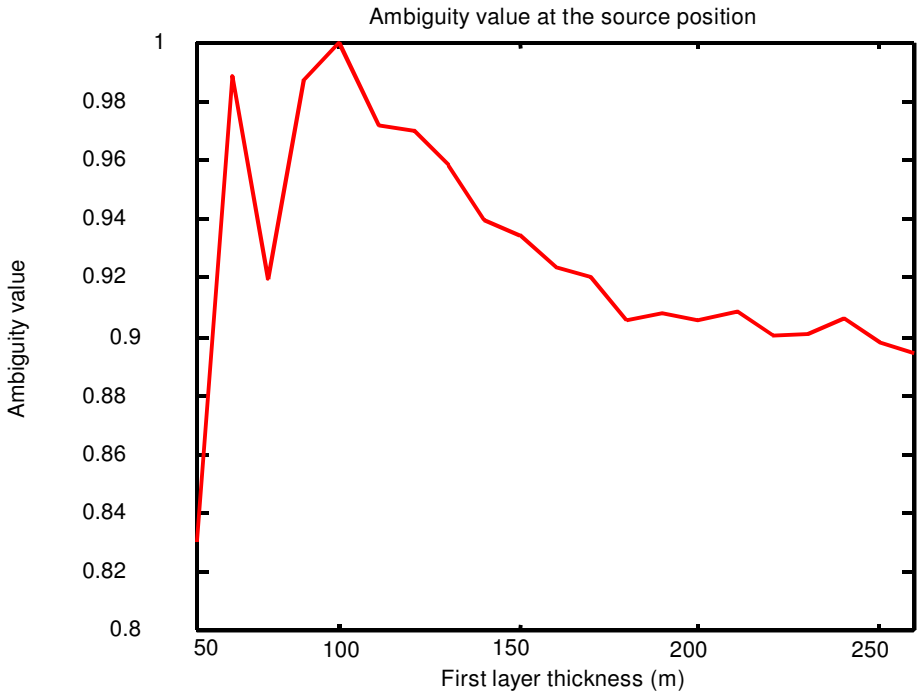

Fig. 6.23 The ambiguity value at the source location for the first layer thickness

After adjusting water depth and the upper compressional speed of the first layer we estimate the first layer thickness using the lower band data, i.e. 73-113 Hz. In Fig. 6.24 the ambiguity surface is shown for the 73-113 Hz band using the estimated values of the adjustable environmental parameters from the step one inversion.

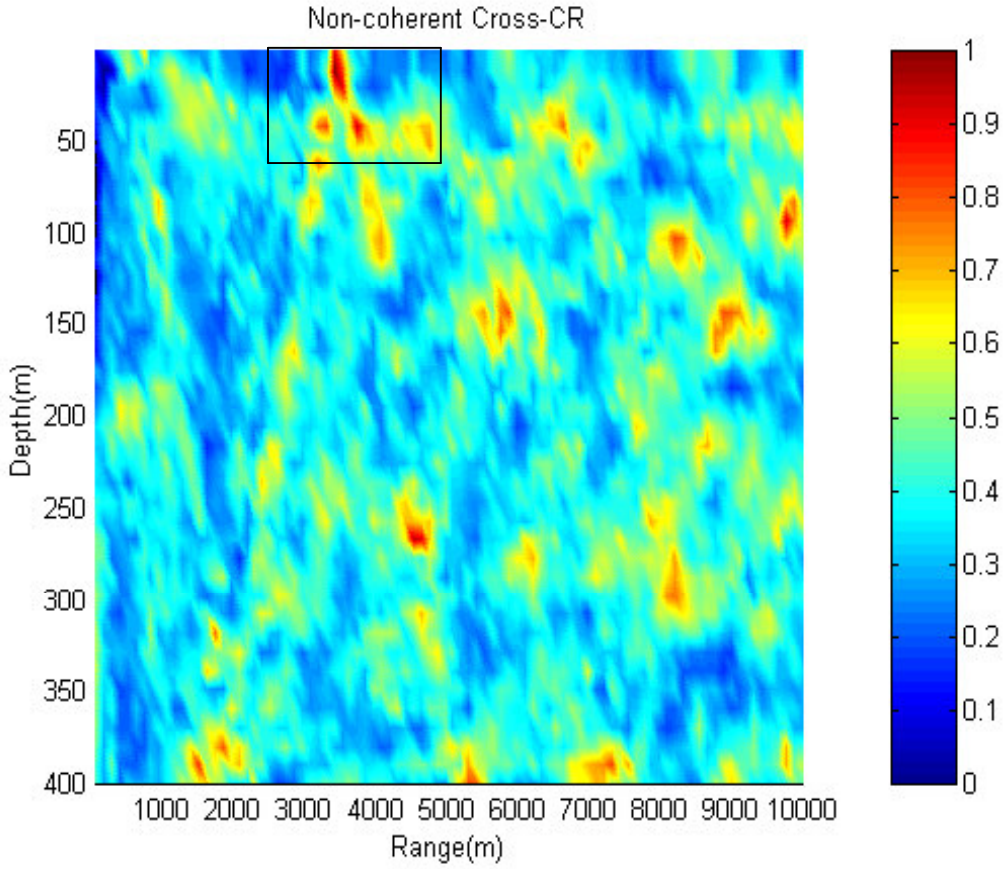

Fig.6.24 The 73-113Hz ambiguity surface obtained from cross CR-MFP in full range-depth space

We estimate value for the first layer thickness using a one-dimensional search over 21 possible parameter values. The search range is 50-250 m with a resolution of 10 m. For a window around the source location from ranges between 3 km and 4km and depths between 1 m and 60 m, the ambiguity surface is shown in Fig. 6.25.

The focal function and the ambiguity surface value at the source location are shown in Figs 6.26 and 6.27, respectively. The focal function shows a significant variation, indicating that the ambiguity surface varies considerably with respect to changes in the first layer thickness parameter. However, the ambiguity surface value at the source location is not as useful for the

layer thickness estimation, since the changes are very small. The focal function minimizes at search indices 6 and 9 corresponding respectively to the layer thickness of 100 m and 130 m.

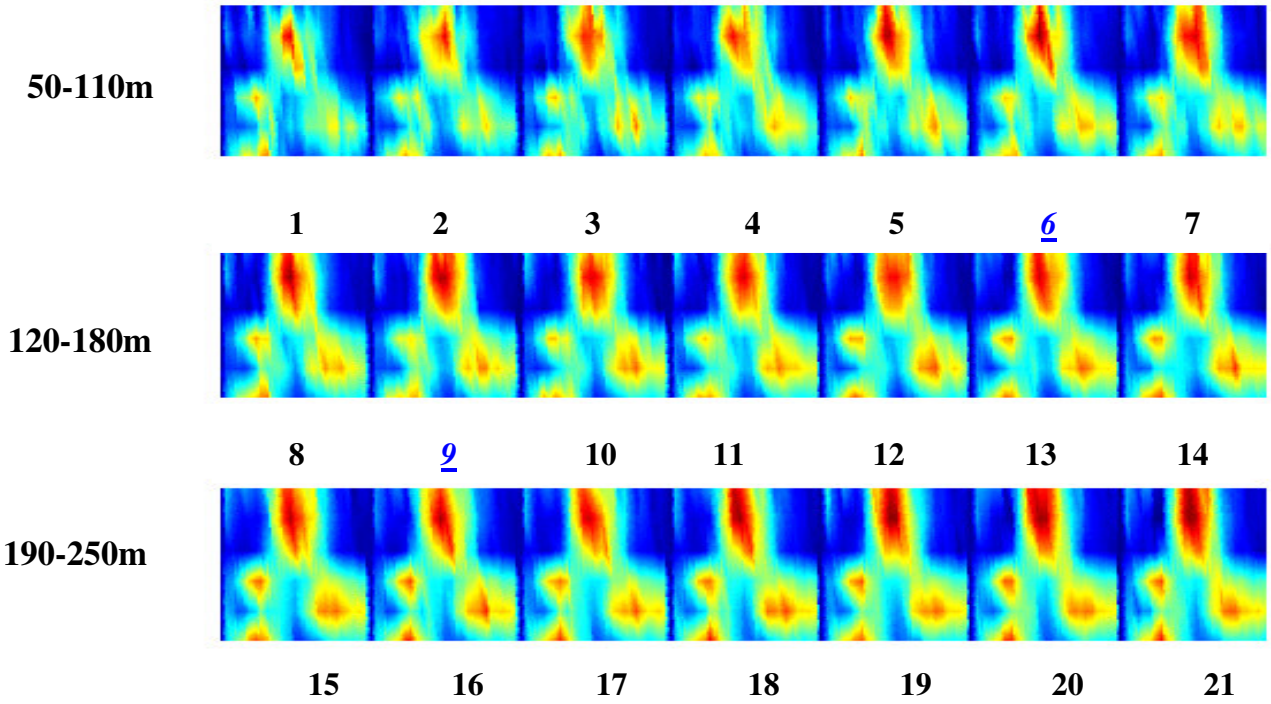

Fig.6.25. The 73-113 Hz ambiguity surface at a window around true source location for 21 search points for the first layer thickness

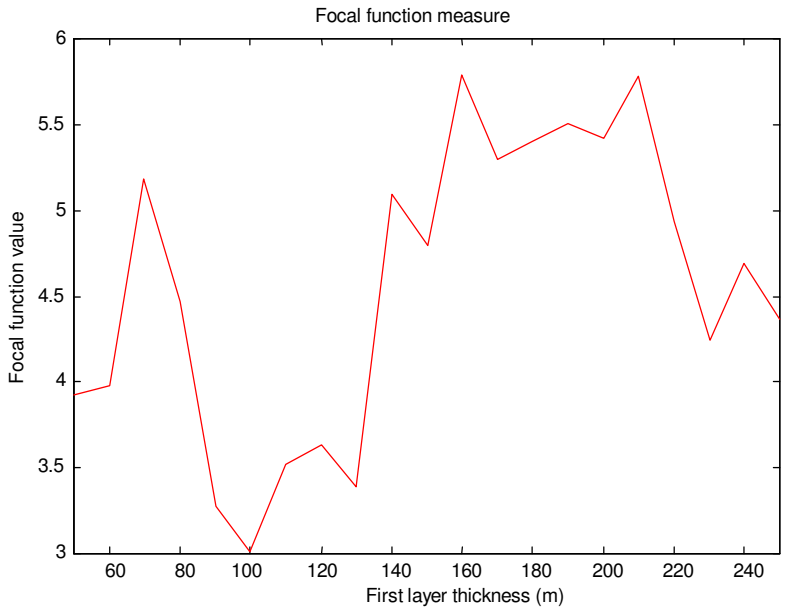

Fig. 6.26 The focal function with respect to the first layer thickness

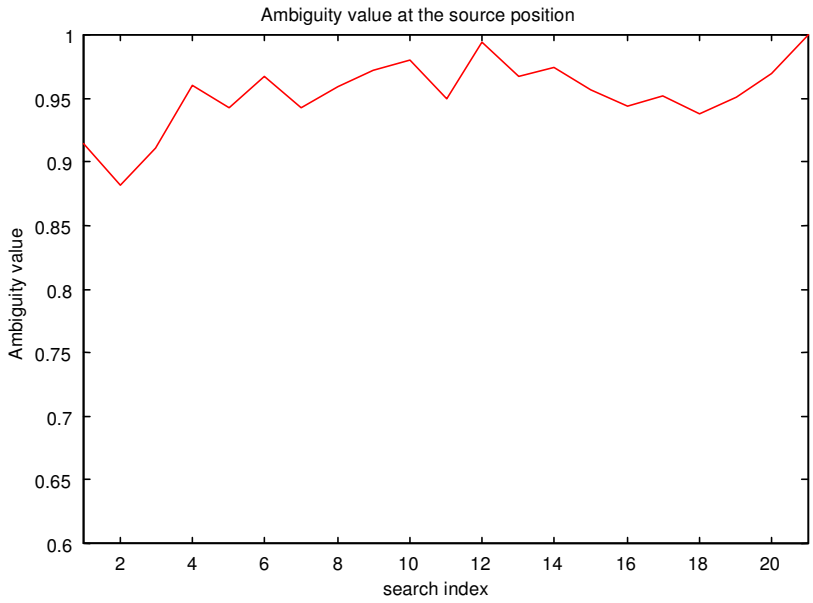

Fig. 6.27 The ambiguity value at the source location with respect to search index for the first layer thickness

This two-step technique is efficient computationally since the search grid decreases from 21*30=630 points to 21+30=51 points using the multi-step process, and is effective in providing realistic estimates. The estimates are consistent with the known bathymetry, and the results of an inversion of broadband shot data [9].

Chapter Seven

Conclusion, future work

The goal of this thesis has been to introduce MFPs for estimating the source location and the environmental parameters of a shallow water waveguide in which source transmits either broadband or narrowband random signals. We introduced a high resolution adaptive matched field processing algorithm for ocean parameter estimation. The algorithm makes use of ship noise as the sound source to estimate the geoacoustic properties of the signal path. We have also proposed a novel phase-regulated back wave propagation technique to increase the sensitivity of the MF inversion for geoacoustic model parameters having low sensitivity.

In chapter two we focused on the relationship between matched field processing and blind system identification (BSI). Blind system identification is a fundamental signal processing technique for estimating both unknown source and unknown system parameters when only the system output data are known. Three popular classes of matched field processors have been considered: 1) Bartlett matched field processor family, 2) maximum likelihood based matched field processors, and 3) bilinear matched field processors. We have shown that the widely used Bartlett family of matched field processors belongs to the class of channel subspace methods within BSI.

We showed that the necessary and sufficient conditions for identifiability of system transfer functions ensure the following intuitive requirements for single-input multiple-output systems:

6. All channels in the system must be sufficiently different from each other. For example, measured outputs can not be the same for any two channels.
7. The number of channels and size of the FIR transfer functions are known a priori
8. There must be a sufficient number of output data samples; the number of data samples can not be less than the number of unknown system parameters.
9. The input source must be sufficiently complex. For example, it can not be a constant or a single sinusoidal.

In practice, especially in underwater acoustics, we often know the sinusoidal model of signal propagation, and the task is to estimate unknown parameters of the model. For the specific problem of estimating the unknown parameters of the transfer function the necessary conditions

are satisfied, but the sufficient conditions are generally not satisfied. In order to reduce the non-uniqueness as much as possible we should carefully set the bounds of parameter variations. In general, the problem of non-uniqueness is greater for the bilinear matched field processors (BMF) due to the bilinear structure of the processor. More research is required to analyze the identifiability conditions and sensitivity, particularly for the BMFP.

We have introduced a cross-relation (CR) based matched field processor technique. The source is assumed to be a broadband or narrow-band random signal. The estimation formulas have been developed for deterministic and random sources, including non-stationary (NS) and wide sense stationary (WSS) random sources. For time varying sources, formulations based on an evolutive spectrum concept have been proposed to obtain the advantages of time-frequency analysis. The known signature of a time-varying source has been used for source localization in an environment that contains correlated interference. We have proposed an approach for designing a signal dependent time-frequency filter that preferentially passes only the known signal. The time-frequency MFP has been categorized as a "blind" processor since we have no information regarding the interference that may appear as correlated noise at the receiver. For each of above formulations, two estimation methods have been proposed, a self-CR or a cross-CR according to which channel output signal is used to construct the estimator. All the above formulations derive second order MFPs. We have extended the second-order cross-relation concept to higher order MFPs.

We have presented an evaluation of cross-relation matched field processors for source localization and estimation of environmental parameters and have compared their performances with those for other MFPs. The evaluation was conducted using both simulations and Pacific Shelf experimental data. In our experiment we considered a medium size merchant ship as the sound source in matched field localization and inversion.

In order to use the non-stationary form of a matched field processor, we must know the probability density function (PDF) of the ship signal. However, the PDF of the ship signal has not been reported in the literature. Further research is required to determine the ship PDF for use in the MFP developed for non-stationary sources.

7.1 Source localization

In the simulations, spatially and temporally white Gaussian random measurement noise with SNR of 20 dB was added to signals at receivers. The performance analysis was carried out by comparing the source location resolution and side lobe level for the Bartlett, MV, Westwood, and the CR-based MFPs (self-CR and cross-CR). The results have demonstrated that all estimators except the Westwood MFP detected the true source location. The cross-CR, self-CR, and MV give superior performance with respect to resolution and side lobe levels than that for the Bartlett. At SNR=-20 dB the results demonstrated that all estimators except the Westwood MFP detected the true source location. The cross-CR gave the best performance with respect to resolution and side lobe levels since it contains no self-spectrum noise components in its structure. The Bartlett and MV estimators show nearly identical performance. The self-CR gives a performance close to that of the Bartlett because of the effect of white noise that contaminates the self-spectrum elements.

In the analysis of the Pacific Shelf experimental data, both the tonal data and radiated ship data were considered. The tonal signals and the ship data were considered separately to demonstrate the performance of the MFPs for narrow band and broadband signals. The normal mode channel simulation code ORCA was used to generate the replica fields because of its versatility to accommodate both compressional and shear waves, its capability to produce accurate low frequency fields and its computational speed. For the 45 Hz and 70 Hz continuous wave (CW) data, the localization results have demonstrated that all MFPs other than MV and Westwood are successful at detecting of the true source location. The cross-CR and self-CR give resolution and side lobe levels performance superior to that of the Bartlett processor. For localization using the radiated ship signal, the signal spectrum was divided into three bands, 1-40 Hz, 73-133 Hz, and 150-270 Hz. The analysis was carried out using the second band, 73-133 Hz, and the third band, 150-270 Hz, to minimize the effect of interfering low frequency noise from other ships in the transportation route near the experimental area. For the band 73-133 Hz, the CR based MFPs gave considerable improvement in side-lobe level reduction and sharpness of the main lobe width in comparison with the Bartlett MFP. The MV MFPs gave poor side-lobe levels, and the Westwood MFP failed to localize the sources. For the third band, 150-270 Hz, all processors except the Westwood processor found the true source location. The reason for better

performance by the Bartlett processor in comparison to its result for the lower frequency band is likely due to the limited penetration depth in the ocean bottom at the higher frequencies in the 150-270 Hz band where the interaction with the ocean bottom is restricted within a few wavelengths at the seafloor. Consequently the localization performance is less sensitive to mismatch in the acoustic model of the bottom.

A simulation was also conducted to evaluate a time-frequency MFP. The source propagates a chirp pulse (unknown to the receiver) in an environment in the presence of an interfering source. The Bartlett processor localized both the chirp source and the interfering signal, but there were several false detections indicated by the ambiguity surface. Because the CR based MFPs do not utilize TF features, they failed to localize the chirp source. Application of the pre-process masking cancelled the interfering sources, and both versions of TF-MFP (self-CR and cross-CR) successfully localized the chirp source. The next step in research is to evaluate TF-MFP with real data.

In another experiment we applied a higher order CR-MFP to localize the ship using the bands 73-133 Hz and 150-270 Hz bands. For the 73-133 Hz frequency band, the 3^{rd} order cross-CR MFP showed a strong peak at the ship position. However the 4^{th} order MFP showed a weak value at the ship position. For the higher frequency band of 150-270 Hz, both 3^{rd} and 4^{th} order CR-MFP showed strong peaks at the ship position. The results suggested weak Gaussian interference in the Pacific Shelf trial. Further research is required in applying the higher order MFPs to data in an environment with strong Gaussian interference.

7.2 Inversion

For the inversion of geoacoustic parameters we have significantly reduced the search space by classifying the geoacoustic parameters based on the acoustic penetration depth in the ocean bottom for different frequencies. We first estimated the environmental parameters of upper sediment layers using high frequency ship noise that effectively samples the sea floor environment and then estimated parameters of deeper layers using lower frequency noise data. We first estimated the water depth and upper compressional speed of the first layer using the frequency band 190-270 Hz. Next we estimated the first layer thickness using the frequency

band 73-133 Hz. This two-step technique was computaionally efficient since the search grid decreased from 630 points to 51 points, and effective in providing realistic estimates,

We have also proposed the back wave propagation (BWP) concept based on the reciprocity and superposition properties of the ocean wave-guide. The concept states that the measured pressure fields can be considered as sources for an array of transmitters; in practice, the conjugate of the measured field at the array is weighted by the range and back propagated from the array. We have shown, given that the ocean field is a passive environment and the geometry of the transmit array is the same as the experimental geometry, that only for the true ocean environmental parameters does the back-propagated wave field converge to the location of the source. The phase regulated BWP technique allows the advantage of adapting to the environmental conditions through variation of the sensitivity factor α, which enhances the phase changes due to model and environmental mismatch. The value of α is limited by the SNR. There is an energy distribution around the source when a mismatch occurs. This fact suggests that the energy distribution of the back-propagated field near the source could be used as a new criterion to assess the best match in searching candidate geoacoustic models.

In order to reduce the D-dimensional search space to the T successive d-dimensional search spaces ($D=Td$ where $T<D$), we have used the fact that the pressure field has different sensitivities with respect to different ocean waveguide parameters that are not strongly correlated. We first adjust the high sensitivity parameters such as water depth, then we search among potential values of medium sensitivity parameters such as compressional speed using a higher value of α, and at the last step we increase the sensitivity factor to a successively higher value to adjust the low sensitivity parameters. This gives a three-step process. The method has been tested in a simulation, and then applied to invert experimental data from the Pacific Shelf experiment. We have estimated values for water depth, compressional speed at the base of sediment (second) layer and the density of the sediment layer. The results show that the BWP is successful for estimating ocean parameters with different sensitivities, however, the inversion results of both methods (BWP and CR-MFP) are self consistent.

References

[1] Tolstoy A., *"Matched field processing for underwater acoustics"*, World scientific, Singapore, 1993

[2] Booth, N.O., et al., "Source localization with broadband matched field processing in shallow water", *IEEE J. Oceanic Eng.,* Vol. 21, pp. 402-412, 1996

[3] Westwood, E.K. "Broad band matched field source localization", *J. Acoust. Soc. Amer.*, Vol. 91(5), pp. 2777-2789, 1992

[4] Knobles, D. P. and Mitchell, S.K, "Broadband localization by matched fields in range and bearing in shallow water", *J. Acoust. Soc. Amer.*, Vol. 96, pp. 1813-1820, 1994

[5] Michalopoulou, Z.H., and Porter, "Matched field processing for broadband localization", *IEEE J. Oceanic Eng*., Vol. 21, pp. 384-392, 1996

[6] Gerstoft, P., "Inversion of seismo-acoustic data using genetic algorithms", *J. Acoust. Soc. Amer.*, Vol. 95, pp. 770-782, 1994

[7] Chapman N. R. and Ozard K. S., "Matched field inversion for geoacoustic properties of young ocean crust", *in Full Filed Inversion Methods in Ocean and Seismo-Acoustics,* O. Diachok, Editor, Kluwer Academic Publishers, Dordrecht, pp. 165-170, 1995

[8] Hermand J.P. and Gerstoft P., "Inversion of broadband multitone acoustic data from the Yellow-Shark summer experiments", *IEEE J. Oceanic Eng.*, Vol. 21, pp. 324-346, 1996

[9] Hannay D.E. and Chapman N.R., "Coherent broadband matched filed processing for geoacoustic parameter estimation", *in Proceedings of 8th Matched Field Processing Workshop*, Victoria, BC, NRAD Technical Document 2932, pp. 163-171, 1996

[10] Deane G. B. and Buckingham M. J., "Vertical coherence of ambient noise in shallow water overlaying a fluid seabed, *J. Acoust. Soc. Amer.*, 1996

[11] Frisk, G. V., *Ocean and seabed acoustics*, PTR Prentice-Hall, Englewood Cliffs, New Jersey, 1994

[12] Chin-Bing S.A., King D. B., and Boyd J. D., "The effect of ocean environmental variability on underwater acoustic propagation forecasting", *in Oceanography and Acoustics-Prediction and Propagation Models*, Edited by R. T. Beyer, pp. 7-49, AIP, New York, 1994

[13] Westwood E. K. and Vidmar P. J., "Eigenray finding and time-series simulation in a layered-bottom ocean", *J. Acoust. Soc. Amer.*, Vol. 81, pp. 912-924, 1987

[14] Porter M., "Ocean acoustic library", *http://oalib.njit.edu*, 1998

[15] Westwood E. K., "ORCA User's Manual", Available via FTP from *ftp.arlut.utexas.edu*

[16] Baggeroer A.B., Kuperman W.A., Schmidt H., "Matched field processing: Source localization in correlated noise as optimum parameter estimation problem", *J. Acoust. Soc. Amer.,* Vol. 83 (2), pp. 571-587, 1988

[17] Baggeroer A.B., Kuperman W.A., Mikhalevsky N., "An overview of matched field methods in ocean acoustic", *IEEE J. Oceanic Engineering*, Vol. 18, No. 4, pp. 401-424, 1993

[18] Kaufhold B., Kirlin R. L., Dizaji R. "Blind system identification using normalized Fourier coefficient gradient vectors obtained from time-frequency entropy-based blind clustering of data wavelets ", *Digital Signal Processing Journal*, Vol. 9, pp. 18-35, 1999

[19] Justice J.H. et al (Haykin S. editor),*"Array signal processing"*, Prentice-Hall, New Jersey, 1985

[20] Bienvenu G. and Kopp L. ,"Optimality of high resolution array processing using the eigensystem approach", *IEEE Trans. on Acoustic Speech and Signal Processing*, Vol. 31, pp. 1235-1247, 1983

[21] Burdic W. S., *"Underwater acoustic system analysis"*, Prentice-Hall, New Jersey, 1991

[22] Fizell R. G., "Application of high resolution processing to range and depth estimation using ambiguity function methods", *J. Acoust. Soc. Amer.*, Vol. 82, pp. 606-613, 1987

[23] Akaike M., "A new look at the statistical model identification", *IEEE Trans. On Automatic Control,* Vol. 19, pp. 716-737, 1974

[24] Wax M., "Model based processing in sensor arrays", *in Advances in spectrum analysis and array processing*, Vol. 3, Edited by S. Haykin, pp. 1-47, Prentice-Hall, Englewood, Cliffs, New Jersey

[25] Papoulis A., *"Probability, random variables, and stochastic processes"*, McGraw-Hill Co., 1990

[26] Daugherty J. R. and Lynch J. F., " Surface wave, internal wave, and source motion effect on matched filed processing in shallow water waveguide", *J. Acoust. Soc. Amer.*, Vol. 87, pp. 2503-2526, 1990

[27] Schmidt H., Baggeroer W., Kuperman A., and Scheer E. K., "Environmentally tolerant beamforming for high resolution matched field processing: Deterministic mismatch", *J. Acoust. Soc. Amer.*, Vol. 88, pp. 1851-1862, 1990

[28] Shang E. C., "Source depth estimation in waveguides", *J. Acoust. Soc. Amer.*, Vol. 77, pp. 1413-1418, 1985

[29] Richardson A. M. and Notle L. W., "A posteriori probability source localization in an uncertain sound speed, deep ocean environment", *J. Acoust. Soc. Amer.*, Vol. 89, pp. 2280-2284, 1991

[30] Abed-Meraim K. et al, "Blind system identification", *Proceeding of the IEEE*, Vol. 85, No. 8, 1997

[31] Abed-Meraim K., Cardoso J. F., Gorokhov A. Y., and Loubaton P., "On subspace methods for blind identification of single-input multiple-output FIR systems", *IEEE Trans. On Signal Processing*, Vol. 45, pp. 42-55, 1997

[32] Abed-Meraim K., Loubaton P., and Moulines E., "A subspace algorithm for certain blind identification problems", *IEEE Trans. On Information Theory*, Vol. 43, 499-511, 1997

[33] Moulines E., Duhamel P., Cardoso J. F., and Mayrargue S., "Subspace methods for the blind identification of multi-channel FIR filters", *IEEE Trans. On Signal Processing*, Vol. 453, pp. 516-525, 1995

[34] Qiu W., and Hua Y., "Performance analysis of the subspace method for blind channel identification", *Signal Processing*, Vol. 50, pp. 71-82, 1996

[35] Tong L., Xu G., and Kailath T., "Blind identification and equalization based on second-order statistics: A time domain approach", *IEEE Trans. On Information Theory*, Vol. 40, pp. 340-349, 1994

[36] Tong L., Xu G., and Kailath T., "Blind identification and equalization based on second-order statistics: A frequency domain approach," *IEEE Trans. On Information Theory*, Vol. 41, pp. 329-348, 1995

[37] Xu G., Liu H., Tong L., and Kailath T., "A least squares approach to blind channel identification", *IEEE Trans. On Signal Processing*, Vol. 43, pp. 2982-2993, 1995

[38] Kirlin R. L., "Estimation of transfer function parameters with output Fourier transform sensitivity vectors", *ICASSP 97*, Vol. 5, pp. 3933-3936, 1997

[39] Frazer N. and Sun X., "New objective function for waveform inversion", *Geophysics,* Vol. 63, pp. 213-222, 1998

[40] Kundur D. and Hatzinakos D., "Blind image de-convolution", *IEEE Signal Processing Magazine*, pp. 43-64, 1996

[41] Yu Y., and Kaveh M. A., "A regularization approach to joint blur identification and image restoration", *IEEE Trans. On Information Theory*, Vol. 5, pp. 416-428, 1996

[42] Abed-Meraim K. and Hua Y., "Blind identification of multiple-input multiple-output system using minimum noise subspace", *IEEE Trans. On Signal Processing*, Vol. 45, pp. 254-258, 1997

[43] Van der Veen A. J., Talwar S., and Paulraj A., "A subspace approach to blind space-time signal processing for wireless communication systems", *IEEE Trans. On Signal Processing*, Vol. 45, No. 1, 1997

[44] Liu H. and Xu G., "Multi-user blind channel estimation and spatial channel pre-equalization, *ICASSP 95*, pp. 1765-1769, 1995

[45] Urick R. J. *"Principles of underwater sound"*, 3rd edition, McGraw-Hill Book Company, 1983

[46] Gray L. M. and Greeley D. S., "Source level model for propeller blade rate radiation for the world's merchant fleet", *J. Acoust. Soc. Amer.*, Vol. 67 (2), pp. 516-522, 1980

[47] Scrimger P. and Heitmeyer R. M., "Acoustic source-level measurements for a variety of merchant ships", *J. Acoust. Soc. Amer.*, Vol. 89 (2), pp. 691-699, 1991

[48] Ross D., *"Mechanics of underwater noise"*, Pergamon Press, New York, 1976

[49] Golub G. and Van Loan C., *"Matrix computations"*, Johns Hopkins Press, Maryland, 1983

[50] Hlawatsch F. and Boudreaux-Bartles G. F., "Linear and quadratic time-frequency signal representations", *IEEE Signal Processing Magazine*, pp. 21-67, April 1992

[51] Papandreou-Suppappola A., Hlawatsch F., Boudreaux-Bartels F., "Quadratic time-frequency representations with scale covariance and generalized time-shift covariance: A unified framework for the affine, hyperbolic, and power classes", *Digital Signal Processing Journal*, Vol. 8, pp. 3-48, 1998

[52] Boashash B. (Editor), "*Time-Frequency signal analysis, methods and applications"*, John Wiley & Sons Inc., New York, 1992

[53] Rihaczeck W. "Signal energy distribution in time and frequency ", *IEEE Trans. On Information Theory*, Vol. 14, No. 3, pages 369-374, 1968.

[54] Mendel J. M., "Tutorial on higher-order statistics (spectra) in signal processing and system theory: theoretical results and some applications", *Proceedings of the IEEE*, Vol. 79, pp. 278-305, 1991

[55] Nikias C. L., and Raghuveer M., "Bispectrum estimation: a digital signal processing framework", *Proceeding of IEEE*, Vol. 75, pp. 869-891, 1987

[56] Pan R., Nikias C. L., "The complex cepstrum of higher-order moments", *IEEE Trans. On ASSP*, Vol. 36, pp. 186-205, 1988

[57] Tappert F.D. et al., "Source localization by using the PE method", *J. Acoust. Soc. Amer*., Vol. 78, S30, 1985

[58] Collins M. D. and Kuperman W. A., "Factorization: environmental focusing and source localization", *J. Acoust. Soc. Amer*., Vol. 90, pp. 1410-1422, 1991

[59] Thomson D. J. et al. "A matched-field backpropagation algorithm for source localization", *Oceans 97*, Vol. 1, PP 602-607, 1997

[60] Chapman N. R. and Lindsay C. E., "Matched-field inversion for geoacoustic model parameters in shallow water", *IEEE J. Oceanic Engineering*, Vol. 21, No.4 , pp. 347-354, 1996

[61] Spence G. D., Minshull T. A., and Fink C., "Seismic studies of methane gas hydrate, offshore Vancouver Island", *in Proceedings ODP, Scientific Results*, Vol. 146, pt. 1, B. Carson, G. K. Westbrook, R. J. Musgrave and E. Seuss, Eds. College station, TX: Ocean Drilling Program, 1995

[62] *Canadian Forces Meteorology and Oceanography Center (METOC)*, Victoria, BC, private communication

[63] Davis E., Currie R. and Sawyer J. F. , "Southern Vancouver Island margin bathymetry chart, map 7, geological survey of Canada", *Pacific Geoscience Center*, Sidney, BC, 1987

[64] Taillefer L. M., *"Range dependent matched filed source localization and tracking in shallow water on a continental slope region of the north-east Pacific Ocean"*, M.Sc. Thesis, School of Earth and Ocean Sciences, University of Victoria, Victoria, BC, 1998

[65] Hannay D., *"Broadband matched field processing for geoacoustic parameter estimation"*, Contractor report 96/402SPK W7707-5-3243/01-HAL, JASCO Research Ltd., July 1996

[66] Chapman N. R., Yeremy M. L., Ozard J. M., and Wilmut M. J., "Range dependence of matched-field source localization in shallow water", *Symposium on Shallow Water Undersea Warfare - From Staging to Sustainment, Proceedings*, Subgroup G – Undersea Warfare, Edited by Canadian Forces Maritime Warfare Center, pp. 227-236, TTCP Halifax, NS 1996

[67] Du W. and Kirlin R. L.," Enhancement of covariance matrix for array processing", *IEEE Trans. On Signal Processing*, Vol. 40, No. 10, pp. 2602-2606, 1992

[68] Guo Z., Durand L., Lee H., "The time-frequency distribution of non-stationary signals based on a Bessel kernel", *IEEE Trans. On Signal Processing,* Vol. 42, No. 7, pp. 1700-1707, 1994

[69] Choi H. and Williams W., "Improved time-frequency representations of multi-component signals using exponential kernels", *IEEE Trans. On ASSP*, Vol. 37, No. 6, pp. 862-871, 1989

[70] Auger F., "Some simple parameter determination rules for the generalized choi-williams and Butterworth distributions", *IEEE Signal Processing Letter*, Vol. 1, No. 1, pp. 9-11, 1994

[71] Czerwinski R. and Jones D. L., "Adaptive cone-kernel time-frequency analysis", *IEEE Trans. On Signal Processing*, Vol. 43, pp. 1715-1719, 1995

[72] Costa A. and Boudreaux-Bartels F., "Design of time-frequency representations using a multiform, tiltable exponential kernel", *IEEE Trans. On Signal Processing,* Vol. 43, No. 1, pp. 2281-2301, 1995

[73] Baraniuk R. and Jones D. L., "A signal-dependent time-frequency representation: optimal kernel design", *IEEE Trans. On Signal Processing*, Vol. 41, No. 4, pp. 1589-1602, 1993

[74] Baraniuk R. and Jones D. L., "A signal-dependent time-frequency representation: Fast algorithm for optimal kernel design", *IEEE Trans. On Signal Processing*, Vol. 42, No. 1, pp. 134-146, 1994

[75] Jones D. L. and Baraniuk R., "An adaptive optimal-kernel time-frequency representation", *IEEE Trans. On Signal Processing*, Vol. 43, No. 10, pp. 2361-2371, 1995

[76] Diachok O., Caiti A., Gerstoft P., and Schmidt H., *Full field inversion methods in ocean and seismo-acoustics*, Kluwer Academic Publishers, 1995

[77] Collins M. D., Kuperman W. A., and Schmidt H., "Nonlinear inversion for ocean-bottom properties", *J. Acoust. Soc. Amer.*, Vol. 92, pp. 2770-2783, 1992

[78] Dosso S. E., Yeremy M. L., Ozard J. M., and Chapman N. R., "Estimation of ocean bottom properties by matched field inversion of acoustic field data", *IEEE J. Oceanic Eng.*, Vol. 18, pp. 232-239, 1993

[79] Laarhoven P. J. and aarts E. H., *Simulated annealing: theory and applications*, Kluwer Academic Publishers, 1409-1412, 1987

[80] Gingras D. F. and Gerstoft P., "Global inversion of acoustic field data in shallow water using genetic algorithms", in *Full field inversion methods in ocean and seismo-acoustics*, Kluwer Academic Publishers, pp. 317-322, 1995

[81] Jensen F.B. et al, *"Computational ocean acoustics"*, AIP, New York, 1994